IntechOpen

Iron Ores
and Iron Oxide Materials

Edited by Volodymyr Shatokha

IRON ORES AND IRON OXIDE MATERIALS

Edited by **Volodymyr Shatokha**

Iron Ores and Iron Oxide Materials
http://dx.doi.org/10.5772/intechopen.69715
Edited by Volodymyr Shatokha

Contributors

Yiwei Zhong, Jintao Gao, Zhancheng Guo, Zhi Wang, Daniel Fernández González, Luis Felipe Verdeja González, Juan Piñuela-Noval, Mehmet Çelikdemir, Musa Sarikaya, Tolga Depci, Ramazan Aydoğmuş, Ayşegül Yücel, Roberto Baca, Yasuhisa Maeda, Guangrong Li, Sandra Lúcia De Moraes, José Renato Baptista De Lima, Tiago Ramos Ribeiro, Davidson Egirani, Mohamed Latif, Nanfe Poyi, Napoleon Wessey, Shukla Acharjee, Iulia Andreea Pinzaru, Cristina Dehelean, Elena Alina Moaca, Dorina Coricovac, Codruta Soica, Cornelia Silvia Pacurariu, Munetoshi Seki, Eri Fumoto, Shinya Sato, Toshimasa Takanohashi, Hayrunnisa Nadaroglu, Azize Alayli Gungor, Semra Cicek, Mehdi Baniasadi, Maryam Baniasadi, Bernhard Peters

© The Editor(s) and the Author(s) 2018
The rights of the editor(s) and the author(s) have been asserted in accordance with the Copyright, Designs and Patents Act 1988. All rights to the book as a whole are reserved by INTECHOPEN LIMITED. The book as a whole (compilation) cannot be reproduced, distributed or used for commercial or non-commercial purposes without INTECHOPEN LIMITED's written permission. Enquiries concerning the use of the book should be directed to INTECHOPEN LIMITED rights and permissions department (permissions@intechopen.com).
Violations are liable to prosecution under the governing Copyright Law.

Individual chapters of this publication are distributed under the terms of the Creative Commons Attribution 3.0 Unported License which permits commercial use, distribution and reproduction of the individual chapters, provided the original author(s) and source publication are appropriately acknowledged. If so indicated, certain images may not be included under the Creative Commons license. In such cases users will need to obtain permission from the license holder to reproduce the material. More details and guidelines concerning content reuse and adaptation can be foundat http://www.intechopen.com/copyright-policy.html.

Notice

Statements and opinions expressed in the chapters are these of the individual contributors and not necessarily those of the editors or publisher. No responsibility is accepted for the accuracy of information contained in the published chapters. The publisher assumes no responsibility for any damage or injury to persons or property arising out of the use of any materials, instructions, methods or ideas contained in the book.

First published in London, United Kingdom, 2018 by IntechOpen
eBook (PDF) Published by IntechOpen, 2019
IntechOpen is the global imprint of INTECHOPEN LIMITED, registered in England and Wales, registration number: 11086078, The Shard, 25th floor, 32 London Bridge Street
London, SE19SG – United Kingdom
Printed in Croatia

British Library Cataloguing-in-Publication Data
A catalogue record for this book is available from the British Library

Additional hard and PDF copies can be obtained from orders@intechopen.com

Iron Ores and Iron Oxide Materials
Edited by Volodymyr Shatokha

p. cm.

Print ISBN 978-1-78923-320-9

Online ISBN 978-1-78923-321-6

eBook (PDF) ISBN 978-1-83881-411-3

Meet the editor

Volodymyr Shatokha graduated in 1982 as a ferrous metallurgy engineer and in 1985 received his PhD degree from the Dnipropetrovsk Metallurgical Institute (since 1999; National Metallurgical Academy of Ukraine). In 1998, he received the title of being a professor with the ironmaking chair. During 1999–2002, he was the dean of the Metallurgical Faculty. Since 2002, he works as the vice rector for Research and Education. His research deals mainly with properties of iron ore materials, physicochemical processes of ironmaking, recycling methods, sustainability analysis, and so on. He is the author of over 150 research papers, 7 books and 7 patents. He is an honorary professor at the Inner Mongolia University of Science and Technology, China; a visiting professor at the University of Tokyo (2013); a laureate of the State Prize of Ukraine in Science and Technology (2010); and a fellow of the Erasmus+ Jean Monnet Programme for the EU climate and energy policy studies (since 2015).

Contents

Preface

Despite an increasing importance of the new materials, iron remains the basis of modern human civilization, and steel (alloy of iron and carbon) is the most important engineering and construction material worldwide. In other words, we still live in the Iron Age. In this respect, iron ore is strategically an important resource and the way how it is mined, processed and applied, determines the framework of our current and future industrial development.

This book encompasses the entire value chain of iron ore mining and processing industries, and therefore is structured into three sections delivering a synergy of multidisciplinary aspects such as (i) geological genesis and characteristics of iron ore deposits; (ii) processing, agglomeration, reduction and smelting of iron ore materials; and (iii) advanced applications of iron oxide materials. The chapters are written by the researchers from all over the world.

I am very grateful to all the authors for their contribution, willingness to share research results and expertise with the reading audience, and for their hard work to make this book happen.

I sincerely thank the publisher *IntechOpen* for the initiative to publish this book. Reading audience of researchers and students has now a rare opportunity to find comprehensive, cutting-edge information covering a wide range of interdisciplinary issues in the domain of science and technology of iron ores and iron oxide materials in a single book.

Volodymyr Shatokha
National Metallurgical Academy of Ukraine
Dnipro, Ukraine

Section 1

Genesis, Properties and Mining

Chapter 1

The Chinese Iron Ore Deposits and Ore Production

Guangrong Li

Additional information is available at the end of the chapter

http://dx.doi.org/10.5772/intechopen.76729

Abstract

Probably due to large national land area and multi-period orogeny, from the view of metallogeny, lots of iron deposits developed in China, and the proven total reserves of iron ores are relatively abundant, but mainly low-grade ores. For years, China's iron ore reserves are far from being able to meet the requirement of rapid development of steel industry. China is the world's largest importer of iron ore, whose imports accounted for one-third of the world's total in recent decades; however, the buyer has not the final say. The strategic importance of iron ore resources in national economy not only depends on the social value and economic value created by the iron ore exploitation, but also depends on whether the requirements of the steel industry and steel downstream industry, and safety ensuring, economy and sustainability of steel and steel downstream industry. Herein, the iron mineral processing and metallurgy technology are also briefly illustrated.

Keywords: iron ore deposits, mineral processing, ore metallurgy, iron ore demand and supply, iron ore metallogeny, China

1. Introduction

This chapter will give a general description on the Chinese iron ore deposits, supply and demand market, mineral processing and iron ore metallurgy technology. For years, the Chinese iron industry is highly dependent on the foreign mines due its quick development on economics. Presently, it is the world's largest importer of iron ore, whose imports accounted for one-third of the world's total. In fact, it holds abundant iron resource, although most are low grade and small. Therefore, the mineral processing and metallurgy technology quickly develop accompanying its iron demand and economic soaring.

IntechOpen

2. China's major iron ore types

Probably due to large national land area and multi-period orogeny, lots of iron deposits developed in China, and the proven total reserves of iron ores are relatively abundant, but mainly low-grade ores. The research shows that the types of iron ore deposits in China are diverse and the metallogenic epoch spanned from the Archean to the Cenozoic, which mainly includes seven types [1–6].

2.1. Sedimentary - metamorphic iron ore deposits

This type of iron deposits is also called banded iron formation (BIF). The mineralization ages were mainly Archean and Paleoproterozoic. The reserves of proven mineral resources were probably more than 33 billion tons, accounting for 55% of the total reserves of the country, which is a very important iron ore in China. According to the ore and gouge mineral association, as well as geological features, it would be subdivided into metamorphic iron-siliceous iron ore deposits and metamorphic carbonate iron ore deposits. Their grades were about 25–40% (w(TFe)).

The BIF were affected by regional metamorphism and associated with volcanic-iron-siliceous sedimentary deposits. They mainly developed in the Precambrian metamorphic rocks, mostly large deposits. The Anshan in Liaoning Province, Jidong in Hebei Province, Wutai-Lvliang in Shanxi Province, and central Inner Mongolia are mainly developed area where the iron ore deposits were thought the most representative. The southern margin of Yangtze plate, Qinling orogenic belt, Qilian orogenic belt, and the East Tianshan region were also distributed.

The metamorphic carbonate iron deposits were carbonate-type sedimentary iron deposits suffered to minor regional metamorphism. They mainly developed in the Proterozoic strata, and the southeast Jilin Province is known for yielding this deposit. That led to it also called "Dalizi type iron ore deposit" in China, although it is also developed in Yimen, Eshan, Huanian in Yunnan Province.

2.2. Late magmatic iron ore deposits

This type of iron ore deposit is associated with the mafic-ultramafic magmatic intrusions of the iron and its iron minerals are rich in vanadium and titanium, commonly referred to as vanadium-titanium magnetite deposits. The mineralization ages are mainly Paleozoic and Proterozoic, with proven reserves of 9 billion tons, accounting for 15% of the total reserves of the country. According to the metallogensis, they can be subdivided into late magmatic differentiated deposits and late magmatic intrusive iron deposits. Late magmatic differentiated iron deposits are formed by the residual magma rich in iron, vanadium and titanium formed by late differentiation of magma crystals. These deposits are mostly of large in reserve and are mainly distributed in Panzhihua and Xichang area in Sichuan Province. They are often called "Panzhihua-type" iron deposits in China. Late magmatic intrusive iron deposits are late-differentiated iron-bearing ore fluids that break into or along the rock mass. The reserve of this type deposit is generally medium to small, mainly distributed in the Damiao and Heishan in Hebei Province, which is called the "Damiao-type" iron deposit.

2.3. Contact metasomatic - hydrothermal iron ore deposits

This type of iron ores are associated with the contact metasomatism resulted from intrusive rocks and carbonate rocks, and are formed by the exchange of iron-bearing gas-water solutions. Such deposits generally have typical skarn mineral assemblages and are also known as silicon carbon type deposit. Skarn iron ore ages were mainly Mesozoic, ore grade is generally rich, the reserves are generally small and medium, although there are some large ones. Identified reserves of this type are 8 billion tons, accounting for 13% of the total reserves. Skarn iron ore is widely distributed in China, with such deposits as Handan, Laiwu, Daye and Linfen in the east. In addition, Cuihongshan in Heilongjiang Province, Huanggang in Inner Mongolia, Lizhu in Zhejiang Province, Dading in Guangdong Province, Mulonggou in Xianxi Province and Nixon in Tibet also yield skarn type iron ore deposits.

2.4. Volcanic - intrusive type iron ore deposits

This type of deposit is associated with volcanic rocks and sub-volcanic rocks in a genetic relationship, with a proven reserve of 2 billion tons, accounting for 4% of the country's total reserves. It would be divided into continental volcano-intrusive iron ore and marine volcano-intrusive iron deposits.

Continental volcanic-intrusive iron ore deposits are mostly associated with middle- or medium-acid volcanic rocks and are mainly produced in volcanic clasts or in the contact zones within and around the pluton. The mineralization age is Mesozoic. It is mainly located in Ningwu-Luzong area, often referred to as "porphyrite iron ore". In addition, the Jiaduoling iron ore deposit in Tibet and the Liangzi iron ore in Sichuan Province are also known as continental volcano-intrusive iron deposits.

2.5. Sedimentary iron ore deposits

This type of deposits was formed by weathering, then broken, decomposed, transported of iron-bearing rock to low-lying basins, and after mechanical deposition, or some through the deposition of differentiation. Metallogenic times of sedimentary iron deposits are diverse with a proven mineral resource of 5 billion tons, accounting for 9% of China's total reserves. According to the sedimentary environment, there are two subtypes of this kind: marine type and lake facies type. Marine sedimentary iron deposits were produced in various geologic periods after Neoproterozoic. It is represented by "Xuanlong" iron ore of Pangjiabao and the "Ningxiang" iron ore Ningxiang in Hebei Province.

2.6. Weathered leaching type iron ore deposits

These deposits are formed by weathering and leaching of the rich iron rocks and/or iron-bearing polymetallic ores, and iron ore was accumulated on the residual slope. This type is shallow and mainly of middle and small in reserve. They are mainly distributed in Guangdong, Guangxi, Fujian, Guizhou and Jiangxi Provinces. The reserves of proven deposits are 300 million tons, accounting for 0.5% of the total reserves of the country.

2.7. Others

This includes mainly two deposits: the Bayan Obo and Shilu in Inner Mongolia and Hainan, respectively.

The Bayan Obo deposit is a world famous super-large iron-niobium-rare earth deposit with extremely rich minerals and elemental assemblages. However, due to the complexity of the iron deposit, there is no unified view on the origin of this deposit. Most believe that the formation and original deposition of iron ore associated with later hydrothermal fluid alteration, which means the iron ore was enriched by alteration on the primary ores. The mineral composition of the Bayan Obo mine is extremely complex. A total of 71 elements have been discovered and the mineral species have reached more than 170 species. There are five major ore bodies, with the iron deposits mainly occurring in the 8th member of the Bayan Obo Group. Proven reserves reach 1.6 billion tons [7–10].

Shilu iron deposit in Hainan Province was hailed as "Asia's largest iron ore rich", and ore mineral is mainly hematite, associated with cobalt, copper and nickel. At present, there is no unified understanding of the ore-forming mechanism of Shilu iron ore deposit. Some argued that formation of Shilu iron ore is mainly due to multiple remodeling and enrichment that is, the formation of iron ore deposits is affected by "volcano-sedimentary metamorphism + structural transformation + hydrothermal". A total of 38 iron ore bodies have been found, most of which are yielded in the 6th layer of Shilu Group. The proven iron ore reserve has exceeded 450 million tons and the grade is high (the average grade of iron ore is 51%) [11, 14, 15].

2.8. Comparison of major iron ore deposits from domestic and abroad

Iron ore resources are distributed in a few countries and regions with high concentration. 75.6% of the world's iron ore reserves are distributed in Russia, Ukraine, Australia, Brazil, Kazakhstan and China. In general, there are more iron-rich mines in the southern hemisphere and less in the northern hemisphere [12]. Among the top 100 iron ore production projects in the world [13], 76 are related to BIF and the output of these 76 BIF-related iron ore projects also accounts for 87% of the world's iron ore production (**Figure 1**). The giant iron deposits in China are all BIF type and were yielded in craton. The largest one hosted about 4 billion tons of iron and was formed in Middle Archeozoic. However, it was low grade, whereas to the giant iron deposits abroad, they are various from skarn-related type, Kiruna type or magmatic type for the metallogeny. Besides, they are not restricted to Precambrian. For the tectonic background, they could develop on craton, as well as on active continental margin.

Among more than 2000 iron ore deposits identified, the contact metasomatic-hydrothermal iron deposits account for 39% of the total iron ore deposits, followed by sedimentary metamorphism (28%) and sedimentary (20%), weathered leaching (7%), volcanic (3%) and magmatic (3%) iron ore are in small numbers. However, most of the large iron deposits are characterized by

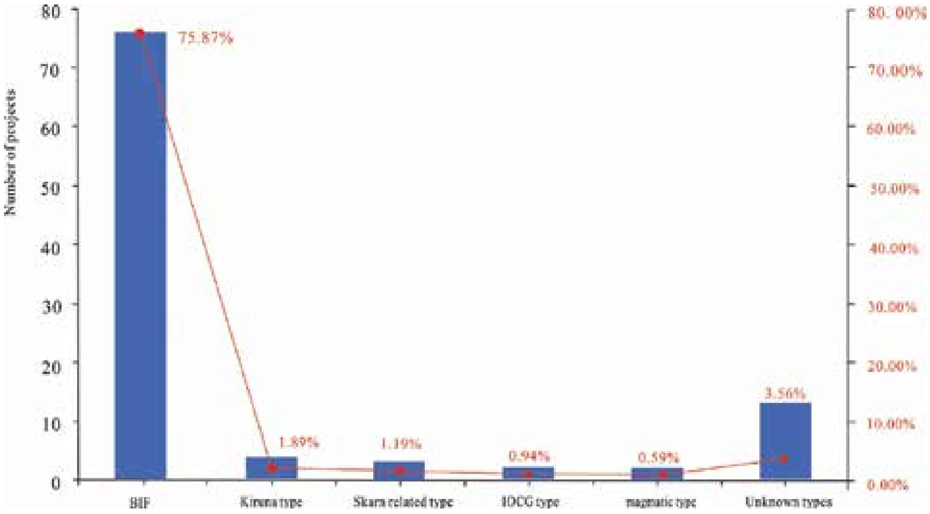

Figure 1. World's top 100 iron ore production projects with different metallogeny and the global proportion of iron ore production of various types.

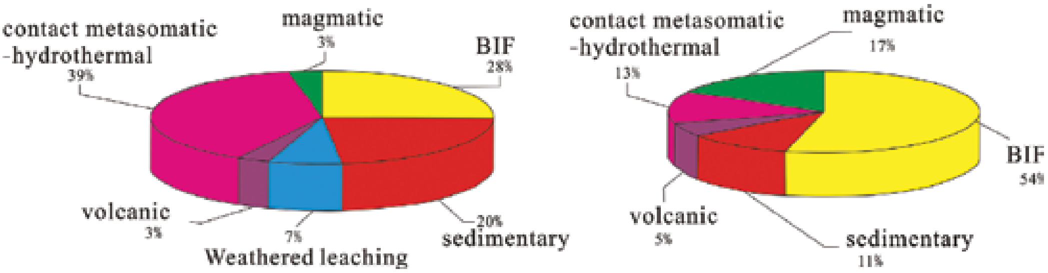

Figure 2. The proportion of different types of iron ore for metallogeny (A) and the proportion of large ones of all six iron ore deposit types (B) in China [4].

sedimentary metamorphism type, accounting for 54% of the total number; followed by magmatic type, accounting for 17%; and the contact metasomatism-hydrothermal iron deposits are dominated by small and medium-sized, while the large ones accounting for only 13%; weathered leaching type do not yield large iron ore deposits (**Figure 2**).

3. Iron ore supply and demand in China

China's iron ore sources are mainly three parts, the first part from the domestic ore, the second part from the overseas rights and interests of ore and the third part from overseas imports of ore. From 2011 to 2015, the proven reserves of iron ore continued to increase. In 2015, the reserves of iron ore reached 20.76 billion tons (note: different from the US Geological Survey released 2015 reserves data, it is mainly caused by different iron ore units of measurement), a slight increase of 0.50% year-on-year. Since 2015, China's iron ore production has gradually declined. In 2016, China's iron ore production (including low grades) was 1.281 billion tons, down 7.27% year-on-year.

3.1. Domestic ore production analysis

As China's crude steel production for many years running high, and more than 90% of the output is made of iron ore as a raw material contribution, resulting in huge demand for iron ore. While importing a large amount of iron ore, the output of China made iron ore is rapidly growing. Before 2000, China's iron ore output has been stable at an annual of less than 200 million tons (**Figure 3**). The output has continued to increase rapidly since 2001, with an annual output of 590 million tons in 2006 and a record high growth rate of 38%. During 2007–2009, China's iron ore demand was strong and the supply of oversea deposits increased more rapidly. Although the total output amount of domestic mines continued to increase, its growth rate slightly decreased from the previous period. In 2010–2011, due to the 4 trillion yuan investment stimulating steel consumption in China and the rapid growth of international iron ore prices, historical records have been continuously refreshed. Many low-grade deposits, previously considered non-economic for mining, have also been gradually exploited. Domestic iron ore in 2011 reached 1.32 billion tons, an increase of 27%. After 2012, the growth of China's economy slowed significantly; however, the supply of oversea deposits continued to accelerate. Therefore the demand exceeds supply was gradually reversed. As a result, the price gradually dropped and the domestic high-cost mines were gradually squeezed out of the market. In 2012–2014, the growth rate of output of domestic iron ore decreased rapidly, and the output of in 2014 was 151,000 tons, an increase of 3.9%, although it slightly increased in 2016. In the past 16 years, China's domestic iron ore production increased 7.4 times, an average

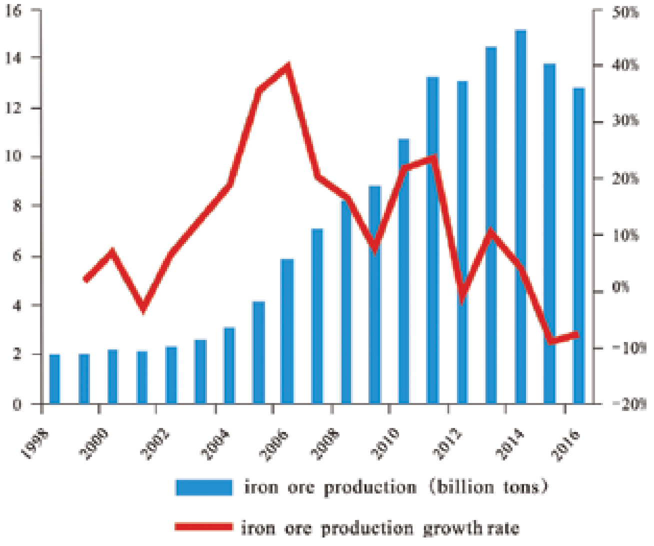

Figure 3. Domestic iron ore production and growth rate.

annual growth rate of 14.6%, and domestic iron ore is an important part of China's steel production of raw materials.

3.2. Analysis on iron ore import

Between 2003 and 2017, the average annual growth rate of China's iron ore output was about 18%. Meanwhile, the average annual growth rate of imported iron ore was 20%. The growth rate of imports was obviously higher than that of self-produced ore. Since 2000, China's iron ore imports, except a slight decrease in 2010, 2012 and 2015, increased substantially, the annual import grew twice over 35%.

By 2000, the major steel-making countries accounted for a relatively large amount of global imports. For example, Japan, the country with the largest import tonnage, accounted for an annual average of 28% in the world (**Figure 4**). Since 2000, due to the rise of China, the world's iron ore import pattern has undergone dramatic changes. China surpassed Japan in 2003 to become the world's largest importer of iron ore. The proportion of South Korea, Germany and Taiwan of China decreased slightly but little changed. The proportion of Japan was smaller; however, it is still the second largest iron ore importer in the world. In 2014, China imported 922 million tons of iron ore, accounting for 48% of the global output, 64.3% of the world's total iron ore imports and more than 70% of the global iron ore seaborne volume, and contributing to more than 90% of global iron ore consumption. In 2017, China's iron ore imports increased to 1.075 billion tons, which is 14 times of 2000. China is the world's most important iron ore consumer market and the world's largest spot market for iron ore. At this stage of relatively stable demand in Japan, South Korea, Germany and Taiwan of China, the proportion of imports from other countries is too small and China imports huge amount of iron ore, the changes in the demand for imported iron ore in China's iron ore market can approximately reflect the changes in the global iron ore spot market.

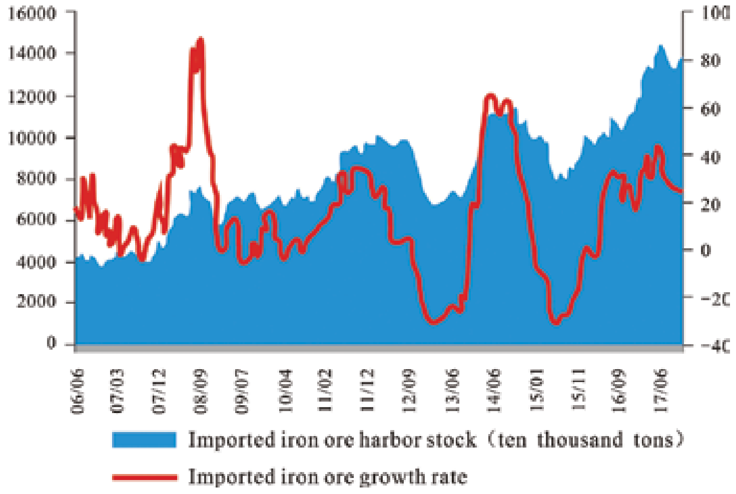

Figure 4. Iron ore imports/growth rate.

3.3. Investment development on overseas rights and interest mines

China's iron ore resources development of "going global" has 30 years of history. In 1987, Sinosteel Australia Limited and Australia's Morris Iron Ore Co., Ltd. formed a contractual joint venture to jointly develop and operate Chana Iron Mine, making it the first overseas iron ore investment project. A total investment of 200 million US dollars, officially put into operation in 1990, iron ore production in 2011 reached 11 million tons. Due to the still low domestic demand at that time, the increase rate of overseas investment and mine development was relatively slow. In recent years, due to the sharp increase of iron ore demand, the scale of overseas investment in iron ore in China began to gradually expand [14–16]. From 2006 to 2017, the investment in the rights and interests of overseas iron mines of various types of enterprises totaled more than 30 billion dollars and participated in the exploration, design and construction of more than 40 large-scale overseas iron ore projects [17].

China's overseas investment in iron ore is mainly concentrated in Western Australia, Quebec of Canada, Brazil, Mongolia and West Africa (**Figure 5**). Among them, there are 19 cooperation projects in Australia with high grade and abundant resources of iron ore, accounting for almost half of all overseas projects [17]. Canada mainly includes five projects of Wuhan Iron and Steel Group Company. There are three projects in West Africa, mainly in Guinea where invested 20 billion yuan, conducted by the Aluminum corporation of China. Due to differences in infrastructure investment, labor costs and resource conditions, the cost of projects invested in West Africa is lower than that in Australia. Up to 2013, China's overseas rights and interests iron ore production capacity of 73 million tons, accounting for about 10% of iron ore imports. However, compared with Japan's overseas rights and interests iron ore production capacity of 74 million tons, accounting for 57–70% of its annual import of iron ore, the gap between China and Japan is too large [17].

The global high-quality resources of iron ore have all been controlled by four enterprises. Oversea investment is high cost. As iron ore prices soared, Chinese enterprises have gone out to prospecting. When the spot price is as high as 130–180 US dollars/ton, the average mining cost can be sufficient for 100 US dollars. Based on this, mining enterprises go out to buy the

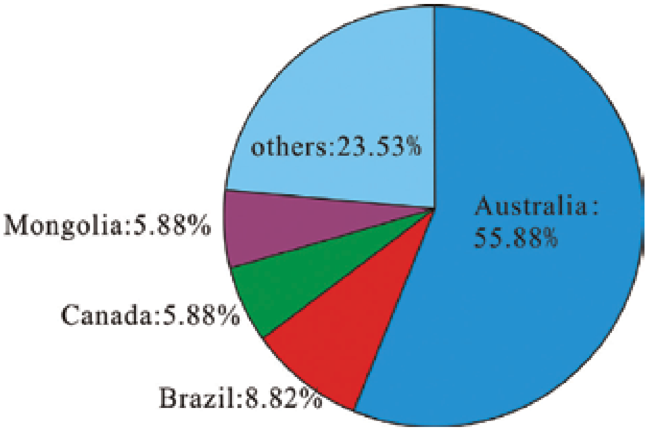

Figure 5. Chinese enterprises overseas iron ore investment.

rights and interests of the cost of the current spot price are very high. According to public information, it is learned that in recent years, the minimum cost for China to go overseas to acquire iron ore right and interests is the iron ore project in Liberia of WISCO, accounting for about 70 US dollars/ton at that time. However, due to the drastic drop of iron ore prices since 2014, up to the beginning of November 2015, the domestic spot price of iron ore has dropped below 50 USD/ton. For the 2 years 2014–2015, the development cost of overseas rights and interests mines are almost totally higher than the spot price, and the volume of iron ore shipped back to the China will inevitably decrease drastically. The high cost of mining, coupled with the cost of repatriation, is completely unmanageable compared to the spot price of $50–40/ton.

3.4. Problems existing in China iron ore supply

3.4.1. *The actual supply of domestic ore is insufficient*

Due to the continuous high output of crude steel in China for many years and the fact that more than 90% of the output is contributed by iron ore (long-flow steel), the demand for iron ore is huge. The output of domestic iron ore increased rapidly, with a compound annual growth rate of about 14%. In terms of quantity, the output of domestic ore is much higher than that of imports. Although the growth of China's own-produced iron ore is rapid, it has been found in actual research that the actual growth of China's domestic iron ore production is much lower than the statistic data. In the statistics data on iron ore production, there is no distinction between finished ore and raw ore, the low grade of raw ore without treatment was put directly into the statistics data, resulting in a sharp rise in China's domestic iron ore output data. In recent years, due to soaring iron ore prices, low grade of 10% of the iron ore is exploited; at the same time, these low grade ore will inevitably push up China iron ore production data.

After iron balance rebound calculation, China made only 210 million tons of domestic finished iron ore in 2014. It is far from 1.5 billion tons which is from statistics data. The self-sufficiency rate of iron ore dropped from nearly 60% in 2002 to a nearly straight decline. The huge contrast between country-made ore and those data of the after iron balance rebound calculation means that the supply of domestic ore is approaching the end of its growth.

3.4.2. *Foreign iron ore dependence is too high*

Although the total reserves of iron ore resources in China are huge, the distribution of iron ore resources is more dispersed, with more lean mines, very few rich mines, and mostly polymetallic iron mines. The ores are difficult to mine, the cost of mining is high, and the actual output cannot meet the production needs of domestic steel mills, therefore domestic steel producers have to choose to import large quantities of iron ore. Since 2000, China's iron ore imports have risen sharply, except a few years. The annual import growth rate once exceeded 40% twice.

With the rapid increase in iron ore imports, there is also a growing dependence on foreign iron ore (**Figure 6**). From only 36% in 2002, China's iron ore dependence on foreign countries has risen to more than 87% in 2016. In the coming years, the imported iron ore will remain at a high level. With the further price drop of imported iron ore, the domestic mines will be discontinued and the scope of bankruptcy will continue to expand. The import volume will continue to increase. The dependence on foreign iron ore will be over 90%.

3.4.3. *Iron ore import source is too concentrated*

China's imports of iron ore are mainly iron ore powder, massive iron ore (raw ore) and pellets, respectively, from more than 30 countries and regions, in which Australia, Brazil, India and South Africa are China's most important source of iron ore imports. The imports from the four countries accounted for about 85% (**Figure** 7). To protect its iron ore resources, the Indian government gives priority to ensuring its domestic steel production needs. Since 2011, the Indian government has increased export tariffs on iron ores and restricted exports. In recent years, the number of imported iron ore from India has been declining year by year. CVRD (Companhia

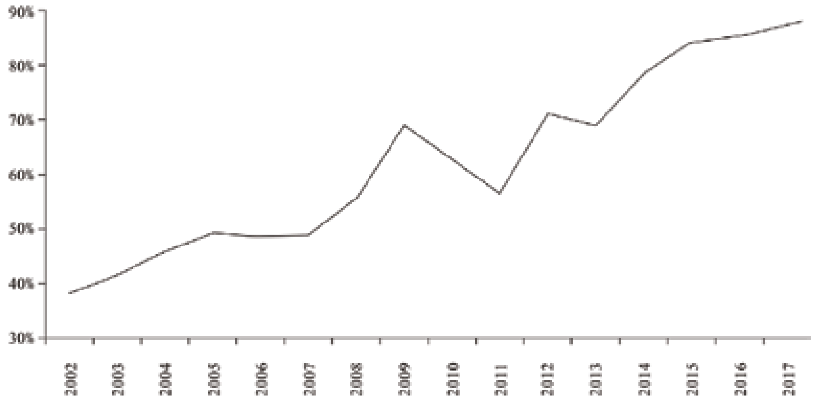

Figure 6. China iron ore dependence on foreign countries.

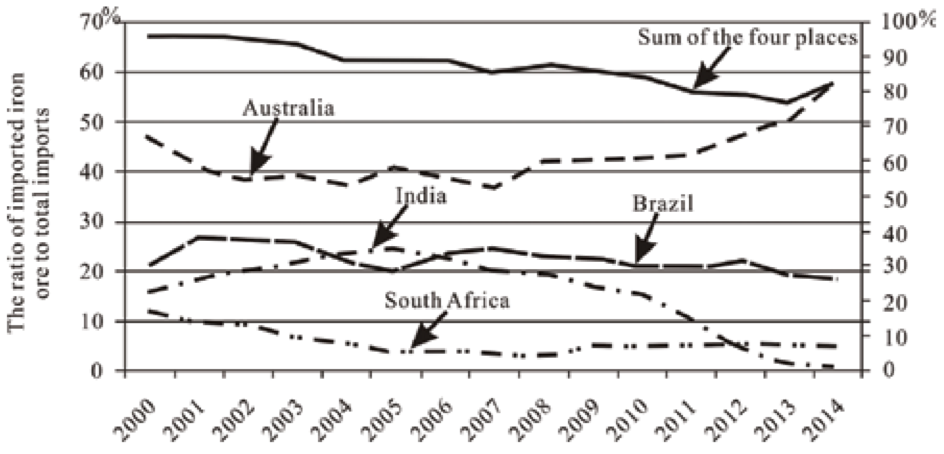

Figure 7. China iron ore import country analysis (left axis account for Australia, India, Brazil South Africa of the total import volume, and right axis account for sum of the four places mentioned above for the total import volume of the whole China).

Vale do Rio Doce in Brazil) is one of the main channels for China's iron ore imports, accounting for an average annual import volume of about 23%, but its proportion has dropped to 18% due to the substantial increase in the supply of iron ore from Australia in 2016 and 2017. South Africa's imports were relatively small, accounting for about 6% of the total. Australia is the most important source of iron ore. The average annual import volume accounted for 44%. Due to economies of scale and the efficiency gains for mining companies, the mining cost was getting down. Rio Tinto said publicly in 2014 that the cost of mining had fallen to less than $18/ton. Therefore, China's total imported iron ore from Australia is likely to continue to increase.

Now that iron ore is no longer a simple mean of production, its financial properties are gradually appearing. The major mines have been firmly controlled by financial capital (**Figure 8**). After understanding the global iron ore production costs, it is possible to speculate on the soaring of iron ore prices in previous years that the huge financial capital behind it is the most important promoter. At the present stage where the political situation is relatively stable, the main risk of over-concentration of import sources is the manipulation of iron ore prices stemming from the financial capital giants behind the mines. If the political situation in the future changes suddenly and the relevant governments at the source of imports restrict the export of iron ore to China, the steel industry will also face a nastier situation, which will in turn affect the social stability.

3.4.4. Iron ore prices fluctuated sharply

Before 2002, iron ore was the absolute buyer's market. In order to facilitate the purchase of Chinese enterprises, the three major companies (Rio Tinto, BHP Billiton and Companhia Vale do Rio Doce) at that time even gave a rebate, and the price of iron ore has been relatively low. However, with the rapid economic growth in China, the continuous expansion of production capacity in the iron and steel industry directly led to the soaring iron ore prices (**Figure 9**). Due to the fact that many Chinese small and medium iron and steel enterprises are not eligible for long-term agreement price, their huge demand has pushed up the price of spot market. From 2007 to 2013, demand growth was too fast, iron ore was in short supply and prices rose sharply. After 2014, due to the newly increased output of iron ore put into operation by the

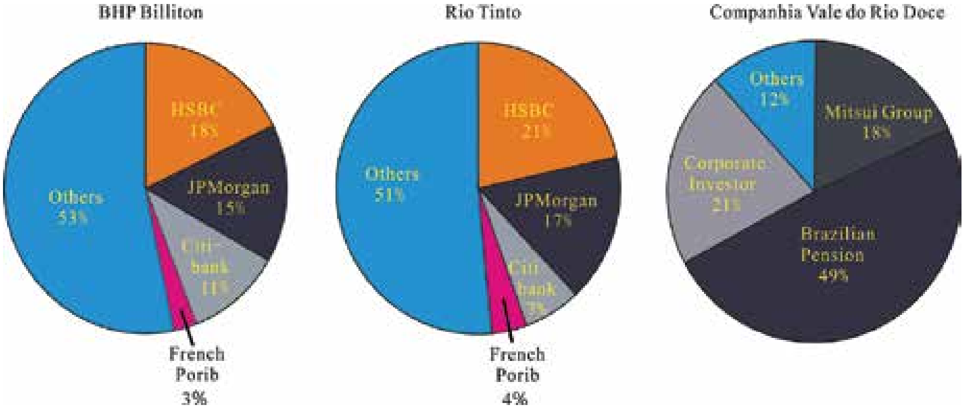

Figure 8. Rio Tinto, BHP Billiton, and Companhia Vale do Rio Doce financial capital structure.

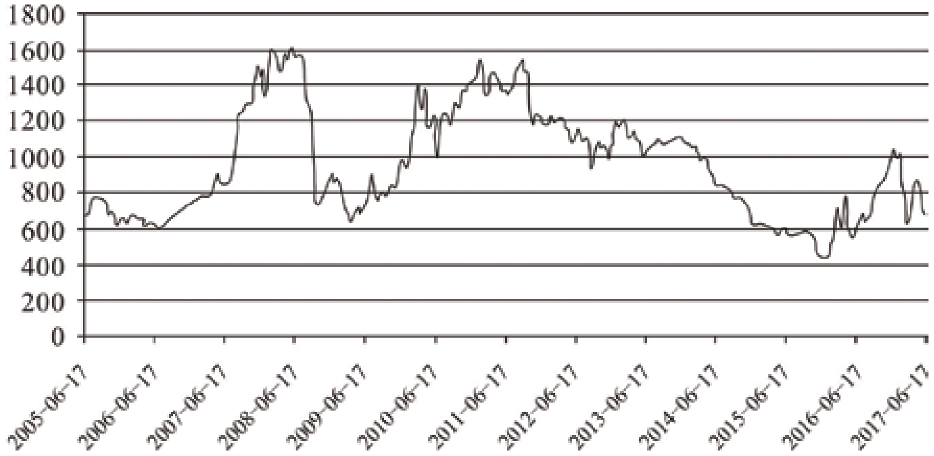

Figure 9. Japan's Shinkansen iron ore price index.

global mining enterprises in 2014–2015, the supply of iron ore will be oversupplied. Iron ore prices fell for 4 consecutive years, until 2016, however, from 2016, it reversed again. It rose slightly (**Figure 9**). Over the past 10 years, iron ore prices have experienced two rounds of highs and lows, and the highest point has surpassed 180 US dollars/ton, while the lows have already broken through 50 US dollars/ton.

3.4.5. Obtaining overseas rights and interests mines is difficult

Iron ore resources in any country belong to the strategic mineral resources, with the interests of nations, in any country are highly concerned about. With the economic development and social construction of third world countries, the demand for iron and steel resources will inevitably increase the demand for iron ore resources. In the future, the emerging economies in the world will compete for iron ore resources more intensively. The high grade and large reserve mines are occupied by the international mining giants. Besides, international mining giants relying on their strong business base for many years, still in the form of acquisitions, mergers and other forms of global search for high-quality iron ore resources, are still constantly expanding their sphere of influence. China's steel enterprises that want to get high-quality mines are very difficult. They missed best time to purchase high-quality mines oversea. In addition, Japanese consortium set malicious difficulties to them. China's steel mills have paid a huge price for this. It mainly include: (A) the acquisition cost is too high. Currently, the average grade of overseas iron ore resource invested by the Chinese side is about 40%. Although its quality is inferior to that of the United States, Europe and Japan, it is still superior to the domestic iron ore [14]. Overseas mines geographical locations are mostly terrible, need to increase a large number of mineral processing, power plants, water and other facilities investment in construction, development and construction costs will inevitably increase [14]. According to the current investment in projects under construction estimates, the first phase of overseas iron ore development projects to build capacity of 10 million tons of investment is about 2 billion US dollars on average; if it is a low grade one, the investment will require nearly 3 billion US dollars, such as the Guinea project, the total investment of the project has now reached as high as 20 billion U.S. dollars [17]. In fact, most overseas iron ore projects cost more than US $100/ton. (B) Large stake, high risk, hard to quit. Chinese enterprises target for the leading enterprises or the top few companies. Most of these large-scale overseas investment enterprises are state-owned. Because their management does not make money for the purpose of their business, but rather their personal performance as the starting point, they just want to make big achievements, win media acclaim and earn their personal social reputation, resulting in state-owned enterprises inefficiency and the investment frequently failed. For example, Shougang group tried to buy most of all stock right of a Peru company, Aluminum Corporation of China bought Rio Tinto and China Minemetals Corporation bought OZ. In certain sense, all failed. This may give the absolute control over the acquisition of the business, but at the same time will inevitably increase the operational burden. This type of large investment, which concerns only one company, will weaken the risk-resist capability greatly. Once a sharp decline in ore prices, lower profitability, or even loss, companies will be difficult to quit smoothly. Japanese did the opposite. Instead of pursuing the holding of the other side's enterprises, they hold mostly 10% or even lower of the stock of target company. In addition, they did not choose the big ones. The manager of the Japanese company did not seek reputation. Japanese businessmen aim at maximizing business profits, and their business decisions are based on costs and benefits. For example, Mitsui & Co., Nippon Steel and Sumitomo Metal jointly owned Robe River Company of Australian, and then supported the expansion of the company, which indirectly press Rio Tinto and BHP Billiton.

Compared with Japan, China's overseas iron ore investment started recently, and is still in the learning stage, compared with Japan's investment efficiency and return on investment is still a big gap. Chinese enterprises and the Chinese government still urgently need to learn from Japan on the concept of iron ore overseas investment, management experience and risk prevention.

4. Mineral processing and ore metallurgy technology

In order to improve the self-sufficiency rate of iron ore and get rid of the shackles of foreign mining giants, a great deal of research work has been carried out by relevant researchers around the efficient utilization of iron ore resources.

4.1. Fine grain iron ore beneficiation

In China, iron ore with hematite grain size of less than 0.045 mm or magnetite grain size of less than 0.03 mm is commonly referred to as fine-grained iron ore [18]. Yuanjiacun Iron deposit and Qidong Iron deposit in Shanxi and Hunan Province, respectively, are the most typical fine grain iron deposits in China. The Taiyuan Iron and Steel Group and scientific research units, who aimed at the Yuanjiacun iron ore recycle and conduct a large number of experimental studies. The original iron ore grade of 31.18%, −0.045 mm particle size accounted for 93.81% of the total ore, they got concentrate iron grade 66.95%, and recovery rate of 72.62%. With this process, the Yuanjiacun iron deposit built a mineral processing plant with annual capacity of

22 million tons by the end of 2012 [19]. Changsha Institute of Mining and Metallurgy proposed a selective flocculation desliming-anti-flotation technology and developed a SA-2 flocculant (for the purpose of fine grain size, complex nature of igneous iron ore in Qidong iron deposit) [20]. At present, the Qidong iron deposit uses this technology to build a beneficiation plant with an annual treatment capacity of 2.8 million tons. Under the conditions of a raw ore grade of 28.36% and a grinding fineness of −0.038 mm (98%), the concentrate iron grade 62.5%, the recovery of 68% have been achieved [18–20]. There are many examples like this. Stage grinding —stage magnetic separation likely is the best process for processing fine-grained magnetite [21, 22]; for fine-grained magnetite-hematite mixed iron ore, weak magnetic—strong magnetic—resurfacing—reverse flotation process can obtain the high recovery rate; that sorting fine particles hematite process mainly has strong magnetic—desliming—reverse flotation [23, 24], selective flocculation—reverse flotation [25] and strong magnetic—centrifugal beneficiation [26].

4.2. Efficient grinding technology

It would be subdivided into: high-pressure roller mill technology, self-grinding/semi-self-grinding technology and stirring mill technology [12]. The high-pressure roller mill technology is highly dependent on ore ultra-fine grinding equipment: high-pressure roller mill. It is a unit of low energy consumption, high handling capacity. Compared with the traditional crushing equipment, high-pressure roller mill pulverized products significantly increase the internal microcracking, ensure high content of fine-grained fraction and mineral dissociation [3, 27–30]. Domestic experts and scholars carried out a great deal of research work on the application of high-pressure roller mill technology in iron ore, and formed the crushing-preselection technology of high-pressure roller mill to maximize the crushing and minimize friction in order to reduce processing costs. Masteel company conducted this technic on low-grade iron ore (including high-pressure roller mill, wet grading, coarse magnetic separation pre-selected tail-polishing technology) in Nanshan iron ore deposit, the annual throughput of the beneficiation plant increased by 2.7 million tons, and the electricity consumption and the consumption of steel per unit ore dropped by about 30% [20]. And then, this technology has been introduced into dozens of iron ore processing plants in Hebei Province such as Sijiaying Iron Mine, Panzhihua Iron Mine in Sichuan and Dachang Iron Mine in Anhui [31]. The grain size, grinding and dissociation characteristics of lean hematite ore after being crushed by a high-pressure roller mill have been studied. Details of this technology are still locked. However, compared with the jaw crusher, the high-pressure roller mill has a high crushing ratio, high content of fine-grained, uniform particle size distribution and the Bond power index decreased by 13.96–28.23%, −0.5 mm grain iron ore monomer dissociation increased by 15.16% [13]. Compared with the conventional three-stage closed-circuit crushing process, the self-grinding/semi-autogenous grinding process has the features of simple process, low capital investment, large-scale equipment efficiency and low dust pollution. At present, China has more than 60 beneficiation plants using more than 160 self-grinding/semi-autogenous mills. For example, Dahongshan Iron Mine of Kunming Iron and Steel Co., Ltd. has used 8.53 m × 4.32 m semiautomatic milling + ball milling + ball milling (SAC) process to crush iron ore from 2006 with the processing capacity of 4 million t/a [1]. Stir mill as a fine to ultra-fine grinding equipment was gradually being applied to the fine-graining of iron mines in China [20, 32]. In 2010, Panzhihua Iron and Steel Co., Ltd. purchased three tower mills from Ericsson of Germany for fine grinding of vanadium-titanium magnetite. In July 2013, three tower mills of Dahongshan Iron Ore from Kungang Steel were put into production. In 2013, Ansteel Mining Company purchased six sets of vertical spiral mixing mill manufactured by Metso for the Guanbaoshan Iron Ore Concentrator. Li et al. [30] explored the possibility of further improving the grade of concentrate obtained by magnetic separation at a grinding stage of a large-scale iron ore mine in Shandong Province. He began with the concentration of iron grade of 62.35% with 0.022 mm and access to iron grade greater than 65%. The comparison of mixing mill and ball mill on Shizhuyuan iron deposit, Hunan Province show that: when using a stirred mill, the content of newly formed −0.038 mm granular material is 8.1% higher than that of the ball mill, and the monomer dissociation degree of the mixed mill product is obviously higher than that of a ball mill, and the grade of the refined mill product after magnetic separation is 5.2% higher than after ball mill [33].

4.3. Magnetization roasting technology

In recent years, many domestic research units aim for magnetization roasting technology and equipment and carry out a large number of studies. Flash magnetization roasting technology was one of them, which was proposed by Yu and his team [34]. And then this technology was applied to the Daxigou siderite deposit, Wangjiatan magnetite deposit, and Jielong magnetite deposit, where they obtained iron grade more than 55 and 70% of recovery rate. In 2009, Lingbao plant started the pilot construction of flash magnetization roasting project of 50,000 tons per year. In 2012, the Institute of Process Engineering of Chinese Academy of Sciences built the pilot project of annual handling capacity of 100,000 tons of refractory iron ore fluidized roasting. Northeastern University put forward a complex refractory iron ore suspension roasting technology, and designed a laboratory batch suspension roaster. Using the designed roaster, restricted the air velocity, reducing gas concentration, calcination temperature and roasting time were tested on the positive flotation tailings and oolitic hematite of Anshan Iron & Steel Co., Ltd. at Dong'anshan Sintering Plant. Under the best experimental conditions, they got iron grade 56–61% and recovery rate of 78–84% [35]. According to the basic research results, Northeastern University and the Institute of Mineral Utilization of Chinese Academy of Geological Sciences and Shenyang XinBo Industrial Design Co., Ltd., designed and built a 150 kg/h complex refractory iron ore suspension roasting pilot system in Emeishan City. In September 2014, the continuous flotation test was carried out with the positive flotation tailings from the tailings of the East Anshan Sintering Factory and the magnetic separation of the tailings of the Ouzanshan Magnetic Puller tailings. The magnetized roasted products produced by this system, after magnetic separation, reached the grade of concentrate iron 63–65%, and the recovery rate of 78–83%.

4.4. Deep reduction and magnetic separation technology

For those beyond conventional processing methods and magnetization roasting technology, the relevant domestic researchers put forward a deep reduction-magnetic separation technology that uses coal as an agent to reduce iron ore minerals to metallic iron below the melting temperature of ore, and then promotes the growth of metal iron particles to a certain size. Deep reduction-magnetic separation technology for the development of complex refractory iron ore provides a new way to become one of the hot topics in the field of mineral processing in recent years. Raw materials of oolitic hematite, hematite with carbonate, iron tailings, red mud, Zinc-bearing iron ore were tested by this technic. After the magnetic separation, the deep reduced iron powder with 85–95% Fe and more than 90% recovery rate can be obtained [36]. Deep reduction temperature is generally higher than 1000°C, iron ore reduction process is $Fe_2O_3 \rightarrow Fe_3O_4 \rightarrow FeO \rightarrow Fe$. The process of reduction can be divided into three stages: initial, middle and late stage. The reaction kinetics models of each stage are Avrami-Erofeev equation, chemical reaction model and three-dimensional diffusion model, respectively. The size of the iron particles in the reduced material can be detected using optical microscopic image analysis techniques. It is noteworthy that the reduction temperature and the reduction time have a significant effect on the size distribution of iron particles [21].

High-phosphorus oolitic hematite is an important iron ore resource in China. Due to the extremely fine grain size (less than 10 μm) and high-phosphorus content of hematite, it is difficult to effectively classify the hematite by conventional beneficiation process. However, the deep reduction-magnetic separation process can be applied to high-phosphorus oolitic hematite iron enrichment. The study found that during the deep reduction process, the phosphate minerals in the ore will be reduced to elemental phosphorus, and a considerable part of the elemental phosphorus enters the metallic iron phase, causing high content of phosphorus in the reduced iron powder [37]. In response to this problem, relevant scholars put forward two solutions: deep reduction of dephosphorization and deep reduction of phosphorus-rich [12]. For the raw ore with phosphorus content less than 0.8%, by adding dephosphorization agent (Na_2CO_3, $Ca(OH)_2$, Na_2SO_4, etc.) the vast majority of phosphorus remains in the slag phase. This way would get the low-phosphorus deep reduced iron powder (phosphorus content ≤ 0.05%) that can be directly used in steel-making [13]. For raw ore containing more than 0.8% phosphorus, by controlling the migration of phosphorus, more than 80% of the phosphorus enters the metallic iron phase. It would get high-phosphorus deep reduced iron powder (phosphorus content ≥ 1.5%), and then use smelting dephosphorization technology to deal with high-phosphorus iron powder, and qualified molten steel at the same time get high-phosphorus steel slag, the high-phosphorus steel slag can be used directly as phosphate fertilizer or acid soil improver. Presently, this technic is not yet widely used because of lacking equipment.

4.5. Others

Other mineral processing and ore metallurgy technology would include the tailings re-separation technology and room temperature collector technology. [12] Due to the low grade of iron ore resources in China, an average of 1 ton of iron concentrates needs to be discharged to 2.5 tons of tailings. With the continuous increase of production capacity of mining enterprises, the discharge of iron tailings has rapidly increased and has become the largest industrial solid waste. Tailings discharge not only occupy a large amount of land, sometimes due to poor management, but also cause tailings dam break, resulting in casualties, environmental pollution, destruction of villages and towns and other serious consequences. The iron tailings usually contain a certain amount of metallic iron with a fine grain size, so the energy consumption of grinding is lower than that of raw ore. Anshan Iron and Steel Mining Company, Qidashan iron plant and Gongchangling beneficiation plant conducted flotation tailings re-separation pilot study. The results show that the pre-enrichment of iron minerals in the tailings can be achieved by the re-separation, grinding-magnetic separation and the iron concentrate with grade greater than 40% can be obtained. And then, via the process of grinding—weak magnetic—strong magnetic—reverse flotation process or 1 rough 1 fine 1 flotation column process sorting, reaching more than 64% of concentrate grade, the recovery rate more than 88% [38–40]. Meishan iron ore processing plant integrated tailings, strong magnetic separation tailings, phosphorus tailings on the basis of a comprehensive analysis of mineralogical characteristics of the re-separation were carried out: iron grade of 18% in the tailings can be concentrated to 56.5%. Experimental studies have shown that the nature of iron tailings in different regions vary greatly, hence iron tailings re-separation process is not the same [13]. Most of the domestic iron ore beneficiation plants use an anionic reverse flotation process to reduce silicon, and the collectors used are fatty acids. Anion reverse flotation process has the advantages of stable production, good indicators, the disadvantage is the collector preparation and the required high flotation temperature (preparation temperature is usually 50–70°C, the slurry temperature is generally 35–40°C). As the result floating pulp slurry needs heating treatment, which increases production costs [41]. Luo et al. [42] developed a new modified fatty acid collector, and flotation tests at 25°C showed that they got grade of 65.79% with 83.01% recovery rate from the Sijiaying iron deposit. This fatty acid collector has good water solubility and collectibility at room temperature [43–46]. Aiming at the flotation of iron ore at room temperature, a series of new efficient collectors with low temperature solubility, strong catching ability and excellent selectivity have been developed in China. The efficient separation of iron ore at room temperature has been achieved for some them. However, at present these new collectors are still in the laboratory research or semi-industrial test stage, and the industrial application process needs to be accelerated.

5. Conclusions

This chapter addresses the topic of iron ore types, structure of import, market analysis, financial aspects, overseas investments, etc. It also covers development of innovative beneficiation processes in China. Probably due to large national land area and multi-period orogeny, from the view of metallogeny, lots of iron deposits developed in China, and the proven total reserves of iron ores are relatively abundant, but mainly low-grade ores. For years, China's iron ore reserves are far from being able to meet the requirement of rapid development of steel industry. China is the world's largest importer of iron ore, which imports accounted for one-third of the world's total in recent decades; however, the buyer has not the final say. The strategic importance of iron ore resources in national economy not only depends on the social value and economic value created by the iron ore exploitation, but also depends on whether the requirements of the steel industry and steel downstream industry, and safety ensuring, economy and sustainability of steel and steel downstream industry. In order to improve the self-sufficiency rate of iron ore and get rid of the shackles of foreign mining giants, a great deal of research work has been carried out by relevant researchers around the efficient utilization of iron ore resources. In the process of fine iron ore beneficiation, ore crushing, roasting-magnetic separation, deep reduction, tailings re-election, low temperature collector research and development has made achievements.

Author details

Guangrong Li

Address all correspondence to: liguangrong0086@ecit.edu.cn

Fundamental Science on Radioactive Geology and Exploration Technology Laboratory,
East China University of Technology, NanChang, Jiangxi, China

References

[1] Zhao ZY. The potential prediction of Fe mineral resources with comprehensive information in China [thesis]. Jilin University; 2005

[2] Jiao YS, Jiang SC. Discussion on development of iron ore industry of China and future planning. Modern Mining. 2009;**25**(01):1-4, 19

[3] Luo HB, Wang YJ, Hu DX, Zhang ZW. The potential analysis of the iron-ore resources in China. Geological Review. 2009;**55**(06):885-891

[4] Xie CX, Li HM, Wang RJ, Xiao KY, Sun L, Liu YL. Structural characteristics of iron ore resources identified to date in China. Geological Bulletin of China. 2009;**28**(01):80-84

[5] Xiao KY, Lou DB, Yin JN, Wang QM, Li JC, Yang YH, et al. Quantified research on iron potential of China. Geological Bulletin of China. 2011;**30**(5):650-660

[6] Zhao YM. Main genetic types and geological characteristics of iron-rich ore deposits in China. Mineral Deposits. 2013;**32**(4):685-704

[7] Wei JY, Shang GZG. Oxygen isotope composition of magnetite and hematite in Baiyun ebo iron deposit, inner mongolia. Scientia Geologica Sinica. 1983;(03):217-224

[8] Bai G. Demonstration on the Geological Features and Genesis of the Bayan Obo Ore Deposit. Beijing: Geological Publishing House; 1996

[9] Xiao RG, Fei HC, An GY, Zhang HC, Hou WR. Lithology and genesis of dolomite in Baiyun' ebo mine, inner mongolia. Geoscience. 2003;**17**(03):287-293, 360

[10] Zhang YX, Lv HB, Wang J, Liu JY, Meng QW, Huang M. Analysis of ore-forming tectonic settings of the Bayan Obo REE deposit. Acta Geologica Sinica. 2012;**86**(05):767-774

[11] Xu DR, Wu J, Xiao Y, Chen FX, Wang L, Liu ZL, Wang ZL. Structural deformation of the Shilu iron ore deposit in Hainan, southern China, and its relationship with the formation and enrichment of iron-polymetallic metals. Geological Bulletin of China. 2011;**30**(4):553-564

[12] Song QH, Liu Z, Yang FD, Wang BJ, Li RS, Xu M, Zhang M. Brief introduction of iron resources at home and abroad. Jilin Geology. 2008;**27**(03):5-7, 12

[13] Wang WP. Metallogenic regularity of major BIF iron ore concentration areas globally and strategy study for M&A and development of international iron ore resources [thesis]. Chinese Academy Geological Science; 2017

[14] Duan HM. The current situation analysis and strategy research of iron ore overseas investment by China. China Mining Magazine. 2013;**22**(10):51-55

[15] Chang XG. Overseas iron ore project investment worries of Chinese enterprises. China Economic Weekly. 2014;(28):68-71

[16] Xia XH. China Metallurgical News. Build an Upgraded Version of Iron Ore Enterprises in China [Internet]. 2013

[17] Li XH. A study on China's policy-based housing finance [thesis]. Liaoning University; 2010

[18] Chen W, Zhang LG. Status quo and development trend of complex refractory iron ore beneficiation technology. Nonferrous Metal (Mineral Processing Section). 2013;(S1):19-23

[19] Tang XF. Research status and development trend of beneficiation technology on complex hematite. Modern Mining. 2014;**28**(3):14-19

[20] Liu ZX. Application of SA-2 Flocculant in the Separation of Fine-Grained Hematite. Nonferrous Metal(Mineral Processing Section). 2013;(6):83-85

[21] Cao JC, Lv L, Cao F, Yue TB. Experimental study on beneficiability of some low-grade iron ore in inner Mongolia. Mining and Metallurgical Engineering. 2012;**32**(5):37-40

[22] Zhang CD, Wu CC, Zhong SL, Yang ZJ. Mineral processing test on a fine disseminated iron ore from Sichuan. Metal Mine. 2014;**43**(6):60-64

[23] Wang QL. Experimental research on high-intensity magnetic separation—Desliming—Reverse Flotation of a complex and micro-fine specularite ore. Multipurpose Utilization of Mineral Resources. 2011;(5):15-18

[24] Hu YM, Han YX. Study on the separation of the oxidized ore from Yuanjiacun iron mine. Metal Mine. 2012;**41**(10):65-69

[25] Yang Y, Zhang WX, Zhao GF, Ding SQ. Process tests on a micro-fine and refractory iron ore. Nonferrous Metals Science and Engineering. 2012;**03**(3):80-84

[26] Fan ZJ, Cao NJ, Rao YH. Investigation of mineral processing of a fine low-grade refractory iron ore. Metal Mine. 2011;**40**(1):51-53

[27] Han YX, Liu L, Yuan ZT. High intensity magnetic pre-concentration of hematite ore comminuted by high-pressure grinding roller. Multipurpose Utilization of Mineral Resources. 2013;(1):14-18

[28] Liu JY, Huang YC. Applications of high-pressure grinding rolls in mineral processing. Nonferrous Metal(Mineral Processing Section). 2016;**39**(5):1-8

[29] Sun SX, Chang WL. Application of high pressure roll grinding process in dressing plant for low grade magnetite concentration. Mining & Processing Equipment. 2012;**40**(2):66-71

[30] Li CH, Xu L, Guo XP. Magnetic separation process on a micro-fine and refractory iron ore. Modern Mining. 2014;**28**(3):131-133

[31] Yuan ZT, Liu L, Yan Y, Han YX. Product size characteristics of low-grade hematite in high pressure grinding roll. Journal of Northeastern University(Natural Science). 2011;**32**(6): 875-878

[32] Luo ZP, Liu JH. Application and prospects of high pressure grinding roll in metal mines of China. In: The Summit Forum on Technology Innovation and Application Technology of China's Mining Industry. 2010

[33] Han YX, Sun YS, Li YJ, Gao P. New development on mineral processing Technology of Iron ore Resources in China. Metal Mine. 2015;**44**(02):1-11

[34] Qi CY, Yu YF. Apply the flash magnetitic roasting to the tailing of Daye mine. In: National Mineral Processing Professional Academic Annual Meeting. 2006

[35] Chen C, Li YJ, Zhang YS, Wang R, Han YX. Study on suspension roasting for oolitic hematite. Multipurpose Utilization of Mineral Resources. 2013;**6**:30-34

[36] Gao P, Sun Y S, Zhou C L, Han Y X. Effect of reduction process on size of iron grain. Journal of China University of Mining & Technology. 2012;**41**(5):817-820

[37] Han YX, Ren DZ, Sun YS, Gao P. Phosphorus migration behaviors in reduction of high phosphorus oolitic hematite ore. Iron and Steel. 2013;**48**(7):7-11

[38] Wang LX, Liu SA, Song JL, Mei CG. Upgrading for rough concentrate from reconcentration of a lean hematite. Modern Mining. 2014;(9):52-55

[39] Yuan ZT, Ma YX, Mao WD, Li LX. Experimental research on collecting magnetic iron from tailing of maerling concentrator. Conservation and Utilization of Mineral Resources. 2014;(2):44-48

[40] Wang KS, Deng QS, Song K, Jin ZQ. Tailings re-concentration tests for Lunan mining company. Modern Mining. 2013;**29**(4):27-30

[41] Luo BB, Zhu YM, Tong LJ, Li YJ, Sun CY. Preformance research of amine modified collector DMP-3 on Qidashan iron ores. China Mining Magazine. 2014;**23**(7):114-117

[42] Luo HH, Ruan YY, Huang J. Reverse flotation of iron ore using new collector at normal temperature. Journal of Wuhan Institute of Technology. 2012;**34**(9):30-33

[43] Xu DR. Metallogenic Model and Ore Predicting of the Shilu Iron Ore Deposit in Hainan Province. Beijing: Geological Publishing House; 2009

[44] Xie SS, Cai SK, Wu XJ. Gravity and magnetic anomaly characteristics of the Shilu iron ore district and deep prospecting. Geophysical & Geochemical Exploration. 2011;**35**(03):313-318

[45] Liu YY. The reviews of the development of major metal mills griding technology around recent years in China. Modern Mining. 2013;**29**(8):150-152

[46] Huang YG. Utilization status and outlook of china's iron ore tailings. Resources & Industries. 2013;**15**(3):40-44

Chapter 2

Genesis, Uses and Environment Implications of Iron Oxides and Ores

Davidson E. Egirani, Mohd T. Latif, Nanfe R. Poyi,
Napoleon Wessey and Shukla Acharjee

Additional information is available at the end of the chapter

http://dx.doi.org/10.5772/intechopen.75776

Abstract

Iron oxides are chemical complexes which occur naturally, comprising iron and oxygen. Here, together, 16 types of iron oxides and oxyhydroxides have been identified. These two components of oxides are widely spread naturally. They are vital to humans and useful in most geological and biological activities. In addition, they are useful as pigments and catalyst in industries and hemoglobin in blood circulation. The interplay and conversion of these components from one form to another are essentially controlled by bacterial species. These contain 70 and 72% iron, respectively. Furthermore, iron ores are classified in terms of occurrence. Banded iron formation (BIF) comprises 15% iron, comprising minerals of iron that are bedded besides silica. Beneficiation processes of iron ore generate dust in the atmosphere, acid mine drainage in the ecosystem and metallic iron for steelmaking. Beneficiation process requires dissolution of minerals surrounding the ore and the release of metals and cement matrix into water courses. These generates acid leading to acid mine drainage. Therefore, there is a need for impact assessment of the environment in the planned beneficiation cycle. Sustainable beneficiation must be done to reduce impact on the natural, social or economic environment.

Keywords: genesis, uses, environmental implications, ochre, oxides of iron, iron ore

1. Introduction

The genesis, uses and environmental implications of iron oxides and ores remain a topic of interest to academics, industrial players and environmentalist. Oxides of iron are chemical compounds widely spread naturally, comprising iron and oxygen. Here, two components of oxides are widely spread naturally. They are relevant to humans and useful in most geological and biological activities [1]. In addition, they are useful as pigments and catalyst in industries and hemoglobin in blood circulation. Iron oxides that are economically viable in natural and beneficiated forms are considered as second to oil and gas in relation to demand and utility in the global market. They occur as divalent compound, trivalent compound and a combination of both. The interplay and conversion of these components from one form to another are essentially controlled by bacterial species. These bacteria use iron and reduce trivalent iron oxides to divalent form during metabolism.

Different geological conditions control the spread of iron ore deposits worldwide. They occur in basins of sedimentation, with eroded, deep-seated intrusive and where deep tropical weathering conditions prevail. Magnetite deposits occur in the deeply dissected regions of plutonic intrusions in North America [2, 3].

Several authors have provided information in the environmental outcome of exploration and exploitation of iron ore. These include pollution of the atmosphere and ecosystem courses of water. Pollution of the atmosphere involves release of poisonous gases such as nitrous oxide, carbon dioxide, carbon monoxide and sulfur dioxide. Pollution of the ecosystem involves release of metal load into courses of water. While there is limited remediation programme on the former, the latter has gained considerable attention, and elaborated ochre is a product of the aqueous oxidation of iron and oxides of iron [4–7].

2. Genesis

Natural iron oxides occur extensively and are obtained from deposit of various types. Hematite is mainly sourced from iron ore of sedimentary origin inclusive hydrothermal, metamorphic and volcanic deposits. Mafic and ultramafic rocks are linked with magnetite. This is also associated with skarn-type metamorphic deposits. Products of weathering such as limonite, ochre, sienna, umber and goethite exist in gossans. In addition, they are obtained from sulphide minerals and other iron-rich rocks [8].

Deposits precipitated from seawater are used in production of umber. These are located on the seafloor. Sulphide deposits are known to provide ochre and iron oxide coatings via oxidation. Black pigments are provided by magnetite deposits besides red and yellow ochre and iron oxide coatings derived from weathering of magnetite. Hematite deposits outcrop around the margins of the great sedimentary basins worldwide. There are oxide-rich deposits of igneous and metamorphic origin in Sweden. In Africa, good quality iron ores lie near the Mediterranean in Morocco and Algeria. There are extensive deposits in Brazil, India and China. Iron ore deposits are distributed widely in different geological formations [9].

The largest concentrations of ore are found in Precambrian age banded sedimentary iron formations. These formations make up the bulk of the world's iron ore incomes. These ores vary from hard blue massive type to soft, friable or schistose texture. The orebodies generally stand out as ridges with the ore both on the crests and on the flanks. Small patches are enriched by manganese derived from surface solution. The iron content extends from 64 to 68% after beneficiation. The leached out iron could be carried downwards to be precipitated as bodies of ochre and iron oxide coatings within the existing sedimentary rocks. This product is a soft earth mixture of hematite, limonite and goethite from which various red and yellow ochre and iron oxide coatings can be extracted [10].

The main product is a dark red hematite variety. Some ore deposits consist of magnetite with occasional hematite; varying amounts of sulphide occur mostly as pyrite and pyrrhotite with minor amount of chalcopyrite. The ore is composed of ferriferous oolites and grains of quartz bounded by a cement of clay minerals or of chlorites and carbonates. The oolites consist of iron hydroxides or limonite, with variable proportions of silica, alumina and phosphorus. The strikes of the orebodies are sometimes in accordance with the iron formation and sometimes discordant. The high-grade ore could be magnetite that is partially oxidized at the outcrops to hematite, with minor quantities of silicate minerals, anthophyllite and chlorite [11].

Deposits of iron may be categorized under the following: magmatic, sedimentary and metamorphic. In some regions of the world, the major sources of high-grade iron ore are derived from magmatic iron and metasomatic hydrothermal iron deposits. These especially the skarn-type iron deposits are mainly associated with intermediate-felsic igneous rocks, with only a minor proportion related to mafic intrusions. The iron redox cycle is a substantial process that exists in most terrestrial environments, which can be conducted by both abiotic and microbial processes. In anoxic, pH-neutral environments, microbial Fe(II) oxidation is driven by either nitrate-reducing bacteria, photoferrotrophic bacteria or neutrophilic microaerophilic bacteria [11, 12].

Microbial Fe(III) reduction forms the other component of the Fe cycle, generated by intracellularly by magnetotactic bacteria [12] or outside of the cell wall by dissimilatory iron-reducing bacteria. These combines with the oxidation of organic substrate or hydrogen with the reduction of poorly crystalline, short-range ordered Fe(III) minerals (e.g. ferrihydrite) [13]. This can lead to the development of many different iron mineral phases and compounds including goethite, magnetite, green rust and siderite (Fe_2CO_3). The mineralogical composition of these products of reduction depends on geochemical parameters, inclusive Fe(III) reduction rate, pH, temperature and the availability of electron shuttle [14, 15].

Based on redox condition, magnetite can donate or accept electron in different metabolic processes involving Fe. In this respect, knowledge of the mineralogical outcomes of biomineralization characteristics can help provide signatures of microbial reactions with fluid, rocks, mineral deposits and subsequent diagenesis. Banded iron formation (BIF) is a chemically produced rock of sedimentary origin. This was precipitated in Precambrian time, comprising intercalated microcrystalline quart, iron oxides and silicates rich in iron. In line with depositional settings, the BIFs fall into Algoma type and superior type [16–18].

The constituents are discontinuous silica- and iron-rich bands with similar mineralogical properties of Fe, chert and carbonate minerals. Arc/back-arc basins or intra-cratonic rift zones host the Algoma type, and the latter is hosted by clastic carbonate rocks linked with shallow marine environments. As the main mineral constituents of BIFs, magnetite has been broadly reported for BIFs' depositional systems, mineralization characteristics and possible microbial involvements. Chemical and sedimentary methods in normal seawater could produce marine

Fe-Mn oxides/oxyhydroxides. These are formed by precipitation of micron range particles of these components onto rock substrates at seabed [19–21].

The Itakpe iron ore deposit in Nigeria with an estimated reserve of about 200 million ton was discovered in 1977. The areal extent of this deposit spans about 3000 m in length inclusively in several layers of ferruginous quartzite. Tectonically, this deposit is located at the southern flank of the Itakpe-Ajabanoko anticline with host rock and ore layers striking sublatitudinally and slightly bending to the north and dipping southwards with local minor-fold complexes. Itakpe iron ore deposit comprises variable constituents of hematite and magnetite and particle sizes. This deposit with an Fe content of 35% consists of fine ores occurring in thin layers and coarse-grained mixed components. Direct-reduced iron (DRI) is the direct reduction of iron ore to iron n steel making. The DRI constituents of the pellet include: slag containing oxides of calcium, magnesium, alumina, silica. DRI pellets contain 67% Fe and 3% silica. In establishing a steel plant, availability of economically beneficiated iron ore deposit stands out as the main factor. The concentrates required at Ajaokuta and Delta steel plant would be supplied by the Itakpe iron ore deposit [22–25].

2.1. Uses

A mixture of ferrous or ferric oxides constitutes iron oxides provided for pigments. These may contain impurities of manganese oxides, clay and silica. Oxides of iron remain one of the pigments of natural origin inclusive titanium dioxide. They are highly valued because they possess non-toxic, inert, opaque and weather-resistant properties. Oxides of iron constitute the main component of products in the pharmaceutical industry, paint industry, plastic industry, ink industry and cosmetic industry. Oxides containing mica provides anticorrosion properties. Natural pigments which qualify for these applications are limited in occurrence. Thus, synthetic iron oxides obtainable from iron compounds have better uniformity, purity of color, consistency and strength [26, 27].

The physical characteristics of these oxides are more valuable than chemical composition. The suitability of a material for pigment application is dependent on grindability, color uniformity and strength of tinting. Besides these properties, chemical purity is also important for its application in the pharmaceutical and cosmetic industries. Calcination of pyrite and siderite provides iron oxides which meet characteristics for these applications. Other beneficiation processes for commercial production of pigments include decomposition of iron compounds by thermal method, oxidative precipitation of iron salts and reductive process on organic compounds [28, 29].

Synthetic pigments override natural pigments due to their proximity to the place of use and meeting required specifications. The use of magnetite in dense medium separation is based on its physical properties: specific gravity and magnetism. Thus, magnetite could be recovered and used again. Magnetite provides separation of high-density minerals and washing of coal. The banded ores contain thin bands of hematite and magnetite alternating with bands of quartz schists, jasper and iron silicates with occasional bands of siderite. In more metamorphosed varieties, hornblende, olivine and garnet are present. Sulfur and phosphorus are low. Concentration is achieved by roasting to reduce the hematite to magnetite, crushing and magnetic separation followed by sintering and briquetting [29, 30].

Iron oxide pellets are used as the raw material in shaft furnace smelting. This is due to their uniformity in size, enormous strength and excellent permeability. However, production may be hampered by the rupture and fragmentation of pellets. Strength of pellet is closely connected to the modification of internal structure. In high-temperature reduction process, the strength changes are led mainly by internal stress. Phase alteration of oxides of iron in process of reduction may generate internal stress. To avoid this, magnetite should take the place of hematite crystalline in the pellet oxide roasting process. This will reduce volume expansion during reduction process [31–33].

Direct-reduced iron (DRI) has been carried out in recent times to provide justifiable metallurgical operations. DRI possesses enormous benefits because it does not depend on coke-making and sintering. Where coke-making and sintering are fronted at the conventional blast furnace, then ironmaking ends up being a costly process and is consistently causing environmental concerns. The DRI procedure consists of reduction of iron oxide by carbothermic method and converted natural gas. In this process, volatiles are directly liberated during coal devolatilization besides carbon monoxide regeneration from coal char. This process provides application prospect for the high volatile coals, which were ordinarily impractical in the steel industry. Extensive work has been reported on reduction of iron ore and coal-ore mixtures and its kinetics [34, 35].

Optimization of the coal-based DRI process requires understanding of the thermal properties of the coal-ore mixtures and mechanism reactions of reduction, which have still not been well understood. It is therefore necessary to have an insight into fundamental mechanisms for these complex reactions. The Itakpe iron ore is the deposit of the main concern to the Nigerian steel industry. The ore comprises substantial quantity of quartz and silica present itself in parallel layers to each other. About 29–37% Fe is contained in the ore grade, thus averaging 35% Fe. High flue dust losses are the basic characteristics of constituents which provide marked interruption during reduction. In addition, this could lead to attenuated furnace operation. Reducibility and clustering behaviour are significantly influenced by additions of 5% slaked lime to Itakpe iron ore pellet [36, 37].

The consequence of iron ore tailings (IOT) on modification of cement tropical black clay was considered. The naturally occurring soil was worked on using 4% cement and 10% IOT per soil dry weight. Samples of tested soil compressed with British Standard measurement mechanism were exposed to catalog, sieve examination, compaction and shear strength parametric study. The outcome of laboratory study displaying attributes of the improved soil was enhanced when tested with cement-IOT blends. Experimental results expressed attenuation of the satisfactory fraction, attenuation in liquid and plastic limits and enhancement in optimum dry density, with a reduction in optimum content of moisture (OMC) besides attenuation in shear strength rate of the natural soil [38].

2.2. Environmental implications

The role of ochre and oxides of iron in copper and zinc adsorption has been studied by [39–48].

Ochre and oxides of iron present in aqueous metal load are known to be good adsorbents. Heavy metal contaminants especially heavy metal load in the aquatic environment, discharged by acid mine drainage and treatment plant liquids, constitute the principal derivatives of tarnished water channels. Limited reports of heavy metal removal exist. However, the utilization of oxides and oxyhydroxides inoculated with sulphide of zinc within sulfidic-anoxic setting is a new dimension of research [39, 40]. This report centred on investigating heavy metal load removal onto ochre and iron oxide coatings from virtual wastewater related to effluents. At ambient temperature, batch mode techniques involved inoculating sulphide containing heavy metal into mineral system of ochre and iron oxide coatings [41].

pH of solution, quantity of metal at the onset of reaction, concentration of adsorbent and reaction time were variables investigated (**Table 1**). There was a strong understanding that goethite-ochre and iron oxide coatings exhibited a linear increase in the adsorption of heavy metal load as solution pH was increased. In addition, quantity of adsorption increased with increase metal concentration [41–44].

Some mineral systems including ochre and oxides of iron coatings confirmed neither promotive nor non-promotive adsorption of heavy metal load throughout the series of concentration of particle investigated. Adsorption of heavy metal load by ochre and iron oxide coatings revealed a complex attitude throughout the period of aging investigated. Performance of adsorption was dependent on availability of different sites of reaction [45].

Adsorption of heavy metal load was examined by means of single and mixed mineral systems containing ochre and iron oxide coatings within sulfidic-anoxic environment in the

Characteristics	**Weight (%)**
SiO_2	0.30
Al_2O_3	0.18
FeO	62.62
MgO	0.03
Na_2O	0.00
CaO	0.23
MnO	0.06
K_2O	0.02
Cu (ppm)	0.14
Zn (ppm)	0.18
Surface area (m^2/g)	97.00
% (<1000 nm) colloid	1.83
Particle size range (μm)	0.01–100.00
pH ± σ	3.00
Point of zero salt effect (PZSE)	7.13

Table 1. Characteristics of Parys Mountain ochre, United Kingdom [46, 47].

characteristics of wastewater obtained from abandoned mine pits at Parys Mountain in the United Kingdom. Bodies of water are the receivers of these contaminants. In these bodies of water, human activities including fishing exist. Effort was made to bring down the levels of heavy metal load intake in the bodies of water by means of ochre and iron oxide coatings. These were verified with the mine liquid waste for adsorption characteristics at different pH, concentration of solid and reaction time. In addition, levels of saturation of hydroxyl chemically bonded components were modeled. Reactions by batch techniques at ambient temperature provided ochre and iron oxide coatings adsorbed more heavy metal load (**Figure 1**). In addition, heavy metal load adsorbed on oxides of iron displayed increases in adsorption with increase in pH [46, 47].

There was cross-cutting pH characteristics of heavy metal load adsorbed on goethite at pH = 7. These provided similar reduction of metal characteristics at the crossover pH. Differences in heavy metal load reduction may be aligned to linkages between adsorbate and water molecules attached to adsorbent and direct attachment of adsorbate to adsorbent. Non-promotive effect of, i.e. attenuation in metal reduction with enhancement in concentration of particle, was detected in ochre and iron oxide coatings. This feature may be aligned to enhanced aggregation of the ochre and iron oxide coatings of particle sizes. Features of aging progress as reaction time was increased. This may be aligned to the availability of thiol and hydroxyl components and chemical sites of responses. There is no link to stable introduction of hydroxyl group to species of copper and zinc that could meaningfully account to the reduction of these metals [48].

Litter by heavy metals of copper and zinc provided by acid mine drainage and liquid waste treatment are the leading sources of blotted water chemistry. Metal plating, mining and painting cause release of heavy metals of copper and zinc. These metals become a serious health problem. This is because they are dogged and have harmful effect on the environment. Heavy metals of copper and zinc are required in small quantity element that is essential for nutrition [46, 47].

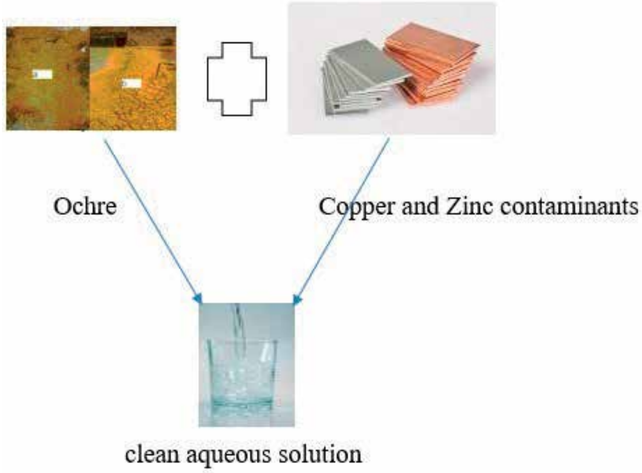

Figure 1. Graphical summary for ochre interaction with copper and zinc ions.

However, when available in overdose, it may be noxious. This could pose adverse danger in groundwater and surface resources as they build-up in living organisms [45]. It is widely known that surplus of heavy metals of copper and zinc provides depression, lethargy and neurological disorder signs such as nervous confiscations and increased dehydration. Therefore, reduction of these metals from water courses is needed. Anthropogenic activities release metal load into bodies of water. These metal loads damage the ecosystem and are toxic to humans and other forms of life. Chemical solution and appropriate sorbents determine the availability of dissolved metal species [44].

Reduction of copper and zinc ions from solutions of aquatic nature is governed by the makeup of the solution. These include the outcome of hydrogen ion concentration and the number of solid particles in the wastewater. pH remains an important factor in reduction of metal ions from the aqueous environments. The amount of dissolved metal in solution is measured by pH. Another effect of pH includes hydrolysis characterization and surface charge. Lower pH attenuates hydrolysis and enhances metal build-up in the solution. Adsorption of heavy metals of copper and zinc is controlled by anion nature and the external layer of the adsorbent [43].

Adsorption related to solute water molecule attachment attenuates as particle concentration increases. Adsorption related to solute direct attachment to adsorbent does not significantly increase in some cases as adsorbent quantity increases. When adsorption is enhanced as particle concentration increases, then promotive particle concentration effect is reported. The reasons for the promotive adsorption effect by concentration of solid particle remains are uncertain. Ionic species available in solution are influenced by the forces at work at the mineral-solution interface. This is controlled by formation of high and newly formed reaction sites [42].

However, adsorption of metalloids and metals does not have a lined-up rapport with respect to these features. The mechanisms of adsorption accountable for heavy metal reduction provide both slow and fast steps of reactions. The slow reaction period is accredited to slow diffusion of interparticle and advanced activation energy when linked with the fast sites of metal reaction. The fast reaction period may be distributed to adsorption by electrostatic pull. Comparable procedures include adsorption that is specific to adsorbent external layer and formation of an insoluble salt in many respects. In naturally controlled systems, adsorption generally takes place on external surfaces of ochre and iron oxide coatings of mineral surfaces [41].

These processes could piece together, and the prevalence of one is hard to determine. This may be characterized by several uncertain mechanisms. Increase in heavy metal reduction from solution as initial concentration of metal increase has been reported. This capacity of adsorption increase in kith and kin to the concentration of metal ions can be clarified with the high columbic force for mass transfer. The presence of ochre and iron oxide coatings attenuated heavy metal removal over the series of pH (i.e. pH = 4–8) investigated. Increased ionic strength (i.e. 0.00–0.1 mol/kg) and concentration of solid (i.e. 0.002–0.01 kg/L) presented a multifaceted response. The uncontrollable discharge of liquid waste comprising heavy metal load into courses of water has occasioned in the degradation of watercourse water chemistry [40].

Thus, reduction of heavy metal load from sewages, before their issue to the ecosystem, is a significant problem of contemporary wastewater handling. Metals are routinely different from other noxious pollutants. They cannot be decomposed and can post up in tissues of humans. Heavy metals of copper and zinc are major pollutants usually found in effluent discharge. Adsorption to ochre especially in their natural states is a fundamental process providing the transport, degradation and biological activity of organic compounds in the ecosystem. Although often regarded as instantaneous for modeling purposes, adsorption may in fact require many months to reach equilibrium. Heavy metal reduction is governed by chemical composition of the aqueous system: solution pH, solution ionic strength and solid particle concentration, as well the reaction time of the solid component in the wastewater [39].

However, the particle size of ochre and iron oxide coatings in adsorption tests could significantly affect the adsorption features related to the tests. Reaction associated with breaking of molecular bond of water linked to reaction pattern is ruled by solution pH and solution ionic strength. Attenuation in metal reduction in ochre medium as solution ionic strength increases supports metal attachment to water molecules in the adsorption process. In the other way around, direct attachment of adsorbate to the adsorbent is involved [40]. The solute contained in a solvent provides the solid concentration effect for mechanism of sorbate reduction, whereby metal reduction models attenuate as solid-to-solvent ratio increases. Different sites of reaction could be created as contact between the sorbate and adsorbate structures is increased [41].

Here, the effect of ochre and oxides of iron on reduction of heavy metal in relation to composition of solution and aging has been discussed. The impacts of various factors, such as reaction time, ionic strength, adsorbent size, initial solution pH and solute-solvent ratio on the adsorption quantity were studied. Models of adsorption kinetic provided illustrated that adsorption quantity of ochre and oxides of iron was dependent on pH (i.e. pH = 4–8), solute-solvent ratio (i.e. 0.002 kg/L to 0.01/L), the reaction time (i.e. 24–720 h) and the sizes of the ochre. The hydronium ion regular diffusion coefficient in the presence of ochre and oxides of iron was enhanced when anoxic solution of iron sulphide was introduced into the reaction system. The net movement of adsorbate to external layer of the adsorbent decreased with contact time increase [42].

Reactions were in three-step processes: chemical species involved were discrete and separate, chemical species were bridged and adsorption of adsorbate on the inner surface of the adsorbent, and these provided the basis for the kinetic models used. The arsenite reduction by the ochre and oxides of iron was altered by the presence of thiol group and submits a non-promotive Cp effect (i.e. adsorption reduced with increase in Cp). Ochre and oxides of iron provided increased arsenite adsorption as reaction time increased until 288 h.

In another study [43], ochre and oxides of iron systems were examined to understand their consequence on heavy metal reduction. Isotherms discovered metal reduction by ochre and oxides of iron which were controlled by ochre size, solution pH, ionic strength, particle quantity and reaction time. Mineral mixtures containing ochre and oxides of iron provided diverse adsorption characteristics from the single ochre and oxides of iron mineral systems. These oxides attenuated heavy metal removal over the series of pH (i.e. pH = 4–8) investigated. Increased ionic strength (i.e. 0.00–0.1 mol/kg) and adsorbent quantity (i.e. 0.002–0.01 kg/L) displayed an intricate response [43].

This study was required because the reckless release of wastewater comprising copper and zinc into water passages has caused dilapidation of stream water chemistry. Thus, reduction of heavy metal ions from sewages, before they are being emptied to the ecosystem, is a key issue of modern wastewater control processes. Metals are usually diverse from other toxic pollutants. They cannot be decomposed and can build up in living tissues. Heavy metals of copper and zinc constitute major pollutants usually located in effluent discharge. Adsorption to natural solids like ochre, oxides of iron and clay minerals is a fundamental process influencing the transport, degradation and biological activity of biological compounds in the ecosystem. Although often regarded as instantaneous for modeling purposes, adsorption may in fact require many months to reach equilibrium [44].

Again, heavy metal reduction is controlled by chemistry and makeup of the aqueous solution, solution pH, ionic strength and adsorbent concentration, besides the reaction time of the solid stage in the wastewater. However, the adsorbent particle size of such usual adsorption methodology could alter the adsorption features involved in the report. Reactions comprising the breakage of bonds in a water molecular form are a function of solution pH and solution ionic strength. Lowering of metal reduction in solution as solution ionic strength increases provides adsorbent water molecular attachment. The opposite describes direct attachment of adsorbate to the external layer of the adsorbent [45]. The quantity of solute-solvent ratio (i.e. solid concentration) consequence is a usual metal removal mechanism, whereby metal reduction in solution isotherm attenuates as quantity of solute-solvent ratio increases. Diverse reaction sites could be formed as contact between the adsorbate and ochre and oxides of iron mineral systems was increased. This study aimed at discovering the outcome of interacting ochre and oxides of iron mineral systems and the mixture components with clays on adsorption behaviour of heavy metals of copper and zinc in relation to chemical composition of solution and reaction time [46].

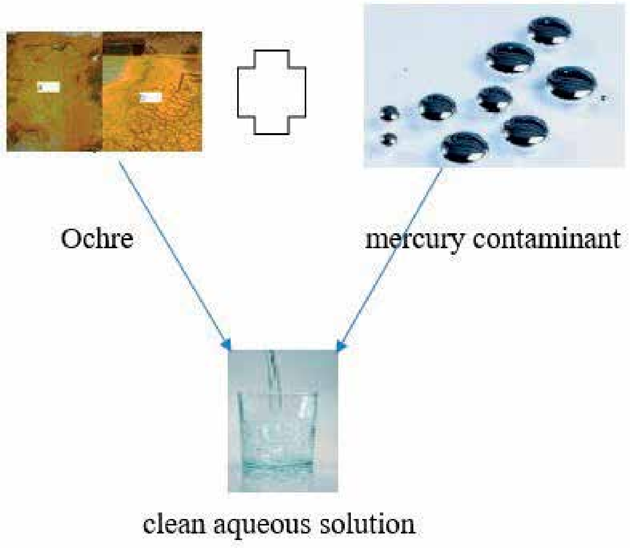

Figure 2. Graphical summary for mercury interaction with ochre.

Figure 3. Graphical summary for lead interaction with ochre.

The influences of various factors, including reaction time, solution ionic strength, adsorbent size, initial pH and solid quantity on the adsorption quantity, were studied. Adsorption of heavy metals of copper and zinc was looked at by means of single minerals of ochre and oxides of iron and their mixed mineral components with clays in sulfidic-anoxic state. Attempt was completed to lower the quantity of metal levels in these mine pits before release into the ecosystem [47].

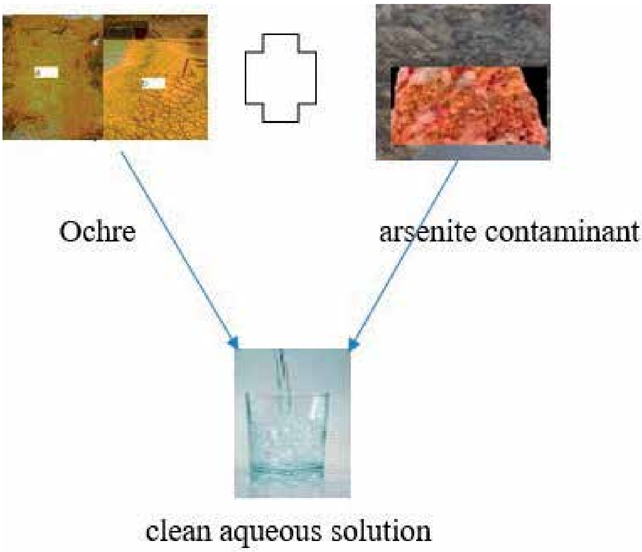

Figure 4. Graphical summary for arsenite interaction with ochre.

Ochre and oxides of iron and their mixtures with clays were tested with the mine wastewater for description of metal reduction in these mine wastewaters. This was conducted at adjustable solution pH, solid quantity and contact time. In addition, levels of saturation of complex compounds containing hydroxyl group were modeled. Batch responses directed at ambient temperature disclosing all mineral systems reduced metal load. Also, metal adsorbed on oxides of iron unveiled enhanced adsorption as solution pH was increased (**Figures 2–4**). There was cross-cutting consequence of heavy metal load attached to ochre and oxides of iron at about pH = 7. These cross-cutting features indicated analogous metal reduction characteristics [48].

3. Conclusions

Genesis, uses and environmental implications of iron oxides and ores have been considered in this chapter. Natural iron oxides occur extensively and are obtained from deposit of various types. Hematite is mainly sourced from iron ore of sedimentary origin including hydrothermal, metamorphic and volcanic deposits. Mafic and ultramafic rocks are linked with magnetite. This is also associated with skarn-type metamorphic deposits.

A mixture of ferrous or ferric oxides constitutes iron oxides provided for pigments. These may contain impurities of manganese oxides, clay and silica. Oxides of iron remain one of the pigments of natural origin including titanium dioxide. They are highly valued because they possess non-toxic, inert, opaque and weather-resistant properties. Oxides of iron constitute the main component of products in the pharmaceutical industry, paint industry, plastic industry, ink industry and cosmetic industry. Oxides containing mica provide anti-corrosion properties. Natural pigments which qualify for these applications are limited in occurrence. Thus, synthetic iron oxides obtainable from iron compounds have better uniformity, purity of color, consistency and strength. Beneficiation processes of iron ore generate dust in the atmosphere, acid mine drainage in the ecosystem and metallic iron for steelmaking.

The main sources of air contamination during the beneficiation processes are emission of poisonous gases such as nitrous oxide, carbon dioxide, carbon monoxide and sulfur dioxide. Beneficiation process requires dissolution of minerals surrounding the ore and the release of metals and cement matrix into courses of water. These generate acid leading to acid mine drainage. Excess acidity and metal load in the ecosystem result in the loss of ecological balance and health hazards. Therefore, there is a need for valuation of the environmental impact in the planned beneficiation cycle. Sustainable beneficiation is required to reduce its impact on the natural, social or economic environment.

Reduction of heavy metal load from sewages, before their issue to the ecosystem, is a significant problem of contemporary wastewater handling. Ochre and oxides of iron have been used to test the removal of heavy metals including copper and zinc from contaminated aqueous environment. This process is governed by solution pH, metal concentration, ochre (i.e. adsorbent) concentration and contact time of reaction.

Author details

Davidson E. Egirani[1]*, Mohd T. Latif[2], Nanfe R. Poyi[3], Napoleon Wessey[1] and Shukla Acharjee[4]

*Address all correspondence to: eenonidavidson@yahoo.com

1 Faculty of Science, Niger Delta University, Wilberforce Island, Nigeria

2 School of Environmental and Natural Resource Sciences, Universiti Kebangsaan, Malaysia

3 Nigerian Institute of Mining and Geosciences, Jos, Nigeria

4 Centre for Studies in Geography, Dibrugarh University, Assam, India

References

[1] Icopini GA, Anbar AD, Ruebush SS, Tien M, Brantley SL. Iron isotope fraction during microbial reduction of iron: The importance of adsorption. Geology. 2004;**32**:205-208

[2] Buxbaum G, editor. Industrial Inorganic Pigments. 3rd ed. Toronto: Weheim; 1998. 265 p

[3] Zhang CJ, Hu RZ, Zhong H, Zhou MF, Ma R, Li YG. Genetic links of magmatic deposits in the Emeishan large igneous province with the dynamics of a mantle plume. Kuangwu Yanshi. 2005;**25**:35-44

[4] Wang T, Duval B, Graedel TE. Exploring the engine of anthropogenic iron. In: Proceedings of the National Academy of Science; United States of America. United Sates of America: National Academy of Science; 2006. p. 44

[5] Mahiuddin S, Bondyopadhway S, Baruah JN. A study on the beneficiation of indian iron-ore fines and slime using chemical. International Journal of Mineral. 1989;**26**:285-296

[6] Egirani DE, Baker AR, Andrews JE. Copper and zinc removal from aqueous solution by mixed mineral systems: Reactivity and removal kinetics. Journal of Colloid and Interface Sciences. 2005;**219**:319-325

[7] Jones JG, Warner CG. Chronic exposure to iron oxide, chromium oxide, and nickel oxide fumes of metal dressers in a steelwork. British Journal Industrial Medicine. 1972;**29**:169-177

[8] Harben W, Kuzvart M. Industrial Minerals: A Global Geology Hardcover. 2nd ed. London: Metal Bulletin; 1996. 462 p

[9] Reed MH. Seawater-basalt reaction and the origin of greenstones and related ore deposits. Economic Geology. 1983;**78**:75-81. DOI: 10.2113/gsecongeo.78.3.466

[10] Kappler A, Straub KL. Geomicrobiological cycling of iron. Reviews in Mineralogy and Geochemistry. 2005;**59**:85-108

[11] Kapple A, Newman DK. Formation of Fe(III)-minerals by Fe(II)-oxidizing photoautotrophic bacteria. Geochimica et Cosmochimica Acta. 2004;**68**(6):1217-1226

[12] Blakemore R. Magnetotactic bacteria. Science New Series. 1975;**190**(4212):377-379

[13] Lovley DRI, Phillips EJ. Novel mode of microbial energy metabolism: Organic carbon oxidation coupled to dissimilatory reduction of iron or manganese. Applied and Environmental Microbiology. 1988;**54**(6):1472-1480

[14] O'Loughlin EJ, Gorski CA, Scherer MM, Boyanov MI, Kemner KM. Effects of oxyanions, natural organic matter, and bacterial cell numbers on the bioreduction of lepidocrocite (γ-FeOOH) and the formation of secondary mineralization products. Environmental Science & Technology. 2010;**44**:4570-4576. DOI: 10.1021/es100294w

[15] Piepenbrock A, Porsch UDK, Appel E, Kappler A. Dependence of microbial magnetite formation on humic substance and ferrihydrite concentrations. Geochimica et Cosmochimica Acta. 2011;**75**(22):6844-6858

[16] Byrne JM, Telling ND, Coker VS, Pattrick RAD, van der LG, Arenholz E, et al. Control of nanoparticle size, reactivity and magnetic properties during the bioproduction of magnetite by Geobacter sulfurreducens. Nanotechnology. 2011;**45**(22):455709. DOI: 10.1088/0957-4484/22/45/455709

[17] Konhauser KO, Hamade T, Raiswell R, Morris RC, Ferris FG, Southam G, Canfield DE. Could bacteria have formed the Precambrian banded iron formations? Geology. 2002;**30**(12):1079-1082

[18] Rasmussen B, Krapež B, Meier DB. Replacement origin for hematite in 2.5 Ga banded iron formation: Evidence for postdepositional oxidation of iron-bearing minerals. GSA Bulletin. 2014;**126**(3-4):438-446

[19] Cox GM, Halverson GP, Minarik WG, Le Heron DP, Macdonald FA, Bellefroida EJ, et al. Neoproterozoic iron formation: An evaluation of its temporal, environmental and tectonic significance. Chemical Geology. 2013;**362**:232-249

[20] Klein C. Some Precambrian banded iron-formations (BIFs) from around the world: Their age, geologic setting, mineralogy, metamorphism, geochemistry, and origins. American Mineralogist. 2005;**90**(10):1473-1499

[21] Bekker A, Slack JF, Planavsky N, Krapez B, Hofmann A, Konhauser KO, Rouxel OJ. Iron formation: The sedimentary product of a complex interplay among mantle, tectonic, oceanic, and biospheric processes. Economic Geology. 2010;**105**(3):467-508

[22] Olubambi PA, Potgieter JH. Effectiveness of gravity concentration for the beneficiation of Itakpe (Nigeria) iron ore achieved through jigging operation. Journal of Minerals & Materials Characterization & Engineering. 2005;**4**(1):21-30

[23] Das B, Prakash S, Das SK, Reddy PSR. Effective beneficiation of low grade iron ore through jigging operation. Journal of Minerals & Materials Characterization & Engineering. 2007;**7**(1):27-37

[24] Ohimain EI. Scrap iron and steel recycling in Nigeria. Greener Journal of Environmental Management and Public Safety. 2013;**2**(1):001-009

[25] Ajaka EO. Recovering fine iron minerals from Itakpe iron ore process tailing. ARPN Journal of Engineering and Applied Sciences. 2009;**4**(9):17-28

[26] Barham LS. Systematic pigment use in the middle Pleistocene of south-Central Africa. Current Anthropology. 2002;**43**(1):181-190

[27] Tartaj P, Morales MP, Gonzalez-Carreño T, Veintemillas-Verdaguer S, Serna CJ. The iron oxides strike back: From biomedical applications to energy storage devices and Photoelectrochemical water splitting. Advanced Materials. 2011;**23**(44):5243-5249

[28] Harben PW, editor. The Industrial Minerals Handybook — A Guide to Markets, Specifications and Prices. 4th ed. Worcester Park, UK: Industrial Minerals Information Services; 2002. 412 p

[29] Roebroeks W, Sier MJ, Nielsen TK, De Loecker D, Pares JM, Arps CE, et al. Use of red ochre by early Neandertals. In: Klein RG, editor. Proceedings of the National Academy of Sciences; United States of America. United States of America: National Academy of Science; 2012. pp. 1889-1894

[30] Karapinar N. Magnetic separation of ferrihydrite from wastewater by magnetic seeding and high-gradient magnetic separation. International Journal of Mineral Processing. 2003;**71**(22):45-54

[31] Chunba Xu C, Cang D-Q. A brief overview of low CO_2 emission technologies for iron and steel making. Journal of Iron and Steel Research, International. 2010;**17**(3):1-7

[32] Halt JA, Silva BB, Kawatra SK. A new on-line method for predicting iron ore pellet quality. Mineral Processing and Extractive Metallurgy Review. 2015;**36**(6):377-384

[33] Kolo K, Konhauser K, Krumbein WE, Ingelgem YV, Hubin A, Claeys P. Microbial dissolution of hematite and associated cellular fossilization by reduced iron phases: A study of ancient microbe-mineral surface interactions. Astrobiology. 2009;**9**(8):777-796

[34] Kumar M, Jena S, Patel SK. Characterization of properties and reduction behavior of iron ores for application in sponge ironmaking. Journal Mineral Processing and Extractive Metallurgy Review. 2007;**29**(2):118-129

[35] Zervas T, McMullan JT, Williams BC. Developments in iron and steel making. International Journal of Energy Research. 1996;**20**(1):69-91

[36] Yang J-B, Cai N-S, Li Z-S. Hydrogen production from the steam–iron process with direct reduction of iron oxide by chemical looping combustion of coal char. Energy. 2008;**22**(4):2570-2579

[37] Olayebi OO. Steel making experience in the use of Nigerian iron ore at the Delta steel company, Nigeria. Journal of Chemical Engineering and Materials Science. 2014;**5**(5):47-62

[38] Osinubi KJ, Yohanna P, Eberemu AO. Cement modification of tropical black clay using iron ore tailings as admixture. Transportation Geotechnics. 2015;**5**:35-49

[39] Egirani DE, Andrews JE, Baker AR. Copper and zinc removal from aqueous solution using mixed mineral systems injected with iron sulfide under sulfidic-anoxic conditions i: Reactivity and removal kinetics. International Journal of Environmental Engineering Science and Technology Research. 2014;**2**(4):1-15

[40] Egirani DE, Baker AR, Andrews JE. Copper and zinc removal from aqueous solution by mixed mineral systems ii. The role of solution composition and aging. Journal of Colloid and Interface Science. 2005;**291**:326-333

[41] Egirani DE, Andrews JE, Baker AR. Copper removal from aqueous solution using mixed mineral systems injected with zinc sulfide in sulfidic- anoxic conditions II. The role of solution composition and ageing. The Journal of Energy and Environmental Science Photon. 2014;**128**:457-466

[42] Egirani DE, Andrews JE, Baker AR. Copper and zinc removal from aqueous solution using mixed mineral systems injected with iron sulfide under sulfidic- anoxic conditions 1: Reactivity and removal kinetics. International Journal of Environmental Engineering Science and Technology Research. 2014;**2**(4):1-15

[43] Egirani DE, Andrews JE, Baker AR. Copper and zinc removal from aqueous solution using mixed mineral systems injected with iron sulfide under sulfidic- anoxic conditions ii. The role of solution composition and ageing. International Journal of Environmental Engineering Science and Technology Research. 2014;(4):1-14

[44] Egirani DE, Andrews JE, Baker AR. Copper removal from aqueous solution using mixed mineral systems injected with zinc sulfide in sulfidic- anoxic conditions I: Reactivity and removal kinetics. The Journal of Energy and Environmental Science, Photon. 2014;**128**:467-478

[45] Egirani DE, Andrews JE, Baker AR. Characterization and geochemical modelling of Cu and Zn sorption using mixed mineral systems injected with iron sulfide under sulfidic anoxic conditions i: Case study of Cwmheidol mine wastewater, Wales, United Kingdom. International Science Index, Geochemical and Geological Engineering. 2015; **9**(8):1075-1083

[46] Egirani DE, Wessey N, Aderogba A. Effect of mineral systems on copper and zinc removal from aqueous solution part ii. Journal of Applied Chemical Science International. 2016;**5**(3):174-181

[47] Egirani DE, Wessey N, Aderogba A. Effect of mineral systems on copper and zinc removal from aqueous solution part i. Journal of Applied and Chemical Science International. 2016;**6**(1):1-9

[48] Egirani DE, Wessey N, Acharjee S. Characterization and geochemical modelling of Cu and Zn sorption using mineral systems injected with iron sulfide: Case study of mine waste water, Wales, United Kingdom. World Journal of Applied Chemistry. 2017;**2**(1):13-23

Section 2

Agglomeration and Processing

Iron Ore Pelletizing Process: An Overview

Sandra Lúcia de Moraes,
José Renato Baptista de Lima and
Tiago Ramos Ribeiro

Additional information is available at the end of the chapter

http://dx.doi.org/10.5772/intechopen.73164

Abstract

The iron ore production has significantly expanded in recent years, owing to increasing steel demands in developing countries. However, the content of iron in ore deposits has deteriorated and low-grade iron ore has been processed. The fines resulting from the concentration process must be agglomerated for use in iron and steelmaking. This chapter shows the status of the pelletizing process with a special focus on binders. Bentonite is the most used binder due to favorable mechanical and metallurgical pellet properties, but it contains impurities especially silica and alumina. The importance of many researches concerning alternative binders is also discussed in this chapter. Better quality wet, dry, preheated, and fired pellets can be produced with combined binders, such as organic and inorganic salts, when compared with bentonite-bonded pellets. While organic binders provide sufficient wet and dry pellet strengths, inorganic salts provide the required preheated and fired pellet strengths.

Keywords: iron ore, pelletizing process, binder, bonding mechanism, induration technology

1. Introduction

Iron ore and iron ore pellets are important sources of iron for manufacturing steel. The iron ore production has significantly expanded in recent years, owing to increasing steel demands in developing countries, such as China and India. However, the content of iron ore in deposits has deteriorated and low-grade iron ore has been processed. The fines resulting from the enrichment by separation after liberation by size reduction must be agglomerated in a pelletizing plant. Consequently, the number of pelletizing plants is expected to increase in the future.

The quality requirements of pellet, such as physical, chemical and metallurgical specifications, depend on each ironmaking furnace and those requirements influence the operation of the iron ore pelletizing plant.

The idea of rolling moist fine ore in a drum to form balls and then drying and firing it was first patented by A. G. Andersson in Sweden in 1912. Further development was performed to bring the idea to reality. In 1943, E. W. Davies and co-workers demonstrated the process using an experimental shaft furnace. Commercial operation started in the 1950s in Sweden using vertical-shaft-kilns for firing the pellets. Plant capacities were between 10,000 and 60,000 tons/year [1].

The world installed pelletizing capacity is currently estimated to be 480.7 million tons/year [2]. As shown in **Figure 1**, China presents the largest production capacity, followed by the United States and Brazil.

The iron ore pelletizing process consists of three main steps:

1. Pelletizing feed preparation and mixing: the raw material (iron ore concentrate, additives —anthracite, dolomite—and binders are prepared in terms of particle size and chemical specifications, dosed, and mixed together to feed the pelletizing process;
2. Balling process: the green pellet is the rolled pellet without any thermal process. It is obtained under strict control of moisture and has a spherical shape and diameter of 8–16 mm;
3. Induration process: the green pellets are hardened in a high temperature processing at controlled heating rates, and aiming to achieve the physical and metallurgical requirements for handling, transportation, and final application.

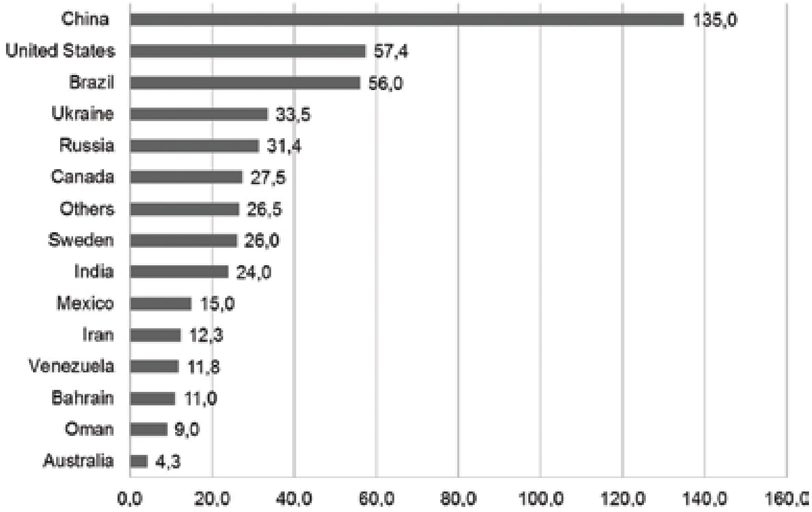

Figure 1. World installed pelletizing capacity (millions of tons/year). Source: Prepared by the authors with data from Tuck and Virta [2].

This chapter aims to provide an overview and the evolution of iron ore pelletizing process including:

- Pelletizing process and raw materials
- Balling technologies
- Bonding mechanisms
- Evolution of binders for iron ore pelletizing
- Induration technologies
- Challenges and innovations in iron ore pelletizing

2. Pelletizing process and raw materials

The iron ore is mined mostly from open pit deposits through mining operations and the raw product, "run of mine," is subjected to mineral processing. Thus, the material is exposed to a series of operations of fragmentation, separation by size, concentration, dewatering, etc., aiming to adequate the chemical, physical, and metallurgical characteristics to meet the demands of ironmaking processes. The particle size distribution of iron ore is a very important requirement to be characterized after its mineral processing.

Materials containing a very fine particle size distribution are not adequate to be used directly in the reduction reactors, requiring to be agglomerated by different processes such as sintering or pelletizing.

The main used reduction reactors are the blast furnace (BF) and direct reduction reactors (DR). In the blast furnace, iron is reduced and melted and the most common product is liquid iron called hot metal. In direct reduction, iron remains in solid state and the product is the so-called direct reduced iron (DRI).

Generically, the iron ore products for ironmaking can be classified as shown in **Table 1**.

Pellets are balls formed by rolling moist concentrates and fines iron ores of different mineralogical and chemical composition, with the addition of additives and binder, in a horizontal drum or in an inclined disc [1, 4].

Product	Size range (mm)	Basic application
Lump	6.3–31.7	Directly fed to blast furnace and direct reduction
Sinter feed	0.15–6.3	Agglomeration by sintering to be fed in blast furnaces
Pellet feed	<0.15	Agglomeration by pelletizing to be fed to blast furnace and direct reduction

Table 1. Iron ore products classification for ironmaking [3].

Pellets produced to be used in ironmaking processes must have characteristics that meet the list of quality specifications regarding physical, chemical, and metallurgical properties. Almost all of those properties are standardized as shown in **Table 2**.

Aiming to achieve those specifications, binders and additives are used in the pelletizing process. Additives such as limestone, dolomite, and hydrated lime are used to modify the chemical composition of the pellets, most often for correction of the basicity.[1] Certain substances such as hydrated lime serve as both additive and binder. Fines of anthracite or coke are also added during the pelletizing process for reducing the consumption of fuel required for internally heating the ball [7].

Pellets are obtained by adding an appropriate amount of water to the iron ore concentrate; this is a fundamental factor in the formation and growth of pellets, which creates a surface tension that holds the mineral grains cohesive, thus allowing their handling [6, 8].

This cohesive tension of fine particles due to water is called neutral tension. Neutral tension, however, is not sufficient to keep cohesive grains as dense as iron minerals. Furthermore, when the pellet is heated, the vaporization of water occurs and the pellets tend to disintegrate.

Type of specification	**Norm**	**Description**
Physical	ISO 4701	Determination of size distribution by sieving
	ISO 4700	Determination of the crushing strength
	ISO 3271	Determination of the tumble and abrasion index
	JIS M 8711	Determination of shatter strength
	Internal procedures (pelletizing companies)	Determination of crashed resistance by the number of drop falls
Chemical		Chemical property of the pellets
Metallurgical	ISO 4698	Determination of the free-swelling index
	ISO 13930	Determination of low-temperature reduction-disintegration index by dynamic method
	ISO 11257	Determination of the low-temperature reduction-disintegration index and degree of metallization
	ISO 11256	Determination of the clustering index
	ISO 7992 / ISO 7215 / ISO 11257	Determination of reduction under load/Determination of the reducibility by the final degree of reduction index/Determination of the low-temperature reduction-disintegration index and degree of metallization
	Internal procedures (pelletizing companies)	Porosity

Source: elaborated by the author with data from Campos et al. [5] and Moraes [6].

Table 2. Quality specification of iron ore pellets.

---

[1] Basicity in this context is the ratio between the weight percent of CaO and SiO_2.

To avoid such effects, binders are added to the material to be pelletized, aiming to:

- increase the strength of pellets before heating (green strength);
- prevent the collapse of pellets during the initial stages of heating, when a large volume of gas generated by water vaporization tends to crack the pellets.

Evenly distributed moisture and binder in the feeding process is decisive to improve the characteristics of pellets, especially to avoid the formation of undesirable agglomerates before the pellet formation.

Bentonite is an effective, widely used binder in the iron ore pelletizing process. Its low price is an important factor for its extensive use.

However, bentonite incorporates silica and alumina, which are undesirable contaminants to pellets. Additionally, it is a natural material with variable composition depending on its origin. Obtaining a suitable binding effect requires a relatively large amount of material, around 0.5% by weight, which makes handling more difficult and increases logistics costs.

Figure 2 shows a flowchart of a typical pelletizing plant, highlighting the additive preparation, mixing and pelletizing feed preparation, the balling step, in this case using a disc pelletizer, and the induration step.

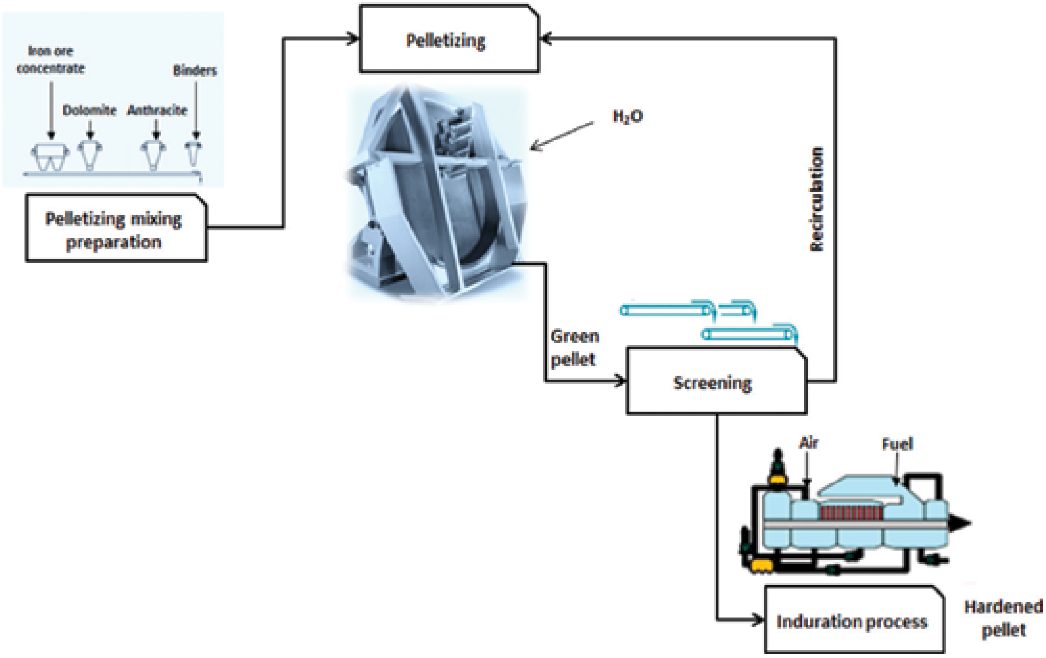

Figure 2. Typical pellet plant using disc pelletizer as balling technology. Source: Elaborated by the authors from Metso [9] and Vale [10].

3. Balling technologies

The balling equipment that can be either a disc or a drum produces green pellets in a variable size distribution.

3.1. Balling disc or disc pelletizer

Figure 3 schematically shows a laboratory disc pelletizer. The balling disc basically consists of a pan with a peripheral wall, which rotates with a certain inclination to the horizontal [1]. In general, in a balling disc, the pan angle can be adjusted between 40 and 60° [11].

When the disc rotates, the feed material with less moisture than that required for the pellets formation, is charged to the bottom of the disc, where it get in contact with the water from the sprayers, initiating the nucleation stage. At this stage, the nuclei begin to take the form of small pellets, which by rolling action, occur in the lower section, to the left of the disc, toward the top. As the added ore aggregates unto the surface of the pellets, they increase in size and the coefficient of friction is reduced causing the pellets to acquire a centrifugal force that carries them out of the nucleation zone. This movement takes the pellets to the top of the disc following a semicircular trajectory before returning to the base of the disc [1, 12].

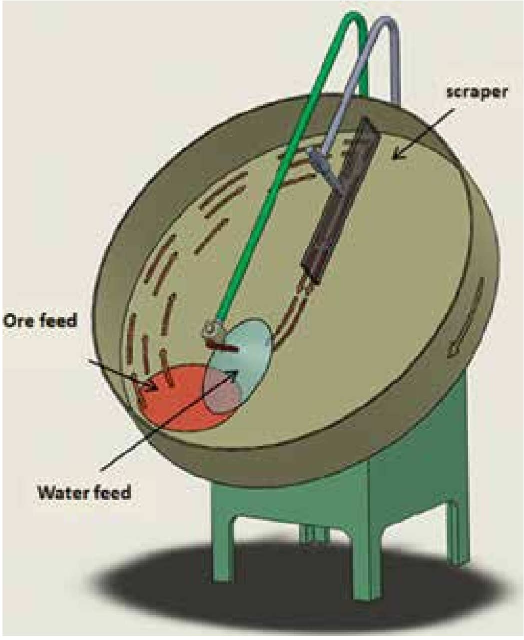

Figure 3. Schematic diagram of laboratory balling disc. Source: Modified by the authors with data from Ball [1].

The height and width of the trajectory increase as the ball size increases until the balls hit the scraper blades. After that, they move down and pass under the water sprayers so that they can find fresh feed.

The balling disc works in close circuit with the screening step, where pellets smaller than 8 mm or larger than 16 mm are desegregated and the material is recirculated to the balling process.

3.2. Balling drum

The balling drum equipment fundamentally consists of an inclined rotating cylindrical shell with water sprays in its inlet end, where the feed material is introduced to make balls. All formed pellets are discharged, regardless of particle size, which is different from the disc where only balls larger than a certain size are discharged. Because of this, the product has to be screened by a roller screen, which has increasingly replaced vibrating screen to extract undersize and oversize [4].

The small pellets in the undersize will serve as seeds forming rightly sized pellets [4], the oversize is shredded, and both return to the feed addition point, forming a closed circuit. The water sprays promote nucleation and seed growth in the feed addition zone, while the assimilation process, responsible for the ball growth, occurs along the length of the drum [1].

The drums usually have a length-to-diameter ratio of 2.5–3.5 and very low slope with angles of inclination of the drum axis to the horizontal between 6 and 10°. The optimum rotating speed is generally between 25 and 35% of the critical speed that is the speed in which balls will centrifuge causing their degradation [1]. Speed control is necessary to develop a correct rolling and tumbling action to produce balls.

The rotation speed, the depth of the material in the drum (controlled by scrappers), and the time required for balling are constraints that need to be satisfied. The residence time in a drum is given by Eq. (1):

$$T = \frac{0.0037(\alpha + 24)L}{nDS} \tag{1}$$

where: T is the residence time (minutes).

L is the drum length (feet).

D is the drum diameter (feet).

n is the speed of revolution (revolutions per minute).

S is the slope of the drum (inches/foot length).

α is the angle of repose of the feed material.

Figure 4 shows a balling drum arrangement.

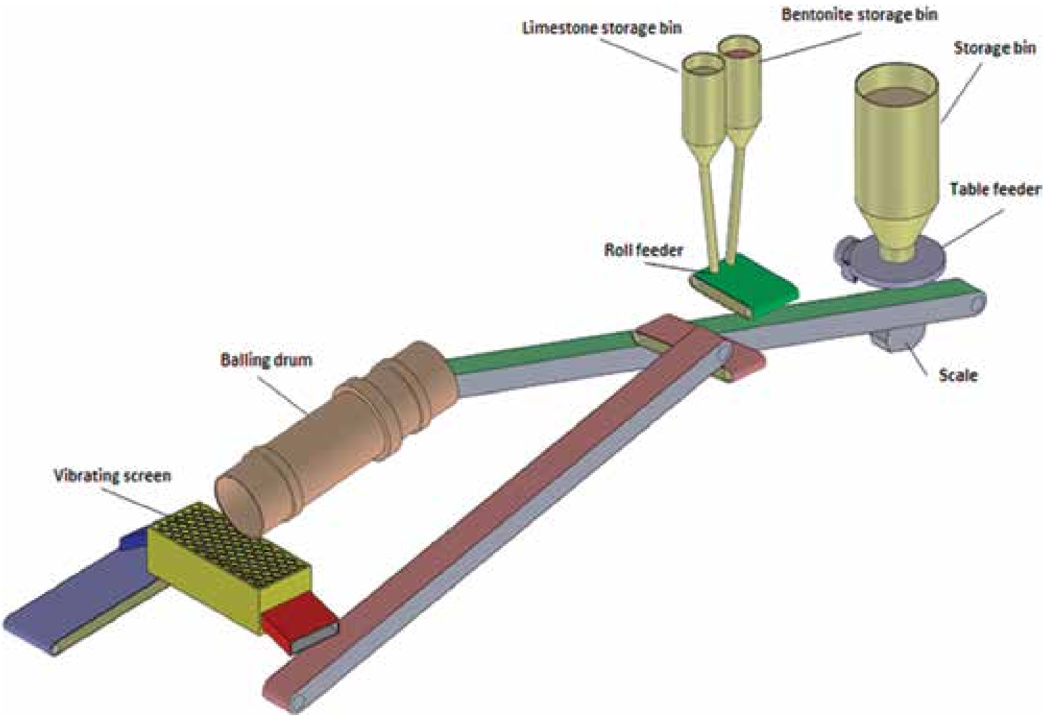

Figure 4. Typical balling drum arrangement. Source: Modified by the authors with data from Ball [1].

4. Bonding mechanisms

The main bonding mechanisms of size enlargement are described as being [11, 13]:

a. solid bridges between agglomerating particles, which may occur by sintering, partial melting, chemical reaction, hardening binders, recrystallization of dissolved substances, and deposition of colloidal particles;

b. interfacial forces and capillary pressure in movable liquid surfaces (liquid bridges);

c. adhesional and cohesional forces in bonding bridges, which are not freely movable (highly viscous binder), adsorption layers <3 nm thickness);

d. attraction between solid particles: molecular forces (Van der Walls forces, free chemical bonds—valence forces—associations—nonvalence—and hydrogen bridges), electric forces (electrostatic, electrical double layers, excess charges), and magnetic forces;

e. interlocking, depending on the shape of particles, for example, fibers, threads, or lamellae.

The agglomerated growth mechanism was defined by Sastry and Fuerstenau [14], considering that in industrial balling systems, the balling devices are continuously operated and the new feed is constantly supplied to previously seed pellets. The authors describe five agglomerate growth mechanisms as shown in **Figure 5**.

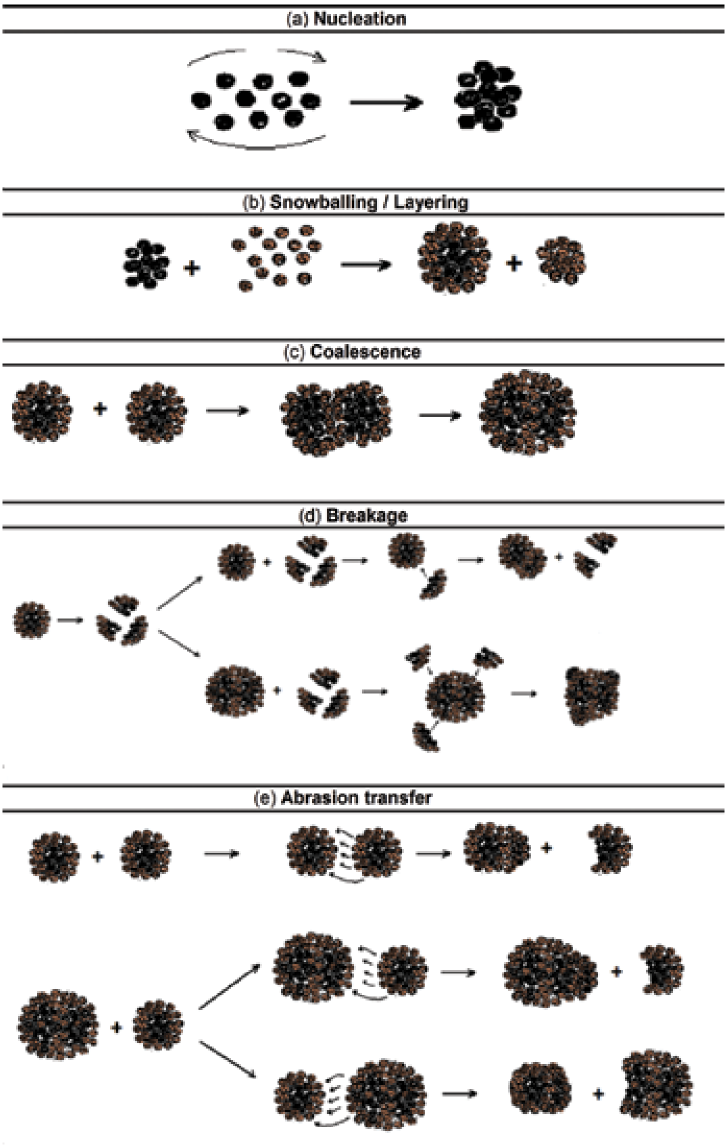

Figure 5. Details of the mechanisms proposed by Sastry and Fuerstenau [14]. (a) Nucleation, (b) snowballing/layering, (c) coalescence, (d) breakage, and (e) abrasion transfer.

Nucleation (**Figure 5a**) is defined as any formation of new pellets in an agglomeration system from an extra feed of moist material. The nucleation of new species results from the capillary attraction between a collection of individual moist feed particles. Thus, the occurrence of nucleation promotes changes in the mass and number of well-formed species in the system.

Whenever a new feed is supplied to a pelletizing system, the pellets act as seeds and tend to accumulate the newly added moist material. This mechanism is called snowballing or layering (**Figure 5b**). In this case, it is considered that all new moist feed nuclei are of unit mass and are not considered to belong to the population of agglomerates undergoing size change. In addition, the snowballing mechanism is considered to cause continuous change in pellet size, resulting in an increase in the total mass of the system and does not change the total number of pellets.

Coalescence (**Figure 5c**) refers to the production of large-size species through the aggregation of two or more colliding granules. Binary coalescence is considered an elementary event. Thus, the collision coalescence of two agglomerated species leads to the formation of a larger sized pellet with mass. The coalescence mechanism causes discrete changes in the agglomerate mass and contributes to the decrease in the number of pellets, but does not change the total mass of the system.

The breakage of pellets (**Figure 5d**) leads to the formation of a collection of fragments that are considered to belong to the class of well-formed species. These fragments are redistributed on the surviving pellets, causing the so-called layering according to the layering mechanism.

In the abrasion transfer mechanism (**Figure 5e**), a certain mass of material is transferred from one species to another due to the interaction and abrasion of the agglomerate during the pelletizing process. Mathematically, it is expected that on each encounter between species, an infinitesimal mass of material will be transferred from one to the other, with no preference of exchange in any direction. The abrasion transfer growth mode does not change the total number or total mass of pellets in the system, causing only continuous changes in size.

The optimum moisture content and particle size distribution are two decisive factors for green pellets formation. The moisture interferes with two important properties of green pellets: compressive strength and drop resistance. These two properties are complementary; to obtain a high compressive strength a lower water addition is necessary, whereas to achieve better resistance to drop the pellet should present higher moisture content [4].

Urich and Han [15] studied the effect of grind on the quality of pellet of specular hematite and found that as the amount of particles smaller than 44 μm increases, the compressive strength (both green and indurated pellets), abrasion resistance, and other related properties improve considerably.

5. Evolution of binder for iron ore pelletizing

Binders are used in the pelletizing of iron ore aiming to improve the performance of the process in the following aspects [1, 4, 11, 16, 17]:

- promoting and facilitating the balling;
- increasing the green and dry strength of the pellets;
- preventing the collapse of pellets in the initial stages of heating, when a large volume of gas generated by water vaporization tends to crack pellets;
- improving the properties of the fired pellets.

Bentonite, an inorganic binder, has been the main binder used in the iron ore pelletizing process since the beginning of pellet production in the 1950s. Bentonite promotes the formation of ceramic bridges between particles, which can minimize the number of pellets that collapse during firing. Despite its low cost, the inorganic compounds from bentonite are contaminants increasing the amount of acid gangue in the pellet. This increases the amount of slag formed in iron and steelmaking, which add to the energy needs of such processes [18].

Organic binders have been used as an attractive alternative to bentonite in iron ore pelletizing process, mainly because it burns without leaving any residue in the final pellet. There are two main types of organic binders, those based on cellulose compounds and other based on polyacrylamide polymers.

Table 3 shows some patents from chemical industries claiming the employment of organic binders in iron ore pelletizing aiming to replace bentonite in the process. The effectiveness of the binders is given in terms of compressive strength of pellets compared with the results from using bentonite.

Regarding research papers, **Table 4** lists some publications, which report studies applying organic binders to iron ore pelletizing since the 1980s. All analyzed publications show results of compression strength (green and dry) and drop test from using organic binders. In some cases, the characterization of binders is also presented along with the discussion of their effects on the pellet properties. However, these studies do not explain how organic binders act to improve the properties of the pellets.

(Patent N°)	Binder	Others compounds	Compressive strength (kg)	
			Green	Dry
Allied Colloids Limited (EU 0225171—1987)	Copolymer of acrylamide	Sodium acrylate (Na$_3$Citrate) Na$_2$CO$_3$	0.4–0.71	2.07–6.02
Allied Colloids Limited (US 4.684.549—1987)	Copolymer of acrylamide/ Carboxymethyl cellulose	Sodium acrylate (Na$_3$Citrate) Na$_2$CO$_3$	0.4–0.71	2.07–6.02
Aqualon Company (US 4.863.512—1989)	Carboxymethyl cellulose	Sodium tripolyphosphate	0.77–1.54	4.76–7.85
Peridur® Nobel (US 5.698.007—1997)	Carboxymethyl cellulose (Peridur®)	Source of hydroxide ions (NaOH)	—	0.64–5.4
Peridur® Nobel (US 6.071.325—2000)	Carboxymethyl cellulose (Peridur®), polyacrylate, polyacrylamide, cellulose derivatives, guar gum, starches, dextrins, pectins	Source of hydroxide ions (NaOH)	—	0.68–3.22
Clariant S.A. Brazil (EP 2548978 A1—2013)	Homopolymer of methacrylic acid, acrylamide, maleic acid	Limestone/esmectite	1.24–1.61/ 1.44–2.61	2.9–6.59

Table 3. Patents about organic binders in the iron ore pelletizing process.

Iron ore	Binder	Characterization		Reference
		Binder	Pellets	
Hematite (CVRD nowadays VALE)	Peridur® and bentonite	No	Drop number, compressive strength (green, dry)	[19]
Magnetite	Peridur®	No	Drop number, strength (green, dry)	[20]
Taconite (Minnesota, USA)	CMC (Na_2CO_3, NaCl), Peridur®, bentonite	Substitution degree, viscosity	Drop number, strength (green, dry, fired) chemical and metallurgical properties	[21]
Magnetite	Organic binders and bentonite	PWA (plate water absorption test) Viscosity	Drop number, strength (green, dry, fired)	[18]
Magnetite (Carol Plant, Canada)	Organic binders (including Peridur®) and bentonite	No	Drop number, strength (green, dry, fired), metallurgical properties	[22]
CVRD Hematite (nowadays VALE)	CMC, TPP	No	Drop number, strength (green, dry)	[8]
Hematite (Ferteco)	CMC, TPP, organic binders	No	Drop number, strength (green, dry)	[23]
Pellet feed (China)	S-1 (modified starch type) and Funa (substance rich in humic acids obtained from lignite by caustic extraction)	Molecular design, wettability, ionization potential, electron affinity, binding energy	Drop number, strength (green, dry), thermal shock (820–780°C)	[24]
Pellet feed (Russia)	(Floform 1049 V) polyacrylamide	No	Physical, chemical and metallurgical properties	[25]
Iron ore concentrate	HS (Humic substances extracted from lignite)	Viscosity as a function of pH and temperature, adsorption	Drop number, strength (green, dry), thermal shock (550–600°C)	[26]
Pellet feed (Baiama Plant—China)	MHA (fulvic acid and humic acid)	Viscosity, zeta potential, pH, adsorption kinetic	Drop number, strength (green, dry), firing	[27]

Source: elaborated by the author with data from [8, 18–27].

Table 4. Scientific papers which investigated the effect of organic binders in iron ore concentrate pelletizing.

There are currently some organic binders available in the market for palletization of iron ore such as Peridur® from Akzo Nobel, Alcotac® from Basf Corporation, FLOFORM™ from SNF Floerger, KemPel™ from Kemira, FLOTICOR PA 8000 from Clariant among others.

6. Induration technologies

The final use of iron ore pellets in ironmaking reactors requires minimum mechanical properties. Pellets must withstand tumbling and falling during transport and mechanical loading inside the reactors due to the charge weight. In order to increase its mechanical strength, green pellets are thermally treated in the induration process.

Pellets undergo drying, firing, and cooling steps. First, the water in the form of moisture is removed from the pellets in the drying steps. There is water in the pores and capillaries of pellets, that is, between different ore particles. In the case of porous ores, water may also be found in the pores of individual grains. Since this type of pores are normally smaller in size than the pellet pores, the temperature required to eliminate this water is expected to be higher. In the industrial process, the maximum temperatures reached in the solid phase during the drying steps are approximately 300°C.

After drying, pellets undergo firing steps, at which temperatures may reach 1350°C. In these steps, the roasting of all pellets components (ore, limestone, binders, etc.) occurs, liberating chemically bonded water and CO_2. Additionally, the sintering of ore grains also happens, leading to the development of mechanical strength. This sintering may be caused by solid state interaction of particles, but also with the presence of liquid phase, which can act as transport media increasing the sintering rate. The liquid phase also acts as bonds among ore particles.

The presence of liquid or semi-liquid phases is more pronounced in fluxed pellets where acid constituents normally from the ore (e.g., SiO_2 and Al_2O_3) may react with basic ones added in the form of fluxes (e.g., CaO and MgO). This reaction may result in the formation of a slag phase. **Figure 6** shows the phase diagram of the ternary system Al_2O_3-CaO-SiO_2 at 1200°C. At this temperature, liquid phase is present and indicated as "ASlag – liq." The reaction between iron oxide and fluxes or impurities is also possible. The interaction of CaO with Fe_2O_3 may lead to the formation of liquid phase below 1250°C.

The major development regarding pellet strength occurs at temperatures above 1200°C and is caused by the formation of necks between ore grains followed by pellet densification. These mechanisms are typical of solid state sintering. Pellet densification with increase in strength is controlled by the rate of oxygen diffusion in the hematite crystal [28].

To finalize the induration process, pellets are cooled down by contact with flow of ambient air. The resulting heated air is used in the upstream steps of firing and drying.

Induration processes were initially developed for ores composed of magnetite, since they are oxidized, producing hematite, and generating heat (−482.4 kJ/mol of Fe_3O_4). In the case of ores composed of hematite, this heat liberation does not happen and needs to be compensated. For this reason, hematite is agglomerated with controlled amounts of carbon (1–2% wt.) that burns during induration, generating the required heat. For both cases, heat is induced inside the pellet by the diffusion of hot air through the pores of pellets and subsequent chemical reaction. In the case of magnetite, heat generation is more uniform over the pellet volume, while for hematite it will be concentrated around carbon particles that must be evenly distributed. This

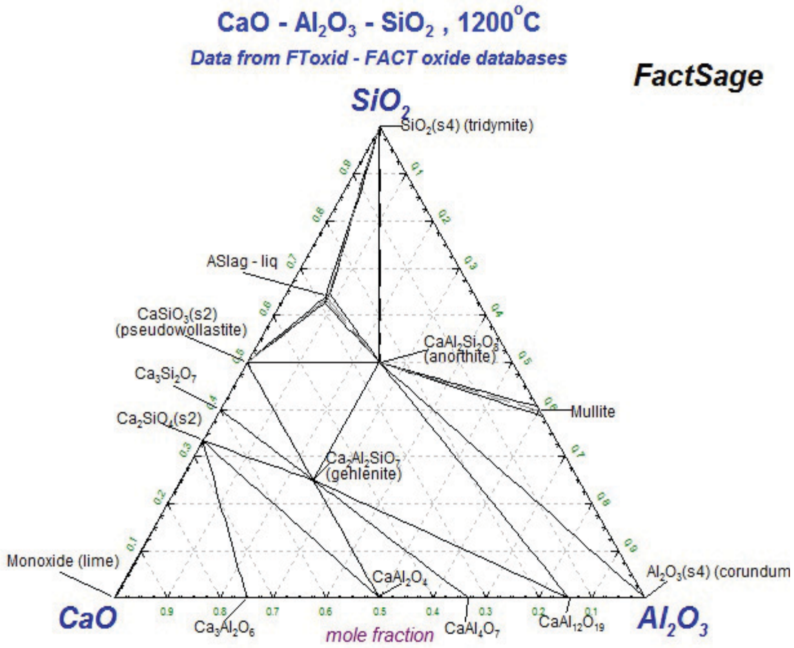

Figure 6. Isotherm at 1200°C phase diagram of $CaO\text{-}SiO_2\text{-}Al_2O_3$ system.

is the reason for using very fine solid fuels such as anthracite or coke breeze in the mixture to be agglomerated during balling.

The most widely used industrial processes for pellet induration are the straight grate and the grate-kiln.

The straight grate process is composed of a single furnace where an endless line of pallet cars moves. A layer of indurated pellets is arranged at the bottom of each car to protect it against the heat. The green pellets are then charged on top of the hearth of indurated pellets. A schematic diagram of this process is shown in **Figure 7**.

The process is designed to enhance heat recovery. Therefore, two flows of ambient air are heated while cooling the hot indurated pellets. These flows are directed to other zones of the furnace. This is a way of recovering the latent heat present in the hot indurated pellets.

The drying of green pellets is performed in two stages by blowing warm air through the bed of pellets. In the first stage, the hot air from the cooling zone is blown from the bottom. In the second drying stage, hot air from the firing zone is blown on the top of the car. The use of both updraft and downdraft drying ensures a more uniform treatment along the height of the bed of pellets.

The high temperature phase is divided into three steps: pre-heating, firing, and after-firing. In all these phases, pre-heated air is fed into burners to produce flue gases that flow through the bed of pellets from the top. The burners are usually fired with gaseous fuels, such as natural gas or atomized liquid fuels, such as diesel.

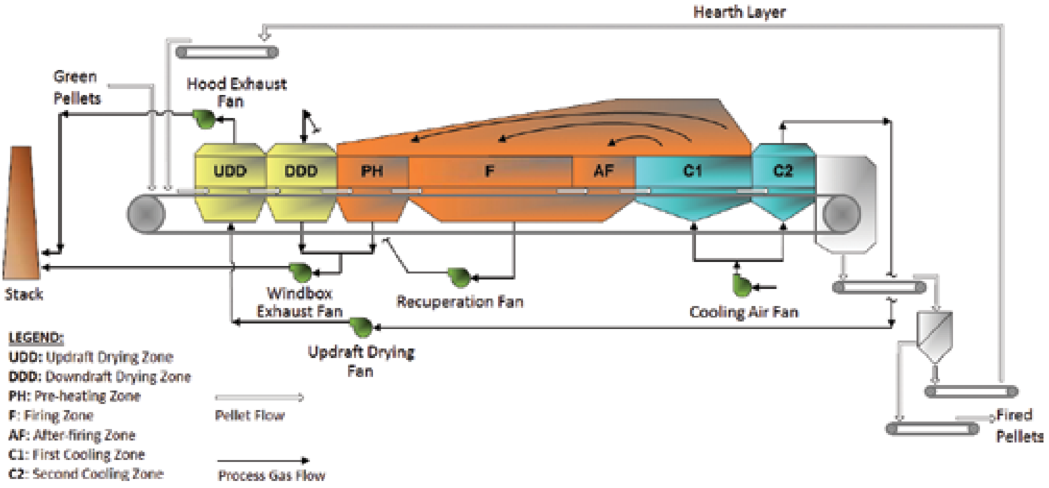

Figure 7. Schematic diagram of the straight grate induration process [29].

Since the hot air flows from the top of the bed in the high temperature steps, firing of pellets is not homogeneous. Pellets close to the top are treated at higher temperatures for longer times, while pellets at the bottom reach lower peak temperatures for shorter residence times. It is been reported [30] that pellets at the top may reach 1300°C for 6 minutes while pellets at the bottom peak at 1200°C with no residence time. These values may vary, but the difference is large enough to generate pellets with different mechanical strengths and different metallurgical proprieties. This is a disadvantage for the straight grate in comparison to the grate-kiln process.

In the grate-kiln process, shown in **Figure 8**, there are three different reactors. The drying, pre-heating, and cooling steps are similar to that of the straight grate process. The general concept

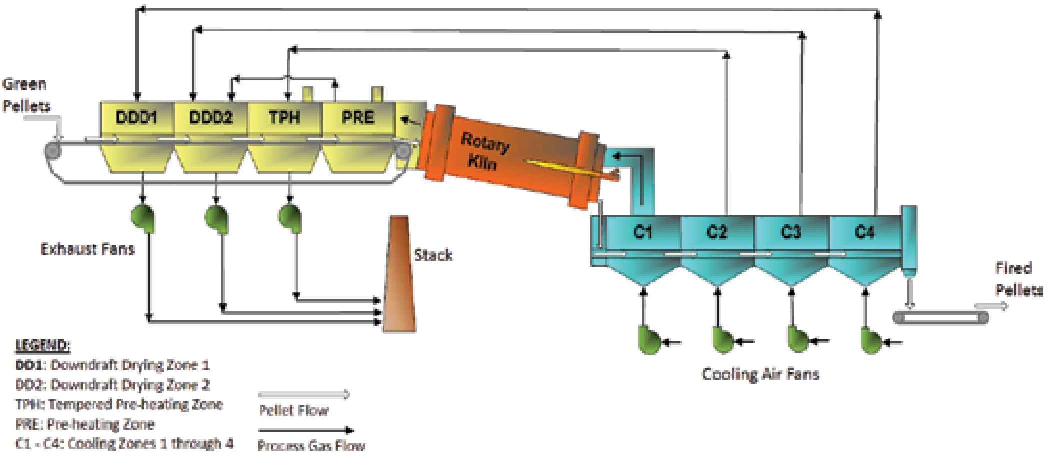

Figure 8. Schematic diagram of the grate-kiln induration process [29].

of heat recovery by using hot gases from downstream in the process for drying and for feeding the burners is also present. However, a rotary kiln is used for the firing step.

The pre-heating zone is divided into two steps: tempered pre-heating zone and pre-heating zone, where maximum temperatures may reach between 1000 and 1100°C. Pellets need to gain some mechanical strength during pre-heating to withstand the tumbling inside the rotating kiln where firing is performed.

The firing in the rotating kiln generates pellets with more uniform properties. The movement of the kiln causes pellets to mix during the firing treatment and the temperature is more even among different pellets. The furnace is heated with a flame on the discharge side. The use of fuel is more flexible in this case in comparison to the straight grate. Besides gaseous and liquid fuels, solid fuels such as coal may also be used. This is of particular interest in regions with availability of cheap solid fuels.

After firing, pellets are discharged in a pallet car for the cooling stages.

Therefore, pellets undergo more charging and discharging operations during the grate-kiln process than in the straight grate. This causes a greater generation of fines during the process. However, the final pellet properties are more uniform, and fines generation during transport for final use is therefore expected to be lower for pellets produced in the grate-kiln process.

The worldwide pelletizing capacity is divided into 60% for the straight grate process and 40% for the grate-kiln. Both systems are used to produce quality blast furnace and direct reduction pellets.

7. Challenges and innovations in iron ore pelletizing

The properties of iron ore depend much on its genesis. Different ores have distinct characteristics and varying performances in the mining and in the metallurgical processes. Ore particle shape, size, texture and capability of water retention, capillarity and cohesive strength among different particles determine the velocity of pellet growth during balling and pellet porosity. Ore characteristics also influence on the required amount of binder to produce pellets with satisfactorily quality. The use of iron ores with smaller crystal size and less dense structure usually results in pellets with better reducibility, impacting the performance of ironmaking reactors. Therefore, different iron ores should be valued in function of the benefit from their use [3].

The influence of ore characteristics on beneficiation, concentration, and pelletizing are important for process optimization, improving product quality, and consequently, more efficient use of natural resources and energy. Hence, as described by Moraes and Ribeiro [31], the growing importance of this topic that is referred to as geometallurgy is evident.

Mining companies work toward obtaining pellets with customized properties for each type of ironmaking process and also to meet specific requirements of different iron- and steelmaking companies. Hence, the amount and quality of supplied iron ore products are important but also to provide a diversity of types of pellets.

Therefore, the reasons why new investments in pelletizing capacity are likely to occur are the following [29]:

- the pelletizing process is currently the most widely used option for producing suitable agglomerates for ironmaking applications from fines of iron ore concentrates;
- quality requirements for DR pellets are higher and since lump ore of the required quality is not available, pellets are the only viable feed for new DR plants;
- pellets provide advantages to end users, such as improved productivity of blast furnaces, opportunity to increase the Fe content of the charge materials, and superior environmental performance of pellet plants as compared to sinter plants;
- the main iron producing systems, blast furnace, and DR reactors, will not be replaced in the near future.

Acknowledgements

The authors would like to thank assistant researcher Dafne Pereira da Silva and interns (mining engineering students) Milton Candido Torres da Silva and Lucas Shin Takyia for helping find and organize figures and references.

Author details

Sandra Lúcia de Moraes[1]*, José Renato Baptista de Lima[2] and Tiago Ramos Ribeiro[1]

*Address all correspondence to: sandralm@ipt.br

1 Institute for Technological Research, Sao Paulo, Brazil

2 School of Engineering of the University of Sao Paulo, Sao Paulo, Brazil

References

[1] Ball D. Agglomeration of Iron Ores. New York: American Elsevier Pub. Co.; 1973

[2] Tuck C, Virta R. 2011 minerals yearbook: Iron ore. USGS [Internet]. 2013. Available from: http://minerals.usgs.gov/minerals/pubs/commodity/iron_ore/myb1-2011-feore.pdf [Accessed: May, 2014]

[3] Mourão J. Estudo Prospectivo do Setor Siderúrgico: NT Minério de Ferro e Pelotas Situação Atual e Tendências 2025. Brasília: Centro de Gestão e Estudos Estratégicos; 2008

[4] Meyer K. Pelletizing of Iron Ores. Heidelberg: Springer-Verlag; 1980. p. 291 não encontrado

[5] Campos A, Fonseca V. Pelotização. In: Luz A, Sampaio J, França S, editors. Tratamento de minérios. 5th ed. Rio de Janeiro: CETEM/MCT; 2010. pp. 705-750

[6] Moraes S, Comparação de desempenho de aglomerante orgânico em relação à bentonita na operação de pelotização de concentrados de minério de ferro brasileiros de diversas procedências. [dissertation]. São Paulo: Escola Politécnica da Universidade São Paulo; 2004

[7] Borim J. Modelagem e controle de um processo de endurecimento de pelotas de minério de ferro [dissertation]. Belo Horizonte: Universidade Federal de Minas Gerais; 2000

[8] Lima J. Estudo da carboxi-metil-celulose como aglomerante para pelotização [thesis]. São Paulo: Escola Politécnica da Universidade São Paulo; 1991

[9] Metso. Iron ore pelletizing [Internet]. 2017. Available from: http://www.metso.com/products/iron-ore-pelletizing/ [Accessed: October 06, 2017]

[10] Vale. Entenda como funciona o processo de pelotização em nossas usinas [Internet]. 2017. Available from: http://www.vale.com/brasil/PT/aboutvale/news/Paginas/entenda-funciona-processo-pelotizacao-usinas.aspx [Accessed: October 06, 2017]

[11] Pietsch W. Agglomeration Process: Phenomena, Technologies, Equipment. Wiley: Weinheim; 2002. p. 614

[12] Bhrany U, Johnson R, Myron T, Pelczarski E. In: Kenepper W, editor. Dynamics of pelletization. Agglomeration. New York: Interscience Publishers; 1962. pp. 229-249

[13] Rumpf H. The strength of granules and agglomerates. In: Knepper W, editor. Agglomeration. New York: Interscience Publishers; 1962. pp. 379-418

[14] Sastry K, Fuerstenau D. Mechanism of agglomerate growth in green pelletization. Powder Technology. 1972;**7**:97-105

[15] Urich D, Han T. A process report on the effect of grind, temperature, and pellet size upon the quality of specular hematite pellets. In: Knepper W, editor. Agglomeration. New York: Interscience Publishers; 1962. pp. 669-719

[16] Abouzeid A, Seddik A. Effect of Iron Ore Properties on its Balling Behavior. Elsevier Sequoia S.A.: Lausanne; 1980

[17] Moraes S, Lima J, Neto J. Influence of dispersants on the rheological and colloidal properties of iron ore ultrafine particles and their effect on the pelletizing process—A review. Journal of Materials Research and Technology. 2013;**2**:386-391

[18] Haas LA, Aldinger JA, Zahl RK. Effectiveness of Organic Binders for Iron Ore Pelletization. Pittsburgh: U.S. Department of the Interior. Bureau of Mines; 1989 (Report of Investigations, RI 9230)

[19] Souza R, Mendonca C, Kater T. Production of acid iron ore pellet for direct reduction using an organic binder. Mining Engineering. 1984;**36**(10):1437-1441

[20] Kater T, Steeghs H. Organic binders for iron ore pelletization. In: 57th Annual Meeting of the Minnesota Section; 45th Annual Mining Symposium Duluth. Litleton: AIME; 1984. pp. 13/1–13/29

[21] Goetzman H, Bleifuss R, Engesser J. Investigation of Carboxymethylcellulose Binders for Taconite Pelletizing. SME: Littleton; 1988. 44p

[22] Martinovic T, Paquet G, Wison J. A Laboratory and Pilot Plant Investigation of the Performance of Various Organic Binders in the Pelletizing of Carol Concentrate. Littleton: Society of Mining Engineers; 1989. p. 9 (Preprint Series, n. 89-19)

[23] Cassola MS, Chaves AP. Effect of the Addition of Organic Binders on the Behavior of Iron Ore Pellets. Vol. 16. Osaka: KONA Powder and Particle; 1998. pp. 136-142

[24] Qiu G, Jiang T, Li H, Wang D. Functions and molecular structure of organic binders for iron ore pelletization. Colloids and Surfaces A: Physicochemical and Engineering Aspects. 2003;**224**:11-22

[25] Chizhikova V, Vainschtein R. Composition of iron-ore pellets with different types of additives. Metallurgist. 2003;**47**:9-10. DOI: 10.1023/B:MELL.0000015261.33342.21

[26] Zhang Y, Han G, Jiang T, Huang Y, Li G, Guo Y, Yang Y. Structure characteristics and adhesive property of humic substances extracted with different methods. Journal of Central South University of Technology. 2011;**18**(4):1041-1046. DOI: 10.1007/s11771-011-0801-8

[27] Han G, Jiang T, Li G, Huang Y, Zhang Y. Journal of Engineering Materials and Technology. 2012;**134**(1):010901/1-010901/5

[28] Wynnckyj J, Fahidy T. Solid state sintering in the induration of iron ore pellets. Metallurgical Transactions. 1974;**5**:991-999

[29] Mourão J, Huerta M, de Medeiros U, Cameron I, O'Leary K, Howey C. Guidelines for selecting pellet plant technology. In: Proceedings of the 6th International Congress on the Science and Technology of Ironmaking—ICSTI; October 14–18, 2012; Rio de Janeiro

[30] Thurlby J, Batterham R, Turner R. Development and validation of a mathematical model for the moving grate induration of iron ore pellets references. International Journal of Mineral Processing. 1979;**6**(1):43-64. DOI: 10.1016/0301-7516(79)90031-0

[31] Moraes S, Ribeiro T. Brazilian iron ore and production of pellets. Mineral Processing and Extractive Metallurgy Review. GMPR-2017-0182. To be published

Iron Ore Agglomeration Technologies

Daniel Fernández-González,
Juan Piñuela-Noval and Luis Felipe Verdeja

Additional information is available at the end of the chapter

http://dx.doi.org/10.5772/intechopen.72546

Abstract

Until the 1950s of the last century, the oxidized iron ores that were loaded into the blast furnace had granulometries within 10 and 120 mm. However, the depletion of high-grade iron ore sources has made necessary the utilization of concentration processes with the purpose of enriching the iron ore. Because of these processes, a fine granulometry is produced, and thus iron agglomeration process is necessary. There are several agglomeration processes including: briquetting, extrusion, nodulization, pelletizing and sintering, although pelletizing and sintering are the most widely used, and especially sintering process (70% blast furnace load). Apart from obtaining an agglomerated product, the objective is reaching the suitable characteristics (thermal, mechanical, physical, and chemical) in a product that is then fed into the blast furnace, achieving a homogenous and stable operation in this furnace with economical profitability.

Keywords: iron ore, sintering, pelletizing, solar energy, environment

1. Introduction

Iron and steel are widely used in modern societies despite the appearance of new materials. In this way, there is a growing tendency in the production of steel as according to the historical data, around 200 Mt were produced in 1950, 595 Mt in 1970, 760 Mt in 1990, 848 Mt in 2000 and 1630 Mt in 2016 [1, 2]. There is an irregular distribution of steel production worldwide as most of the steel is produced in Asia (more than 50%, mainly in China), followed by Europe (205 Mt in 2013), Russia, and USA. In the same line, Asia was the place where the steel production grew more in the last 40 years (from 121 Mt in 1970 to 1123 Mt in 2013), while in Europe the production remains stable in around 200 Mt, and in North America (USA and Canada) decreased from 131 Mt in 1970 to 102 Mt in 2013 [1, 2]. This growing tendency has led to the depletion of high-quality iron ore resources, and the use of concentration processes to increase the iron content, but also the agglomeration processes to achieve a homogeneous material's size that could ensure a suitable operation in the furnace.

Until the 1950s of the last century, oxidized iron ores with a granulometry within 10 and 120 mm were loaded into the blast furnace (lower sizes led to permeability problems in the furnace bed) [3]. However, nowadays, 70% of the blast furnace ferrous bed belongs to sinter [4], and is for that reason the main agglomeration process. As we said previously, the depletion of the high-quality iron sources has caused the utilization of concentration operations after size reduction processes, having as objective enriching the ore by eliminating the gangue, but causing a fine granulometry that makes necessary the utilization of agglomeration processes, such as nodulizing, briquetting, extrusion, pelletizing, and sintering. Concentration processes can be classified into four categories according to the properties of the materials to separate them from the gangue [5]: *classification*, based on particle size; *gravimetric concentration*, based on density and/or volume differences; *flotation*, based on superficial properties; and, *magnetic or electrostatic separation*, based on magnetic susceptibility or electric conductivity. The obtained product is rich in iron but with a fine granulometry, making necessary the utilization of the previously mentioned agglomeration processes. However, increasing the particle size is not the single aspect that makes necessary the utilization of agglomeration processes. Nowadays, the existence of a global iron ore market with ores with different precedence and quality is responsible of that the raw material that reaches the iron and steelmaking factories has neither the same chemical composition nor the same granulometry. This question could affect blast furnace behavior, when a stable and homogenous operation is pursued with the objective of achieving economic efficiency, consistency in the pig iron and minimal coke consumption [6].

2. Iron ore agglomeration technologies

Five iron ore agglomeration technologies can be defined: briquetting, nodulization, extrusion, pelletization and sintering. Sintering and pelletization are the most important agglomeration technologies, in this way, in the EU-27, 14 countries operate 34 iron ore sinter plants with 63 iron ore sinter strands, producing in the first decade of the twenty-first century 130 million tons of sinter annually, on its behalf, 6 pelletization plants produce 27 million tons of pellet annually [7]. Here we are going to describe all these agglomeration technologies, with special dedication to pelletizing and sintering as they are the most used worldwide.

2.1. Briquetting

Briquetting is the simplest agglomeration process. Fine grained iron ore is pressed into two pockets with the addition of water or some other binder agent (molasses, starch, or tar pitch) to form briquettes [8]. A traditional application is the agglomeration of coal [8], other example is the agglomeration of ultrafine oxidized dust produced in the ferroalloys industry [9].

2.2. Nodulization

Nodulization is a process like sintering as it does not need a binder agent. The iron ore concentrate is mixed with carbon, and fed into a rotary kiln, where the material is tumbled at high temperature to form nodules [8]. Reached temperature is enough to soften the ore but not to fuse it. Problems of the nodules are the considerable differences in composition and density (they are too dense), and the lack of a well-developed porosity (permeability) which is of great importance for the operation in the blast furnace. This process, as briquetting, is mainly used for the recycling of iron ore wastes in steel plants.

2.3. Extrusion

Extrusion is a process widely used in the ceramic industry, but it has begun to be used in the ironmaking and steelmaking industry in the agglomeration of powders generated in the factories as Basic Oxygen Furnace and Electric Arc Furnace powders. A certain level of moisture is required, as well as a binder agent, for instance bentonite or Portland cement. The mixture is sent to the extrusion machine to obtain the agglomerated product [8].

2.4. Pelletization

Pelletization is an agglomeration process of iron ore concentrates with a granulometry lower than 150 μm and low concentration of impurities [10, 11]. This iron ore is mixed with water, bentonite (or other organic binders less expensive and contaminant [12]), and lime and treated in a furnace at temperatures of around 1200°C, with the purpose of obtaining a product of 10–20 mm in diameter with suitable physical, chemical, and mechanical properties to be fed into the blast furnace or to the production of DRI (Direct Reduction Iron) [10]. Sintering raw mixes with a high proportion of fines (<150 μm) deteriorates the operation of the Dwight-Lloyd sinter machine, and for that reason pelletizing is the best method for treating this kind of material. The formation of liquid phases, which agglomerate the iron ore, in pellets is achieved by an external source of energy (fuel, natural gas or pulverized coal), as opposed to sintering, where liquid phases are consequence of the combustion of coke breeze [2].

Chemically, pellets are characterized by (approximately): 94% Fe_2O_3, 3.3% SiO_2, 1.0% CaO, 0.20% MnO, 0.50% MgO and 1.0% Al_2O_3, and as we mentioned previously, a granulometry of 10–20 mm [2]. According to this question, it is possible to say that pellets are characterized by [10]: great uniformity regarding the size (10–20 mm in diameter); high mechanical strength; almost inert behavior facing to water as a consequence of the low CaO content that makes possible storing and transporting pellets outside; good reducibility; and, high iron content.

As in the case of the sintering, mixing is an important step to obtain homogenous pellets. This mixing is easy when the materials to be mixed have the same particle size and physical properties, however, binder additions (around 1%) are necessaries and they are less dense than the ore. For that reason, segregation between particles must be considered when mixing the materials in the production of pellets.

Bentonite clay is the most common binder agent in iron ore pelletization as we mentioned previously, and is added at levels of 0.5–1.5% by weight [8]. There are others, that can be classified into two categories: organics (do not add impurities to the pellet and can be added in amounts of 1/10 of the equivalent in bentonite, although sometimes do not provide sufficient strength to the indurated pellets), and inorganics (usually result in strong pellets, which is good for shipping and handlings, but have the problem of impurities) [8]. Examples of inorganic pellets are: bentonite, sodium carbonate, calcium carbonate or calcium hydroxide; while examples of organic pellets are: carboxymethylcellulose (CMC), other CMC-based polymers, corn starch, wheat flour or molasses [8].

Regarding pelletizing technologies, it is possible to mention two that are used at industrial scale: rotary drum and rotary disc. The rotary drum is a large drum-shaped cylinder that is elevated at one of its ends (3–4°). The mixture (iron ore-binder) is fed at the elevated zone of the drum and lefts the drum at the lower zone, where it is classified into three groups, the undersize pellets (which are recirculated), the oversize pellets (which are recirculated after crushing), and the final product [8]. The pelletizer discs are the second technology, having as advantage if compared with the rotary drum that there is no recirculation. The mixture is fed to an inclined large disc (40–60° to the horizontal), and the rotation of the disc causes the formation of balls, which remain in the disc until they reached the adequate pellet size. The variables that should be controlled are the disc angle, feed rate, water addition, and rotation speed [8].

Once the green pellet is obtained, it must be subjected to induration as it is too weak for its application. Pellets are for that reason processed at high temperatures to strengthen them. Three types of furnaces are used: shaft furnace, traveling grate, and grate-kiln, and temperature will depend on the kind of pellet. Pellets can be classified into three groups:

- *Blast Furnace grade*. They are dried at 105–120°C, and then indurated at high temperature (1200–1400°C, depending on the kind of both ore and binder, the same for the time), allowing for a strong pellet that can resist shipping, handling, and processes in the blast furnace. This kind of pellets can have certain level of impurities since all constituents of the iron feed are melted during the process in the blast furnace, and they can float as slag above the reduced iron (being then removed). Typically contain 58–65% Fe and size range of 9–12 mm [8].
- *Direct Reduction grade*. As opposed to blast furnace process, direct reduction of iron oxide happens in solid state (components are not melted). For that reason, impurities are necessary to be controlled. They are first dried at 105–120°C, and then indurated at high temperature (1200–1400°C, depending on the kind of both ore and binder, the same for the time, as in Blast Furnace grade pellets), allowing for a strong pellet that can resist shipping, handling, and steelmaking processes [8].
- *Rotary Heating Furnace pellets*, or iron ore-coal composite pellets. This kind of pellets does not require high strength as in the other two types, since in the same vessel that the green pellets are fed, they are transformed into direct reduction iron. The resistance is required only for feeding as they are dried in the first part of the furnace and then are reduced without requiring more handling than that to feed them into the furnace [8, 13].

2.5. Sintering

Sintering is a thermal process (1300–1400°C) by which a mixture of iron ore, return fines, recycled products of the iron and steel industry (mill scale, blast furnace dusts, etc.), slag-forming elements, fluxes and coke are agglomerated in a sinter plant with the purpose of manufacturing a sintered product of a suitable chemical composition, quality (physically) and granulometry to be fed into the blast furnace, ensuring a homogenous and stable operation in the blast furnace [2]. This definition proposed in [2], describes the sintering process, but prior to sintering there is an important process called granulation that is deeply reviewed also in [2]. Granulation is the homogenization of the iron ore mixture in a rotatory drum with 7–8% water having as objective the obtaining of a pre-agglomerated product, which is then delivered as a layer over a continuously moving grate or "strand" (Dwight-Lloyd machine) to obtain the sintered product. This process that takes between 30 and 60 min. (including the addition of moisture, granulation and feeding to the sintering machine) has a fundamental role as it ensures an adequate sinter bed permeability and hence good productivity [2].

Dwight-Lloyd technology is the main iron ore sintering technology. Basically, this equipment consists in a sintering grate that is a continuous chain of large length and width, which is formed by the union of a series of pallet cars making the sintering strand. The process in the Dwight-Lloyd machine begins with each pallet car passing below the charging hopper. Feeding is carried out in two layers: the hearth layer that protects steel grates from over-heating during the sintering process, which is formed by sinter of coarse granulometry (10–20 mm, with a granulometry not enough to be sent to the blast furnace) in a layer of 3–6 cm [14, 15]; and the layer of fine material (0–8 mm) granulated to be sintered (fine material, return fines, fluxes, and coke). Once charged, the pallet car passes below an initializing furnace, causing the combustible ignition on the surface of the mixture, and being at the same time the mixture subjected to downdraught suction through the load. The combustion of the coke breeze (or alternative combustible in the corresponding case) does not take place in the whole thickness of the bed instantaneously, on the contrary, combustion happens as a horizontal layer that moves vertically through the bed. In this way, permeability is important, and for that reason granulation is a fundamental step [16]. This movement of the combustion zone defines several zones in the sinter bed (from the lower to the upper zone) [16]: *cold and wet zone*, is the zone of the sinter mix to be sintered at a temperature lower than 100°C; *drying zone*, zone at temperatures between 100 and 500°C where the vaporization of moisture and dehydration of hydroxides take place; *reaction zone*, where the maximum temperatures are reached during the combustion of coke (exothermic), decomposition of carbonates (endothermic), solid phase reactions, reduction and re-oxidation of iron oxides and reactions of formation of the sintered mass take place; and finally, *cooling zone*, is the zone where the cooling and re-crystallization of the sintered product take place. The high thermal efficiency is consequence of the heat accumulation in a partial layer called sintering zone or flame front (which progresses at 10–30 mm/min) toward the sintering grate, and in this way a 500–600 mm bed height would be sintered in around 25 min [16, 17]. Finally, the flame front reaches the bottom of the layer at the end of the strand, where the sintered product is discharged and subjected to cooling, crushing, and screening, being three kinds of product finally obtained: 0–5 mm (or 0–10 mm depending on the author, see [16]), called return fines and sent back to the beginning of the sintering process; 5–20 mm (or 10–20 mm or 10–15 mm depending on the author, see [16]), used as hearth layer in the sinter strand with the functions previously mentioned; and, > 20 mm (or >15 mm depending on the author, see [16]), sent to the blast furnace directly. Maximum sizes around 50 mm [18].

As we mentioned, flame front is the region limited by the moment where the coke begins to combust and the moment where the coke burned [19]. There are other definitions that can be read in [16]. The temperature at which the coke begins to burn depends on the size, oxygen partial pressure, volatile content, and component types in the coke. The ideal flame front thermal profile is characterized by short heating time (1.5 min) up to the high temperature zone (1100°C) to avoid the formation of important amounts of FeO due to the low partial pressure of oxygen, and long cooling times (3–5 min) down to the room temperature to avoid a strong sinter structure by the formation of a gangue matrix [16]. Anyway, maximum temperature and heat distribution should be uniform to obtain a homogenous sinter with suitable quality, and with the maximum process efficiency. In this way, a double layer sintering is used in some plants to satisfy this question, the upper layer would have higher coke content than the lower one, and under that conditions the tendency of T_{max} of being higher in the lower layer is avoided [16].

There is a strong relationship between sinter structure and sinter characteristics. Sintering process is based on rising the temperature with the objective of producing a molten phase, which, during the cooling period, will crystalize or solidify into several mineral phases and will agglomerate the mixture. In this way, from a mixture whose main constituents are Fe_2O_3, CaO, SiO_2 and Al_2O_3, it is possible to obtain a product having the following constituents: Fe_2O_3, Fe_3O_4, FeO, metallic iron, calcium ferrites and silicates. Calcium ferrites and silicates bond metallic oxides. It is, for that reason, possible to establish five categories of constituents that we can find in the sinter structure [20]: *hematite* (Fe_2O_3), primary (original mineral) and secondary or recrystallized (directly crystallized, formed by oxidation of magnetite crystals in liquid phase or formed by magnetite oxidation in solid phase); *magnetite* (Fe_3O_4), formed from the minerals or crystallized from the liquid phase; *wüstite* (FeO), formed by precipitation from the liquid in low potential of oxygen (typically associated to excesses of coke in the sinter, retained carbon grains or magnetite reduction in solid state); *calcium ferrites* ($xSIO_2 \cdot yFe_2O_3 \cdot 5CaO \cdot zAl_2O_3$ with $x + y + z = 12$), they are difficult to define as there is partial replacement of Ca^{2+} by Mg^{2+}, Fe^{2+} by Mn^{2+}, Fe^{3+} by Al^{3+} and Si^{2+}, etc., so they include several chemical compounds formed by crystallization of the liquid phase according to the reaction above mentioned, and they are known as silicoferrites of calcium and aluminum (SFCA); and, *silicates*, which include olivine, fayalite, and calcium silicates. Reactions involved in the formation of these constituents are described in [16, 20]. It is obvious that each constituent has a certain influence in the quality of the sinter produced, in this way, for instance primary hematite is considered beneficial for the sintered product as improves reducibility index, and SFCA are also beneficial for the sinter structure as they have good reducibility, improve shatter index and tumbler index [20]. The optimum sinter structure for sinter reducibility in the blast furnace would be hematite nuclei (un-melted) surrounded by an acicular ferrite network [21, 22]. Considering the temperature of operation, the best sinter quality (maximum percentage of ferrites, high primary hematite, good porosity, and good quality indices) is reached when sintering at 1225–1275°C [23].

2.5.1. Sinter quality indices

As it was mentioned previously, blast furnace operators require a homogeneous product with the suitable thermal, chemical, physical, and mechanical properties to be fed into the blast furnace, ensuring the highest productivity and performance. The main quality indices are:

Softening melting test: this test was developed in Japan and UK to simulate the behavior of iron ore materials in the cohesive zone of the blast furnace (defined as the zone of the blast furnace where the load formed by coarse mineral grains, sinter and pellets begins to soft [20]). See [20] to enlarge information.

Tumbler Index (TI) (% > 6.3 mm) (min. 63, max. 79, typical > 74 [20]**):** this test was developed with the purpose of knowing the cold strength of the sinter, and in this way, evaluating the tendency to the formation of fines during the handling and transportation of the sinter from the sintering machine to the blast furnace throat (obviously informing about the losses of material as fines). The Tumbler index depends on the strength of each component, as well as on the strength of the bonding matrix components and ore composition [24]. Standards to calculate this index are IS 6495:2003 and ISO 3271:2015. There are other indices used with the same purpose as for instance Micum and Irsid indices. The generation of fines was studied by using a method different from TI in [25]. They simulated different steps of handling and transportation by using customized drop and vibration tests and considering sinter size, drop height and conveying time [25].

Low temperature degradation tests: degradation that happens during reduction in the low temperature zone has harmful effects on burden strength in the blast furnace (loss of permeability to reducing gas and increase of coke consumption [26]). To have more information about the tests you can read [20]. Low Temperature Breakdown Test (LTB) was developed by the British Iron and Steel Research Association (BISRA) and Luossavaara-Kirunavaara AB (LKAB) with the purpose of evaluating the abrasion resistance of iron bearing materials under reducing conditions, simulating those in the upper zone of a blast furnace stack [20].

Reducibility index (RI) (R_{60}, %)) (min. 49, max. 78 [20]**):** this test informs about the ability of the sintered products for transferring oxygen during the indirect reduction process in the blast furnace stack. The porosity (non-occluded porosity is the surface available for gas–solid contact) and the mineralogical composition. RI is related with FeO content in the sinter (the higher the FeO content, the lower the reducibility) as FeO reacts with SiO_2 to form calcium ferrites, which are difficultly reduced. There are eight tests to calculate the reducibility: Midrex-Linder, HYLSA Batch, VDE (Verein Deutcher Eisenhuttenleute), Japanese Industrial Standard, Gakushin, ISO Relative Reducibility Test, ISI test, and HYL-III test. They are described in [20].

Reduction Degradation Index (RDI) (% < 3 mm) (min. 27, max. 33, typical < 33 [20]**):** This test gives a measure of the sinter strength after the partial reduction of the material, and provides information about the degradation behavior in the lower part of the blast furnace stack [20].

Coke consumption (min. 39 kg t^{-1} sinter, max. 54 kg t^{-1} sinter [20]**)** is one important factor, as nowadays is the main combustible for the sintering process (around 88% [7], there are other traditional combustibles such as anthracite (with low volatile matter content), and other modern combustibles (biomass, biochar, etc.) developed in an attempt of reducing CO_2, NO_X and SO_X as coke breeze (<5 mm) has 0.42–1% S and 1.06–1.23% N [7]) and for that reason it is necessary to guarantee the coal for coking production. The problem is that coking coal is only available in some regions, but also rises in coke price, unstable supply of anthracites and global warming by CO_2 [2, 16, 27]. Size is an important factor in sinter productivity and reducibility, being the best results found when coke size is 0.25–3 mm [28]. The fraction 1–3.15 mm is more economical in terms of consumption [28–30]. The reduction in coke breeze consumption is being carried out mainly by replacing coke breeze by new renewable solid fuels as biochar, biomass, or charcoal [31–33].

Fe total (%) (min. 51, max. 61, typical > 56 [20]**):** iron ore market is mainly composed by hematite (Fe_2O_3), goethite (α-FeOOH) and magnetite (Fe_3O_4), with low impurities content (alkalis, sulfur and phosphorus) and iron average content of 60–65% in 2016 (around 40% in 1940) [2]. However, the depletion of rich iron ore mines will lead to exploitation of complex chemistry ores and low-grade iron ore mines, considering in some cases the bioprocessing [5].

Basicity index (typical 1.70 [20]**):** reduction degradation index (RDI) decreases when basicity increases [20]. Obviously, basicity index has importance in the hardness and reducibility of the sinter as expresses the relation CaO/SiO_2. See [20] for a deeper explanation on sinter basicity index and sinter structure.

FeO content (%) (min. 4.0, max. 11 [20]**):** this parameter informs about the thermal state of the sintering process [20] and about coke rate. RDI is reduced when FeO content is increased [20, 34]. The problem is that increasing FeO content affects coke rate, deteriorates the sinter reducibility [35, 36], and can also affect blast furnace productivity [35].

Al_2O_3 content (%) (min. 0.6, max. 1.8, typical 1.35 [20]**):** sinter quality is related with Al_2O_3 content as when Al_2O_3 content is increased, RDI is higher. This point is under discussion as Kumar et al. observed that with 10–10.5% CaO an increase of 0.1% in Al_2O_3 increases RDI 2 points [34], while Hiesch observed no relation between RDI and Al_2O_3 [37]. Alumina is also related with reducibility, but the same as for RDI, there are different opinions, Yu et al. observed that maximum reducibility is reached when Al_2O_3 content is 2.5% in the sinter ore [38], while Umadevi et al. observed that reducibility increased when alumina content is raised from 2 to 5.5% [39].

MgO content (%) (min. 0.7, max. 2.2, typical 1.65 [20]**):** MgO is related with the obtaining of an optimum blast furnace slag (flowability and desulphurization). For that reason, MgO is added as dolomite or dunite, directly or through the sinter. It was observed an increase in the utilization of dolomite (containing CaO and MgO) or other MgO-bearing materials with low SiO_2 (as dunite) due to the use of iron ores with high SiO_2 content. There are mixed opinions regarding how this constituent affects reducibility, RDI, Tumbler and productivity. Umadevi et al. observed that reducibility was decreased with increasing MgO addition (in low and high silica iron ore fines) [40]. Kalenga and Garbers-Craig observed an increase in Tumbler index and coke rate with increasing MgO content [41]. Bhagat observed that varying MgO content within certain limits (1.5–2.5%) did not affect productivity and Tumbler, while coke breeze consumption was reduced [42]. On their behalf, Umadevi et al. observed that increasing MgO content from 1.4 to 2.6% increased heat consumption, and productivity was reduced [43]. And Yadav et al. observed that raising MgO content from 1.75 to 3.25% caused a deterioration in productivity and an increase in Tumbler index [44]. With regard to how MgO content affects RDI, there are several opinions, and in this way, [41, 43, 45] observed that RDI improved when

MgO content was increased, but [42] observed that MgO did not affect RDI, and [44] observed that increasing MgO increased RDI.

Alkalis content (%) (min. 0.11 [20]**):** they are mainly K and Na compounds and enter in the blast furnace with the charge materials (sinter, 32–58%; coke ash, 21–33%; pellets, 16–37% [46]). They cause several problems in the blast furnace performance: decrease coke hot strength, deteriorate sinter RDI, weak refractory lining and facilitate the formation of slag crusts, scaffolding and burning of the tuyeres [47].

2.5.2. Multivariate statistics in the sintering process

Data analysis is nowadays widely used with the purpose of correlating variables and, in this way, evaluating the effect of them in a certain process, whose have a higher influence, and how changing them will affect the sintering process. We have studied what variables are and what weight have them on three sinter quality indices as Tumbler Index, Reduction Degradation Index, and Reducibility Index. The objective of our work was to estimate them by using multivariate statistics, and thus avoiding long and expensive laboratory tests. Once each index was defined by a mathematical equation whose parameters are easily measured, we used fuzzy inference to develop a fuzzy control system that could warn in case of deviations from the conditions that ensured the best quality indices.

For our work, we used real data from a sintering machine. The variables with a higher weight for each quality index are: ***RDI (% < 3.15 mm)***: fines (%), fluxes (%), Fe_2O_3 (%), FeO (%), CaO (%), S (%), 10–20 mm (%), average particle size (mm), productivity (t/h), basicity index, and abrasion (% < 0.6 mm); ***Tumbler Index (% > 6.35 mm)***: Fe_2O_3 (%), CaO (%), MgO (%), MnO (%), P_2O_5 (%), 0–10 mm (%), 10–20 mm (%), basicity index, and maximum temperature in box prior to sinter discharge (°C); and, ***RI:*** Recoveries from other stages of the ironmaking and steelmaking process (%), FeO (%), P_2O_5 (%), MgO (%), S (%), Al_2O_3 (%) and >50 mm (%).

We elaborated a mathematical equation that correlated the RDI, the TI and the RI with those variables mentioned above, and in this way, it is possible to predict the indices by using these easily measured variables.

2.5.3. Environmental issues

Avoiding or minimizing pollutants is of large importance in nowadays environmental industrial policies, but also the objective is reducing the ecological footprint of the sintering process. In a second plane, environmental improvements will enhance the profitability of the sintering process from the economical point.

Sintering process is also used in the ironmaking and steelmaking as recycling system as apart from using iron ore fines and additives (such as fluxes and coke breeze), mill scale, collected dusts (and to a much lower extent sludges) from gas cleaning, other recycled by-products of steel manufacture and recycled sinter particles from sinter screening are treated in the sintering machine. Air pollutants are the most significant and are presented here:

Carbon dioxide: primary metal production is responsible for around 5% of the total world anthropogenic greenhouse gas emissions, while the iron and steel industry accounts for around 70% of this 5% [48], around 200 kg CO_2/t sinter are generated in European plants [49] mainly as a consequence of fossil fuels combustion and carbonate's decomposition. JFE Steel Corporation developed a hydrogen-based gas fuel injection technology, reducing CO_2 emissions by 60,000 tons/year [50]. Yabe and Takamoto proposed a process that used pre-reduced iron ore as sinter raw material (produced by reducing the iron ore to the degree of wüstite with blast furnace gas [51]). Coke breeze consumption is reduced (40,000 tons/year less of coke breeze in integrated plant of 4 Mt/year hot metal production) and 50,000–12,000 tons CO_2/year less by using 10% pre-reduced iron ore.

NO_X: NO_X emissions can be reduced by using low nitrogen content combustibles as 90% vol.% of NO_X comes from the fuel [52]. Using additives to inhibit the NO_X generation: hydrocarbons (1% sugar addition) reduced NO_X emissions from 533.8 g/t sinter to 283.3 g/t sinter [53]; or increasing Ca-Fe pellets in sintering bed [54]. End of pipe technologies could be other option but the huge volume of gas to be treated makes this option expensive. Flue gas recirculation lead to a significant reduction of pollutants emissions: 35–45% dust, 20–45% NO_X, 60–70% dioxins, 25–30% SO_2 and 40–50% CO reduction [55].

SO_X: sulfur is present as sulfide and sulfate (FeS_2, CuS, $BaSO_4$, $MgSO_4$, etc.) in iron ore fines and as elemental sulfur and organic sulfur in solid combustibles, which is oxidized and enters sinter flue gas as SO_2, but low SO_2 content in flue gas (400–1500 mg/Nm^3, [56]) is responsible of low desulphurization efficiency of desulphurization processes. Li et al. studied the behavior of SO_2 in different zones of sintering bed for flue gas circulation sintering, and observed that moisture condensation zone and sinter mix zone are characterized by a strong SO_2 absorption ability, mainly by reaction of SO_2 with CaO [56].

Particulate matter ($PM_{10/2.5}$): the sintering process is the main contributor to PM emissions in an integrated steel factory [57, 58], around 45% of the total emissions. Due to the temperatures reached during the sintering process, components with noticeable vapor pressure like alkalis and heavy metal chlorides are volatilized and then re-condensed in the off-gas system resulting in a high fraction of $PM_{10/2.5}$ in the dust emission of sinter plants [59]. End of pipe measures include electrostatic precipitators high-quality filter bags, etc. [7, 59]. Gan et al. observed that from over-wetted layer to the burning through point is the main area of PM_{10} emitting [57]. Ji et al. observed that increasing moisture content and extending granulation time the emission concentration of $PM_{10/2.5}$ is reduced, while increasing coke breeze rate increases the emission concentration of $PM_{10/2.5}$ the same as adding recycled materials [58].

Dioxins: sintering has been recognized as an important source of organic micro-pollutants such as PCDDs and PCDFs [7, 60–63]. The mechanism of PCDD and PCDF formation in sinter plants is complex and associated to a de novo synthesis process [64]. The range of PCDD/F emissions in the EU-25 in 2004 is from 0.15 to 14.64 μg I-TEQ/t sinter expressed on an annual average basis [7], with most plants in the range 0.2 to 6.0 μg I-TEQ/t sinter [7]. The best option in the problem of dioxins is minimizing their formation instead of end of pipe treatments as is the most effective method. Several primary measures are considered in [65], we want to emphasize the addition of urea in the raw mix to inhibit the dioxin formation. In this way, Long et al. observed that with 0.05% urea, it was achieved a decrement of 63.1% in urea emission if compared with sinter without urea [66]. Lechtanska and Wielgosinski proposed the use of ammonium sulfate as inhibitor of dioxin formation [67].

Heavy metals: metals and heavy metals emissions are other important problem in the iron ore sintering, specially associated with $PM_{10/2.5}$. See in [65] the sources of heavy metals.

PAH (Polycyclic Aromatic Hydrocarbons): are generated by the inhomogeneous and incomplete combustion processes. Several techniques are described in [7] to reduce PAHs emission concentrations from 591.7 mg/t sinter to 0.2 mg/sinter.

Measures to enhance air quality can be divided into three categories [65]: primary measures, based on preventing or minimizing the release of pollutants; secondary measures, consist in basically end-of pipe treatments; tertiary measures, consist in treating polluting wastes and raw materials in a single facility, concentrating there the source of pollutants.

Sintering is an energy and polluting intensive process in integrated steelworks. Around 9–12% of the energy consumed in an integrated steelwork is consumed in the sintering process, and 75–80% of this energy is produced by using contaminant solid fuels, such as coke breeze, anthracite, etc. [68]. These fossil fuels generate diverse pollutants, mainly CO_2, SO_X and NO_X, and have made researchers to focus on studying more ecological alternatives as biochar, straw, or charcoal [65]. These new fuels are CO_2-neutral, and lead to a significant reduction in SO_X and NO_X emissions. Other possibility is using blast furnace dust, as it has 24–40% carbon [69], although the amounts that are possible to recycle are limited fundamentally because of the zinc emissions.

Secondary measures, as we mentioned, have the objective of reducing pollutant emissions in sinter plants. They have been applied since the last decades of the last century [65], in general combined with other primary measures. In this way, for instance, in an attempt of reducing PCDD/Fs in Servola sinter plant (Italy), they used urea (primary measure) and the WETFINE (Wet electrostatic Precipitator, secondary measure or end of pipe measure), reaching <0.4 ng I-TEQ/Nm^3 when using both systems (around 2 ng I-TEQ/Nm^3 when using only one) [70].

Secondary measures are deeply described in [65], but the main technologies of this group of end of pipe technologies are: WETFINE system, MEROS process, EOS system, AIRFINE system and EFA process.

2.5.4. Solar energy in the ironmaking and steelmaking

Solar energy when properly concentrated offers a great potential in applications where high temperature is required as for instance metallurgical processes [71]. Even when the possibility of using concentrated solar energy in the sintering process is very limited because of the large volume of material to be treated, it could find a great potential in iron recovery from metallurgical wastes such as slags or other by product. In our basic researches in this field, we used iron oxide (III) mixed with carbon, and a 1.5 kW medium size vertical axis solar furnace at the laboratory PROMES-CNRS (Font Romeu-Odeillo-Via, France). Sun radiation is concentrated in a spot of 12.2 mm in diameter, being controlled the power by means of a venetian blind. 14 samples were prepared by mixing iron oxide (III) (100% Fe_2O_3, d_{50} = 6.7 μm) with different carbon (100% C, d_{50} = 10.2 μm) excesses (10, 25 and 40%) over the stoichiometric. Samples of 0.8–2.5 g were loaded into crucibles of 75 mm length, 12 mm width and 8 mm depth, with three thermocouples placed at the bottom of the crucible. This crucible is then placed below the solar beam and displaced at a controlled speed of 0.25–0.76 mm/s.

Samples were analyzed by x-ray diffraction and SEM–EDX. It was observed that the main phases were Fe_2O_3, Fe_3O_4 and in some cases FeO. This indicates that a transformation took place during the experiments, carbon was mainly burnt during the process, so it was not used as reductant agent [71], and for that reason, the appearance of Fe_3O_4 and FeO takes place because of thermal decomposition of the iron oxide. It is possible to see in **Figure 1** the influence of displacement speed and power in the formation of magnetite.

From SEM–EDX, it is clearly observed that the disperse constituent is magnetite (white), while the matrix constituent is a phase formed by silica and alumina (both coming from the crucible [72]), iron and oxygen (see **Figure 2**). There are, for that reason, both diffusion and melting phenomenon during the process.

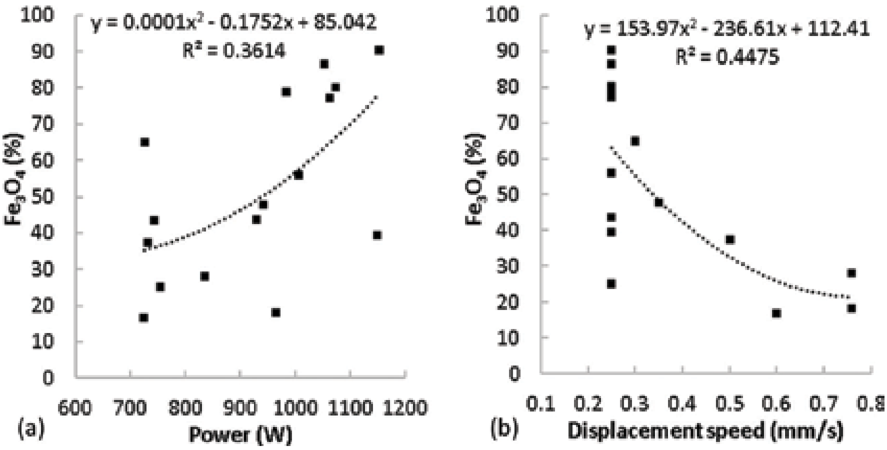

Figure 1. Magnetite formation as a function of power (a) and displacement speed (b).

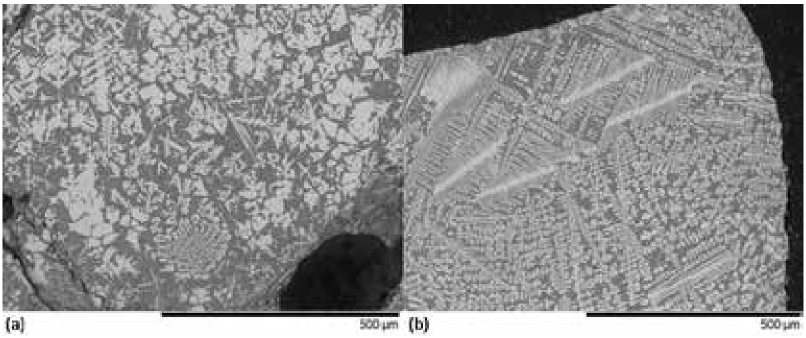

Figure 2. Micrographs obtained with an electronic microscope (E34 P2 (a) and E25 P2 (b)).

Knowing that the formation of magnetite is easily achieved by using concentrated solar energy, it is possible to think in recovering iron from wastes of the metallurgical industry containing iron as oxide, as for instance slags.

2.5.5. Other alternative processes to sintering and pelletizing

2.5.5.1. HPS process: hybrid pelletized sinter

This process was developed by the Nippon Kokan Keihin company (nowadays JFE Steel Corporation) with the objective of using fine iron-rich ores in their plants. The process is based on using pelletizing discs to obtain green pellets that are then coated with coke breeze before their disposal over the sinter strand. A commercial plant with an annual capacity of 6 million tons is working using HPS process at Fukuyama (belonging to JFE Steel Corporation) [18].

2.5.5.2. MEBIOS: mosaic embedding iron ore sintering

In 2001, Iron and Steel Institute of Japan began a research project on porous meso-mosaic texture sinter with the purpose of incorporating Australian goethite/limonite ores (characterized by a high proportion of ultrafine particles, up to 30% <150 μm) [16]. In this way, the purpose was to use important amounts of fine ores by controlling the void structure of the sinter bed structure (achieving a good sinter bed permeability and sinter yield). Consequence of the project is the MEBIOS process [73], which organizes dense granulated pellets in a conventional sinter mixture, allowing for obtaining well-developed voids and few pores that define a ventilation route, where the aging bed is based on Marra Mamba ore (fine ore and coarsely granulated material) while the induction bed is based on pisolitic limonite ore blended with coke and CaO [16]. In this way, dense large pellets support sinter bed and avoid sinter shrinkage, allowing the appearance of ventilation routes that improve permeability [18].

This process has another version known RF-MEBIOS (Return Fine-Mosaic Embedding Iron Ore Sintering). It was applied on Number 3 sinter plant in the NSSMC Kashima Steel Works, and then it was installed on three commercial sintering machines (Kashima, Wakayama, and Kokura) belonging to Sumitomo Metal Industries Ltc [18].

2.5.5.3. CAP: composite agglomeration process

Sinter and pellets are loaded in the blast furnace together, but this causes several problems associated to two aspects: spherical shape of pellets (responsible of the tendency to flow toward the center of the furnace, causing unstable operation); and, higher bulk density of pellets, making them to sink into the coke layer during the burden descent [74]. Jiang et al. developed the Composite Agglomeration Process with the purpose of solving the problems caused by the spheroidal shape of pellets and the increase in the supply of fine grained ores [74]. The process consists in: part of fine grained iron ore is transformed into 8–16 mm green pellets, while the rest and the coarse fine ores are mixed with fluxes, fuels and return fines, and then granulated (primary mixture); green pellets and primary mixture are blended (secondary mixture) and then fed to the sintering machine; the mixture is transformed into the composite agglomerate by ignition and down draft firing; finally, the composite agglomerate is crushed and screened, being the fraction <5 mm considered as return fine.

The process was used for first time in 2008 by Baotuo Iron and Steel Company, and improvements in sinter bed permeability, decrements in fuel consumption and increases in productivity were observed [75]. Other authors studied the use of CAP in specularite ores [76], titanomagnetite concentrate [77] or fluoric iron concentrates [78].

Acknowledgements

This research was supported by the Spanish Ministry of Education, Culture, and Sports via and FPU (Formación del Profesorado Universitario) grant to Daniel Fernández González (FPU014/02436).

Author details

Daniel Fernández-González*, Juan Piñuela-Noval and Luis Felipe Verdeja

*Address all correspondence to: fernandezgdaniel@uniovi.es

Departamento de Ciencia de los Materiales e Ingeniería Metalúrgica, Universidad de Oviedo, Oviedo, Asturias, Spain

References

[1] United States Geological Survey. Available from: https://minerals.usgs.gov/minerals/ [Accessed: October 8, 2017]

[2] Fernández-González D, Ruiz-Bustinza I, Mochón J, González-Gasca C, Verdeja LF. Iron ore sintering: Raw materials and granulation. Mineral Processing and Extractive Metallurgy Review. 2017;**38**(1):36-46. DOI: 10.1080/08827508.2016.124459

[3] Peacey JG, Davenport WG. El Alto Horno de Hierro. Teoría y Práctica. 1st ed. Limusa: México; 1986

[4] Lu L. Important iron ore characteristics and their impacts on sinter quality–A review. Minerals and Metallurgical Processing. 2015;**32**(2):88-96

[5] Ballester A, Sancho JP, Verdeja LF. Metalurgia Extractiva. Volumen I. Fundamentos. 1st ed. Madrid: Síntesis; 2003

[6] Fernández-González D, Martín-Duarte R, Ruiz-Bustinza I, Mochón J, González-Gasca C, Verdeja LF. Optimization of sinter plant operating conditions using advanced multivariate statistics: Intelligent data processing. JOM. 2016;**68**(8):2089-2095. DOI: 10.1007/s11837-016-2002-2

[7] Remus R, Aguado MA, Roudier S, Delgado L. Best Available Techniques (BAT) Reference Document for Iron and Steel Production. Industrial Emissions Directive 2010/75/EU (Integrated Pollution Prevention and Control). 1st ed. Seville: European Commission, Joint Research Centre, Institute for Prospective Technological Studies; 2013

[8] Battle T, Srivastava U, Kopfle J, Hunter R, McClelland J. The direct reduction of iron. In: Seetharaman S, editor. Treatise on Process Metallurgy. Volume 3: Industria Process, Part A. 1st ed. Oxford: Elsevier; 2014. pp. 89-176

[9] Ordiales M, Iglesias J, Fernández-González D, Sancho-Gorostiaga J, Fuentes A, Verdeja LF. Cold agglomeration of ultrafine oxidized dust (UOD) from ferromanganese and siliconmanganese industrial process. Metals. 2016;**6**:203. DOI: 10.3390/met6090203

[10] Sancho J, Verdeja LF, Ballester A. Metalurgia Extractiva. Volumen II. Procesos de Obtención. 1st ed. Madrid: Síntesis; 2000

[11] Palacios JM, Arana JL, Larburu JI, Iniesta L. La Fabricación del Acero. 1st ed. Madrid: UNESID (Unión de Empresas Siderúrgicas); 1998

[12] Halt JA, Kawatra SK. Review of organic binders for iron ore concentrate agglomeration. Minerals and Metallurgical Processing. 2014;**31**(2):72-94

[13] Mishra S, Roy GG. Reduction behavior of iron ore-coal composite pellets in rotary hearth furnace (RHF): Effect of pellet shape, size, and bed packing material. Transactions of the Indian Institute of Metals. 2017;**70**(4):967-978. DOI: 10.1007/s12666-016-0890-z

[14] Umadevi T, Brahmacharyulu A, Roy AK, Mahapatra PC, Prabhu M, Ranjan M. Influence of iron ore fines feed size on microstructure, productivity and quality of iron ore sinter. ISIJ International. 2011;**51**(6):922-929. DOI: 10.2355/isijinternational.51.922

[15] Gupta RC. Theory and Laboratory Experiements in Ferrous Metallurgy. 1st ed. PHI Learning Private Limited: New Delhi; 2010

[16] Fernández-González D, Ruiz-Bustinza I, Mochón J, González-Gasca C, Verdeja LF. Iron ore sintering: Process. Mineral Processing and Extractive Metallurgy Review. 2017;**38**(4): 215-227. DOI: 10.1080/08827508.2017.1288115

[17] Gosh A, Chateterjee A. Ironmaking and Steelmaking. 1st ed. New Delhi: PHI Learning Private Limited; 2008

[18] Lu L, Ishiyama O. Iron ore sintering. In: Iron Ore. Mineralogy, Processing and Environmental Sustainability. 1st ed. Cambridge: Wordhead Publishing-Elsevier; 2015. pp. 395-429

[19] Loo CE. Changes in heat transfer when sintering porous goethitic iron ores. Transactions of the Institution of Mining and Metallurgy Section C- Mineral Processing and Extractive Metallurgy. 2000;**109**(1):11-12. DOI: 10.1179/mpm.2000.109.1.11

[20] Fernández-González D, Ruiz-Bustinza I, Mochón J, González-Gasca C, Verdeja LF. Iron ore sintering: Quality indices. Mineral Processing and Extractive Metallurgy Review. 2017; **38**(4):254-264. DOI: 10.1080/08827508.2017.1323744

[21] Toda H, Senzaki T, Isozaki S, Kato K. Relationship between heat pattern in sintering bed and sinter properties. Transactions of the Iron and Steel Institute of Japan. 1984;**24**(3):187-196. DOI: 10.2355/isijinternational1966.24.187

[22] Ishikawa Y, Shimomura Y, Sasaki M, Hida Y, Toda H. Improvements of sinter quality based on the mineralogical properties of ores. In: Proceedings of the 42th Ironmaking Conference (AIME); Atlanta; 1983. pp. 17-29

[23] Cores A, Verdeja LF, Ferreira S, Ruiz-Bustinza I, Mochón J. Iron ore sintering. Part 1. Theory and practice of the sintering process. DYNA Colombia. 2013;**80**(190):152-171. DOI: 10.15446/dyna.v82n190.44054

[24] Mochón J, Cores A, Ruiz-Bustinza I, Verdeja LF, Robla JI, García-Carcedo F. Iron ore sintering. Part 2. Quality indices and productivity. DYNA Colombia. 2014;**81**(183):168-177. DOI: 10.15446/dyna.v81n183.41568

[25] Harsha Nistala S, Sinha M, Kumar Choudhary M, Bose G, Sinha S. Study of generation of sinter return fines during transportation. Ironmaking and Steelmaking. 2015;**42**(3):226-232. DOI: 10.1179/1743281214Y.0000000224

[26] Kortman HA, Burghardt A. Test methods for evaluating iron ores, pellets and sinters. In: Conference Proceedings of Agglomeration 77: 2nd International Symposium of Agglomeration, AIME (American Institute of Mining, Metallurgical, and Petroleum Engineers); 1977. pp. 219-242

[27] Murakami K, Sugawara K, Kawawuchi T. Analysis of combustion rate at various carbon materials for iron ore sintering bed. ISIJ International. 2013;**53**(9):1580-1587. DOI: 10.2355/isijinternational.53.1580

[28] Tahanpesaranedezfuly N, Heidary A. The effect of coke particle size on the thermal profile of the sintering process product. In: TMS 2012 141st Annual Meeting and Exhibition. Supplemental Proceedings. Volume I: Materials Processing and Interfaces. New Jersey: John Wiley and Sons, Inc.; 2012

[29] Loo CE. The role of coke size in the sintering of a hematite ore blend. Ironmaking and Steelmaking. 1991;**18**(1):33-40

[30] Peters KH, Beer H, Kropla HW, Rinne K. Granulation behavior of sinter mix components, with particular respect to coke breeze particle size and its influence on the iron ore sintering process. In: Fifth International Symposium on Agglomeration (Institute of Chemical Engineering); 1989. pp. 51-70

[31] Fan X, Ji Z, Gan M, Chen X, Yin L, Jiang T. Characteristics of prepared coke-biochar composite and its influence on reduction of NOX emission in iron ore sintering. ISIJ International. 2015;**55**(3):521-527. DOI: 10.2355/isijinternational.55.521

[32] Kagawuchi T, Hara M. Utilization of biomass for iron ore sintering. ISIJ International. 2013;**53**(9):1599-1606. DOI: 10.2355/isijinternational.53.1599

[33] Lu L, Adam M, Kilnburn M, Hapugoda S, Somerville M, Jahanshahi S, Mathieson JG. Substitution of charcoal for coke breeze in iron ore sintering. ISIJ International. 2013;**53**(9):1607-1616. DOI: 10.2355/isijinternational.53.1607

[34] Kumar CU, Ramana RV, Ali S, Das AK. Quality of sínter in the light of blast furnace performance. Tata Search. 1995:20-25

[35] Nandy B, Chandra S, Bhattacharjee D, Gosh D. Assessment of blast furnace behavior through softening-melting test. Ironmaking and Steelmaking. 2006;**33**(2):111-119. DOI: 10.1179/174328106X94744

[36] Umadevi T, Karthik P, Mahapatra PC, Prabhu M, Ranjan M. Optimization of FeO in iron ore sinter at JSW steel limited. Ironmaking and Steelmaking. 2012;**41**(3):180-189. DOI: 10.1179/1743281211Y.0000000080

[37] Hiesch L. Effect of raw material composition on the sintering properties. ISIJ International. 2005;**45**(4):551-559. DOI: 10.2355/isijinternational.45.551

[38] Yu W, Zuo H, Zhang J, Zhang T. The effects of high Al_2O_3 on the metallurgical properties of sinter. In: Characterization of Minerals, Metals and Materials. 1st ed. New Jersey: TMS-Wiley; 2015. pp. 419-425

[39] Umadevi T, Deodar AV, Mahapatra PC, Prabhu M, Rajan M. Influence of alumina on iron ore sínter properties and productivity in the conventional and selective granulation sintering process. Steel Research International. 2009;**80**(9):686-692. DOI: 10.2374/SRI08SP009

[40] Umadevi T, Brahmacharyulu A, Sah R, Mahapatra PC, Prabhu M. Optimization of MgO addition in low and high silica iron ore sinter to improve sinter reducibility at JSW steel limited. Ironmaking and Steelmaking. 2014;**41**(4):270-278. DOI: 10.1179/1743281213Y.0000000124

[41] Kalenga MK, Garbers-Craig AM. Investigation into how the magnesia, silica, and alumina contents of iron ore sinter influence its mineralogy and properties. The Journal of the Southern African Institute of Mining and Metallurgy. 2010;**110**(8):447-455

[42] Bhagat RP. Reduction of solid fuel consumption in sintering of Indian iron ore. Science of Sintering. 2015;**47**(2):205-213

[43] Umadevi T, Roy AK, Mahapatra PC, Prabhu M, Ranjan M. Influence of magnesia on iron ore sinter properties and productivity- use of dolomite and dunite. Steel Research International. 2009;**80**(11):800-807. DOI: 10.2374/SRI09SP010

[44] Yadav US, Pandey BD, Das BK, Jena D. Influence of magnesia on sintering characteristics of iron ore. Ironmaking and Steelmaking. 2002;**29**(2):91-95. DOI: 10.1179/030192302225002018

[45] Lu L, Holmes RJ, Manuel J. Effects of alumina on sintering performance of hematite iron ore. ISIJ International. 2007;**47**(3):349-359. DOI: 10.2355/isijinternational.47.349

[46] Gridasov VP, Logachev GN, Pishnograev SN, Pavlov AV, Gostenin VA, Chevychelov AV. Behavior of alkalis in blast furnace. Metallurgist. 2016;**59**(9-10):761-765. DOI: 10.1007/s11015-016-0171-4

[47] Kurunov IF, Titov VN, Emel'yanov VL, Lysenko SA, Arzamastsev AN. Analysis of the behavior of alkalis in a blast furnace. Metallurgist. 2009;**53**(9-10):533-542. DOI: 10.1007/s11015-010-9210-8

[48] Norgate T, Haque N, Somerville M, Jahanshasi S. Biomass as a source of renewable carbon for iron and steelmaking. ISIJ International. 2012;**52**(8):1472-1481. DOI: 10.2355/isijinternational.52.1472

[49] Pardo N, Moya JA, Vatopoulos. Prospective Scenarios on Energy Efficiency and CO2 Emission in the EU Iron and Steel Industry. 1st ed. Petten: European Commission, Joint Research Centre, Institute for Energy and Transport; 2012

[50] Oyama N, Iwami Y, Yamamoto T, Machida S, Higuchi T, Sato H, Sato M, Takeda K, Watanabe Y, Shimizu M, Nishioka K. Development of secondary-fuel injection technology for energy reduction in the iron ore sintering process. Tetsu to Hagane. 2011;**97**(10):510-518. DOI: 10.2355/tetsutohagane.97.510

[51] Yabe H, Takamoto Y. Reduction of CO_2 emissions by use of pre-reduced iron ore as sinter raw material. ISIJ International. 2013;**23**(9):1625-1632. DOI: 10.2355/isijinternational.53.1625

[52] Chen Y, Gou Z, Wang Z, Feng G. NOx reduction in the sintering process. International Journal of Minerals, Metallurgy, and Materials. 2009;**16**(2):143-148. DOI: 10.1016/S1674-4799(09)60024-8

[53] Mo C, Teo C, Hamilton I, Morrison J. Admixing hydrocarbons in raw mix to reduce NOx emission in iron ore sintering process. ISIJ International. 1997;**37**(4):350-357. DOI: 10.2355/isijinternational.37.350

[54] Morioka K, Inaba S, Shimizu M, Ano K, Sugiyama T. Primary application of the in-bed-deNOx process using Ca-Fe oxides in iron ore sintering machines. ISIJ International. 2000;**40**(3):280-285. DOI: 10.2355/isijinternational.40.280

[55] Fan X, Yu Z, Gan M, Chen X, Chen Q, Liu S, Huang Y. Elimination behaviors of NOx in the sintering process with flue gas recirculation. ISIJ International. 2015;**55**(10):2074-2081. DOI: 10.2355/isijinternational.ISIJINT-2015-180

[56] Li G, Liu C, Rao M, Fan Z, You Z, Zhang Y, Jiang T. Behavior of SO_2 in the process of flue gas circulation sintering (FGCS) for iron ores. ISIJ International. 2014;**54**(1):37-42. DOI: 10.2355/isijinternational.54.37

[57] Gan M, Ji Z, Fan Z, Chen X, Li Q, Yin L, He X, Zhou Y, Jiang T. Emission behavior and physicochemical properties of aerosol particulate matter (PM10/2.5) from iron ore sintering process. ISIJ International. 2015;**55**(12):2582-2588. DOI: 10.2355/isijinternational.ISIJINT-2015-412

[58] Ji Z, Fan Z, Gan M, Chen X, Li Q, Tian Y, He X, Zhou Y, Jiang T. Influence factors on PM2.5/10 emissions in iron ore sintering process. ISIJ International. 2016;**56**(9):1580-1587. DOI: 10.2355/isijinternational.ISIJINT-2016-169

[59] Fleischanderl A, Plattner T, Lanzerstorger C. Efficient reduction of PM10/2.5 emissions at iron ore sinter plants. In: Proceedings of the Dust Conf 2007; Maastricht; 2007

[60] Anderson DR, Fisher R. Sources of dioxins in the United Kingdom: The steel industry and other sources. Chemosphere. 2002;**46**(3):371-381. DOI: 10.1016/S0045-6535(01)00178-3

[61] Quab U, Fermann M, Bröker G. The European dioxin air emission inventory project-final results. Chemosphere. 2004;**54**(9):1319-1327. DOI: 10.1016/S0045-6535(03)00251-0

[62] Aries E, Anderson DR, Fisher R, Fray TAT, Hemfrey D. PCDD/F and dioxin-like PCB emissions from iron ore sintering in the UK. Chemosphere. 2006;**65**(9):1470-1480. DOI: 10.1016/j.chemosphere.2006.04.020

[63] Dopico M, Gómez A. Review of the current state and main sources of dioxins around the world. Journal of the Air and Waste Management Association. 2015;**65**(9):103-1049. DOI: 10.1080/10962247.2015.1058869

[64] Boscolo M, Padoano E, Tommasi S. Identification of possible dioxin emission reduction strategies in pre-existing iron ore sinter plants. Ironmaking and Steelmaking. 2008;**35**(2): 146-152. DOI: 10.1179/174328107X247815

[65] Fernández-González D, Ruiz-Bustinza I, Mochón J, González-Gasca C, Verdeja LF. Iron ore sintering: Environment, automatic, and control techniques. Mineral Processing and Extractive Metallurgy Review. 2017;**38**(4):238-249. DOI: 10.1080/08827508.2017.1288118

[66] Long HM, Li JX, Wang P, Gao G, Tang GW. Emission reduction of dioxin in iron ore sintering by adding urea as inhibitor. Ironmaking and Steelmaking. 2011;**38**(4):258-262. DOI: 10.1179/1743281210Y.0000000008

[67] Lechtanska P, Wielgosinski G. The use of ammonium sulfate as an inhibitor of dioxin synthesis in iron ore sintering process. Ecological Chemistry and Engineering S. 2014;**21**(1): 59-70. DOI: 10.2478/eces-2014-0005

[68] Fan X, Ji Z, Gan M, Chen X, Li Q, Jiang T. Influence of preformation process on combustibility of biochar and its applications in iron ore sintering. ISIJ International. 2015;**55**(11): 2342-2349. DOI: 10.2355/isijinternational.ISIJINT-2015-33

[69] Lanzerstorfer C, Bamberger-Strassmayr B, Pilz K. Recycling of blast furnace dust in the iron ore sintering process: Investigation of coke breeze substitution and influence on off-gas emissions. ISIJ International. 2015;**55**(4):758-764. DOI: 10.2355/isijinternational.55.758

[70] Boscolo M, Padoano E. Investigations into dioxin emissions at Italian iron ore sintering plant. Ironmaking and Steelmaking. 2008;**35**(5):338-342. DOI: 10.1179/174328108X287739

[71] Mochón J, Ruiz-Bustinza I, Vázquez A, Fernández D, Ayala JM, Barbés MF, Verdeja LF. Transformations in the iron-manganese-oxygen-carbon system resulted from treatment of solar energy with high concentration. Steel Research International. 2014;**85**(10):1469-1476. DOI: 10.1002/srin.201300377

[72] Verdeja LF, Sancho JP, Ballester A, González R. Refractory and Ceramic Materials. 1st ed. Madrid: Síntesis; 2014

[73] Hayashi N, Komarov S, Kasai E. Heat transfer analysis of the mosaic embedding iron ore sintering (MEBIOS) process. ISIJ International. 2009;**49**(5):681-686. DOI: 10.2355/isijinternational.49.681

[74] Jiang T, Li GH, Wang HT, Zhang KC, Zhang YB. Composite agglomeration process (CAP) for preparing blast furnace burden. Ironmaking and Steelmaking. 2010;**37**(1):1-7. DOI: 10.1179/174328109X462995

[75] Jiang T, Hu Y, Li G, Guo Y, Yu Z, Fan X, Zhang Y, Yang Y. Composite agglomeration process of iron ore fines. In: 3rd International Symposium on High Temperature Metallurgical Processing, TMS (The Minerals, Metals and Materials Society); March 11-15, 2012; Orlando; 2012. pp. 7-15

[76] Zhang H, Yu H, Li G, Zhang Y, Li Q, Jiang T. Characteristic of mineralization of specularite iron ores during composite agglomeration processing. In: 2nd International Symposium on High-Temperature Metallurgical Processing, TMS (The Minerals, Metals and Materials Society); March 15-19, 2011; Orlando; 2011. pp. 191-198

[77] Jiang T, Yu Z, Peng Z, Rao M, Zhang Y, Li G. Preparation of BF burden from titanomagnetite concentrate by composite agglomeration process (CAP). ISIJ International. 2015;**55**(8):1599-1607. DOI: 10.2355/isijinternational.ISIJINT-2015-094

[78] Jiang T, Hu Y, Li Q, Li G, Yang Y, Zhang Y, Guo Y. Mechanisms of composite agglomeration of fluoric concentrate. Journal of Central South University of Technology. 2010; **17**(6):1190-1195. DOI: 10.1007/s11771-010-0617-y

Calcination and Pelletizing of Siderite Ore

Mehmet Celikdemir, Musa Sarikaya, Tolga Depci,
Ramazan Aydogmus and Aysegul Yucel

Additional information is available at the end of the chapter

http://dx.doi.org/10.5772/intechopen.72808

Abstract

In the present study, calcination properties of Hekimhan-Deveci siderite ($FeCO_3$) ore and the effect of calcination process before the pelletization on strength of pellet were investigated and evaluated. Two different calcination processes were followed. One of them is the traditional calcination process and the other one is microwave assisted calcination process which is a new process for siderite ore. The characterization of the calcined and uncalcined siderite ore was done using X-ray diffraction, X-ray fluorescence spectrometry and thermogravimetric analysis. The physical and mechanical properties of pellets which were obtained using the raw siderite and the calcined siderite were compared with each other. As a result of experimental studies, it was found that the calcination process decreased the milling time, causing the significant energy saving and the most suitable calcination process for siderite ore was found as 15 min at 700°C temperature. It was the first time that the calcination process of the siderite ore was achieved by microwave by adding 30 wt% sucrose as a thermal auxiliary. The microwave conditions were determined as 900 W at 3 min. In 3 min, the temperature of the siderite ore increased up to 1100°C and 32.14% weight loss for the sample was achieved.

Keywords: siderite ore, furnace, microwave heating, calcination, pelletizing

1. Introduction

1.1. Importance of the steel and iron industry

The iron and steel industry produces products with desired chemical and physical properties from the melting iron ore in blast furnaces or the melting scrap in arc furnaces by different processes [1]. Changing consumer needs, developments in technology and competition are further increasing the product diversity in the iron and steel sector. Final steel products have numerous types and different application areas. The iron and steel industry, which is the most important of the heavy industry sectors, supplies raw materials to many important industries such as construction, infrastructure, automotive, white goods and machinery industry. Therefore, it can be said that industrialization of a country is directly related to its strong iron and steel sector and consumption [2]. **Table 1** gives the top 10 countries producing the crude steel in the world.

Today iron constitutes the basic raw material of the industry and plays an important role in the economic development of the countries. The economic development indicators of countries are also determined by per capita iron and steel consumption. **Table 2** shows the consumption of steel per capita.

In the past, iron ore with the characteristics required for blast furnace charging was met directly from iron mines. The need for iron in the industry has increased rapidly and also the reserve of the iron ore which can be directly loaded into the blast furnace has gradually decreased. Therefore recently, the irons ores with low grade have been started to be evaluated. The crude iron ore reserves and its iron content in the world are given in **Table 3**.

The main raw material of the iron and steel industry is iron ore. It must be economical to operate and use a mine as an ore. It is desirable that the blend grade of the iron ores used in the steel industry is at least 57% Fe grade. The iron ore is found in the form of magnetite (Fe_3O_4), hematite (Fe_2O_3), limonite ($FeO(OH)\cdot nH_2O$), goethite (α-$Fe^{3+}O(OH)$), siderite ($FeCO_3$) and pyrite (FeS_2) minerals in the nature.

1.2. Siderite

The name of the siderite mineral is derived from the word sideros (σίδηρος), meaning iron in Greek. Technically, siderite minerals contains about 48.02% iron (Fe) and be crystal trigonal (hexagonal scalenohedral) system, mostly rhombohedral crystalline; plate, prismatic, massive;

No	Country	2011	2012	2013	2014	2015	2015 (%)
1	China	701.9	731.0	822.0	822.8	803.8	49.60
2	Japan	107.6	107.2	110.6	110.7	105.1	6.48
3	India	73.4	77.2	81.2	87.2	89.0	5.49
4	USA	86.3	88.6	88.8	88.1	78.8	4.86
5	Russia	68.8	70.2	69.0	71.4	70.8	4.36
6	South Korea	68.5	69.0	66.0	71.5	69.6	4.29
7	Germany	44.2	42.6	42.6	42.9	42.6	2.62
8	Brazil	35.2	34.5	34.1	33.8	33.2	2.04
9	Turkey	34.1	35.8	34.6	34.0	31.5	1.94
10	Ukraine	35.3	32.9	32.7	27.1	22.9	1.41
	EU (28 countries)	177.7	168.5	166.3	169.3	166.1	10.25
	World	1538.0	1560.1	1650.3	1669.8	1620.4	100

Table 1. Top 10 countries in world crude steel production (million metric tons) [3].

Countries/region	2011	2012	2013	2014	2015
South Korea	1190.1	1135.3	1081.7	1155.0	1155.7
Czech Republic	663.1	639.8	641.5	678.6	723.9
Japan	546.9	541.1	558.3	574.9	535.7
Germany	561.3	507.3	517.0	530.1	523.9
China	495.4	507.3	562.0	540.6	509.0
Australia	527.1	488.1	475.1	480.4	466.2
Turkey	389.9	404.6	436.9	422.5	464.7
Canada	456.4	496.3	466.8	492.5	412.5
EU (28 countries)	343.0	306.2	311.1	322.0	331.6
North America	267.4	285.2	276.7	311.1	282.9
Asia	256.4	261.7	282.2	277.8	266.1
Middle East	257.6	250.3	248.8	251.9	244.4
World	221.3	223.3	234.5	234.1	224.4
South America	126.4	128.0	132.3	122.8	112.4
Africa	30.1	32.8	35.4	35.4	35.7

Table 2. Crude steel consumption per capita of the country and regions (kg/person) [3].

medium-fine grained; rarely kidney, oolitic crystal habits. Siderite minerals have transparent-semi-transparent appearance and have different colours like yellowish-brown to greyish-brown, pale yellow to tannish, grey, brown, green, red, black and sometimes nearly colourless; tarnished iridescent at times; colourless to yellow and yellow-brown in transmitted light. The specific weight of siderite mineral is 3.96 g/cm^3 and its Mohs hardness is between 3.5 and 4.5. A sample of siderite giving large crystals is given in **Figure 1**.

Massive siderite is commonly found in layered sedimentary beds, especially in mudstones and marls. In addition, it was found as a gangue mineral in hydrothermal ore vein which contains pyrite, chalcopyrite and galenite. It is also found in basaltic volcanic rocks, sometimes in pegmatites and metamorphic rocks.

1.3. Calcination

Calcination is the breakdown of carbonates and hydrates by the effect of temperature in order to obtain oxide form compounds. Calcination not only involves removing of water in the crystal structure, but also removes carbon dioxide or other chemically bound gases such as hydrates, carbonates.

All calcination reactions are endothermic. In terms of thermodynamic rule, the decomposition of a carbonate at a constant temperature is a function of CO_2 partial pressure. The calcination reaction is given in the following Eq. (1) for carbonate compounds.

$$\mathrm{MeCO}_{3_{(s)}} \rightarrow \mathrm{MeO}_{(s)} + \mathrm{CO}_2 \quad (1)$$

Countries	Reserves	
	Crude ore	Iron content
Australia	52.000	23.000
Russia	25.000	14.000
Brazil	23.000	12.000
China	21.000	7.200
India	8.100	5.200
Ukraine	6.500	2.300
Canada	6.000	2.300
Sweden	3.500	2.200
United States	3.000	790
Iran	2.700	1.500
Kazakhstan	2.500	900
South Africa	1.200	770
Other countries	18.000	9.500
World total (rounded)	170.000	82.000

Table 3. Iron ore reserves and its iron content in the world (million metric tons) [4].

The equilibrium constant of the reaction equals the partial pressure of the CO_2 if the solids activities are equal to one another. Therefore, the complete decomposition temperature of a carbonate compound is the temperature at which the P^0_{CO2} pressure equals an atmospheric pressure.

Figure 1. Crystal-shaped siderite sample [5].

The calcination process for siderite ore aims to remove the bound CO_2 in the formation of $FeCO_3$. Siderite calcination reactions are given in the following short chemical Eqs. (2)–(4)

$$FeCO_3 \rightarrow FeO + CO_2 \tag{2}$$

$$3\,FeCO_3 \rightarrow Fe_3O_4 + 2\,CO_2 + CO \tag{3}$$

$$3FeO + CO_2 \rightarrow Fe_3O_4 + CO \tag{4}$$

During the calcination process, CO_2 composition is removed from the siderite ore structure. So, it lose about 30 wt% of its weight. However, it is necessary to reach a temperature of at least 700°C for this weight loss. The calcination of siderite ore is mostly carried out in rotary kilns. The ore entering the rotary kiln as siderite; leaving the furnace turned into a mixture of hematite, magnetite and maghemite. The distribution of the minerals in this mixture depends on the working temperature of the oven and the duration time. At low temperatures, primarily hematite and then magnetite transformation occurs. However, the mixture is predominantly hematite in every case.

1.4. Traditional and microwave heating methods

Conventional heating principles have been utilized in the heating and/or roasting processes of some raw ores or materials from the past to the present day. There are three basic mechanisms of conventional heating, namely convection, conduction and diffusion. These three heat transfer mechanisms in conventional heating heat the material from the outside to the inside. This method causes large time and energy losses to occur during conduction by conduction into inside of materials. Microwave energy is non-ionizing electromagnetic radiation (radiation) having a frequency in the range of 300 MHz to 300 GHz, with intensive application in the field of communication; only certain frequencies are allowed for industrial, scientific and medical (ISM) applications [6]. Microwave heating is different from conventional heating because it is in the form of electromagnetic energy that can penetrate the depths of the sample [7]. The samples are heated inside to outside in microwave heating systems [8]. The differences between microwave and conventional heating systems and principles are represented in **Figure 2**.

In microwave heating systems, electromagnetic energy is directly converted into heat inside of the material and heating starts inside to outside contrary to the conventional heating. The microwaves propagate at the speed of light and as soon as the source is turned on the electromagnetic wave immediately penetrates to materials and starts to energy conversion. Long heating and cooling phases are not required when the source is turned off, since the heating process is stopped immediately [10].

1.5. Pellets

Pellets are the oval/spherical shaped pieces of ore having high compression strength which are obtained from fines or from finely ground ores by adding various additives like bentonite and whose diameter is generally between 8 and 20 mm as shown in **Figure 3**.

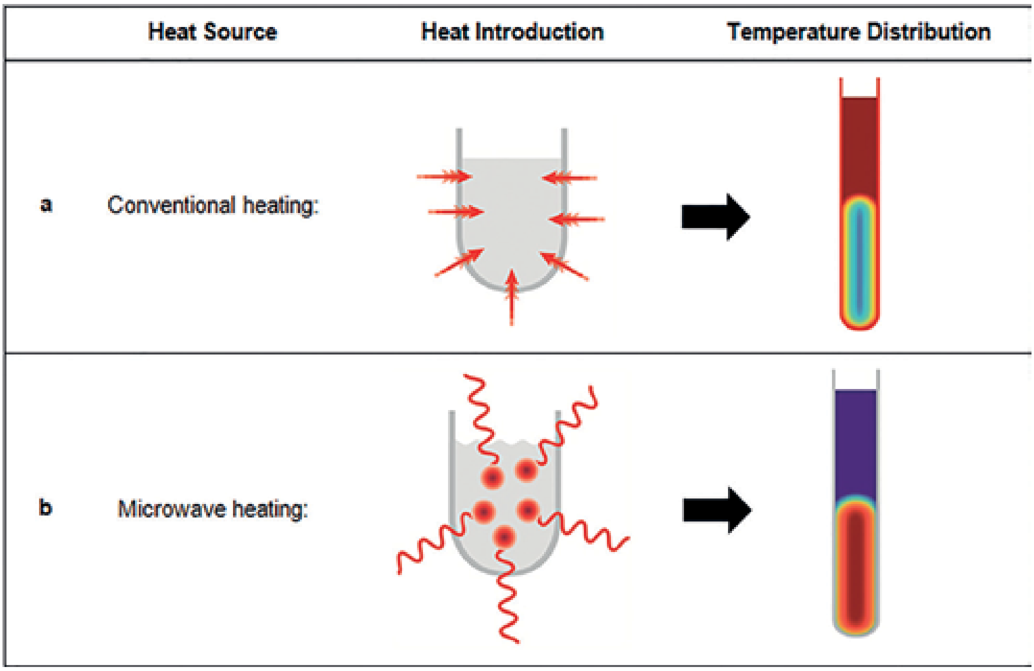

Figure 2. Schematic representation of the comparison of the microwave and conventional heating process [9].

Iron ore pellets can be used as a substitute to sinter and calibrated lump ores in the blast furnace burden. Apart from these pellets can be applied to some non-ferrous metal ores such as lead and chromium ores [11].

Since the 1960s, pelletizing technology has been rapidly developed and provided a quality chargeable material for iron making.

According to 2011 data the world pellet production on the basis of countries and regions is given in **Table 4**.

The purpose of the iron pelletizing process is to convert the iron-rich fine-grained minerals into blast furnace charging material, which is defined as pellet, through agglomeration and hardening. The pellets are rigid and generally spherical shape and must have the following properties to be used in the high-temperature furnace:

Figure 3. The pellets form of iron ore.

Iron ore, world pelletizing capacity by content and country in 2011	
	Rated capacity gross weight (million metric tons)
North America	
Canada	27.5
Mexico	15.0
United States	57.4
Total	99.9
South America	
Brazil	56.0
Chile	5.3
Peru	3.5
Venezuela	11.8
Total	76.6
Europe and Central Eurasia	
Kazakhstan	8.4
Netherlands	4.4
Russia	31.4
Slovakia	0.4
Sweden	26.0
Turkey	1.5
Ukraine	33.5
Total	105.6
Asia	
Bahrain	11.0
China	135.0
India	24.0
Iran	12.3
Oman	9.0
Japan	3.0
Total	194.3
Ocenia, Australia	4.3
Grand total	480.7

Table 4. Pellet production in the world and in the region (million metric tons) [12].

a. must be free from dust and fines.

b. must show physical strength against breakage during transportation and storage.

c. must be resistant to crumbling which will occur during various reactions occurring in the blast furnace depending on the heating process.

The ore to be pelletized may be enriched low-grade iron ore or high-grade powder forms ores which cannot be directly charged into the blast-furnace. The pelletizing process consists of two main parts: raw pellet (green ball) and product pellet. The raw pellet is obtained by mixing the enriched ore with the binders followed by the agglomeration process, the product pellet is obtained by heating and cooling the raw pellet [13].

The pelletizing process occurs in four basic stages, as shown in **Figure 4**. First, the ore and the various additives are mixed to obtain a homogeneous form. The distribution of the materials forming the pellet cake is of great importance in terms of pellet strength. After mixing operation, the mixture is transferred balling discs to obtain pellet form.

This product is called green pellet. Optionally, the process may be ended at this step depending on the needed or, the pellet is transferred to the next device and subjected to the induration to obtain the product pellet as shown in **Figure 5**. After this process, the cooled material is now named the product pellet.

- **i.** Mixing
- **ii.** Agglomeration
- **iii.** Induration
- **iv.** Cooling

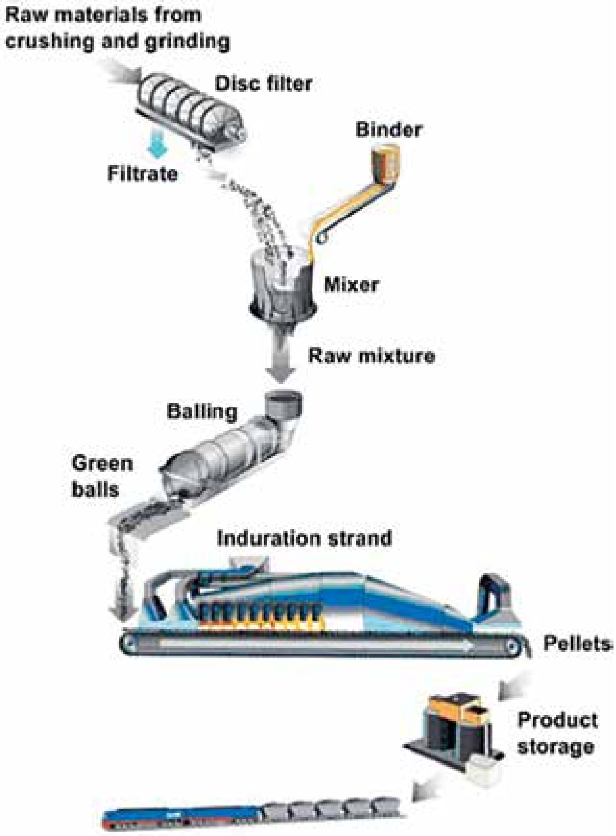

Figure 4. Schematic of a pelletizing plant with wet grinding [14].

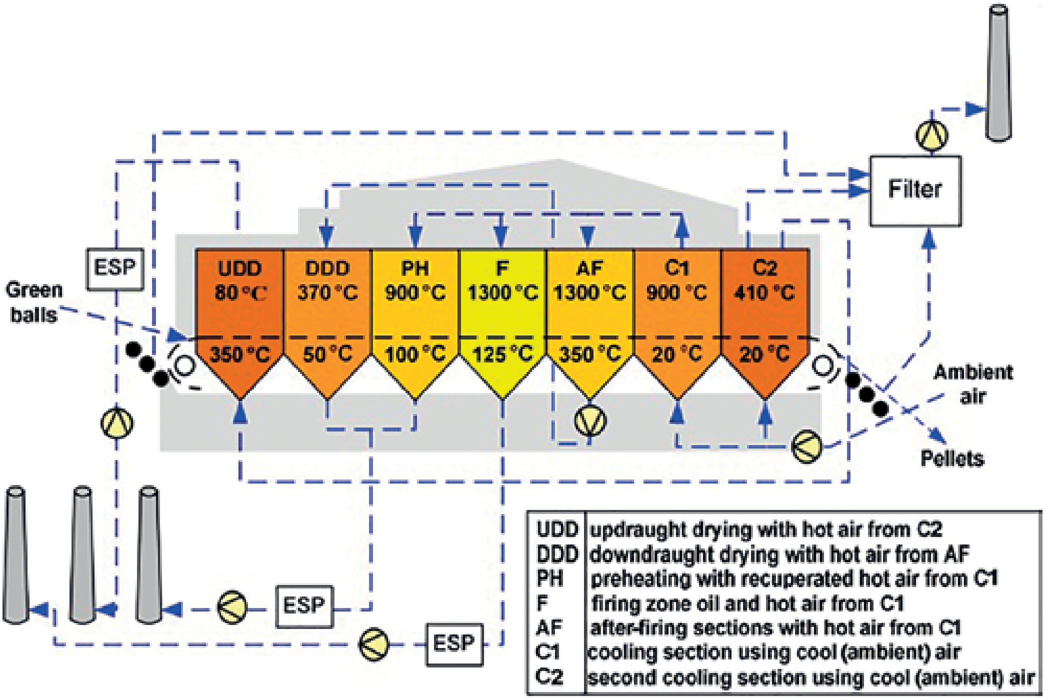

Figure 5. Schematic of the straight grate process [14].

In the process of obtaining the product pellet, the principle is that the material be heated at a recrystallization temperature according to the compound type. The recrystallization temperature for siderite is about 1300°C. If this temperature level is exceeded too much, liquid phase formation is occurred and undesirable sintering process starts.

2. Materials

2.1. Ore and chemicals

In this study, siderite ore was obtained from the Deveci district of Hekimhan Malatya Province. **Figure 6** shows the pictures of the raw siderite ore and the calcined siderite ore used in the study. The elemental analyses of raw siderite ore is given in **Table 5**.

In addition, the bentonite which was used during the pelletizing process was also obtained from Hekimhan/Malatya. Its density is 2.60 g/cm^3 and colours are white, grey, yellow, pink and green. Bentonite, a volcanic mineral formed by the decomposition of volcanic ash in situ and composed of montmorillonite clay mineral of large size which absorbs water and is used commercially in drilling mud, catalyst, paint, plastic filling works [15].

In the microwave experiment part, sucrose—$C_{12}H_{22}O_{11}$ (Merck 99.5%) and urea CH_4N_2O (Merck 99.5%) was used as a thermal auxiliary and consolidate purposes, respectively.

Figure 6. Raw siderite (on the left) and calcined siderite (on the right).

3. Experimental part

3.1. Milling operation

The raw siderite ore used in the study was sieved and weighed. The results of the sieve analysis are given in **Figure 7**. When the graph was examined, it was determined that P_{80} (80% of the feed passed through the sieve) was 7.9 mm and d_{50} (50% of the feed passed through the sieve) was 5.6 mm.

The raw siderite ore was both directly grounded and calcined before grinding operation. During this calcination process, CO_2 is removed by the effect of temperature, causing the capillary cracks in the ore, as a result fragmentation and crumbling is occurred. This situation is evident in the cumulative undersize graph given in **Figure 8** showing that calcination process slightly decreased the particle size of the siderite.

Component	Concentration (%)
Fe_2O_3 (Fe %)	53.21 (37.25)
MgO	18.88
Al_2O_3	0.25
SiO_2	4.42
SO_3	0.84
K_2O	0.81
CaO	9.87
MnO	11.39

Table 5. Chemical analysis of raw siderite ore sample.

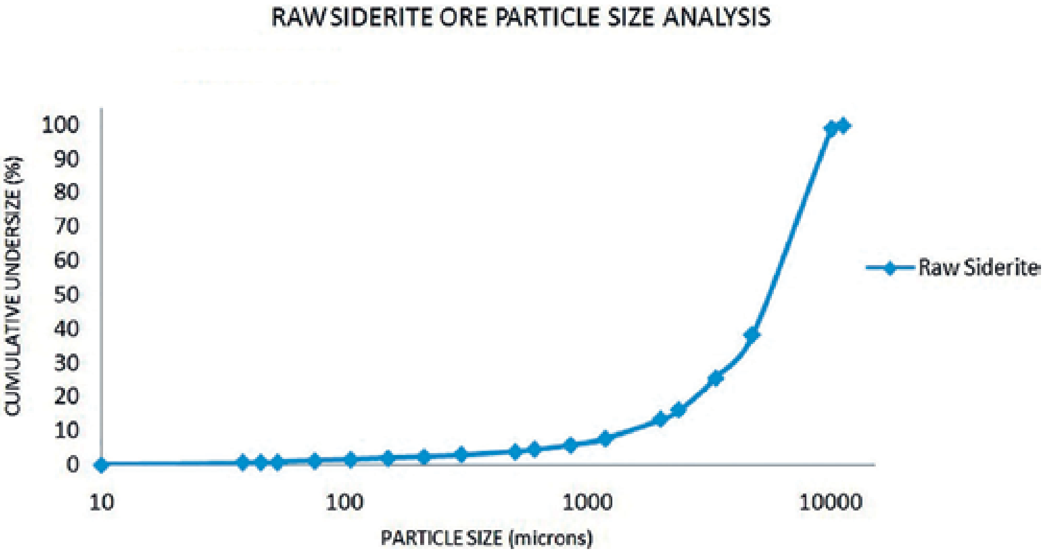

Figure 7. Cumulative undersize graph of raw siderite.

Grinding operation was done by a laboratory-type ball mill not only to examine the grindability properties of the siderite ore but also to produce fine fractions required for pelletizing. **Figure 9** shows the undersize graphs of raw siderite ore grounded at different times.

As milling media, four different sizes of balls were charged with diameters of 20, 25, 30 and 40 mm and milling parameters are given in **Table 6**.

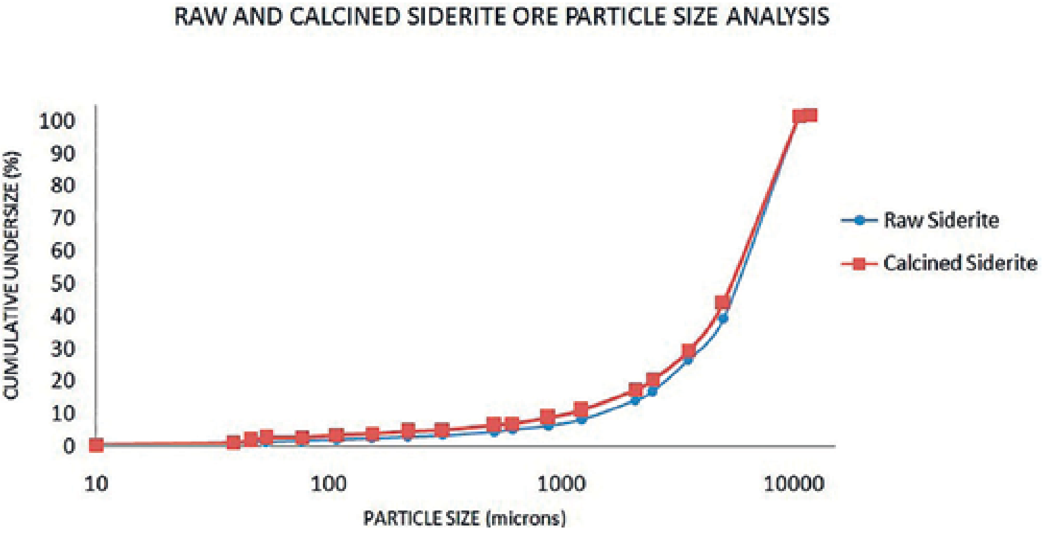

Figure 8. Comparison of raw and calcined siderite cumulative undersize graphs.

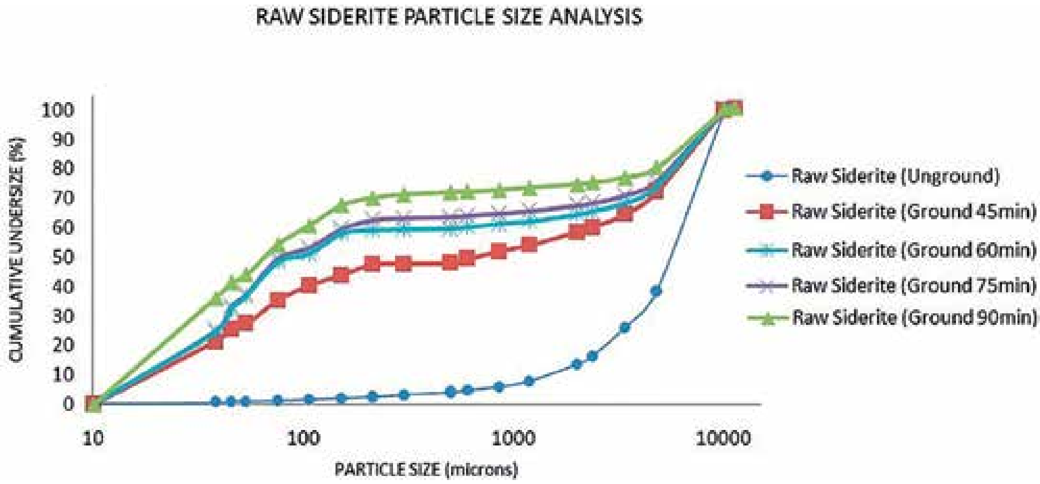

Figure 9. Cumulative undersize graphs of raw siderite ore that milled at different times.

The raw siderite was also calcined and then subjected to grinding. The cumulative undersize curves of calcined siderite ore are given in **Figure 10**.

Aforementioned, the cracking occurs in the siderite structure due to CO_2 escaping from its body during the calcination process. A similar situation is also in the grinding process. The calcined siderite was ground much easier than raw siderite when the raw and calcined siderite were grounded at the same conditions (90 min) as shown in **Figure 11**.

As can be seen from the above graph, the size fraction of both raw siderite and calcined siderite is quite different with each other after the same milling operation. In the graph, the size of d_{50} grain for the raw siderite is 66 μm while calcined siderite for d_{50} is found as 54 μm. Although there are minor differences in the small size fraction, the raw and the calcined siderite are not noteworthy in scale. However, it is not possible to mention about fractions of large grain size from the same situation. The value of P_{80} for the raw siderite is 4.75 mm while for the calcined siderite this value is 110 μm. P_{80} value of the calcined siderite is about 43 times smaller than that of the raw siderite. Thus, the grinding effect of the calcination process increases as the size increases. Moreover, calcined siderite has reached these grinding values with a feed of 40% higher than the raw siderite volume.

Ball diameter (mm)	Ball mass (g)	Charge (piece)	Real and bulk density (g/cm³)	Ball charge ratio (% volume)	Feed (g)	Feed ratio (% volume)	Calcined siderite feed (% volume)
20	32.78	30	7.82–4.57	32	3000	20	28
25	64.00	20					
30	110.70	20					
40	262.34	17					

Table 6. Grinding parameters.

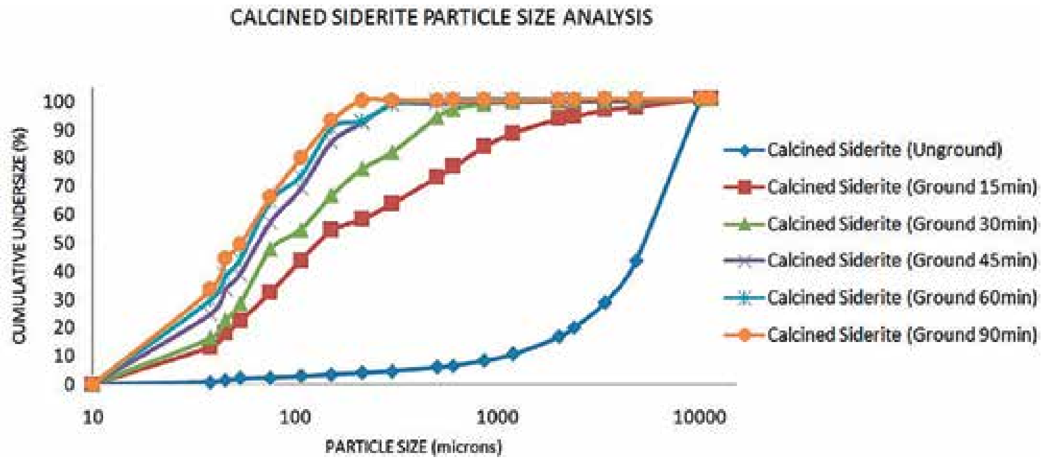

Figure 10. Cumulative undersize graphs of calcined siderite ore, which were milled at different times.

Minimizing the size of raw materials such as ores and rocks also seriously damages the machinery and milling equipments, as well as the enormous energy consumption. Today, about 40% of the energy consumed in mining operations is spent for size reduction. It takes 3.3% of the total electricity energy consumed in the world. This demonstrates the importance of energy efficiency in size reduction processes [10, 16].

In this respect, the production of the fine material required for the production of the pellet should be done after the calcination step. In this way it will be possible to save a great deal of energy and extend the life of grinding machines. This is only one of the advantages to be achieved as a result of making changes in the pellet production process.

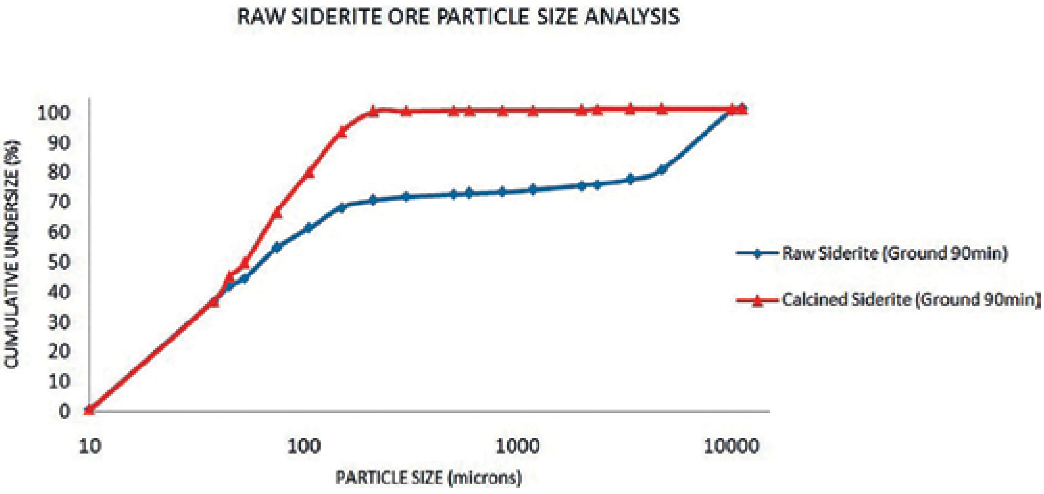

Figure 11. Cumulative undersize graphs of raw and calcined siderite at equidistant times.

3.2. Calcination experiments

Thermogravimetric analysis (TGA) was used to determine the weight loss of raw siderite exposed to temperature and the result is given in **Figure 12**. Calcination experiments of siderite ore were carried at temperatures of 465-500-550-600-650-700-750-800°C. In these experiments; the effects of two different sizes, large (−14 + 4.35 mm) and small (−300 μm), calcination temperatures and duration time on the calcination yields were investigated.

The optimum calcination temperature was determined as 700°C based on the calcination experiments and the TGA graph (**Figure 12**). The weight loss depending on the duration time at 700°C is given in **Figure 13**. In the same graph, the effects of size were also investigated.

In the calcination experiments, weight loss of the siderite ore was found to be 31.01 wt%. According to above graphs, it was found that the CO_2 in the siderite was completely removed from the body in terms of weight loss (calcination loss: 31.04%) at the temperature of 700°C and for 15 min and these calcination conditions were selected as a reference conditions and applied in subsequent experiments. No remarkable difference was recorded for the weight loss and magnetic susceptibility balance (**Table 7**) after 15 min at 700°C. It is therefore unnecessary to keep the calcination time longer than 15 min.

Also at this point it was found that the material grain size had no effect on the calcination process (except when it has a heat capacity that is too high to slow the heat transfer too much). The large particle size is also advantageous because it easily provides a comfortable circulation of hot air flow.

Calcination experiments were also carried out in a microwave oven. Microwave oven application offers great advantages especially for short heating and calcination time [17]. In microwave

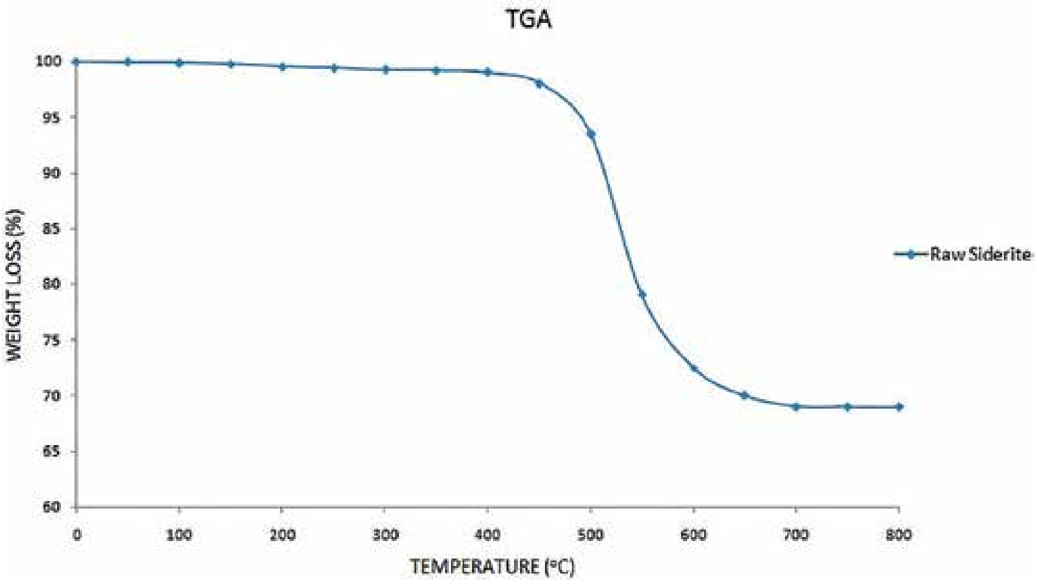

Figure 12. Thermogravimetric analysis (TGA) of siderite ore.

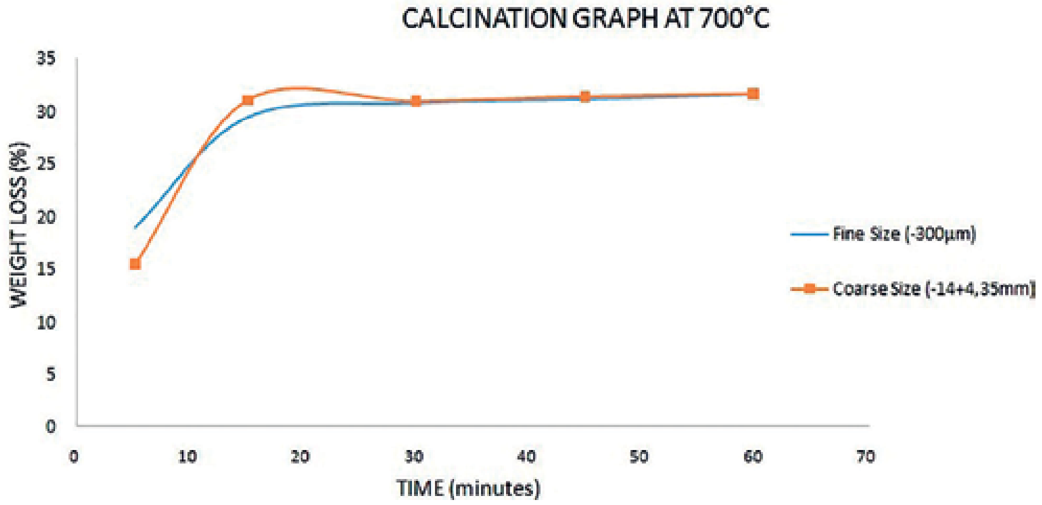

Figure 13. Calcination graph of raw siderite ore at 700°C.

heating method, 32.14% weight loss of the siderite was detected. In microwave calcination operation, the siderite ore was mixed with the sucrose (30 wt% by weight of siderite) and the mixture was put into the microwave oven. After 3 min, the temperature of the mixture was detected as 1100°C. In the microwave heating method, sucrose was used as thermal auxiliary to heat siderite ore. The calcination results, showing the weight loss versus time, of the electrical furnace and the microwave furnace are given in **Figure 14**. Apart from the partial reduction in the magnetic susceptibility balance, the microwave oven has no disadvantages over the electrical furnace. On the contrary, higher weight loss was achieved.

Calcination procedures which were carried out using the electrical furnace and the microwave oven were achieved. The results showed that necessary weight losses and high iron content in the calcined samples were obtained and the calcination process in electrical furnace and microwave oven caused the hematite transformation which was provided the magnetic properties. The chemical structure of the raw siderite and the calcined siderite in the electrical furnace and the microwave oven were checked using Rigaku Miniflex 600 XRD (Cu Kα (40 kV, 15 mA, λ: 1.54051 Å). Comparison of the XRD patterns (**Figure 15**) showed that by addition of sucrose the siderite can be calcined by using microwave oven in 3 min.

Sample no	Calcination temperature (°C)	Magnetic susceptibility (×10^{-8} m^3/kg)
1	465	1708.16
2	500	17690.50
3	600	19780.03
4	700	19530.93
5	1100 (microwave method)	15410.03

Table 7. Magnetic susceptibility balance values.

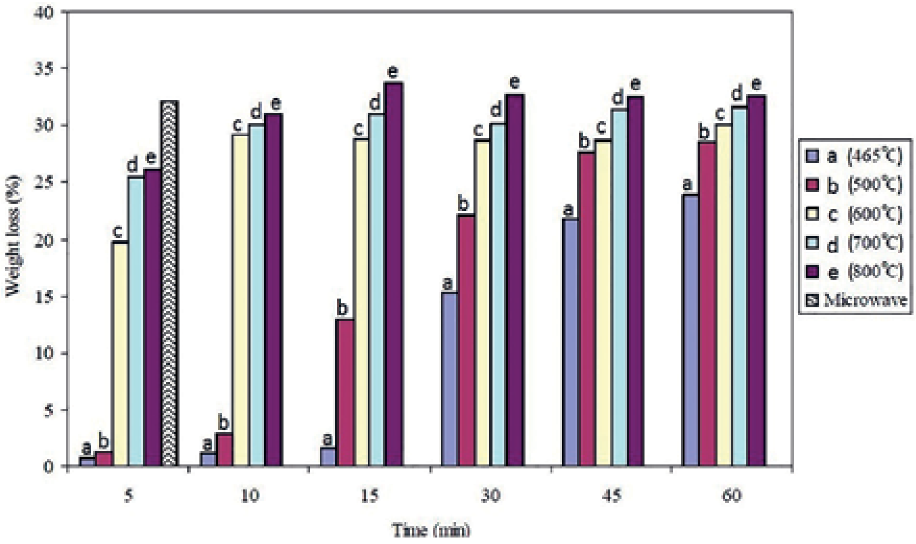

Figure 14. The weight loss versus time obtained from the electrical furnace and the microwave oven.

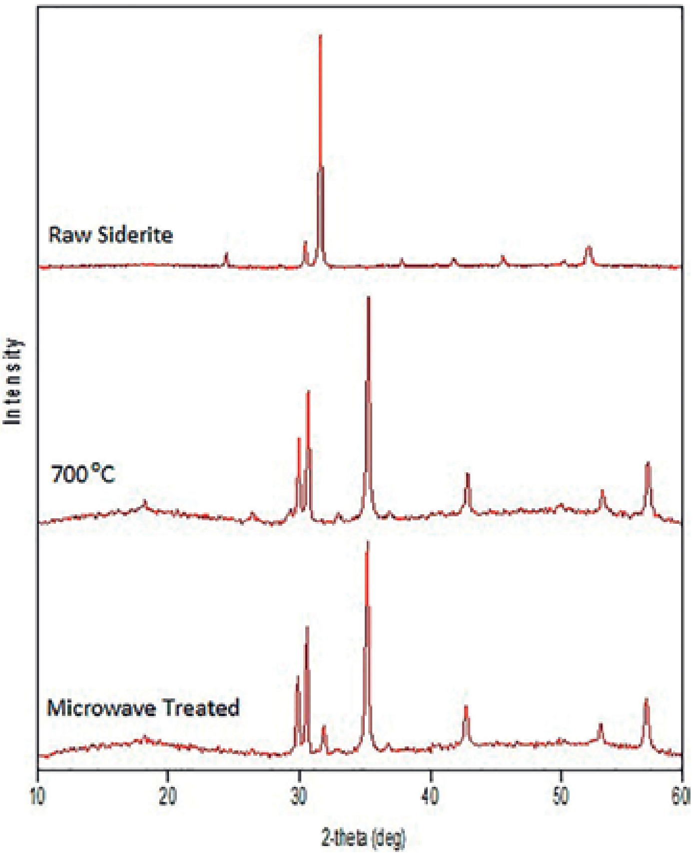

Figure 15. XRD patterns of the raw and the calcined siderite.

3.3. Pelletizing experiments

The green pellets were obtained by pelletizing machine which has a disc diameter of 60 cm and an angle of 50° and operated at a speed of 20 rpm. Pellets were produced by adding bentonite in proportions of 8, 10, 12% by weight into the raw and calcined ore. The mixture conditions are given in **Table 8**. The best pellet strength results were obtained for the calcined siderite sample with 10% bentonite addition which had been subjected to 90 min in mill.

Figure 16 indicates the raw pellets which were obtained from the raw and calcined siderite.

Examples of product pellets which were obtained using the electrical chamber furnace are given in **Figure 17**. After heating process, there was no visual difference observed between the pellets made with the raw siderite and the calcined siderite.

The SEM images belonging to the pellets obtained by mixing the siderite and 10 wt% bentonite are given in **Figure 18**. Trigonal crystals were observed in the SEM images, indicating the recrystallized hematite minerals. It can be said that the pellet heating process is performed at the proper temperature.

The resulting product pellets were subjected to a compressive strength test at a constant loading rate of 10 mm/min according to ISO/TC 102/SC 3 ISO 4700: 2015 coded standards of the International Organization for Standardization. The data obtained in the test result are presented in **Table 9**. According to the results, the pellets with the highest compressive strength obtained from the raw material added with 10% bentonite and milled for 90 min after being calcined.

The compressive strengths of the obtained pellets are shown on the graph in **Figure 19**. As it can be seen in the graph pellets obtained from calcined ores have more strength than that obtained from uncalcined ore. The improvements in the milling parameters of the calcined

Sample type	Clay ratio (%)
Raw siderite (90 min milling)	8
	10
	12
The calcined siderite (60 minutes milling)	8
	10
	12
The calcined siderite (90 minutes milling)	8
	9
	10
	11
	12

Table 8. Raw materials and clay rates used in pelletizing.

Figure 16. The pellets obtained from the raw and calcined siderite.

siderite ore was further reduced the size distribution in the raw material, making it possible to do more durable pellets. The smaller the size distribution in a raw material, the more resistant the pellets to be obtained from it [18].

The most basic way to increase the specific surface area is milling operation. In the previous sections, we have mentioned that grinding is not a very economical process in terms of both machine-equipment and energy costs, and that work should be done in large grain sizes as possible. For this reason, in order to investigate the possibility of using large grain size materials for pellet production, an urea (30% by weight) was added into the raw siderite with the size of the −150 + 75 μm, which cannot be pelletized by conventional methods. The mixture was put into the microwave oven with a frequency of 900 W for 5 min. The photo of the pellets is given in **Figure 20**.

The pellets which were obtained by this method had very high porosity. It is very advantageous to use large-sized material as pellet raw material. For example, with the aid of a sieve to be used after grinding, the product can be divided into two different fractions. The small size fractions may be fed to the conventional pelletizing plant and the large size may be fed into the microwave pelletizing plant.

Figure 17. The products pellets.

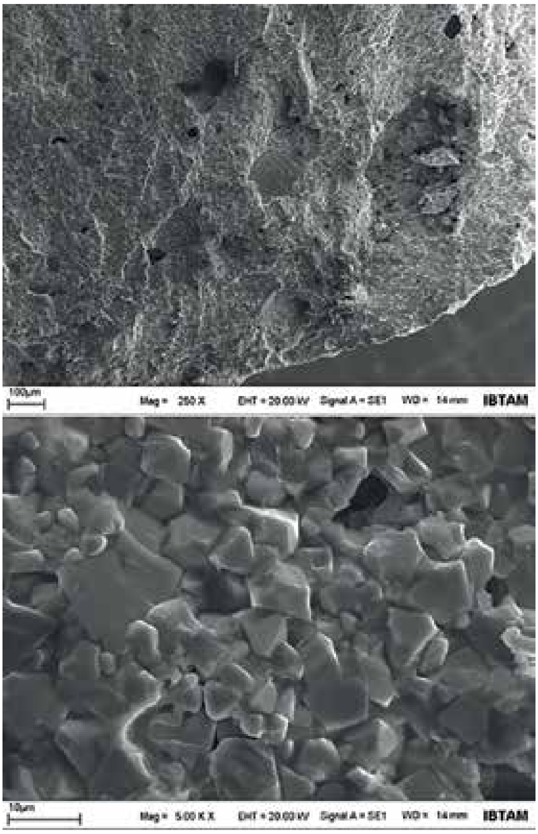

Figure 18. SEM images of the pellets.

Sample type and grinding time	Clay ratio (%)	Density (g/cm³)	Pellet diameter (mm)				
			9	10	11	12	13
			Compressive strength (kgf)				
Raw siderite 90 min	8	4.05	129	146	153	179	199
	10	3.77	155	164	179	191	211
	12	3.52	139	152	160	167	200
Calcined siderite 60 min	8	4.38	139	147	156	168	189
	10	4.28	159	162	166	176	205
	12	4.06	149	154	165	182	213
Calcined siderite 90 min	8	3.86	155	159	164	169	198
	9	3.84	174	190	192	200	207
	10	3.84	199	215	225	232	268
	11	3.81	149	183	205	230	258
	12	3.75	142	144	146	156	171

Table 9. Pellet compression strengths according to pellet diameters and clay rate.

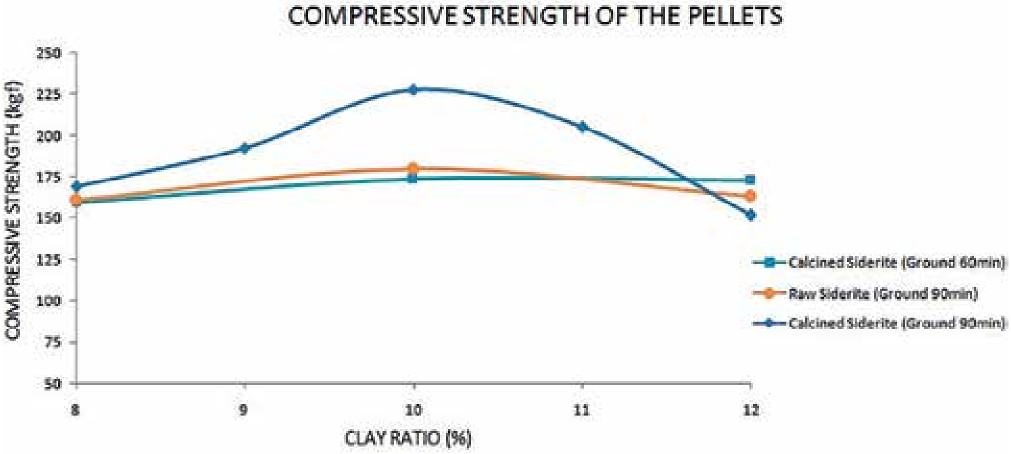

Figure 19. The effects of the bentonite ratio on the compressive strength of the pellets.

Figure 20. 30% by weight urea-added pellet obtained by microwave irradiation.

4. Conclusions

The raw siderite samples from the Hekimhan/Deveci region were subjected to calcination treatments at different temperatures (465, 500, 550, 600, 650, 700, 750, 800°C) for various duration time (5, 10, 15, 30, 45, 60 min) using the electrical furnace. Both the results of the experiments and the thermogravimetric analysis (TGA) showed that the most suitable calcination process was decided as 700°C for 15 min. The raw siderite (45, 60, 75, 90 min) and siderite calcined at 700°C (15, 30, 45, 60, 90 min) were milled. Significant behavioural differences between the two materials were identified. Calcination makes the grinding process much easier. The raw pellets were prepared by adding different bentonite ratios (8, 9, 10, 11, 12%) to the raw siderite and the calcined siderite which were milled for 90 and 60 min, respectively. The raw pellets were heated at a temperature of 1300°C which is the recrystallization temperature of hematite. Recrystallization was confirmed by SEM images and the process was confirmed to be successful. The product pellets were tested for compressive strength. The highest level of pellet strength was determined from the material obtained by grinding calcined siderite for 90 min. This pellet, which has a maximum strength value of 268 kgf, has an average durability of 28% higher than the pellet made of the raw siderite.

The results obtained in this study are listed below:

1. Calcination treatment caused big difference in the grinding behaviours of the ore. It has been found that the milling of the ore after calcination is much easier than the raw siderite.
2. The 31.01% weight loss material that was obtained from the calcination process with the conventional heating method will have great benefits from cost of transportation both in the plant and outside of the plant.
3. It has been determined that the most suitable calcination process for siderite ore is to be carried out at 700°C for 15 min.
4. The calcination process increased the Fe content from 37.25 to 55.61%.
5. The raw siderite was treated by microwave radiation (P: 900 W, f: 2.45 GHz) but neither heating nor weight loss was detected.
6. The addition of the 30 wt% sucrose into the raw siderite before the irradiation of microwave increased the temperature up to 1100°C in a 3 min. The XRD result showed that the calcination was successfully accomplished in 3 min by microwave. However, in terms of magnetic susceptibility balance, microwave-derived calcined siderite has lower values of about 23% than the conventional method.
7. Pellets obtained from calcined ores have more strength than that obtained from uncalcined ore. The highest compressive strength was obtained with addition of 10% bentonite and ground for 90 min. The highest compressive strength of this pellet is determined as 268 kgf. This pellet is about 28% more durable than the others.
8. As it is known, the strength of the pellets, which are blast furnace charging materials, determines the charge amount of the furnaces. The material charge to the blast furnaces is such that the pellets at the bottom end are not broken. More durable pellets were obtained in the present study.
9. Pellets with the addition of 30 wt% urea admixture into the coarse size of −150 + 75 μm the siderite ore were obtained using microwave. This method is promising in terms of the reducing the grinding costs.

Acknowledgements

This research was supported by Inonu University with the project numbers of 2015/54 and 2016/120.

Author details

Mehmet Celikdemir[1]*, Musa Sarikaya[1], Tolga Depci[2], Ramazan Aydogmus[1] and Aysegul Yucel[1]

*Address all correspondence to: celikdemirmehmet@gmail.com

1 Inonu University, Malatya, Turkey

2 Iskenderun Technical University, Hatay, Turkey

References

[1] TOBB. Turkiye Demir ve Demir Disi Metaller Meclisi Sektor Raporu [Internet]. 2014 [Updated: 2014]. Available from: https://www.tobb.org.tr/Documents/yayinlar/2014/Demir%20ve%20Demir%20D%C4%B1%C5%9F%C4%B1%20Rapor%20web.pdf [Accessed: 9 September 2017]

[2] T.C. Dogu Akdeniz Kalkinma Ajansi. Demir Celik Sektor Raporu [Internet]. 2014 [Updated: 2014]. Available from: http://www.dogaka.gov.tr/Icerik/Dosya/www.dogaka.gov.tr_523_TN1D55SP_Demir-celik-Sektor-Raporu-2014.pdf [Accessed: 9 September 2017]

[3] World Steel Association Economics Committee. World Steel Statistical Yearbook 2016 [Internet]. 2016 [Updated: 2016]. Available from: https://www.worldsteel.org/en/dam/jcr:37ad1117-fefc-4df3-b84f-6295478ae460/Steel+Statistical+Yearbook+2016.pdf [Accessed: 9 September 2017]

[4] United State Geological Survey (USGS). Mineral Commodity Summaries 2017 [Internet]. 2017 [Updated: 2017]. Available from: https://minerals.usgs.gov/minerals/pubs/mcs/2017/mcs2017.pdf [Accessed: 5 October 2017]

[5] Anonymous. Rocks [Internet]. 2017 [Updated: 2017]. Available from: http://www.rocksrock.com.au/wp-content/uploads/2017/02/IMG_0008.jpg [Accessed: 5 September 2017]

[6] Toraman OY, Depci T. Komurde Mikrodalga ile Onislem Uygulamalari. Madencilik. 2007;**46**:43-53

[7] Jones DA, Lelyveld TP, Mavrofidis SD, Kingman SW, Miles NM. Microwave heating applications in environmental engineering—A review. Resources, Conservation and Recycling. 2002;**34**:75-90

[8] Kingman SW, Rowson NA. The effect of microwave radiation on the magnetic properties of minerals. Journal of Microwave Power and Electromagnetic Energy. 2000;**35**:144-150

[9] Anonymous. Microwave heating [Internet]. 2017 [Updated: 2017]. Available from: https://wiki.anton-paar.com/wp-content/uploads/05_microwave-heat-introduction.jpg [Accessed: 5 October 2017]

[10] Eskibalci MF. Investigating of conventional and microwave heat effect on grindability of quarsite. Erzincan University Journal of Science and Technology. 2014;**7**(2):169-190. DOI: 10.18185/eufbed.38561

[11] Mohammed OA, Shalabi MEH, El-Husiny NA, Khedar MH, Mostafa F. The role of normal and activated bentonite on the pelletization of barite iron ore concentrate and the quality of pellets. Powder Technology. 2003;**130**(1-3):277-282. DOI: 10.1016/S0032-5910(02)00205-X

[12] United State Geological Survey. 2011 Mineral Yearbook [Internet]. 2013 [Updated: 2013]. Available from: https://minerals.usgs.gov/minerals/pubs/commodity/iron_ore/myb1-2011-feore.pdf [Accessed: 9 October 2017]

[13] Yildiz N. Demir Cevherinin Peletlenmesi. Madencilik. 2014;**29**:88-92

[14] European Commission. Best Available Techniques (BAT) Reference Document Iron and Steel Productions [Internet]. 2010 [Updated: 2010]. Available from: http://eippcb.jrc.ec.europa.eu/reference/BREF/I&S/IS_Published_0312.pdf [Accessed: 11 October 2017]

[15] Cosar S. Demir Konsantrelerinin Peletlenmesinde Bor Minerallerin ve Atiklarinin Kullaniminin Arastirilmasi [thesis]. Istanbul: Istanbul Technical University; 2006. 93p. Available from: https://polen.itu.edu.tr/bitstream/11527/8396/1/4352.pdf

[16] United States Department of Energy. Mining industry energy bandwidth study [Internet]. 2007 [Updated: 2008]. Available from: https://www1.eere.energy.gov/manufacturing/resources/mining/pdfs/mining_bandwidth.pdf [Accessed: 5 October 2017]

[17] Celikdemir M, Sarikaya M, Depci T, Aydogmus R. Influence of microwave heating and thermal auxiliary on decomposition of siderite. IOP Conference Series: Earth and Environmental Science. 2016;**44**:052002

[18] Sevinc N, Tosun Y. Hekimhan Siderit Demir Cevheri Tozundan Pelet Uretilmesi. In: 5. Metalurji Kongresi, TMMOB Metalurji Muhendisleri Odasi, Ankara, Turkiye, November 21-25, 1988. pp. 302-325

Chapter 6

Mechanism and Prevention of Agglomeration/ Defluidization during Fluidized-Bed Reduction of Iron Ore

Yiwei Zhong, Jintao Gao, Zhancheng Guo and
Zhi Wang

Additional information is available at the end of the chapter

http://dx.doi.org/10.5772/intechopen.68488

Abstract

The mechanisms of agglomeration and defluidization and fluidization characteristic of iron oxide particles were investigated based on the theory of surface diffusion, interface reaction, surface nano/microeffect, and phase transformation. Moreover, a mathematical model was developed to predict the high-temperature defluidization behavior by the force-balance and plastic-viscous flow mechanism, and the fluidization phase diagram was obtained. On these bases, a control method of defluidization and its inhibition mechanism were proposed. As a result, the theoretical system of agglomeration/defluidization in the gas-solid fluidization was developed, and thus afforded theory support and technological bases for the solution of defluidization in industrial fluidized-bed reactors.

Keywords: fluidized-bed reduction, iron ore, agglomeration, defluidization, prevention, model

1. Introduction

Fluidized-bed reactors can improve the reaction kinetics and realize better utilization of resource/energy and lower pollutant emissions [1]. Therefore, as a trend in the industrial application, fluidized beds are ideally suited to the processing of these finely sized raw materials and have great competitiveness. However, fluidized beds were tested but failed because of the serious problem of particles agglomeration and subsequent defluidization [2]. The continuous operation and high productivity was often limited by partial or complete defluidization. It is, therefore, a critical problem to solve defluidization and particle agglomeration at high temperatures for the application of fluidized beds.

Particle agglomeration in fluidized-bed systems has received considerable attention due to its close association with industrial processes. Gluckman [3] indicated that the generation of agglomerations depended on the cohesiveness of particles collisions. Seville and coworkers [4, 5] pointed that the defluidization phenomenon was attributed to an increased rate of sintering at elevated temperatures, and the tendency of particle to agglomerate depended strongly on their physical and chemical characteristics at high temperature. Two types of adhesion are considered [4–7]: (1) Visco materials cause sintering on glassy materials. Increasing the operating temperature can reduce the viscosity of the materials and cause a larger adhesive force. (2) Melting and chemical reaction produces liquid-phase materials. These liquid-phase materials can form a bridge between two particles and cause agglomeration and defluidization.

In the case of fluidized-bed reduction of iron ore, earlier works [8–10] indicated that sticking occurred mostly during metallization of ore. The defluidization tended to be preferred at a high fractional reduction and metallization degree. Some ore particles were precipitated by the metal iron with the fibrous shape on the particle surface. The sticking was initiated by the contact of the needles that hooked mechanically the particles together. Moreover, the work of Gransden et al. [9, 10] showed that the sticking was associated with the iron-iron contact regardless of formation of iron whiskers or not. They believed that the fresh precipitated iron had a high activity or surface energy, and thus appeared high adhesion energy to agglomeration. Zhong et al. [11] also reported agglomerates formed due to sintering of reduced iron, and nano/mircostructure on the particle surface had a promotive effect on particle agglomeration. Therefore, the sticking tendency depended strongly on iron precipitation of particles. With respect to adhesion of metallic iron, a sintering mechanism of iron particles has been reported involving the relationship between the bed temperature and the minimum gas fluidizing velocity required to prevent defluidization [12, 13]. However, most research studies focused on the metallic iron content and morphologies at the defluidization point [2, 8–11] and thus did not involve the evolution of particle properties during metallization. In the gas-solid reaction, new components were produced and thus caused the changes in surface structure and the particle properties. Therefore, the new phase formation can significantly affect the particle cohesiveness.

2. Mechanism of agglomeration and defluidization of iron/iron oxide particles

2.1. Effect of metallization degree on agglomeration tendency

The fluidized-bed apparatus is shown in **Figure 1**, which is a bubbling fluidized bed consisting of a transparent silica tube with an inner diameter of 2.5 cm. The reactor is heated by a transparent electric resistance, and the fluidization state in the reactor can be observed at high temperature. Bed temperature is measured and controlled by a PID controller connected with a K-typed thermocouple. The gas flow rate and pressure drop across the bed is measured by a digital mass flow meter and a pressure transmitter, respectively. The pressure sensor is located at 1 cm below the gas distributor.

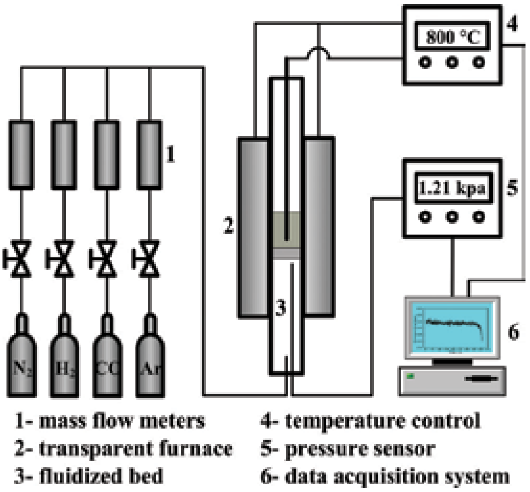

Figure 1. Schematic diagram of fluidized-bed apparatus.

To determine the evolution of the real-time bed agglomeration tendencies and agglomeration potential, the controlled bed defluidization tests (CBD) were carried out, which were adapted from Öhman [14, 15]. Each experiment with a 5 g of iron oxide was started by a normal fluidized-bed reduction by CO at 700°C (1.0 NL/min, about 12.2 cm/s) to obtain a series of reduced samples with different metallization degrees (M_{Fe}). Preliminary reduction experiments indicated that when M_{Fe} was higher than 25%, the bed agglomeration would appear. Thus, M_{Fe} of all the reduced samples was controlled below 25%. And then at a point where a designated metallization degree was achieved by controlling the reducing time, the reduction was stopped and the fluidizing gas was switched to N_2 atmosphere (1.0 NL/min, about 12.2 cm/s). Then, the bed was heated up at a rate of 3°C/min until a bed agglomeration was achieved. The bed defluidization temperature, T_{def}, was determined by online analysis of the variations in the measured bed temperatures and differential pressures and was used to characterize bed agglomeration tendency at various metallization degrees. Defluidization is defined as any condition where a well-fluidized bed loses fluidization, whether partial or total [16]. A typical illustration of fluctuations in temperatures and differential bed pressures versus time in a controlled bed defluidization test is shown in **Figure 2**. Meanwhile, the controlled bed defluidization tests can also be carried out as a series of interrupted experiments to investigate the evolution of particles in the course of metallization.

The real-time agglomeration tendency of the reduced samples represented by the defluidization temperature T_{def} was obtained by the controlled bed defluidization tests. As shown in **Figure 3**, the defluidization temperature decreases with the increase of the metallization degree, indicating an increase of agglomeration tendency. The analysis of XRD (X-ray diffraction) shows that all the reduced samples in the controlled defluidization tests only contain metallic iron and FeO (**Figure 4**). The diffraction peaks of metallic iron obviously strengthened with increasing reduction time, indicating the content of precipitated iron increased. Therefore, the agglomeration tendency depended strongly on the metallic iron content. At the metallization degree

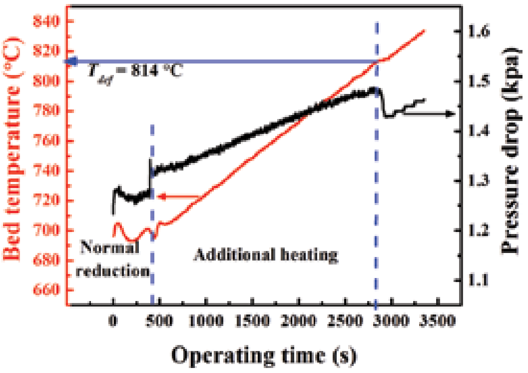

Figure 2. Illustration of a typical controlled defluidization test for Fe_2O_3 reduction.

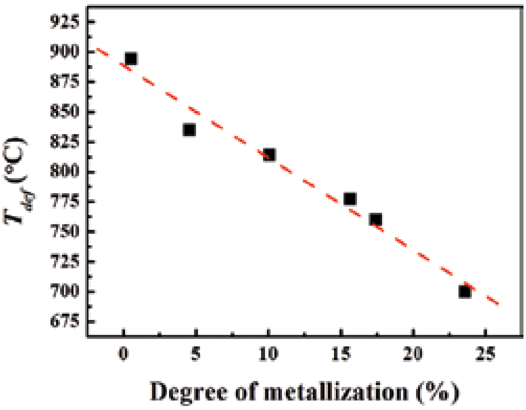

Figure 3. Influence of metallization degree on the defluidization temperature in the controlled defluidization tests.

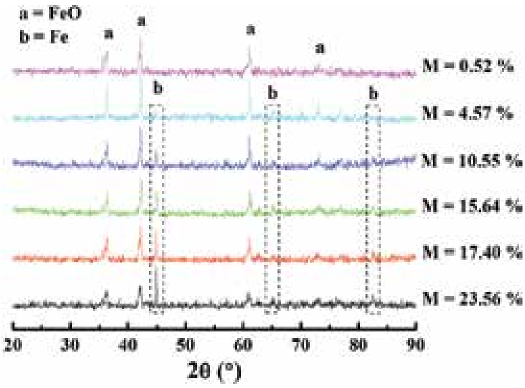

Figure 4. X-ray patterns of each sample from the controlled bed defluidization tests.

below 0.52%, no indication of defluidization is observed. This was because that the particle with lower amount of precipitated iron did not have enough adhesion force to form agglomerates and thus maintained a good quality of fluidization. When the metallization degree reached to 23.56%, the defluidization approached, indicating the defluidization was accompanied with the accumulation of precipitated iron. This result suggested that large quantities of metallic iron can increase the stickiness of particles by providing enough contact area of iron. This conclusion was in accord with that found by Gransden et al. [9, 10], who indicated that the agglomeration was caused by the iron-iron contact. Therefore, the reduced Fe_2O_3 particle with a higher metallization degree had a larger agglomeration tendency.

Typical morphologies of reduced samples at various metallization degrees are shown in **Figure 5**. At lower metallization degree (i.e., <4.57%), numerous pits are formed on the oxide surface prior to iron nucleation, and the morphology presents smooth. But at higher metallization degree (i.e., >15.64%), the iron nuclei tend to appear (about 0.1−0.15 μm in a diameter), forming microconvexities on the surface. These iron nuclei with nano/microsize were prone to soften and sinter together due to a higher surface energy [11]. Thus, the reduced particles with a higher metallization degree had a stronger adhesive force for agglomeration. On the other hand, the particle surface becomes rough due to the formation of iron nuclei. Such rough surface caused the enhancement of friction force among bed particles to result in a poor fluidization quality.

2.2. Effect of iron precipitation on particle cohesiveness

To investigate the evaluation of particle cohesiveness responsible for agglomeration, the thermomechanical analysis (TMA) was carried out by a dilatometer (NETZSCH-DIL402C,

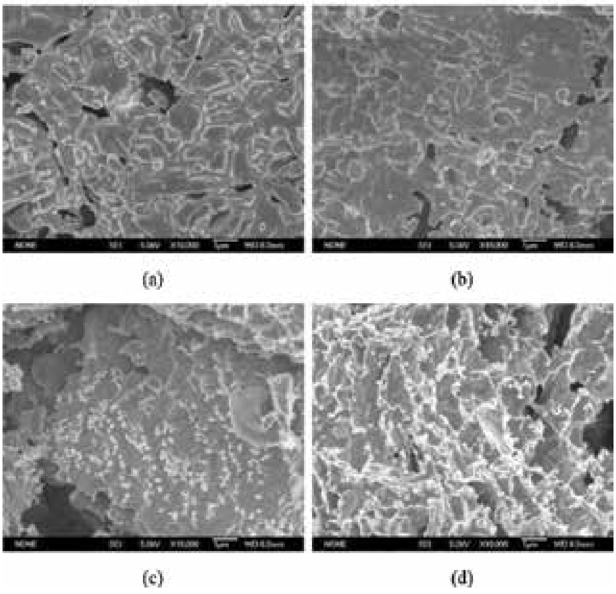

Figure 5. Evolution of surface morphology of Fe_2O_3 particles in the controlled defluidization tests: (a) M_{Fe} = 0.52%; (b) M_{Fe} = 4.57%; (c) M_{Fe} = 15.64%; and (d) M_{Fe} = 23.56%.

Germany). The thermal expansion or contraction was measured to obtain the temperature at which sintering and surface softening became significant. The sample was heated up to 800°C at a rate of 10°C/min. The sample was in a flow of 50 ml/min of pure Ar, and the load on it was 30 cN.

The samples from the controlled bed defluidization tests were examined. The greatest change in $\Delta L/\Delta L_0$ gradient occurs for each curve is a measure of the minimum sintering temperature (T_s) [4, 5]. As shown in **Figure 6(a)**, the sample with a higher metallization degree has a lower value of T_s. This result showed that iron precipitation reduced significantly the minimum sintering temperature of the whole particle and thus enhanced the sintering activity of the reduced particle. The sintering rate depended on the diffusion coefficient (D_s) of materials. The value of D_s for α-iron self-diffusion was calculated to be approximately 10 times larger than that for the diffusion of Fe in FeO at 800°C according to the empirical correlations [17, 18]. This indicated that metallic iron had a higher sintering activity than FeO. Therefore, the tendency of the reduced particles to sinter together was intensified due to iron precipitation.

Many investigations showed the importance of the initial sintering temperature in fluidization quality [4, 5], because it is an indicator of the onset of agglomeration and is a softening point where the rate of sintering dramatically accelerated. Previous research studies [4, 5] have confirmed that the cohesiveness and sintering of the fluidized particles can lead to the uncontrolled particle agglomeration and subsequent defluidization at temperatures at or above the sintering point. A special class of agglomeration was due to the formation of new species on the surface of the solid particle during a chemical reaction. At temperatures well below the softening (sintering) points of both the reactants and the products, particle agglomeration can occur during the process of product formation [19]. Accordingly, in the case of reduction Fe_2O_3 to Fe, when metallic iron formed above sintering temperature, the adhesive force due to sintering was increased. Therefore, the sintering of metallic iron on the surface provided favorable conditions for agglomeration.

At the minimum sintering temperature (T_s), the surface of material began to soften and deform, and the surface stickiness began to appear [20, 21]. And the agglomeration and defluidization occurred as a result of having "sticky" bed materials. In this study, the surface viscosities of the reduced samples in the controlled bed defluidization tests at various metallization degrees were

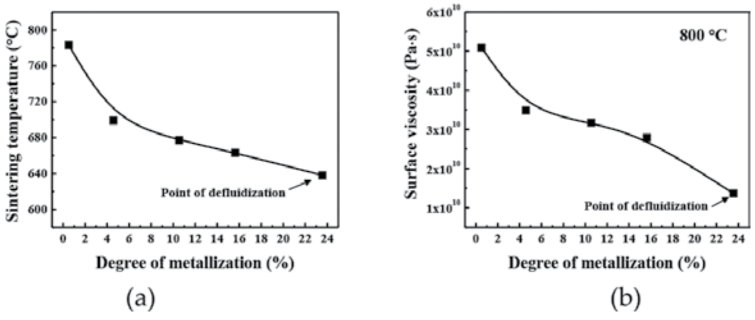

Figure 6. Influence of iron precipitation on particle cohesiveness of reduced Fe_2O_3 particles: (a) the minimum sintering temperature; (b) (the surface viscosity of Fe_2O_3 particles at 800 °C).

measured at 800°C using the thermomechanical analysis as reported by Tardos [20]. **Figure 5(b)** shows that the surface viscosities gradually decreased as the metallization degree increased. When the metallization degree approaches to 23.56% (point of defluidization), the viscosity drops significantly, indicating a strong surface softening and stickiness of particles. This result suggested that the particle adhesion of iron oxide was enhanced with the increase of the amount of metallic iron on the surface.

For crystalline materials, the Huttig temperature is defined as the temperature where the lattices and surface atoms become appreciably mobile. For pure metals, this temperature was approximately $0.3T_m$ (about 330°C for iron) [22]. It was inferred that the Fe_2O_3 particle surface preformed viscosity because of the iron precipitation when the temperature was higher than 330°C. This fresh precipitated iron had high particle cohesiveness due to the higher activity and surface energy [8–11]. In the course of Fe_2O_3 reduction, numerous Fe vacancies were formed, and iron atoms were released from the oxide lattice due to oxygen removal. Consequently, the migration of iron atoms to the reducing front through Fe vacancies was accelerated due to the chemical potential gradient of O/Fe [23]. Therefore, the particle surface softened as metallic iron precipitating, resulting in a decrease of apparent surface viscosity.

Some of the agglomerates, sampled from controlled bed defluidization tests, were examined by SEM/EDS analysis. As seen in **Figure 7**, sintered necks instead of iron whiskers were observed between particles. The reduced particles are sticked together by the sintered neck, the diameter of which was roughly 0.8 μm. The EDS analysis showed that Fe was the dominant species (97 wt.%) in the connect position. Thus, the reduced particle was connected by a connective bridge composed of metallic iron. These results proved that the presence of iron, rather than iron oxide (FeO, Fe_3O_4), caused the formation of the sticky particle surfaces readily for agglomeration. In addition, it was noted that the agglomerates contained particles only several microns in diameter between coarse particles. These fine particles played a role of "bridge" in the formation of agglomerates.

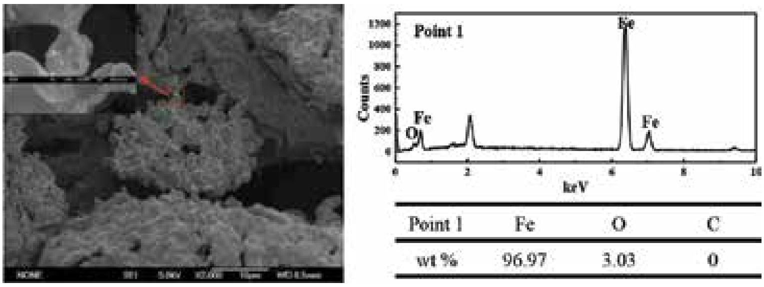

Point 1	Fe	O	C
wt %	96.97	3.03	0

Figure 7. SEM image and EDS analysis of agglomerate sample at metallization degree of 15.64%.

3. Model to predict agglomeration and defluidization

The aim of this work is modeling the high-temperature defluidization behavior of iron powders involving the effects of gas velocity and gas properties. The calculation is focused on the evolution of forces acting on particles with temperature based on the surface viscosity and bubble motion. By analyzing the experimental data with a statistical regression, a force balance model is developed to describe the defluidization processes in a fluidized bed, by which the temperature dependence of the defluidization behavior is predicted.

3.1. Modeling defluidization phenomena

3.1.1. Assumptions

The fluidization behavior of bed particles depended on the forces acting on them. Therefore, this model employed the balance of cohesive and segregate forces to simulate agglomeration/defluidization and predict the defluidization temperature. Taking account of particle moving, colliding, coalescing, and breaking in a fluidized-bed system, the following assumptions are made to describe the main characteristics of the defluidization phenomena based on the previously described experimental results:

1. Bed material particles are spherical and in uniform size.
2. The fluidizing gases do not react with the bed particles, and no coating layer form on the surface.
3. The adhesive force between two particles arises from surface viscosity and is determined by the plastic-viscous flow mechanism.
4. The force against agglomeration is the drag force acted on particles due to bubble motion.
5. If the adhesive force equals or exceeds the segregation force, the bed defluidization appears.

3.1.2. Model formulation

As the temperature increases, the effect of adhesion force becomes dominant due to surface softening, resulting in a quick defluidization. The adhesive force associated with the plastic-viscous flow mechanism can be described by:

$$F_{\mathrm{ad}} = \pi b^2 \sigma \tag{1}$$

where σ represents the tensile stress of the agglomerate and b is the radius of the connection between the particles.

According to Benson et al. [24], the tensile stress of the agglomerate is

$$\sigma = \frac{At}{\mu_s d_p} \tag{2}$$

where A is a constant; t represents the connect time of two particles; d_p is the mean size of the particle; and μ_s is the surface viscosity of the particle materials.

In a fluidized bed where particles are intermittently mixed, the contact time of particles is dependent on the bubbles motion. The residence time is required to be sufficiently long for particle connection to form agglomerates. Therefore, in this study, the connect time of two particles was considered as the characteristic residence time for which particles within a fluidized bed remain in contact with each other as reported by Seville et al. [13, 25]:

$$t = \frac{\beta}{(U_g - U_{\mathrm{mf}})} \tag{3}$$

where β is a proportional coefficient; U_g is the operating gas velocity; and U_{mf} is the minimum fluidization velocity.

The surface viscosity of solid is a function of temperature and is assumed be estimated by the Arrhenius' expression [25]:

$$\mu_s = \mu_{s0} \exp\left(\frac{E_s}{RT}\right) \tag{4}$$

where E_s is the activation energy for the surface viscosity and T the absolute temperature.

To accurately predict the segregate force, this model employs the drag force acting on particles to represent the force against agglomeration, which is related to the effect of the particle size, gas velocity, and gas properties. The expression is [26]:

$$F_d = \alpha C_d \frac{\pi}{8} d_p^2 \rho_g U_g^2 \tag{5}$$

$$C_d = \frac{24}{\mathrm{Re}}(1 + 0.173\mathrm{Re}^{0.657}) + \frac{0.413}{1 + 16300\mathrm{Re}^{-1.09}} \tag{6}$$

$$\mathrm{Re} = \frac{d_p \rho_g U_g}{\mu_g} \tag{7}$$

where α is a proportional coefficient, representing the unknown errors in this equation. C_d is the drag coefficient; Re is Reynolds number; ρ_g and μ_g are the gas density and viscosity, respectively.

If the adhesive force equals the drag force, the bed is defluidized:

$$\frac{\pi A \beta b^2}{\mu_s d_p (U_g - U_{\mathrm{mf}})} = \alpha C_d \frac{\pi}{8} d_p^2 \rho_g U_g^2 \tag{8}$$

In this work, we defined two number groups, N_a and N_d, representing the adhesion force and the drag force, respectively:

$$N_a = \frac{\pi}{\mu_s d_p (U_g - U_{\mathrm{mf}})} \tag{9}$$

$$N_d = C_d \frac{\pi}{8} d_p^2 \rho_g U_g^2 \tag{10}$$

Therefore, the defluidization criterion (Eq. (8)) can be expressed as:

$$N_a = K \cdot N_d \tag{11}$$

$$K = \frac{\alpha}{Ab^2\beta} \tag{12}$$

where K is a regressive constant, representing the unknown errors in this equation. The variables in the model are as a function of temperature, and the correlations are nonlinear. Therefore, by combining Eqs. (9)–(12), the temperature to reach defluidization was obtained by a numerical method.

3.2. Modeling results and comparison with experimental data

3.2.1. *Influence of gas velocity*

Figure 8 presents the results obtained at different gas velocities. According to the definition of defluidization criterion, the temperature corresponding to the intersection of the curves of N_a and $K{\cdot}N_d$ is the defluidization temperature. As it can be seen, the temperature to reach defluidization increases with increasing the gas velocity for all the fluidizing gases. In previous studies [27–29], the generation of agglomeration and defluidization depended on the balance of the cohesive and breaking forces. And if the adhesive force between particles exceeded the breakage force, agglomeration and defluidization in the bed probably occur. As shown in

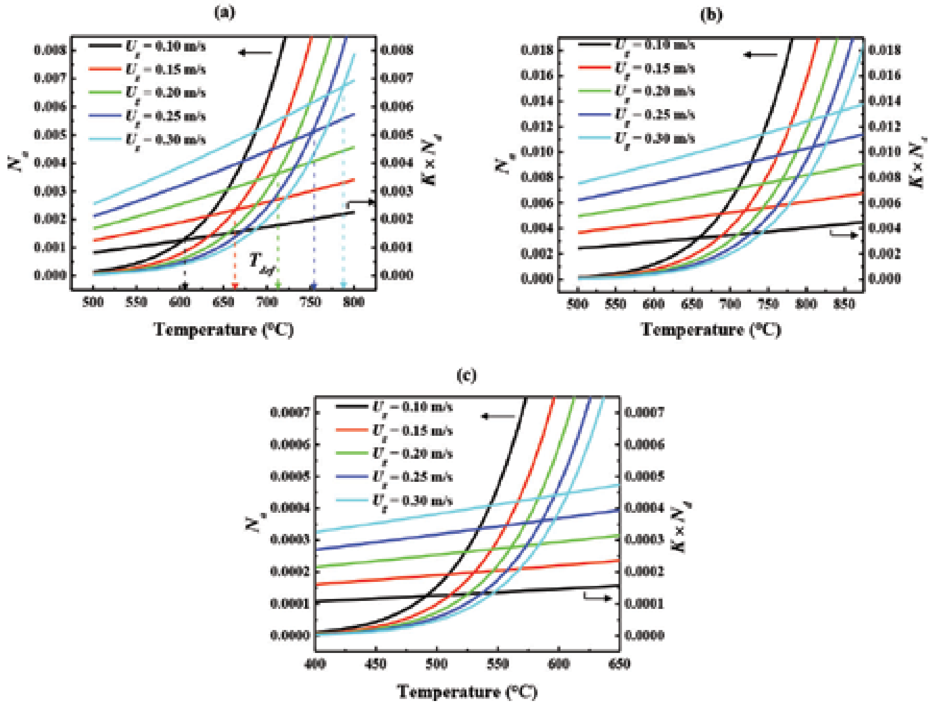

Figure 8. The variation of the calculated values of N_a and $K{\cdot}N_d$ with temperature: (a) N_2; (b) Ar; and (c) H_2.

Figure 8, at a constant fluidizing velocity, both the adhesion force and the drag force increase with increasing temperature. However, the increase of adhesion force is much more rapid than that of drag force, especially at the temperatures above the initial sintering temperature. Therefore, at a given temperature, namely, the defluidization temperature, the adhesion force begins to be greater than the drag force, and thus the defluidization appears. This explained the temperature dependence of defluidization behavior. On the other hand, as the gas velocity increases, the drag force of the particles increases, whereas the adhesion force decreases at a constant temperature. As a result, the state of fluidized particles gets out of the defluidization region because the drag force is greater than the adhesion force. Therefore, the temperature to reach defluidization is delayed by increasing the gas velocity. Comparing the calculated defluidization temperature with the experimental data in **Figure 9(a)**, both the tendencies are in a good agreement, although the calculated values are to some extent lower than the experimental ones.

3.2.2. Influence of gas properties

Figure 9(b) presents the effect of gas type on defluidization temperature. According to the calculated results, the defluidization temperature decreases when using the gas with greater viscosity and density as a fluidizing agent. As seen in **Figure 9(b)**, at a constant gas velocity the adhesion force for different gases almost has no change, whereas the drag force is strongly dependent on the gas properties and increases with increasing the gas viscosity. Comparing the three fluidizing gases, the defluidization temperatures are in the following sequence: $H_2 < N_2 < Ar$. This was because the fluidizing gas with greater viscosity can produce a stronger drag force to resist agglomeration, which was in accord with the experimental results [21].

The calculated defluidization temperatures were in a good agreement with the experimental results in all experiment conditions, and thus confirmed the predicted modeling. The model successfully described the defluidization temperature as a function of gas velocity and gas property. According to the results above, the fluidizing phase diagram was obtained as shown in **Figure 10**, which was divided into the stable fluidization and the defluidization region. The fluidization state was maintained below the curve intersection of N_a and $K{\cdot}N_d$, while the bed was defluidized above the intersection. This suggested that at a certain operating parameter,

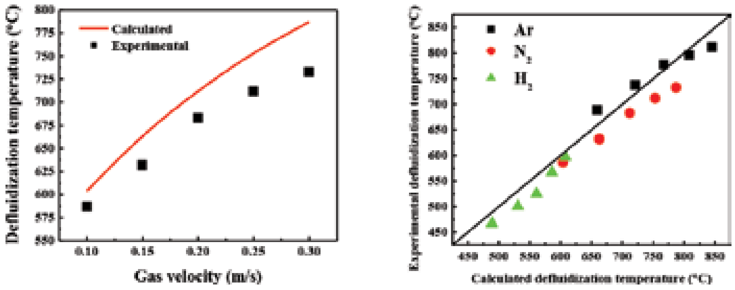

Figure 9. Comparison of calculated defluidization temperature with experimental data: (a) Influence of gas velocity; and (b) influence of gas properties.

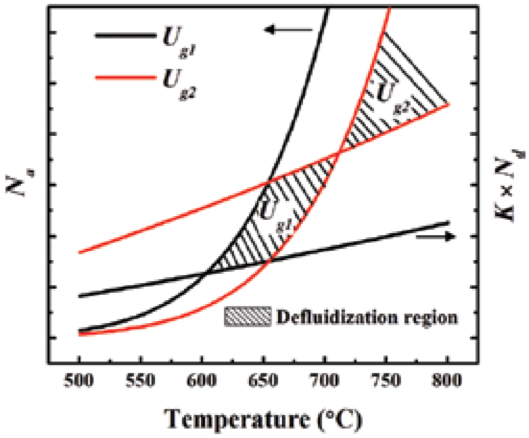

Figure 10. The fluidization phase diagram of iron powders at elevated temperatures.

there was a limiting operating temperature and gas velocity, above which the defluidization occurred. Therefore, the model can be considered as a theory reference to avoid defluidization in the actual fluidizing operations. However, the model cannot simulate the agglomeration involving chemical reaction and phase transformation. More work is needed for a comprehensive model of agglomeration in a fluidized-bed reactor.

4. Prevention of agglomeration by surface coating of Mg and Ca oxides

4.1. Effect of MgO and CaO addition on defluidization

Figure 11 shows the effects of the addition of MgO and CaO on the defluidization time of Fe_2O_3 particles at various operating temperatures. It was found that adding Mg and Ca had the similar effect on prolonging the defluidization time. As the addition content of MgO and CaO increased, the defluidization time was delayed. The defluidization time of adding MgO

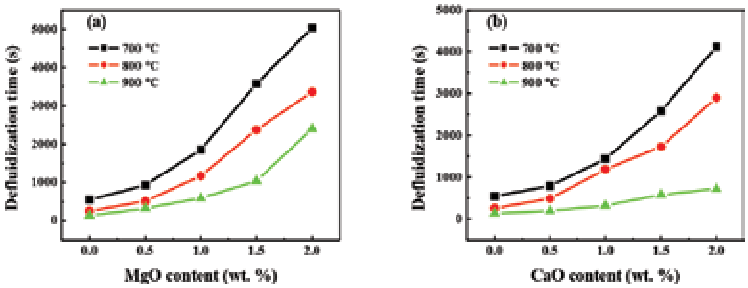

Figure 11. Influence of operating temperature on the defluidization time (50–74 μm, 36.5 cm/s): (a) adding MgO and (b) adding CaO.

are higher than that of adding CaO. It was indicated that MgO species had a better effect to reduce the bed agglomeration tendency and inhibit the defluidization.

However, previous research studies suggested that some compounds with low melting points or iron whiskers were formed by adding MgO and CaO. These compounds and iron whiskers provided a favorable condition to form agglomeration of the Fe_2O_3 particles during reduction [8, 30]. With inconsistent results as compared to those of the experiment, this work was focused on investigating the relationship between the new phase formation and particle adhesion during Fe_2O_3 reduction. It has been confirmed that agglomeration at high temperature was attributed to the activity of metallic iron [10, 21]. The surface energy of precipitated iron may be deactivated or reduced by Mg/Ca oxide, and thus the surface cohesiveness was eliminated. On the other hand, MgO and CaO may react with Fe_2O_3 to generate some eutectics with high melting points or some stable compounds hard to be reduced to metallic iron. In these conditions, the formation of liquid phase and the connection of metallic iron on the surface can be avoided at high temperature. Therefore, MgO and CaO inhibited the formation of agglomeration and delayed the defluidization time.

4.2. Behaviors of Mg and Ca species during reduction

In previous studies [31, 32], the formation of coating layer and connective bridge among the bed particles had been found based on the SEM (scanning electron microscopy)/EDS (energy dispersive spectrometry) analysis. However, in the case of no liquid phases, the physicochemical behavior of Mg/Ca species on the surface and their effects on the bed particles has not been determined yet. Therefore, the focus was the role of Mg and Ca species in the formation of the coating layer. The surfaces of bed particle samples were analyzed by SEM/EDS after the test at

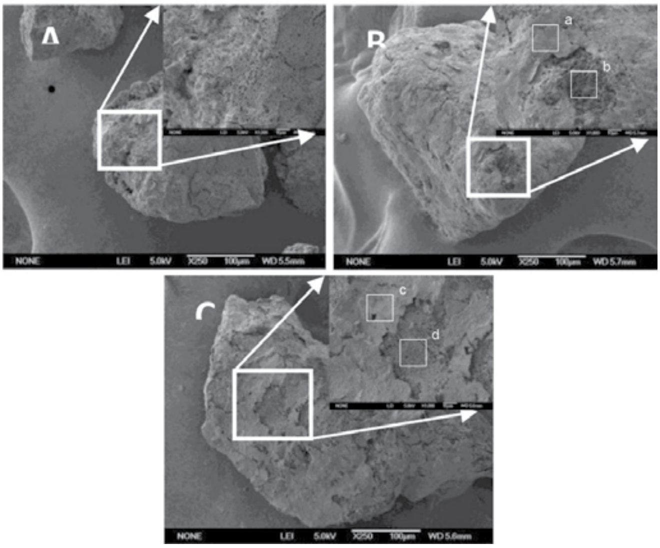

Figure 12. The SEM images of reduced particles (800°C, 74–149 μm, 24.3 cm/s): (a) no additive; (b) adding 2% MgO; and (c) adding 2% CaO.

the bed temperature of 800°C. As shown in **Figure 12(a)**, the morphology of sample was porous when no MgO or CaO was added, and many tiny iron grains appeared on the surface. But the bed particles were covered by the local coating layer when adding MgO and CaO (**Figure 12(b)** and **(c)**). And no obvious iron whiskers and substance in molten state were found on the surface, which was inconsistent with the results suggesting cation additions promoted fibrous iron [33, 34]. The reason was that the growth of iron whiskers was suppressed due to the formation of coating layer. The EDS spot analysis (**Figure 13(a)** and **(c)**) shows that the compositions of this coating layer were not only Mg and Ca but also large amount of Fe. It was inferred that this layer consisted of some complex compounds where Fe_2O_3 were not reduced completely. However, unlike the coating layer, the uncoated surface appears the porous morphology. The EDS analysis (**Figure 13(b)** and **(d)**) show that the compositions of the uncoated surface were element Fe, suggesting that metallic iron was precipitated under the coating layer. This was because that the coating layer was porous and cracked, and thus the external/internal diffusion for Fe oxides was easy. The metallization in bulk was slightly affected by surface coating. Therefore, it was inferred that the coating layer behaved like shell structure and inhibited the precipitated iron to expose on the surface of bed particle. The coating layer formed by adding MgO and CaO had a suppressive effect on defluidization and agglomeration.

To further identify the formation of new phase of Mg or Ca compounds during the reduction, the dominant species in the agglomerates was analyzed by XRD. **Figure 14** shows the phase composition with adding MgO and CaO before and after reduction. Before reduction the bed particles contained mainly Fe_2O_3 and a little $MgO{\cdot}Fe_2O_3$. However, after reduction a great number of metallic irons were observed, and the Mg and Ca species were in the formation of $MgO{\cdot}FeO$ and $CaO{\cdot}FeO$. Mg and Ca species can react with Fe_2O_3 to generate magnesium ferrite and calcium ferrite after pretreatment at 400−700°C [35], and these Fe compounds can

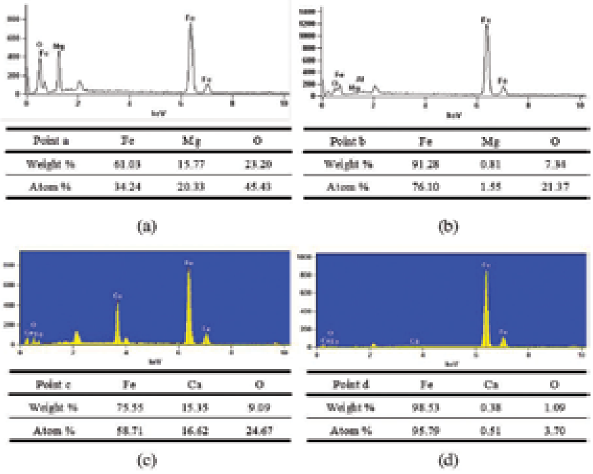

Point a	Fe	Mg	O
Weight %	61.03	15.77	23.20
Atom %	34.24	20.33	45.43

(a)

Point b	Fe	Mg	O
Weight %	91.28	0.81	7.91
Atom %	76.10	1.55	21.37

(b)

Point c	Fe	Ca	O
Weight %	75.55	15.35	9.09
Atom %	58.71	16.62	24.67

(c)

Point d	Fe	Ca	O
Weight %	98.53	0.38	1.09
Atom %	95.79	0.51	3.70

(d)

Figure 13. The EDS spot analysis of reduced particles (800°C, 74–149 μm, 24.3 cm/s): (a) Point a; (b) Point b; (c) Point c; and (d) Point d.

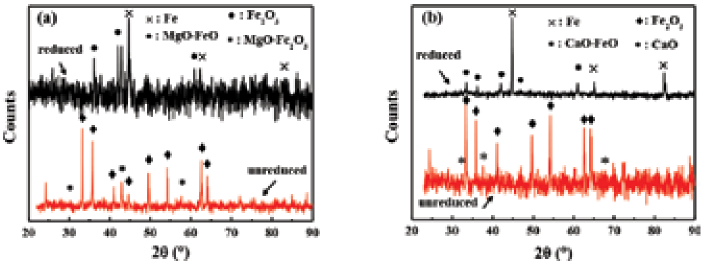

Figure 14. The XRD patterns of Fe_2O_3 particles before and after reduction (800°C, 74–149 μm, 24.3 cm/s): (a) adding 2% MgO and (b) adding 2% CaO.

be reduced to low-valent oxides, whereas the reaction rate was much lower than that of pure Fe_2O_3. Therefore, the rate of surface metallization was decreased by adding MgO and CaO. Because the defluidization occurred at a critical metallization degree, agglomeration/defluidization was delayed by reducing the time to reach the critical metallization degree by adding MgO and CaO.

The composition and reducibility of the coating layers formed by adding MgO and CaO were different. For adding MgO, $MgO{\cdot}Fe_2O_3$ was observed, which was reduced to $MgO{\cdot}FeO$ based on XRD analysis. But the reduction of $MgO{\cdot}FeO$ to Fe hardly happens below 1100°C [36]. And the surface not only contains Fe and Mg, but also considerable O (**Figure 13(a)**), indicating the outer layer was mainly composed of oxides. Therefore, an unreduced coating layer in the formation of $MgO{\cdot}FeO$ generated on the surface, and thus prevented the contact of iron precipitated. As a result, the defluidization was inhibited. However, for adding CaO, the Fe oxides in the calciowustite coating can be reduced thermodynamically to metallic iron [37]; and the outer layer (**Figure 13(c)**) contains Fe, Ca, and a little O, suggesting that the phases of Fe were mainly metallic iron and a little oxide. It indicated that the calciowustite was reduced finally to iron. Therefore, the inhibition effect of Ca species can only temporarily inhibit defluidization. When metallic iron appeared on the surface, the defluidization occurred again. Thus, the inhibition effect of CaO on defluidization was less than that of MgO, especially at high temperatures

5. Conclusions

1. Particle cohesiveness and agglomeration tendency were initiated by metallization and depended strongly on the amount of iron precipitation. As the metallization degree increased, the fluidization behavior of Fe_2O_3 particles evolved from cohesiveness to sticky, and thus agglomeration appeared. The precipitation of metallic iron with submicro size was clearly identified as the necks on the Fe_2O_3 surfaces, which caused the formation of agglomerates.
2. Based on force balance, a quantitative model for the fluidization characteristics of iron powders was developed to describe the defluidization behavior at elevated temperatures. The theoretical model successfully predicted the defluidization temperature as a function of fluidizing gas velocity and gas properties. The simulated defluidization temperatures

were in a good agreement with the experimental results. According to the operating phase diagram of fluidization obtained by this model, the stable fluidization and the defluidization region were determined.

3. Mg- and Ca-coating Fe_2O_3 particles were shown to significantly extend the defluidization time, and this inhibition effect was increased by increasing the addition amount. A coating layer on the surface was found to mainly contain magnesiowustite (MgO·FeO) and calciowustite (CaO·FeO) generated by the reactions between Mg/Ca oxides and Fe_2O_3/FeO during reduction process, and this coating layer was effective in preventing the connection of precipitated iron. And compared with CaO, MgO was more effective in delaying defluidization at the same conditions, because the unstable calciowustite was reduced to metallic iron and cannot completely suppress the precipitation of iron.

Nomenclature

A	Proportional constant for adhesion force	$kg^2 \cdot m/s^4$
b	Radius of the connection between the particles	m
C_d	Drag coefficient	–
$(C_d)_{\mathrm{mfs}}$	Drag coefficient in initial fluidization	–
d_p	Mean particle size	m
E_s	Activation of surface viscosity	J/mol
F_{ad}	Adhesion force	$kg \cdot m/s^2$
F_d	Drag force	$kg \cdot m/s^2$
K	Regressive constant	$s^4/(kg^2 \cdot m^4)$
N_a	Number group for adhesion force	$s^2/(kg \cdot m)$
$(N_a)_{\mathrm{mfs}}$	Number group for adhesion force in initial fluidization	$s^2/(kg \cdot m)$
N_d	Number group for drag force	$kg \cdot m^3/s^2$
$(N_d)_{\mathrm{mfs}}$	Number group for drag force in initial fluidization	$kg \cdot m^3/s^2$
R	Gas constant	J/(K·mol)
Re	Reynolds number	–
T	Bed temperature	°C
T_{def}	Defluidization temperature	°C
$(T_{\mathrm{def}})_{\mathrm{cal}}$	Theoretical results of T_{def}	°C
$(T_{\mathrm{def}})_{\mathrm{exp}}$	Experimental results of T_{def}	°C
t	Connect time of two particles	S

U_g	Operating gas velocity	m/s
U_{mf}	Initial fluidizing velocity in nonsintering condition	m/s
U_{mfs}	Initial fluidizing velocity in sintering condition	m/s
α	Proportional constant for drag force	–
β	Proportional constant for connect time	m
μ_{s0}	Proportional constant for surface viscosity	Pa·s
μ_s	Surface viscosity	Pa·s
μ_g	Gas viscosity	Pa·s
ρ_g	Gas density	kg/m^3
ρ_s	Particle density	kg/m^3
σ	Tensile stress of agglomerate	Pa
δ	Relative error of T_{def}	%

Author details

Yiwei Zhong[1]*, Jintao Gao[1], Zhancheng Guo[1] and Zhi Wang[2]

*Address all correspondence to: ywzhong@ustb.edu.cn

1 State Key Laboratory of Advanced Metallurgy, University of Science and Technology, Beijing, PR China

2 Institute of Process Engineering, Chinese Academy of Sciences, Zhongguancun, Haidian District, Beijing, PR China

References

[1] Johannes LS. Recent status of fluidized bed technologies for producing iron input materials for steelmaking. Particuology. 2011;**9**:14–23

[2] Komatina M, Gudenau HW. The sticking problem during direct reduction of fine iron ore in the fluidized bed. Journal of Metallurgy. 2004;**11**:309–328

[3] Skrifvars BJ, Hupa M, Hiltunen M. Sintering of ash during fluidized bed combustion. Industrial & Engineering Chemistry Research. 1992;**31**:1026–1030

[4] Seville JPK. High-temperature defluidization. Powder Technology. 1984;**38**:13–22

[5] Compo P, Pfeffer R, Tardos GI. Minimum sintering temperatures and defluidization characteristics of fluidizable particles. Powder Technology. 1987;**51**:85–101

[6] Seville JPK, Willett CD, Knight PC. Interparticle forces in fluidization: A review. Powder Technology. 2000;**113**:261–268

[7] Bartels M, Lin W, Nijenhuis J, Kapteijn F, Ruud van Ommen J. Agglomeration in fluidized beds at high temperatures: Mechanisms, detection and prevention. Progress in Energy and Combustion Science. 2008;**34**:633–666

[8] Hayashi S, Iguchi Y. Factors affecting the sticking of fine iron ores during fluidized bed reduction. ISIJ International. 1992;**32**:962–971

[9] Gransden JF, Sheasby JS, Bergougnou MA. An investigation of defluidization of iron ore during reduction by hydrogen in a fluidized bed. Chemical Engineering Progress. 1970;**66**:208–214

[10] Gransden JF, Sheasby JS. The sticking of iron ore during reduction by hydrogen in a fluidized bed. Canadian Metallurgical Quarterly. 1974;**13**:649–657

[11] Zhong Y, Wang Z, Gong X, Guo Z. Sticking behavior caused by sintering in gas fluidisation reduction of hematite. Ironmaking Steelmaking. 2012;**39**:38–44

[12] Mikami T, Kamiya H, Horio M. The mechanism of defluidization of iron particles in a fluidized bed. Powder Technology. 1996;**89**:231–238

[13] Knight PC, Seville JPK, Kamiya H, Horio M. Modelling of sintering of iron particles in high-temperature gas fluidization. Chemical Engineering Science. 2000;**55**:4783–4787

[14] Öhman M, Nordin A. A new method for quantification of fluidized bed agglomeration tendencies: A sensitivity analysis. Energy Fuels. 1998;**12**:90–94

[15] Öhman M, Pommer L, Nordin A. Bed agglomeration characteristics and mechanisms during gasification and combustion of biomass fuels. Energy Fuels. 2005;**19**:1742–1748

[16] Tardos GI, Mazzone D, Pfeffer R. Destabilization of fluidized beds due to agglomeration. Part 1: Theoretical model. Canadian Journal of Chemical Engineering. 1985;**63**:377–383

[17] Buffincton FS, Hirano K, Cohen M. Self-diffusion in iron. Acta Metallurgica. 1961;**9**:434–439

[18] Himmel L, Mehl RF, Birchenal CE. Self-diffusion of iron in iron oxides and the Wagner theory of oxidation. Transactions of the Metallurgical Society of AIME. 1953;**197**:827–833

[19] Tardos GI, Pfeffer R. Chemical reaction induced agglomeration and defluidization of fluidized beds. Powder Technology. 1995;**85**:29–35

[20] Tardos GI. Measurement of surface viscosities using a dilatometer. Canadian Journal of Chemical Engineering. 1984;**62**:884–887

[21] Zhong Y, Wang Z, Guo Z, Tang Q. Defluidization behavior of iron powders at elevated temperature: Influence of fluidizing gas and particle adhesion. Powder Technology. 2012;**230**:225–231

[22] Satterfield CN. Heterogeneous Catalysis in Industrial Practice. 2nd ed. New York: McGraw-Hill; 1992

[23] Hembree P, Wagner JB. Diffusion of Fe55 in wustite as a function of composition at 1100°C. Transactions of the Metallurgical Society of the American Institute of Mining, Metallurgical and Petroleum Engineers. 1969;**245**:1547–1552

[24] Benson SA, Jones ML, Harb JN. Ash formation and deposition. In: Smoot LO, editor. Fundamentals of Coal Combustion-for Clean and Efficient Use. Amsterdam: Elsevier; 1993

[25] Seville JPK, Silomon-Pflug H, Knight PC. Modelling of sintering in high temperature gas fluidisation. Powder Technology. 1998;**97**:160–169

[26] Turton R, Levenspiel O. A short note on the drag correlation for spheres. Powder Technology. 1986;**47**:83–86

[27] Moseley JL, O'Brien TJ. A model for agglomeration in a fluidized bed. Chemical Engineering Science. 1993;**48**:3043–3050

[28] Lin CL, Wey MY, Lu CY. Prediction of defluidization time of alkali composition at various operating conditions during incineration. Powder Technology. 2006;**161**:150–157

[29] Kuo JH, Shih KM, Lin CL, Wey MY. Simulation of agglomeration defluidization inhibition process in aluminum-sodium system by experimental and thermodynamic approaches. Powder Technology. 2012;**224**:395–403

[30] Hayashi S, Sawai S, Iguchi Y. Influence of coating oxide and sulfur pressure on sticking during fluidized bed reduction of iron ores. ISIJ International. 1993;**33**:1078–1087

[31] Lin CL, Wey MY. The effect of mineral compositions of waste and operating conditions on particle agglomeration/defluidization during incineration. Fuel. 2004;**83**:2335–2343

[32] Lin CL, Kuo JH, Wey MY, Chang SH, Wang KS. Inhibition and promotion: the effect of alkali earth metals and operating temperature on particle agglomeration/defluidization during incineration in fluidized bed. Powder Technology. 2009;**189**:57–63

[33] Geva S, Farren M, St. John DH, Hayes PC. The effects of impurity elements on the reduction of wustite and magnetite to iron in CO/CO_2 and H_2/H_2O gas mixtures. Metallurgical Transactions B (Process Metallurgy). 1990;**21**:743–751

[34] Sesen MK. The influence of CaO on the precipitation behaviour of iron in the reduction of iron oxide. Scandinavian Journal of Metallurgy. 2001;**30**:1–7

[35] Wang Z. Ferrous Metallurgy. 2nd ed. Beijing: Metallurgical Industry Press; 2002

[36] Strelov KK, Safin IM, Fedotov VI. Reduction of iron oxide from commercial magnesite refractory. Inorganic Materials. 1981;**17**:1344–1347

[37] Du S, Srinivasan NS, Staffansson LI. Reduction of calcium ferrites by hydrogen in the temperature interval 1191-1426 K. Scandinavian Journal of Metallurgy. 1988;**17**:233–238

Chapter 7

The eXtended Discrete Element Method (XDEM): An Advanced Approach to Model Blast Furnace

Bernhard Peters, Maryam Baniasadi and
Mehdi Baniasadi

Additional information is available at the end of the chapter

http://dx.doi.org/10.5772/intechopen.75436

Abstract

The blast furnace iron making is the oldest but still the main method to produce liquid iron through sequential reduction processes of iron ore materials. Despite the existence of several discrete and continuous numerical models, there is no global method to provide detailed information about the processes inside the furnaces. The extended discrete element method known as XDEM is an advance numerical tool based on Eulerian–Lagrangian framework which is able to cover more information about the blast furnace process. Within this platform, the continuous phases such as gas and liquid phases are coupled to the discrete entities such as coke and iron ore particles through mass, momentum and energy exchange. This method has been applied to the shaft, cohesive zone, dripping zone and hearth of the blast furnace. In this chapter, the mathematical and numerical methods implemented in the XDEM method are described, and the results are discussed.

Keywords: XDEM, CFD-DEM, blast furnace, numerical models

1. Introduction

A blast furnace is charged with ore and coke from the top, so that a packed bed is formed. Hot gas also referred to as blast is introduced to the furnace through the tuyeres in the lower part. The combustion of coal and coke takes place that generates reducing gas. It ascends mainly in a countercurrent flow reducing iron-bearing materials to form liquid iron and slag in the cohesive zone. The liquids percolate through the coke bed towards the hearth. Unburned coal powder may leave the raceway entrained in the gas flow due to high injection rates. The multiphase flow of solids, liquids, gas and fines in conjunction with reaction kinetics, heat and mass transfer reveals the complexity of a blast furnace and the difficulties to comprehend the process. Since measurements in a blast furnace are very difficult to carry out due to size and limited accessibility, mathematical modelling based on computational fluid dynamics, reaction kinetics and transport phenomena is an applicable tool to investigate into the complex characteristics of a blast furnace.

Multiphase flow phenomena consisting of a fluid, e.g. gas or liquid and a solid phase, could be classified into main categories: On a macroscopic level, all phases are considered as a continuum that has resulted in the well-known two-fluid model [1]. It is a preferred approach due to computational efficiency and convenience for a variety of engineering applications such as process engineering. However, inherent to the averaging concept in the continuum approach, major features of the particulate phase, e.g. material properties, size distribution or shape of individual particles, are lost. Therefore, this gap of information on the particle level usually is compensated for by additional closure or constitutive relations.

Alternatively, the particles are treated as discrete entities, while the fluid phase in the void space between the particles is still considered as a continuum and, therefore, is referred to as the Combined Continuum and Discrete Model (CCDM) [2, 3]. It bears the valuable advantage that constitutive relations are avoided and the particulate phase is resolved on a fundamental level. An analysis of results related to particles offers a finer resolution than a continuum method and, therefore, leads to a deeper understanding of particle processes which is confirmed by Zhu et al. [4, 5] in a review for the applicability of the CCDM approach. It has developed significantly during the last two decades and represents the dynamics of the particles by the discrete element method (DEM), while the remaining continuum phases are described by differential conversation equations. Hence, CCDM is established as a powerful tool to describe the complex interaction between particles and a fluid as stated by Yu and Xu [6], Feng and Yu [7] and Deen et al. [8]. Although CCDM is the method of choice to reveal underlying physics for challenging multiphase flow applications as reviewed by Zhu et al. [4, 5], current methodologies should be developed for nonspherical particle shapes to accommodate efficiently engineering needs and to quantify results for process modelling.

At an early stage, only simple multiphase configurations have been investigated [9, 2] that were extended to more and more complex engineering applications such as conveyor belt, cyclone and fluidised bed as demonstrated by Chu and Yu [10]. Chu et al. [11] described the complex flow of water, air, magnetite and coal particles of various sizes in a dense medium cyclone (DMC). Similarly, Zhou et al. [12] were able to model rich/lean combustion of pulverised coal in a complex burner with CCDM. Both predictions agreed remarkedly well with experimental data. CCDM is also well suited to describe the chaotic motion of a particulate phase in a gas-fluidised bed as shown by Feng and Yu [13] and Kafuia et al. [14].

A similar development has been seen for modelling of blast furnaces. Computational fluid dynamics (CFD) as a tool for continuous flow modelling has been applied with success to a large extent as reviewed by Chattopahyay et al. [15, 16]. However, experimental observations [17–21] show that a pure continuous approach to the blast furnace is inaccurate. Therefore, the flow of the solid phase consisting of particles is to be modelled by a discrete approach as suggested by Dong et al. [22] and reviewed by Yu [23] for several engineering applications. Simsek et al. [24] predicted grate ring systems by the CCDM method but obtained only qualitatively reasonable results highlighting the fact that more research is required that should point into polydisperse particle systems [7].

Although CCDM has seen significant progress during the past decade [2, 25], applications including heat transfer are rarely attempted. A gas-fluidised bed with heat exchange for polymerisation reactions was undertaken by Kaneko et al. [26] employing the Ranz-Marshall correlation [27]. Only convective transfer was predicted for a two-dimensional spouted bed by Swasdisevi et al. [28]. Additional heat transfer due to conduction between particles during gas–solid transport in horizontal pipes was taken into account by Li and Mason [29–31]. Both convective and conductive heat transfer in a gas-fluidised bed for coal combustion were considered by Zhou et al. [32, 33]. Similarly, Malone and Xu [34] estimated heat transfer for liquid-fluidised beds with CCDM and concluded that further investigations concerning heat transfer have to be carried out.

A newly developed extended discrete element method (XDEM) introduced by Peters [35–38] is a coupled continuum and discrete method and a novel approach to answer most challenging questions. The XDEM is an extension to the classical discrete element method with considering thermo-physical state of the particles as well while being in combination with the CFD. It is well described in the mathematical section and applied to different parts of a blast furnace with the following features:

- Microscale: Generating a more concrete basis of the particle scale in both dynamic and conversion modules to develop a more comprehensive theory to study the interactions between particles and between particle and fluid under various conditions.
- Macroscale: To provide a general information on the continuum-based process modelling in terms of solving governing equations and to develop a general methodology to link the discrete and continuum approach modelling.
- Application: To present a robust and reliable model capable enough to be applied to the different parts of the blast furnace with transferring data between the multiphase system and particles.

2. Methodology

2.1. The mathematical model for the continuous phases

The widely used Eulerian volumetric average [39] in the porous media concept was applied to the governing equations of the continuum phases denoted as *phasei*. In this regard, the conservation of mass, momentum and energy can be summarised as

$$\frac{\partial}{\partial t}\left(\epsilon\alpha_i\rho_i\phi_\mathrm{i}\right) + \nabla\cdot\left(\epsilon\alpha_i\rho_i\vec{v}_i\phi_i\right) = \nabla.\left(\epsilon\alpha_i\,\Gamma\nabla.\left(\phi_\mathrm{i}\right)\right) + S \tag{1}$$

where $\epsilon, \alpha, \rho, v, \Gamma$ *and* S are void space, volume fraction, density, velocity, diffusion term and source term, respectively. In order to derive each equation, the variable, ϕ, should be replaced by the values reported in **Table 1**.

Equation	ϕ	Γ	S
Continuity	1	0	m^0
Momentum	$\vec{v}$	μ	$\nabla P + g + F$
Energy	h	κ	H

Table 1. Values for the governing equations.

The $m^0, F\ and\ H$ on the right hand side of each equation are the source terms representing mass, momentum and energy transfer between phases. The very well-known Ergun and Ranz-Marshall correlations are used to consider momentum transfer and energy exchange between phases.

The void space and particle diameter must also be known to solve the governing equations for the fluid phases. To this purpose, the XDEM calculates the volumetric average value of void space for each CFD cell by knowing the number of particles in each CFD cell based on a kernel-based interpolation procedure proposed by Xiao et al. [40].

2.2. The mathematical model for discrete entities

The XDEM predicts both dynamics and thermochemical conversion of a particulate system. The thermochemical conversion of a particle includes not only the internal temperature distribution but also transport of species through diffusion and/or convection and chemical conversion via reactions in a porous media. The velocity, position and acceleration are calculated in the dynamics module via the DEM method while the temperature and species distribution in the conversion module of the XDEM via the DPM method.

2.2.1. Dynamics module

The proved DEM is based on the soft sphere model applied in the dynamic module. In this method, the particles are assumed to be deformable and allowed to overlap. The motion of each separate particle is tracked using the equations of classical mechanics. Newton's and Euler's second law for translation and rotation of each particle are integrated over time, and the particle positions are updated accordingly during time integration.

- Equation of motion:

$$m_i \frac{d\vec{v_i}}{dt} = m_i \frac{d^2\vec{x_i}}{dt^2} = \vec{F_i^c} + \vec{F_i^g} + \vec{F_i^{\text{ext}}} \tag{2}$$

$$I_i \frac{d\vec{\omega_i}}{dt} = \sum_{j=1}^{n} \vec{M_{i,j}} \tag{3}$$

Here, $\vec{F_i^{\text{ext}}}$ is the summation of external forces acting on a particle such as drag and buoyancy forces from surrounding fluids. The contact force $\vec{F_i^c}$ of a particle is the sum of all normal $\vec{F_{i,j}^{c,n}}$

Mass conservation	$\boldsymbol{\frac{\partial}{\partial t}\left(\varepsilon_p\rho_f\right)+\vec{\nabla}\,.\left(\varepsilon_p\rho_f\vec{v}_f\right)=\dot{m}_{s,f}}$
Momentum conservation	$-\frac{\partial}{\partial x}\left(\varepsilon_p p\right)=\frac{\varepsilon_p\mu_f}{K}\vec{v}_f$
Energy equation	$\frac{\partial}{\partial t}\left(\rho h_p\right)=\frac{1}{r^n}\frac{\partial}{\partial r}\left(r^n\lambda_{eff}\frac{\partial T}{\partial r}\right)+q^{'''}$ $q^{'''}=\sum_{k=1}^{l}\dot{\omega}_k H_k \quad \textit{in case of chemical reaction}$ $q^{'''}=-\acute{m}L_f-\acute{m}\left(h_{l,m}-h_{l,ref}\right) \quad \textit{in case of melting}$ $\acute{m}=\begin{pmatrix}\frac{\rho\left(h_{p,T}-h_{p,m}\right)}{L_f\Delta t} & h_{p,T}\geq h_{p,m}\\ 0 & h_{p,T}<h_{p,m}\end{pmatrix}$
Species equation	$\frac{\partial}{\partial t}\left(\varepsilon_p\boldsymbol{\rho}_{f,i}\right)+\vec{\nabla}\,.\left(\varepsilon_p\boldsymbol{\rho}_{f,i}\vec{v}_f\right)=\frac{1}{r^n}\frac{\partial}{\partial r}\left(r^n\varepsilon_p D\frac{\partial\rho_{f,i}}{\partial r}\right)+\varepsilon_p\dot{m}_{s,f,i}$
Boundary conditions	$-\lambda_{eff}\left(\frac{\partial T}{\partial r}\right)_R=\alpha\left(T_R-T_\infty\right)+\dot{q}_{rad}+\dot{q}_{cond}$ $-D_i\left(\frac{\partial\rho_{f,i}}{\partial r}\right)_R=\beta_i\left(\boldsymbol{\rho}_{f,i,R}-\boldsymbol{\rho}_{f,i,\infty}\right)$
Reaction	$r_i=k_r e^{-\frac{E}{RT}}\,T^m\prod_{j=i}^{n}\boldsymbol{\rho}_j^{\gamma_j}$

Table 2. Particle equations.

and tangential $\vec{F}_{i,j}^{c,t}$ collision forces generated while colliding with the neighbouring bodies. Hertz-Mindlin model [41, 42] is used to calculate the contact forces.

2.2.2. Conversion module

The current approach accounts for thermal conversion of a single particle via heat and mass transfer and chemical reactions. A discrete particle may be considered to consist of a solid, inert, liquid and gaseous phase, whereby local thermal equilibrium between the phases is assumed. The distribution of temperature and species within a single particle is accounted for by a system of one-dimensional and transient conservation equation as shown in **Table 2**.

3. Shaft

A blast furnace is a vertical shaft furnace that reduces iron ores to the so-called pig iron for subsequent processing into steels of various qualities. Metallic ore, coke and flux, containing elements such as limestone, are charged in layers into the top of a blast furnace, while usually air is introduced under pressure through the tuyeres (nozzles) at the bottom of the blast furnace. The air is preheated to temperatures between 900° and 1250° C and reacts vigorously with preheated coke to form reducing gas (carbon monoxide). It streams upwards through the void space between the solid materials at high temperatures of app. 1650° C. Hence, a significant reduction of the iron ores takes place in the upper shaft or stack between the top and the cohesive zone of the blast furnace. During indirect reduction with carbon monoxide as opposed to direct reduction with carbon, the iron-bearing materials are stepwise reduced from haematite (Fe_2O_3) to magnetite (Fe_3O_4) and wustite (FeO) to produce liquid iron following three equilibrium reactions:

$$3\,Fe_2O_3 + CO \rightarrow 2\,Fe_3O_4 + CO_2$$

$$Fe_3O_4 + CO \rightarrow 3\,FeO + CO_2$$

$$FeO + CO \rightarrow Fe + CO_2$$

These reactions were experimentally investigated by Murayama et al. [43] under different CO-CO_2 gas mixtures and were employed to predict and validate the individual reaction rate of the abovementioned reduction scheme for a single ore particle. The reduction degree was measured and is defined as the fractional removal of oxygen related to the initially available oxygen as

$$F = \frac{m_O^0 - m_O}{m_O^0} = 1 - \frac{m_O}{m_O^0} \tag{4}$$

where the total mass of removable oxygen is defined as the oxygen mass to reach the next lower oxide in the sequence of haematite (Fe_2O_3), magnetite (Fe_3O_4), wustite (FeO) and iron (Fe) so that the reduction degree always varies between 1 and 0 for each individual reduction reaction. The reaction rate is expressed by an Arrhenius equation for which the relevant parameters are listed in **Table 3**.

The predicted results were compared to experimental data at different temperatures and are shown in the **Figures 1–3**. In general, a very satisfactory agreement between predicted and experimental data is achieved taking into account the temperature spread and experimental uncertainties such as material data. Hence, deviation occurrence is attributed to morphological changes such as porosity or crystal structure. In particular the latter was excluded from the study since crystal and grain structures address a length scale outside the scope of these investigations. Therefore, deviations of this scale are in general acceptable as pointed out by Peters [44].

The validated reaction mechanism was applied to a non-isothermal packed bed of iron ore particles [45] as encountered in the stack of a blast furnace, and the predicted reduction degree was compared to measurements as depicted in **Figure 4**. Both experiments and predictions were carried out for a packed bed consisting of pellets and pellets/nut coke. For both setups, the predicted integral reduction degree agrees well with experimental data and thus proves the superiority of the current DEM-CFD approach for predicting thermal conversion of packed beds.

Reduction	E (J/mol)	K_r (−)
$Fe_2O_3 \rightarrow Fe_3O_4$	$7.5010 \cdot 10^4$	8.58
$Fe_3O_4 \rightarrow FeO$	$7.8102 \cdot 10^4$	25
$FeO \rightarrow Fe$	$1.4601 \cdot 10^5$	2300

Table 3. Kinetic parameters used in the XDEM simulation for reduction reactions.

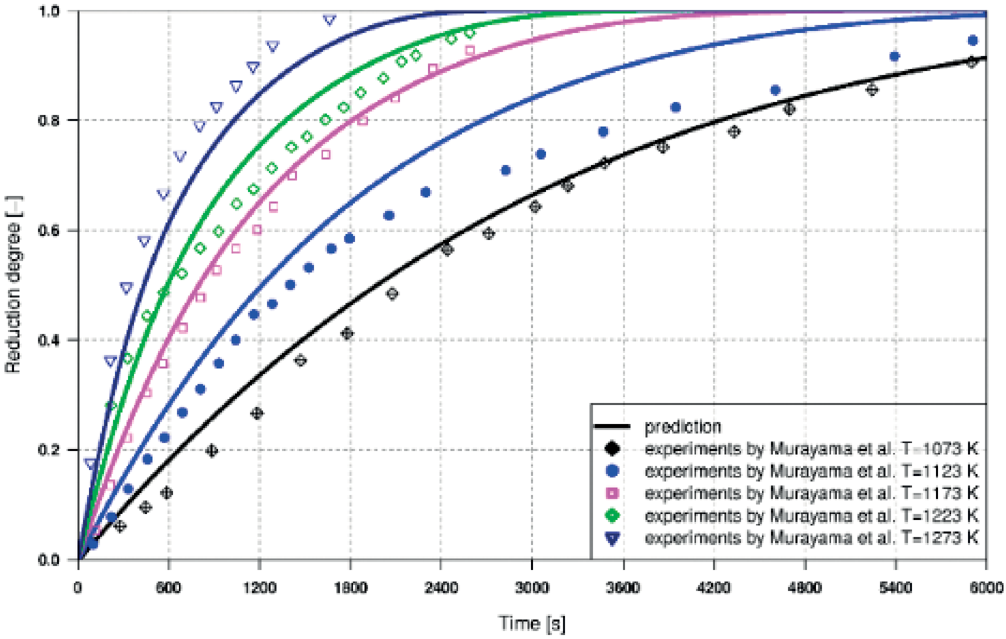

Figure 1. Comparison between experimental data and predictions for isothermal reduction [44] of haematite to magnetite.

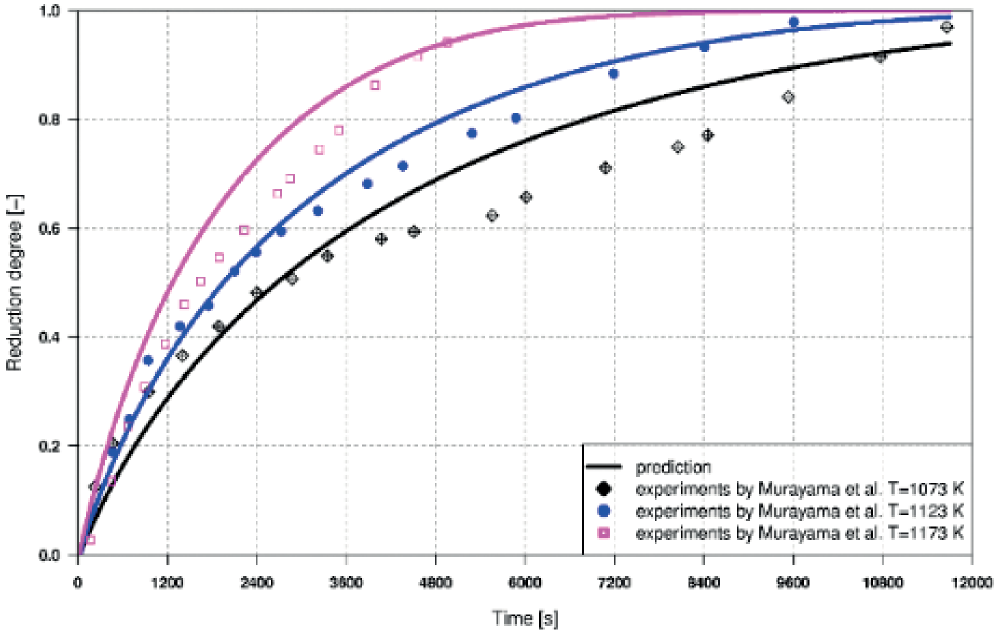

Figure 2. Comparison between experimental data and predictions for isothermal reduction of magnetite to wustite [44].

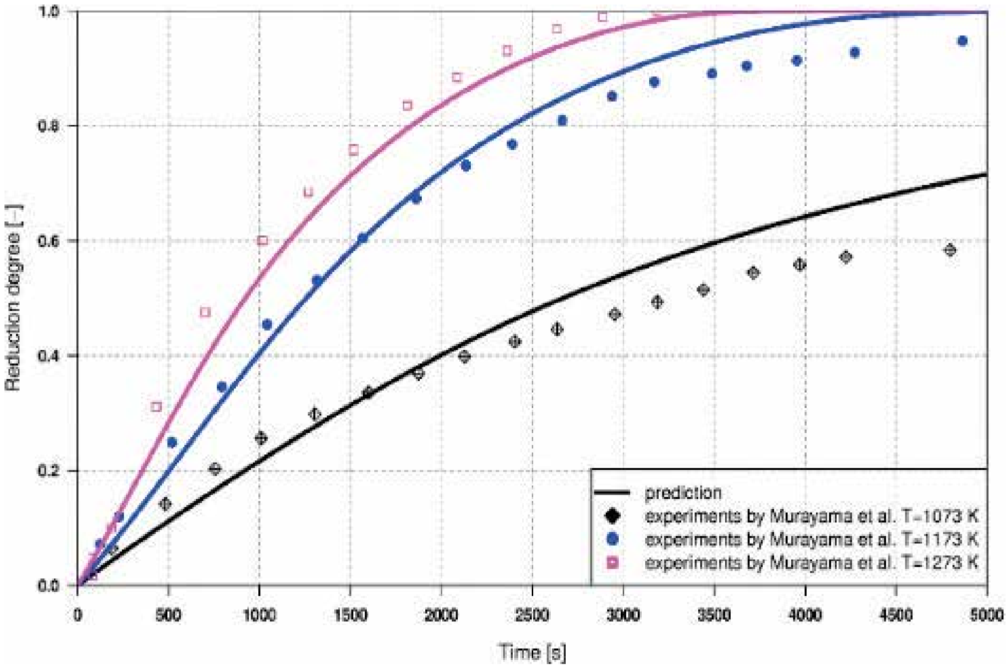

Figure 3. Comparison between experimental data and predictions for isothermal reduction of wustite to iron [44].

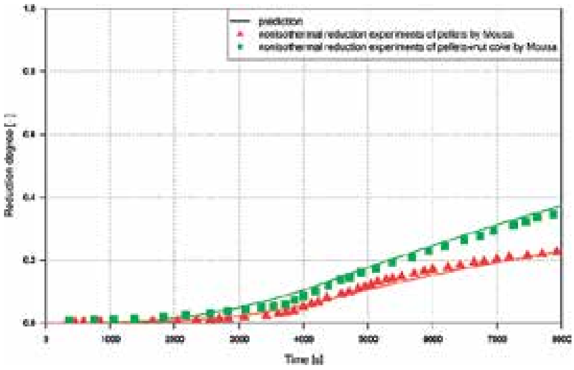

Figure 4. Comparison of model prediction and experiments for reduction of a bed of pellets (red triangles) and pellets mixed with nut coke (green squares) [45].

4. Cohesive zone

Cohesive zone (CZ) is formed between shaft and dripping zone. In this region, the reduced iron-bearing particles start softening because of the weight of burden above and the high temperature in the CZ. As particles soften, the porosity of the ore layer decreases causing a high pressure drop. As the temperature increases further, the softened particles start melting and generate two different liquids, molten iron and slag. The softening and melting process makes the CZ to form impermeable ferrous layers forcing gas to flow horizontally through the permeable coke slits. This means that the CZ has remarkable effects on the operation of the blast furnace and the description of the characteristics of the CZ is extremely important. Since it is not possible to interrupt the BF to investigate details of the phenomena occurred inside, the numerical simulation becomes more practical.

The iron-bearing materials start softening at a temperature depending on the chemical composition, reduction degree and the load of burden. In this study, the softening range is considered to be from 1200 K to 1400 K according to Yang et al. [46, 47]. To describe the softening process in the CZ, a packed bed is randomly filled with particles assuming pellet which is shown in **Figure 5**. The radius of pellets varies in the range of 5.4–6.6 mm in a cylindrical vessel with 50 mm in diameter and height. The particles are coloured by their sizes. The value of load acting on the top of particles is determined 100 KPa according to the standard conditions in the softening test [48, 49]. For this test case, the conversion and dynamic modulus of the XDEM are used. The conversion module allows to heat up the particles from 1200 K to 1400 K, and the other module is responsible for the movement and the deformation of particle with the assistance of the relationship of Young's modulus (E) and temperature. It was assumed that this relationship is linear within the softening range of pellets. **Figure 6** shows the influence of the changes of Young's modulus (E) within XDEM simulation on the rearrangement of pellets in the packed bed. It is observed that to reach %40 in bed shrinkage, it is needed that the value of Young's modulus (E) is decreased approximately by two orders.

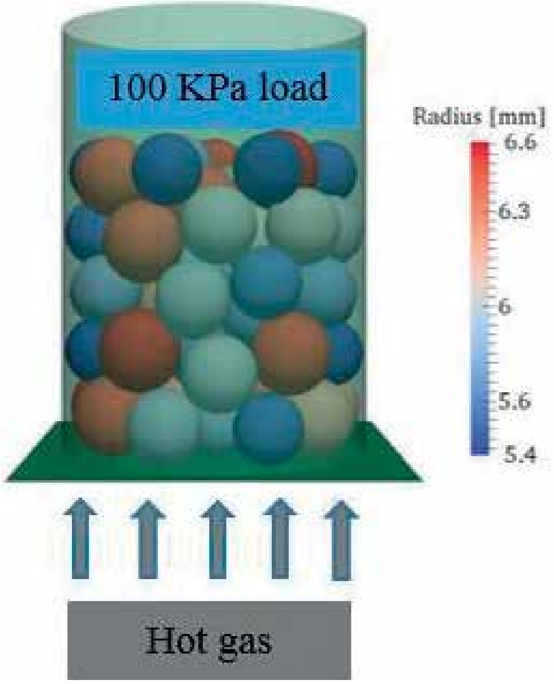

Figure 5. The geometry used in XDEM simulation for softening behaviour of some pellets.

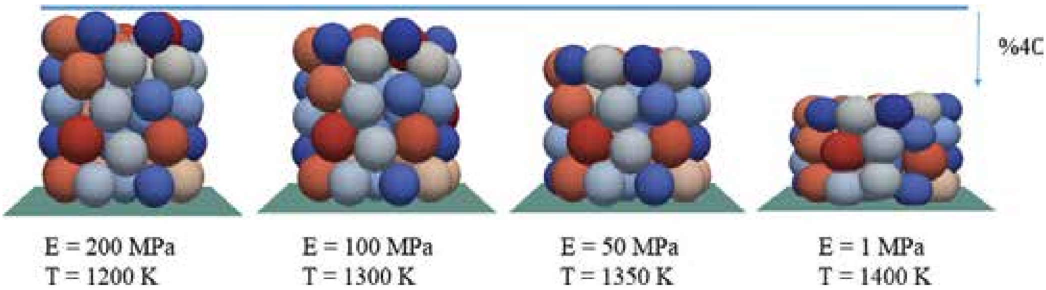

Figure 6. The effect of Young's modulus on structural rearrangement of the packed bed of pellets.

Due to the lack of appropriate experimental data for the melting of iron-bearing material by a hot gas in a real condition occurring in a CZ, the melting of a packed bed of ice particles in a solid–liquid system is selected. The simulation setup is shown in **Figure 7**. **Figure 8** compares the predicted results with experimental data [51] of the mass loss history for a packed bed exposed to an water mass flow of a velocity of 0.1 m/s. The comparison shows that the predicted mass

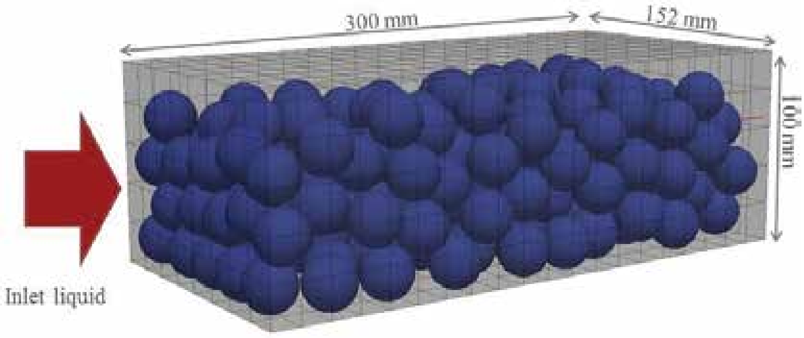

Figure 7. Schematic representation of the packed bed of particles used in the simulation [50].

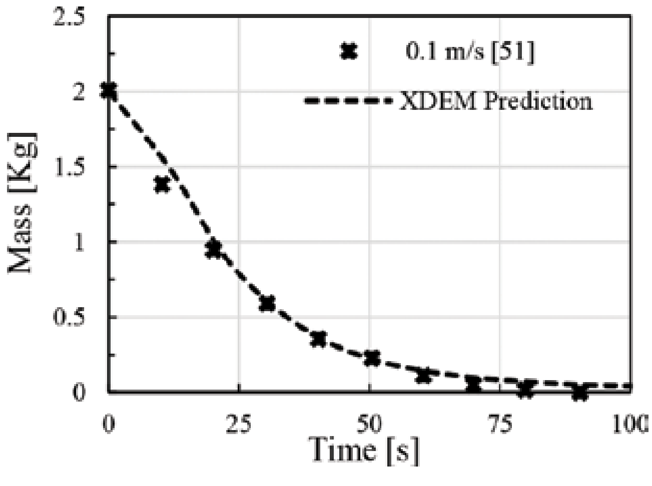

Figure 8. Comparison between experiments and predictions of the mass loss history of a melting packed bed.

variations with time agree well with the experimental results. **Figure 9** shows that the ability of the XDEM to fully describe solid and liquid flows in a four-way CFD-DEM coupling considering particle-particle, particle-wall and particle-fluid interaction in terms of dynamics and thermal conversion. As it can be observed, the particles are risen and pushed downwards due to the buoyancy and drag force. Moreover, the particles which are faced the warm liquid earlier are heated up and melted faster than the others. It can be also seen that liquid flows downwards gradually because of the flow resistance from the particles and its temperature decreases by exchanging convection heat with the ice particles and mixing with produced melt. Moreover, The XDEM has been validated for one single ice particle that undergoes melting [52].

Although we modelled solid–liquid flows under the melting process, the present technique is adequately robust and efficient to be applied to the complex melting process of granular packed bed by a hot gas which is a solid-gas-liquid system appropriate for many industrial applications particularly blast furnace modelling.

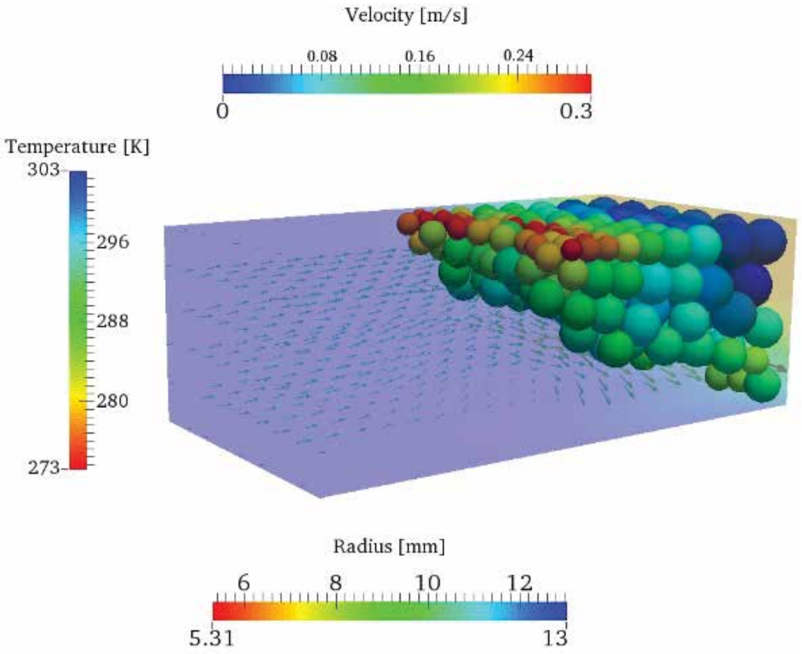

Figure 9. The evaluation of temperature and velocity of liquid and the size distribution of particles at t = 20 s.

5. Dripping zone and hearth

The liquid iron and slag produced in the cohesive zone trickle down through the packed bed of coke particles towards the hearth in a zone known as the dripping zone. It is located deep inside the blast furnace where measurements are not easy to perform. It highly affects the production rate, the quality of hot metal and process efficiency [53]. In this region, the two liquid phases descend slowly and hot gas introduced through the tuyeres ascends upwards while exchanging heat and mass with the particles. The presence of solid particles besides the fluid phases makes the coupled discrete-continuous methods suitable for this application. In our previous study [54], the XDEM approach has been validated by comparing the numerical results with the experimental data [55] for a case representing the dripping zone. The experimental setup and the simulation domain are shown in **Figure 10**. A liquid distributor is located on the upper part, which is indicated as a mass source for some cells in the simulation domain in order to produce the same amount of liquid as the experimental study. The gas phase is introduced through a nozzle in the experimental study, which is specified as fixed uniform inlet velocity boundary condition in the modelling, while no slip boundary condition was used for the walls and the total pressure for the outlet boundary condition. Results obtained under these conditions are shown in **Figure 11**. The total absolute mean error of 3.27% was achieved, which shows the robustness of the XDEM for modelling of such cases. This model has also been applied to the trickle bed reactors [56].

In this regard, the model is applied to the lower part of the blast furnace including both dripping zone and hearth shown in **Figure 12**. The domain is randomly filled with non-uniform particle sizes of $\boldsymbol{d_p = 1 \pm 0.1\ cm}$ since the coke particles do not have the same sizes in this particular part. The molten iron and slag produced in the cohesive zone have completely different properties, thus showing different flow behaviours. Most of the previous studies considered only one liquid phase with either slag properties or iron, whereas in this study, both liquid phases are considered, and their mutual effects are studied. Therefore, the simultaneous downward flow of molten iron and slag through a packed bed of coke particles with the upward flow of gas phase is investigated. Despite the existence of several forces, drag force is the only force considered between each pair of phases. In this figure, the calculated porosity field is also illustrated. A predefined cavity is considered right in front of the gas inlet in order to avoid numerical instabilities as shown in **Figure 12**.

The liquid saturation, which is defined as the volume of the fluid per volume of the void space for both liquid iron and slag, is illustrated in **Figure 13** over time. An incline mass source representing

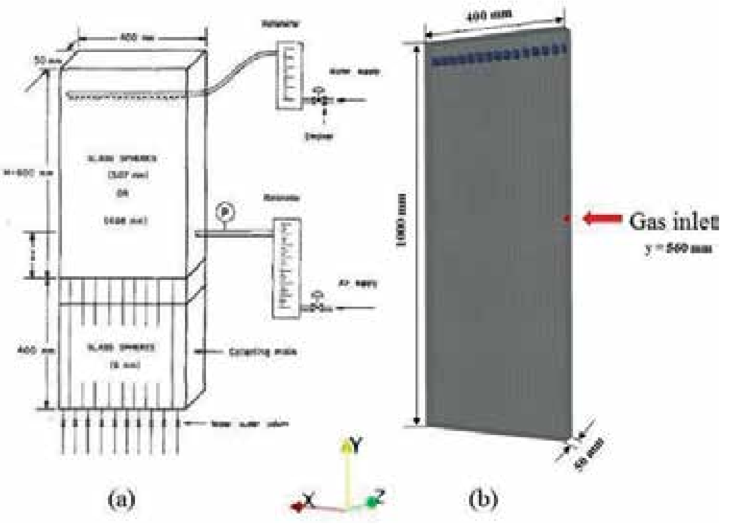

Figure 10. Experimental set-up [53] (a) and simulation domain (b).

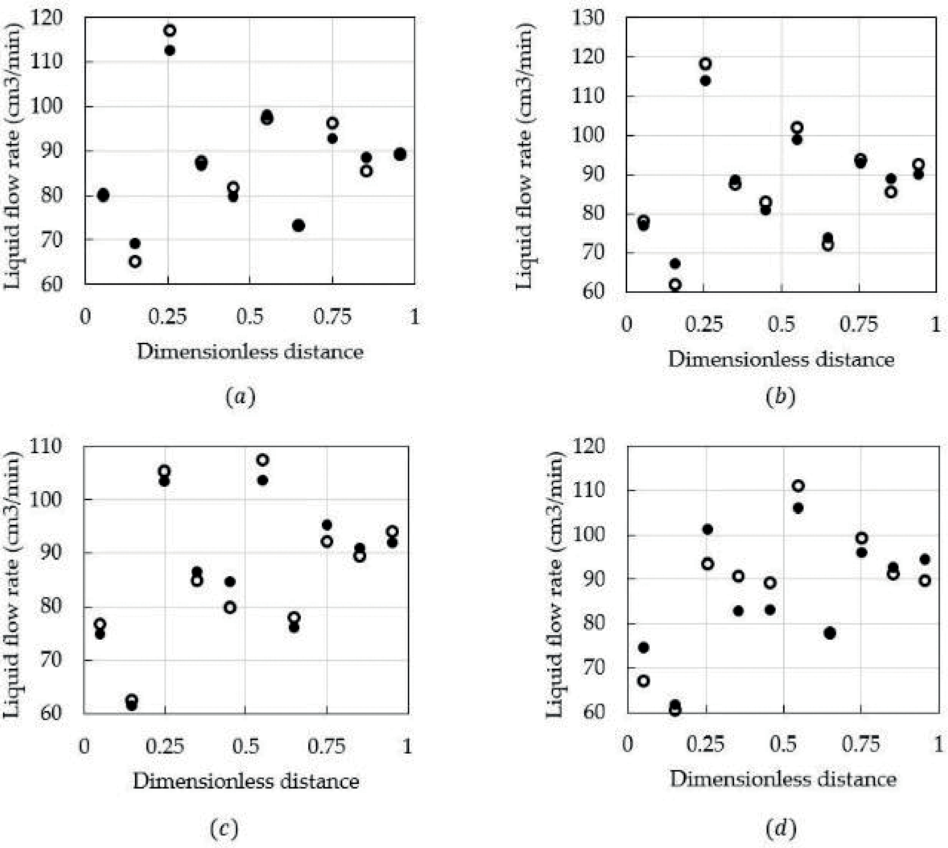

Figure 11. The XDEM results (unfilled) versus the experimental data (filled) for constant liquid mass flow rate of 650 cm^3/min where the gas flow rates are (a) 0.08 m^3/min, (b) 0.14 m^3/min, (c) 0.28 m^3/min and (d) 0.34 m^3/min [54].

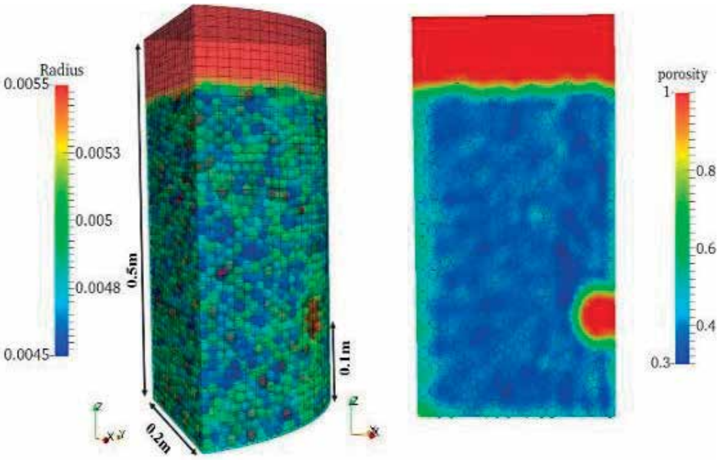

Figure 12. The simulation domain and the porosity distribution.

the cohesive zone was specified to investigate its effect on the movement of liquid phases as well as the gas phase. The figures on the left are showing slag saturations and on the right the molten iron saturations. Higher saturations are calculated for the slag, which is due to the higher viscosity and lower density. The slag properties create higher resistance due to the solid particles and in consequence higher saturations. Therefore, the liquid iron flows with higher velocities and lower hold ups through the packed bed. The velocity difference of the two liquid phases causes a slip velocity, which accelerates the slag movement and decelerates the iron downward flow.

Within this concept, the stratification of liquid iron and slag can also be studied. The liquid-liquid interface affects the mass and heat transfer rates between liquid iron and slag and thus, determines the final product quality. The molten iron with higher density is settling at the bottom where the slag floats on the top of it.

The effect of the gas phase due to the drag force on the deviation of the liquid phases from the raceway zone, which leads to the formation of the dry zone, is shown in **Figure 14**. The gas phase tends to replace the liquid phase at the entrance of the gas phase. This behaviour creates a dry zone, whose size is proportional to the gas inlet magnitude [54]. It can also be concluded that the liquid iron is pushed more towards the centre than the slag phase due to the larger drag force between liquid iron and gas phase. Although constant properties are considered for all phases, it should be noted that the fluid properties are not constant while moving through the blast furnace. They are mainly function of temperature, pressure and composition.

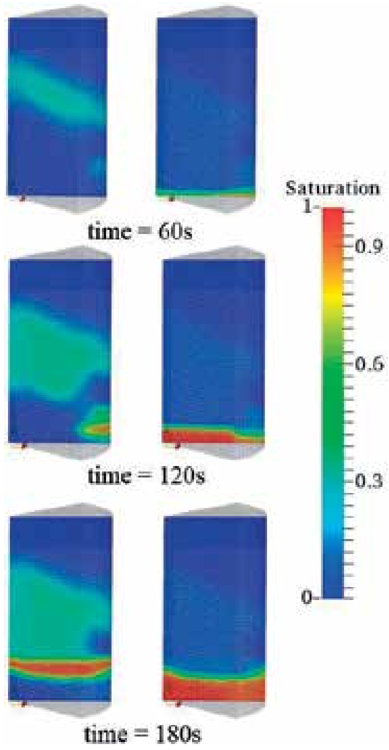

Figure 13. The slag (left) and the molten iron saturation (right) at different time instances.

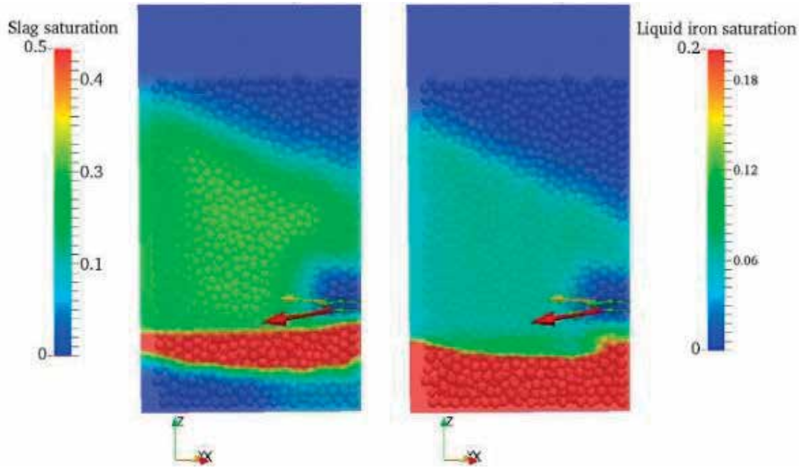

Figure 14. Formation on the dry zone.

The gas phase stream lines for gas inlet velocity of **30** m/s are illustrated in **Figure 15**. The gas velocity loses its energy dramatically as it touches the particles. The recirculation of the gas phase in the raceway besides the redirection of the stream lines in the cohesive zone is observed.

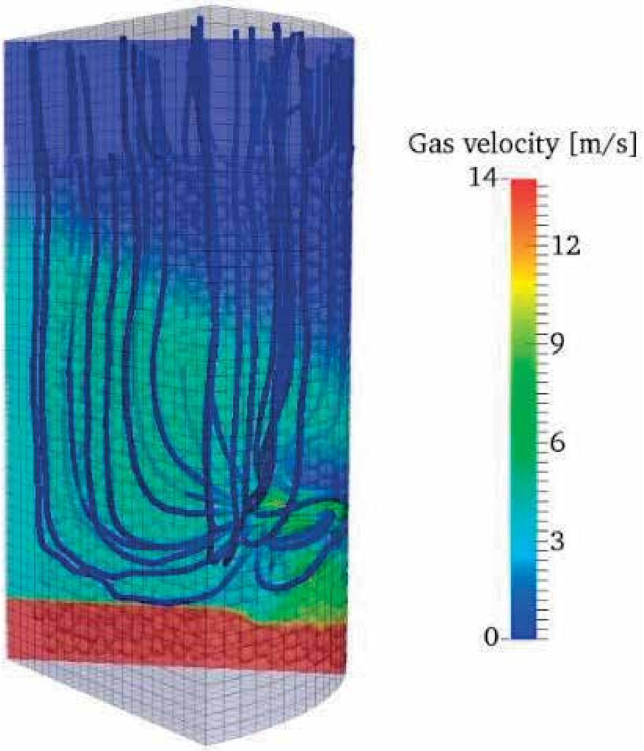

Figure 15. The gas phase streamlines.

6. Conclusion

In this study, a coupled discrete-continuous method known as XDEM is introduced, which is able to model different zones of a blast furnace. The governing equations for both continuous and discrete phases are solved through a coupling procedure for mass, momentum and energy equations. The multi-scale and multi-physics characteristic of the XDEM method make it suitable for the complex phenomena modelling such as blast furnace process. The proposed model was applied to different parts of the blast furnace. The results for the shaft, cohesive zone and dripping zone have been validated and compared to experimental data, which shows the reliability of the XDEM method to take into account the whole blast furnace process in the near future.

Nomenclature

m	Mass (kg)
I	Momentum of inertia $(Kg.m^2)$
F	Force (J)
g	Gravitational acceleration $\left(m.s^{-2}\right)$
K	Momentum transfer $(J.s.m^{-1})$
M	Torque $(N.m)$
$\dot{m}$	Mass flow rate $\left(Kg.m^{-3}.s^{-1}\right)$
p	Pressure (Pa)
t	Time (s)
T	Temperature (K)
V	Volume $\left(m^3\right)$
h	Enthalpy $\left(J.Kg^{-1}\right)$
L_f	Latent heat of fusion $\left(J.Kg^{-1}\right)$
$\acute{m}$	Melting rate $\left(Kg.m^{-3}.s^{-1}\right)$
H_k	Enthalpy of reaction $\left(J.Kg^{-1}\right)$
D	Diffusion coefficient $(m^2.s^{-1})$
k_r	Kinetic frequency factor $(-)$
E	Activation energy $\left(J.mol^{-1}\right)$

R	Universal gas constant $\left(J.mol^{-1}.K^{-1}\right)$
r	Reaction rate

Greek symbols

∂	Differential operator
∇	Nabla operator
Δ	Difference
ρ	Density $\left(Kg.m^{-3}\right)$
ψ	Variable
ν	Velocity $\left(m.s^{-1}\right)$
ϵ	Volume fraction
τ	Stress strain tensor $\left(Kg.m^{-1}.s^{-2}\right)$
μ	Dynamic viscosity $\left(Kg.m^{-1}.s^{-1}\right)$
ϕ	Porosity
α	Heat transfer coefficient $\left(W.m^{-2}.K^{-1}\right)$
β	Mass transfer coefficient $\left(m.s^{-1}\right)$
ω	Angular velocity $(Rad.s^{-1})$
λ	Thermal conductivity $\left(W.m^{-1}.K^{-1}\right)$
$\dot{\omega}$	Reaction source term $\left(mol.m^{-3}.s^{-1}\right)$
γ	Stoichiometric coefficient $(-)$
ε_p	Porosity within a porous particle $(-)$

Subscripts and superscripts

f	Fluid
g	Gas
s	Solid
l	Liquid

i, j	Phase
∞	Ambient
p	Particle
c	Contact force
ref	Reference
rad	Radiation
cond	Conduction
g	Gravitational acceleration
ext	External
eff	Effective

Author details

Bernhard Peters*, Maryam Baniasadi and Mehdi Baniasadi

*Address all correspondence to: bernhard.peters@uni.lu

Faculty of Science, Technology and Communication, University of Luxembourg, Esch-sur-Alzette, Luxembourg

References

[1] Gidaspow D. Multiphase Flow and Fluidisation. San Diego, California: Academic Press; 1994

[2] Tsuji Y, Kawaguchi T, Tanaka T. Discrete particle simulation of two-dimensional fluidized bed. Powder Technology. 1993;**77**:79

[3] Xu BH, Yu AB. Comments on the paper numerical simulation of the gas-solid flow in a fluidized bed by combining discrete particle method with computational fluid dynamics. Chemical Engineering Science. 1998;**53**:2646-2647

[4] Zhu HP, Zhou ZY, Yang RY, Yu AB. Discrete particle simulation of particulate systems: Theoretical developments. Chemical Engineering Science. 2007;**62**:3378-3396

[5] Zhu HP, Zhou ZY, Yang RY, Yu AB. Discrete particle simulation of particulate systems: A review of major applications and findings. Chemical Engineering Science. 2008;**63**:5728-5770

[6] Yu AB, Xu BH. Particle-scale modelling of gas-solid flow in fluidisation. Journal of Chemical Technology and Biotechnology. 2003;**78**(2–3):111-121

[7] Feng YQ, Yu AB. Assessment of model formulations in the discrete particle simulation of gas-solid flow. Industrial & Engineering Chemistry Research. 2004;**43**:8378-8390

[8] Deen NG, Annaland MVS, Van Der Hoef MA, Kuipers JAM. Review of discrete particle modelling of fluidized beds. Chemical Engineering Science. 2007;**62**:28-44

[9] Hoomans BPB, Kuipers JAM, Briels WJ, Van Swaaij WPM. Discrete particle simulation of bubble and slug formation in a two-dimensional gas-fluidized bed: A hard-sphere approach. Chemical Engineering Science. 1996;**51**

[10] Chu KW, Yu AB. Numerical simulation of complex particle-fluid flows. Powder Technology. 2008;**179**:104-114

[11] Chu KW, Wang B, Yu AB, Vince A, Barnett GD, Barnett PJ. CFD-DEM study of the effect of particle density distribution on the multiphase flow and performance of dense medium cyclone. Minerals Engineering. 2009;**22**:893-909

[12] Zhou H, Mo G, Zhao J, Cen K. DEM-CFD simulation of the particle dispersion in a gas-solid two-phase flow for a fuel-rich/lean burner. Fuel. 2011;**90**:1584-1590

[13] Feng YQ, Yu AB. An analysis of the chaotic motion of particles of different sizes in a gas fluidized bed. Particuology. 2008;**6**:549-556

[14] Kafuia KD, Thornton C, Adams MJ. Discrete particle-continuum fluid modelling of gas-solid fluidised beds. Chemical Engineering Science. 2002;**57**:2395-2410

[15] Chattopadhyay K, Isac M, Guthrie RIL. Applications of computational fluid dynamics (CFD) in iron- and steelmaking: Part 1. Ironmaking and Steelmaking. 2010;**37**(8): 554-561

[16] Chattopadhyay K, Isac M, Guthrie RIL. Applications of computational fluid dynamics (CFD) in iron- and steelmaking: Part 2. Ironmaking and Steelmaking. 2010;**37**(8):562-569

[17] Gupta G, Litster JD, White ET, Rudolph VR. Nonwetting flow of a liquid through a packed bed with gas cross-flow. Metallurgical and Materials Transactions B. 1997;**28B**:597-604

[18] Liu DY, Wang GX, Litster JD. Unsaturated liquid percolation flow through nonwetted packed beds. AICHE Journal. 2002;**48**:953-962

[19] Wang GX, Chew SJ, Yu AB, Zulli P. Model study of liquid flow in blast furnace lower zone. Iron and Steel Institute of Japan (ISIJ-International). 1997;**37**:573-582

[20] Yagi J. Mathematical modelling of the flow of four fluids in a packed bed. Journal of Iron and Steel Research, International. 1993;**33**:619-639

[21] Liu DY, Wijeratne S, Litster JD. Scandinavian Journal of Metallurgy. 1998;**26**:79

[22] Dong X, Aibing Y, Yagi J i, Zulli P. Modelling of multiphase flow in a blast furnace: Recent developments and future work. ISIJ International. 2007;**47**(11):1553-1570

[23] Yu AB. Encyclopedea of Condensed Matter Physics, Chapter Powder Processing: Models and Simulations. Oxford, UK: Elsevier; 2005. pp. 401-414

[24] Simsek E, Brosch B, Wirtz S, Scherer V, Krüll F. Numerical simulation of grate_ring systems using a coupled CFD/discrete element method (DEM). Powder Technology. 2009;**193**:266-273

[25] Xu BH, Yu AB. Numerical simulation of the gas-solid flow in a fluidized bed by combining discrete particle method with computational fluid dynamics. Chemical Engineering Science. 1997;**52**:2785

[26] Kaneko Y, Shiojima T, Horio M. Dem simulation of fluidized beds for gas-phase olefin polymerization. Chemical Engineering Science. 1999;**54**:5809

[27] Ranz WE, Marshall WR. Evaporation from drops. Chemical Engineering Progress. 1952; **48**:141

[28] Swasdisevi T, Tanthapanichakoon W, Charinpanitkul T, Kawaguchi T, Tsuji T. Prediction of gas-particle dynamics and heat transfer in a two-dimensional spouted bed. Advanced Powder Technology. 2005;**16**:275

[29] Li JT, Mason DJ. A computational investigation of transient heat transfer in pneumatic transport of granular particles. Powder Technology. 2000;**112**:273

[30] Li JT, Mason DJ. Application of the discrete element modelling in air drying of particulate solids. Drying Technology. 2002;**20**:255

[31] Li JT, Mason DJ, Mujumdar AS. A numerical study of heat transfer mechanisms in gas-solids flows through pipes using a coupled CFD and DEM model. Drying Technology. 2003;**21**:1839

[32] Zhou H, Flamant G, Gauthier D. Dem-les of coal combustion in a bubbling fluidized bed. Part i: Gas-particle turbulent flow structure. Chemical Engineering Science. 2004;**59**:4193

[33] Zhou H, Flamant G, Gauthier D. Dem-les simulation of coal combustion in a bubbling fluidized bed. Part ii: Coal combustion at the particle level. Chemical Engineering Science. 2004;**59**:4205

[34] Malone KF, Xu BH. Particle-scale simulation of heat transfer in liquid-fluidised beds. Powder Technology. 2008;**184**:189-204

[35] Peters B, Hoffmann F. Iron ore reduction predicted by a discrete approach. Chemical Engineering Journal. 2016;**304**:692-702

[36] Peters B, Hoffmann F, Senk D, Babich A, Simoes J, Hausemer L. Experimental and numerical investigation into iron ore reduction in packed beds. Chemical Engineering Science. 2015;**140**:189-200

[37] Copertaro E, Chiariottia P, Estupinan A, Paone N, Peters B, Revel GM. A discrete-continuous approach to describe caco3 decarbonation in non-steady thermal conditions. Powder Technology. 2015;**275**:131-138

[38] Donoso AAE, Peters B. XDEM employed to predict reduction of tungsten oxide in a dry hydrogen atmosphere. International Journal of Refractory Metals and Hard Materials;**2014**

[39] Amir Faghri YZ. Transport Phenomena in Multiphase Systems. Academic Press; 2006

[40] Xiao H, Sun J. Algorithms in a robust hybrid CFD-DEM solver for particle-laden flows. Commun. Comput. Phys. 2011;**9**(2):297-323

[41] Hertz H. Ueber die beruehrung elastischer koerper. Journal fur die Reine und Angewandte Mathematik. 1881;**92**:156-171

[42] Mindlin R. Compliance of elastic bodies in contact. Appl. Mech. 1949;**16**:259-268

[43] Murayama T, Ono Y, Kawai Y. Step-wise reduction of hematite pellets with CO-CO2 gas mixtures. Transactions ISIJ. 1978;**18**:579-587

[44] Peters B, Hoffmann F. Iron ore reduction predicted by a discrete approach. Chemical Engineering Journal. 2016;**304**:692-702

[45] Peters B, Hoffmann F, Senk D, Babich A. Experimental and numerical investigation into iron ore reduction in packed beds. Chemical Engineering Science. 2016;**140**:189-200

[46] A new approach for studying softening and melting behavior of particles in a blast furnace cohesive zone. Metallurgical and Materials Transactions B. 2015;**46**(2):977-992

[47] Yang W, Zhou Z, Yu A, Pinson D. Particle scale simulation of softening–melting behaviour of multiple layers of particles in a blast furnace cohesive zone. Powder Technology. 2015;**279**:134-145

[48] Bakker T. Softening in the blast furnace process: local melt formation as the trigger for softening of ironbearing burden materials, PhD thesis, Delft University of Technology, 1999

[49] Kemppainen A, Iljana M, Heikkinen E, Fabritius T. Softening behavior of iron ore pellets in the cohesive zone of a blast furnace contact data summary key words. ISIJ International. 2015;**55**(10):2039-2046

[50] Baniasadi M, Baniasadi M, Peters B. Coupled CFD-DEM with heat and mass transfer to investigate the melting of a granular packed bed. Chemical Engineering Science;**178**:136-145

[51] Hao Y, Tao Y-X. Non-thermal equilibrium melting of granular packed bed in horizontal forced convection. Part i: Experiment. International Journal of Heat and Mass Transfer. 2003;**46**(26):5017-5030

[52] Baniasadi M, Baniasadi M, Peters B. Application of the extended discrete element method (XDEM) in the melting of a single particle. AIP Conference Proceedings. 2017;**1863**:180003

[53] Ghosh S, Viswanathan NN, Ballal NB. Flow phenomena in the dripping zone of blast furnace: A review. Steel Research International. 2017;**87**(9999)

[54] Baniasadi M, Peters B. Preliminary Investigation on the Capability of eXtended Discrete Element Method for Treating the Dripping Zone of a Blast Furnace. 2018;**58**(1)

[55] Szekely J, Kajiwara Y. The interaction between gas and liquid flow in a simulated blast furnace: A preliminary investigation. Metallurgical Transactions B. 1979;**10B**:447

[56] Baniasadi M, Peters B. Resolving multiphase flow through packed bed of solid particles using eXtended discrete element method with porosity calculation. Industrial and Engineering Chemistry Research. 2018;**56**(41):11996-12008

Section 3

Advanced Applications

Chapter 8

Photoelectrochemistry of Hematite

Yasuhisa Maeda

Additional information is available at the end of the chapter

http://dx.doi.org/10.5772/intechopen.73228

Abstract

It was possible to prepare a hematite film by electrochemical deposition of iron oxide in aqueous solution and its heat treatment at 500°C or higher temperature in air. The deposition process of iron oxide film from current and potential pulse methods was mentioned in relation to the equilibrium potential for iron oxide. The hematite in aqueous solution showed a clear photoanodic current due to visible light irradiation. The photo-oxidation response of hematite electrode to organic and inorganic materials in aqueous solution was summarized through the examples of citric acid, Pb^{2+} and aniline.

Keywords: iron oxide, electrochemical deposition, hematite, photoelectrochemistry, visible light

1. Introduction

Hematite (α-Fe_2O_3), one of iron oxides, has merits of abundance, harmlessness and stability. Hematite is expected to be utilized as a photo-functional material for the purpose of conversion of visible light energy to chemical and electric energy because it is an n-type semiconductor with band gap energy of about 2.0 eV. There are several reports concerning photoelectrochemical characteristics [1–7], photo-oxidation of water [8–15] and photocatalytic water purification [16–21] by using hematite. It is known that oxygen evolution due to photo-oxidation of water could occur on the hematite irradiated with visible light. This may be an interesting and important process from the viewpoint of artificial photosynthesis. Hematite is also one of the candidates for photocatalyst acting under visible light irradiation. Titanium dioxide with band gap energy of about 3.0 eV shows strong photocatalytic performance for environmental purification such as air purification, anti-soiling, self-cleaning, deodorizing, water purification and anti-bacterial [22–23], but it has disadvantage for utilization of visible light energy. In order to use hematite for photocatalysis and photosynthesis effectively, it is necessary to make clear its photoresponse to chemical species. Knowledge about hematite electrode/electrolytic solution interface is important to understand a reactivity of photo-generated hole in the valence band of hematite to chemical species during irradiation. For the use of hematite as a photo-functional material, preparation of hematite film may be useful from the aspect of its repetitive performance. We have prepared the hematite film by electrochemical deposition of iron oxide and its heat treatment, and studied photo-oxidation of organic and inorganic materials on the hematite photoelectrode. Investigation of photo-oxidation of organic materials on hematite may lead to a new development of organic materials synthesis based on visible light energy conversion.

In this chapter, I would like to describe photoelectrochemistry of hematite in terms of electrochemical preparation of iron oxide film, photoelectrochemical characterization of hematite and photo-oxidation reaction of chemical species on hematite mainly based on the results we have obtained [24–29].

2. Electrochemical preparation of iron oxide film

On photocatalysis and photo-conversion by using hematite, preparation of hematite film is useful from the point of view of repetitive performance. Iron oxide film is prepared by spray pyrolysis, electrochemical deposition, sputtering method and so on. Electrochemical method may provide easy and reproducible preparation of iron oxide film. Here, based on the results we have obtained, the current and potential pulse deposition process of iron oxide film is mentioned as follows.

2.1. Current pulse deposition of iron oxide film

An iron oxide film (geometric surface area of 1.0 cm^2) was prepared on a titanium substrate by current pulse deposition with repetition of cathodic pulse (current (I_c); time (t_c): 1 s) and anodic pulse (current (I_a); time (t_a): 1 s) as shown in **Figure 1**. The surface of titanium substrate was polished with alumina powder, immersed in aqueous HCl solution, washed with pure water and cleaned ultrasonically before electrolysis. The working electrode of titanium substrate and

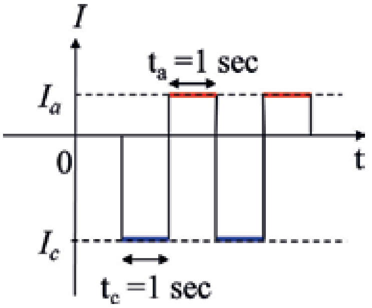

Figure 1. Current pulse deposition of iron oxide film with repetition of cathodic pulse (current: I_c, time: t_c = 1 s) and anodic pulse (current: I_a, time: t_a = 1 s).

the counter electrode of iron plate were connected to a potentio-galvanostat with a function generator. The aqueous solution of 10 mM $FeCl_2$–0.15 M NaCl (pH = 4.4) under oxygen gas bubbling was used for the electrochemical deposition of iron oxide film. The temperature of this solution was kept constant at 25°C by circulation of thermo-stated water [29, 26].

Figure 2 shows the potential of titanium working electrode during the electrolysis by repetition of cathodic pulse ($I_c = -7$ mA, $t_c = 1$ s) and anodic pulse ($I_a = +1$ mA, $t_a = 1$ s) in aqueous 10 mM $FeCl_2$–0.15 M NaCl solution under O_2 bubbling for 100 s. The potential changed periodically with the cathodic and anodic current pulses. The potential depending on anodic current pulse approached to the value of −0.68 V vs. Ag/AgCl gradually. In the case of galvanostatic deposition with the current of −7 mA for 50 s in the same solution as above, the potential of working electrode became almost constant value of −1.60 V vs. Ag/AgCl.

Figure 3 shows the XRD of the film by current pulse deposition ($I_c = -7$ mA, $I_a = +1$ mA, $t_c = t_a = 1$ s) for 100 s, the upper representing the pattern of the film after heat treatment at the temperature of 600°C for 1 h in air and the lower pattern corresponding to the as-deposited film before heat treatment. The diffraction peaks of Fe_3O_4 (magnetite) and FeO (wustite) and the peaks of α-Fe_2O_3 appeared on the film before and after heat treatment, respectively. On the as-deposited film by galvanostatic reduction (current: −7 mA) for 50 s in the presence of O_2, the diffraction peaks of $Fe(OH)_2$, FeO and Fe were confirmed, but the peak of Fe_3O_4 was not observed. From a consideration of the XRD result, the reaction for the formation of iron oxide film by current pulse deposition in the solution with O_2 gas bubbling could be shown as Eqs. (1)–(4). The reaction in the heat treatment of film in air could be represented as Eqs. (5) and (6).

$$1/2O_2 + H_2O + 2e^- \rightarrow 2OH^- \tag{1}$$

$$Fe^{2+} + 2OH^- \rightarrow Fe(OH)_2 \tag{2}$$

$$Fe(OH)_2 \rightarrow FeO + H_2O \tag{3}$$

$$3FeO + H_2O \rightarrow Fe_3O_4 + 2H^+ + 2e^- \tag{4}$$

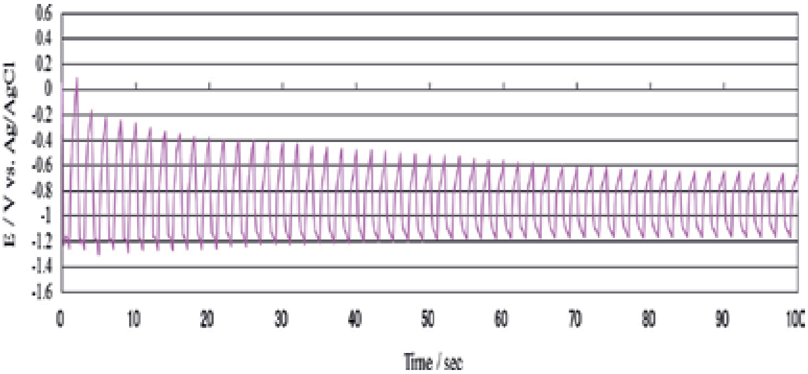

Figure 2. Change of electrode potential of working electrode by repetition of cathodic pulse ($I_c = -7$ mA, $t_c = 1$ s) and anodic pulse ($I_a = +1$ mA, $t_a = 1$ s) in aqueous 10 mM $FeCl_2$–0.15 M NaCl solution under O_2 bubbling for 100 s.

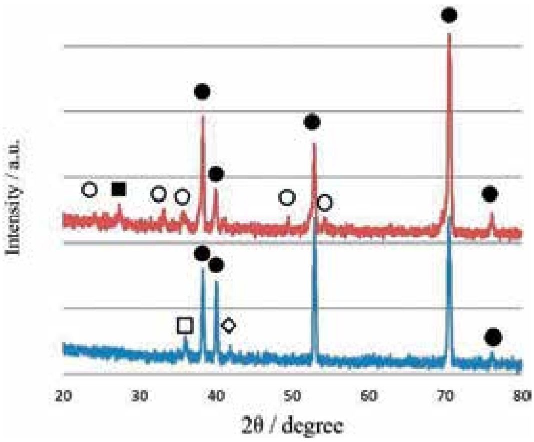

Figure 3. XRD of the iron oxide film deposited on the titanium by current pulse method (I_c = −7 mA, I_a = +1 mA, t_c = t_a = 1 s) in aqueous 10 mM $FeCl_2$–0.15 M NaCl solution under O_2 bubbling for 100 s (the lower pattern), and heated at 600°C for 1 h in air (the upper pattern). ● titanium ○ hematite □ magnetite ◇ wustite ■ titanium dioxide (rutile).

$$2FeO + 1/2O_2 \rightarrow Fe_2O_3 \tag{5}$$

$$2/3Fe_3O_4 + 1/6O_2 \rightarrow Fe_2O_3 \tag{6}$$

Figure 4a shows the SEM image of the film deposited on the titanium by repetition of cathodic pulse (I_c = −7 mA, t_c = 1 s) and anodic pulse (I_a = +1 mA, t_a = 1 s) in aqueous 10 mM $FeCl_2$–0.15 M NaCl solution under O_2 bubbling for 100 s, and heated at 600°C for 1 h in air. The film with the thickness of about 1.0 μm had the network morphology. As shown in **Figure 4b**, the film prepared by galvanostatic reduction with the current of −7 mA for 50 s in the same solution as above, and heated in the same condition showed the similar morphology, but less homogeneous deposition compared with the film by the current pulse method.

The current pulse deposition of iron oxide film in the solution under N_2 gas bubbling was compared with that in the solution under O_2 gas bubbling. **Figure 5** shows the potential of titanium working electrode during the electrolysis by repetition of cathodic pulse (I_c = −7 mA, t_c = 1 s) and anodic pulse (I_a = +1 mA, t_a = 1 s) in aqueous 10 mM $FeCl_2$–0.15 M NaCl solution under N_2 bubbling for 100 s. The appearance of iron, wustite and magnetite XRD peaks was confirmed in the as-deposited film due to the repetition of current pulse in this solution as shown in **Figure 6**. The film after heat treatment at 600°C for 1 h in air had the hematite structure. The SEM image of this hematite film is shown in **Figure 7**. The deposition of particles was observed in this film. The hematite film preparation under N_2 bubbling could be represented as the process of current pulse deposition of iron oxide film (Eqs. (7)–(9), (4)) and its thermal oxidation process (Eqs. (10)–(12)).

$$Fe^{2+} + 2e^- \rightarrow Fe \tag{7}$$

$$Fe + H_2O \rightarrow FeO + 2H^+ + 2e^- \tag{8}$$

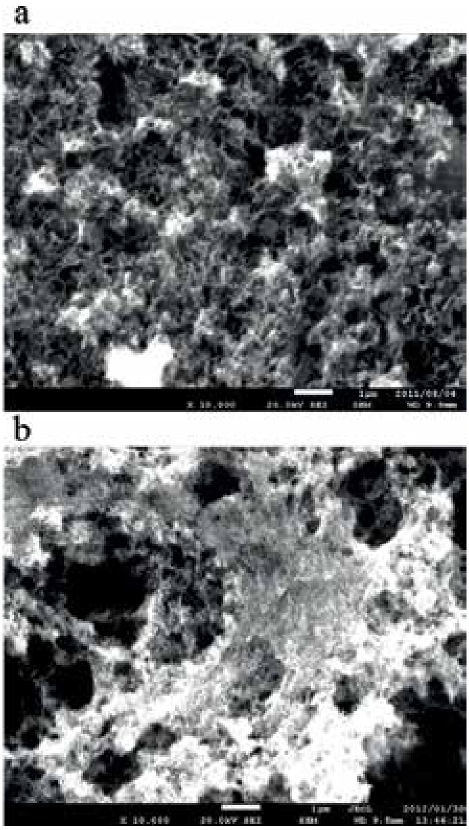

Figure 4. SEM image of the iron oxide film by current pulse deposition ($I_c = -7$ mA, $I_a = +1$ mA, $t_c = t_a = 1$ s) for 100 s (a) and galvanostatic reduction (current: −7 mA) for 50 s (b) in aqueous 10 mM $FeCl_2$–0.15 M NaCl solution under O_2 bubbling, and heated at 600°C for 1 h in air.

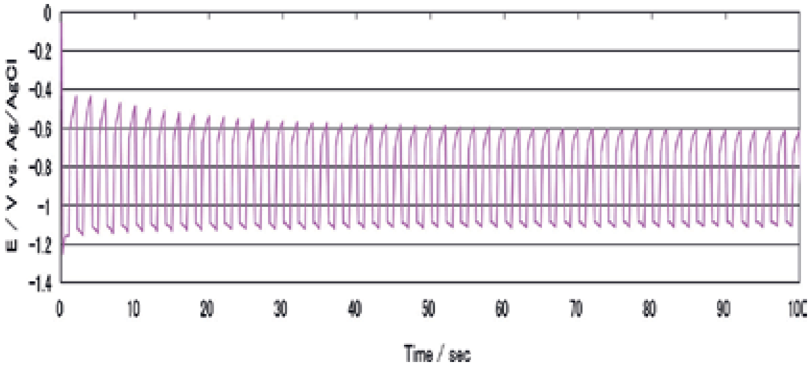

Figure 5. Change of electrode potential of working electrode by repetition of cathodic pulse ($I_c = -7$ mA, $t_c = 1$ s) and anodic pulse ($I_a = +1$ mA, $t_a = 1$ s) in aqueous 10 mM $FeCl_2$–0.15 M NaCl solution under N_2 bubbling for 100 s.

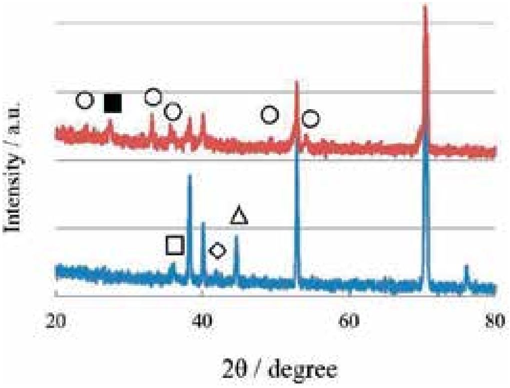

Figure 6. XRD of the iron oxide film deposited on the titanium by current pulse method ($I_c = -7$ mA, $I_a = +1$ mA, $t_c = t_a = 1$ s) in aqueous 10 mM $FeCl_2$–0.15 M NaCl solution under N_2 bubbling for 100 s (the lower pattern), and heated at 600°C for 1 h in air (the upper pattern). ○ hematite □ magnetite ◇ wustite △ iron ■ titanium dioxide (rutile).

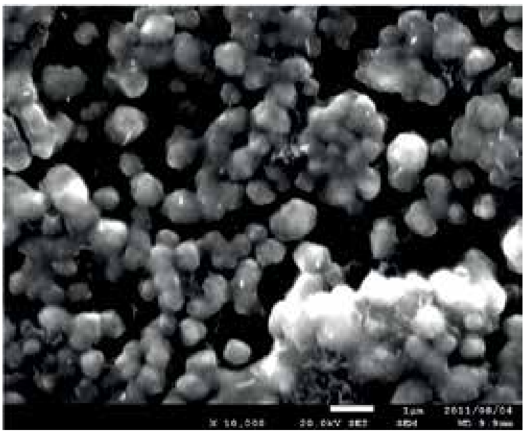

Figure 7. SEM image of the iron oxide film by current pulse deposition ($I_c = -7$ mA, $I_a = +1$ mA, $t_c = t_a = 1$ s) for 100 s in aqueous 10 mM $FeCl_2$–0.15 M NaCl solution under N_2 bubbling, and heated at 600°C for 1 h in air.

$$3Fe + 4H_2O \rightarrow Fe_3O_4 + 8H^+ + 8e^- \tag{9}$$

$$2Fe + 3/2O_2 \rightarrow Fe_2O_3 \tag{10}$$

$$2FeO + 1/2O_2 \rightarrow Fe_2O_3 \tag{11}$$

$$2/3Fe_3O_4 + 1/6O_2 \rightarrow Fe_2O_3 \tag{12}$$

For the electrochemical reactions of (1), (4), (7), (8) and (9), the corresponding equilibrium potentials can be evaluated by using the values of standard chemical potential of −237.178, −157.293, −91.2, −245.211 and −1015.359 KJ/mol [30] as $\mu^0(H_2O)$, $\mu^0(OH^-)$, $\mu^0(Fe^{2+})$, $\mu^0(FeO)$ and $\mu^0(Fe_3O_4)$, respectively. The equilibrium potentials (versus normal hydrogen electrode, NHE) of (1), (4), (7), (8) and (9) are represented in Eq. (13)–(17).

$$E_{eq}(\mathrm{O_2/OH^-}) = 0.401 - 0.0591 \times \log_{10} a_{\mathrm{OH^-}} \tag{13}$$

$$E_{eq}(\mathrm{Fe_3O_4/FeO}) = -0.220 - 0.0591 \times p\mathrm{H} \tag{14}$$

$$E_{eq}\left(\mathrm{Fe^{2+}/Fe}\right) = -0.473 + 0.0296 \times \log_{10} a_{\mathrm{Fe^{2+}}} \tag{15}$$

$$E_{eq}(\mathrm{FeO/Fe}) = -0.042 - 0.0591 \times p\mathrm{H} \tag{16}$$

$$E_{eq}(\mathrm{Fe_3O_4/Fe}) = -0.086 - 0.0591 \times p\mathrm{H} \tag{17}$$

The electrochemical formation of magnetite could be also considered in Eq. (18) and this equilibrium potential is represented as Eq. (19).

$$3\mathrm{Fe^{2+}} + 4\mathrm{H_2O} \rightarrow \mathrm{Fe_3O_4} + 8\mathrm{H^+} + 2\mathrm{e^-} \tag{18}$$

$$E_{eq}\left(\mathrm{Fe_3O_4/Fe^{2+}}\right) = 1.072 - 0.2364 \times p\mathrm{H} - 0.0886 \times \log_{10} a_{\mathrm{Fe^{2+}}} \tag{19}$$

The electrochemical reactions concerning hematite are shown in Eqs. (20)–(23).

$$2\mathrm{FeO} + \mathrm{H_2O} \rightarrow \mathrm{Fe_2O_3} + 2\mathrm{H^+} + 2\mathrm{e^-} \tag{20}$$

$$2\mathrm{Fe} + 3\mathrm{H_2O} \rightarrow \mathrm{Fe_2O_3} + 6\mathrm{H^+} + 6\mathrm{e^-} \tag{21}$$

$$2\mathrm{Fe_3O_4} + \mathrm{H_2O} \rightarrow 3\mathrm{Fe_2O_3} + 2\mathrm{H^+} + 2\mathrm{e^-} \tag{22}$$

$$2\mathrm{Fe^{2+}} + 3\mathrm{H_2O} \rightarrow \mathrm{Fe_2O_3} + 6\mathrm{H^+} + 2\mathrm{e^-} \tag{23}$$

The corresponding equilibrium potential evaluated by using the standard chemical potential of hematite, −743.608 KJ/mol are represented in Eqs. (24)–(27).

$$E_{eq}(\mathrm{Fe_2O_3/FeO}) = -0.083 - 0.0591 \times p\mathrm{H} \tag{24}$$

$$E_{eq}(\mathrm{Fe_2O_3/Fe}) = -0.055 - 0.0591 \times p\mathrm{H} \tag{25}$$

$$E_{eq}(\mathrm{Fe_2O_3/Fe_3O_4}) = 0.192 - 0.0591 \times \mathrm{pH} \tag{26}$$

$$E_{eq}\left(\mathrm{Fe_2O_3/Fe^{2+}}\right) = 0.779 - 0.1773 \times p\mathrm{H} - 0.0591 \times \log_{10} a_{\mathrm{Fe^{2+}}} \tag{27}$$

These standard equilibrium potentials are slightly different from the values in Pourbaix Diagram [31] due to the used standard chemical potential of component. With regard to the equilibrium potential in the case of pH = 4.4 and $\mathrm{Fe^{2+}}$ concentration of 10 mM, $E_{\mathrm{eq}}(\mathrm{O_2/OH^-})$ is 0.969 (0.747), E_{eq} ($\mathrm{Fe_3O_4/FeO}$) -0.480 (−0.702), E_{eq} ($\mathrm{Fe^{2+}/Fe}$) -0.532 (−0.754), E_{eq} (FeO/Fe) -0.302 (−0.524), E_{eq} ($\mathrm{Fe_3O_4/Fe}$) -0.346 (−0.568), E_{eq} ($\mathrm{Fe_3O_4/Fe^{2+}}$) 0.209 (−0.013), E_{eq} ($\mathrm{Fe_2O_3/FeO}$) -0.343 (−0.565), E_{eq} ($\mathrm{Fe_2O_3/Fe}$) -0.315 (−0.537), E_{eq} ($\mathrm{Fe_2O_3/Fe_3O_4}$) -0.068 (−0.290) and E_{eq} ($\mathrm{Fe_2O_3/Fe^{2+}}$) 0.117 V vs. NHE (−0.105 V vs. Ag/AgCl). The electrode potential approached to the equilibrium potential of $\mathrm{Fe_3O_4/FeO}$ system with repetition of anodic current pulse as shown in **Figures 3** and **5**.

2.2. Potential pulse deposition of iron oxide film

Potential pulse method as shown in **Figure 8** is also useful in preparation of iron oxide film [28]. In this case, electrochemical reduction and oxidation occurs with repetition of a periodic change in the working electrode potential between cathodic potential (E_c) with the time of t_c and anodic potential (E_a) with t_a. The working electrode of titanium substrate and the counter electrode of graphite were connected to a potentio-galvanostat with a function generator. The aqueous solution of 10 mM $FeCl_2$–0.1 M KCl (pH = 4.4) under O_2 or N_2 gas bubbling was used for the electrochemical deposition of iron oxide film.

Figure 9 shows the XRD of the film prepared by potential pulse deposition ($E_c = -1.0$ V vs. Ag/AgCl, $t_c = 1$ s, $E_a = 0.2$ V vs. Ag/AgCl, $t_a = 1$ s) for 30 min under O_2 bubbling to the solution, the upper representing the pattern of the film after heat treatment at the temperature of 500°C for 1 h in air and the lower that before heat treatment. The magnetite peaks and the wustite peak were observed on the as-deposited film. Because the value of 0.2 V vs. Ag/AgCl of E_a is more positive than the equilibrium potentials of E_{eq} (Fe_2O_3./FeO) of −0.565, E_{eq} (Fe_2O_3/Fe) of −0.537, E_{eq} (Fe_2O_3/Fe_3O_4) of −0.290 and E_{eq} (Fe_2O_3/Fe^{2+}) of −0.105 V vs. Ag/AgCl, there is a possibility of anodic formation of hematite. But the hematite peaks did not appear on the as-deposited film. The hematite structure was confirmed after heat treatment. **Figure 10** shows the XRD of the film by potential pulse deposition under N_2 bubbling to the solution before and after heat treatment. The peaks of magnetite and wustite and hematite peaks were observed on the film before and after heat treatment, respectively. **Figure 11** shows the SEM images of the hematite films prepared from the solution with O_2 bubbling and with N_2 bubbling. A different morphology of these hematite films was observed. The deposition state of iron oxide film was

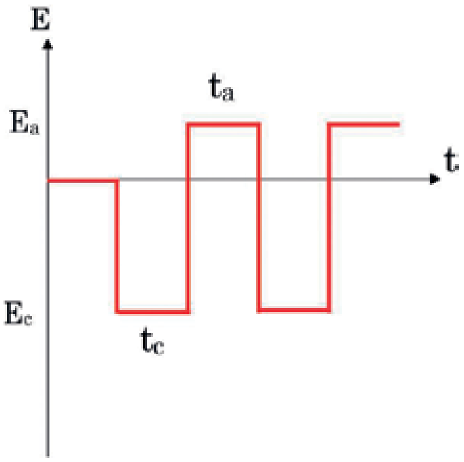

Figure 8. Potential pulse deposition of iron oxide film with repetition of cathodic pulse (potential: E_c, time: t_c) and anodic pulse (potential: E_a, time: t_a).

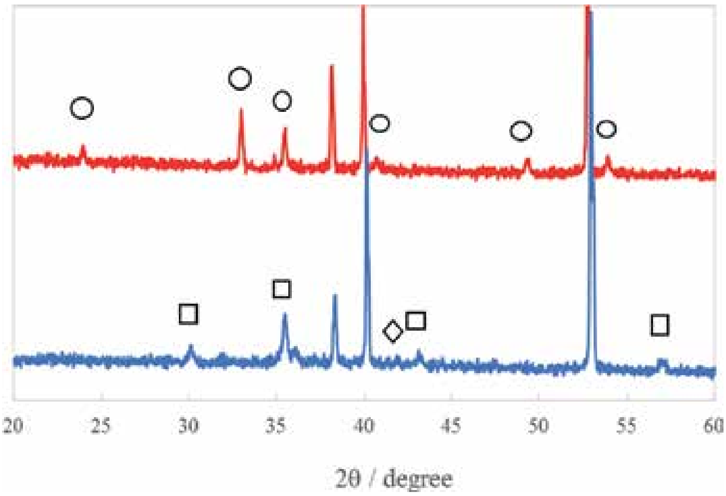

Figure 9. XRD of the iron oxide film deposited on the titanium by potential pulse method ($E_c = -1.0$ V, $E_a = 0.2$ V vs. Ag/AgCl, $t_c = t_a = 1$ s) in aqueous 10 mM $FeCl_2$–0.1 M KCl solution under O_2 bubbling for 30 min (the lower pattern), and heated at 500°C for 1 h in air (the upper pattern). ○ hematite □ magnetite ◇ wustite.

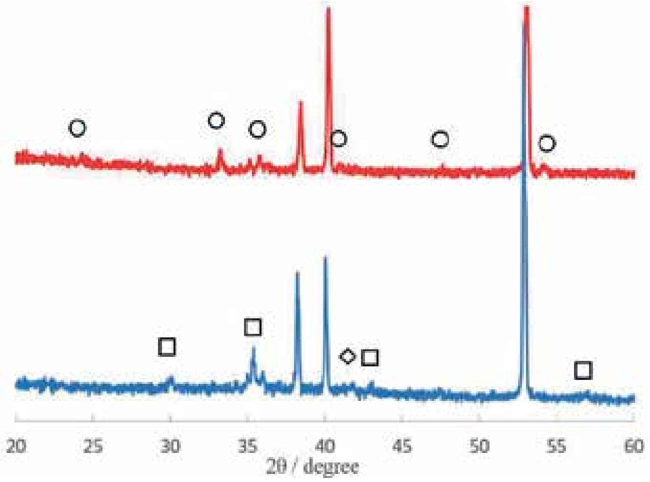

Figure 10. XRD of the iron oxide film deposited on the titanium by potential pulse method ($E_c = -1.0$ V, $E_a = 0.2$ V vs. Ag/AgCl, $t_c = t_a = 1$ s) in aqueous 10 mM $FeCl_2$–0.1 M KCl solution under N_2 bubbling for 30 min (the lower pattern), and heated at 500°C for 1 h in air (the upper pattern). ○ hematite □ magnetite ◇ wustite.

dependent on current magnitude, potential value and pulse width. A photocurrent response of hematite film was strongly related to the deposition state of iron oxide by current and potential methods.

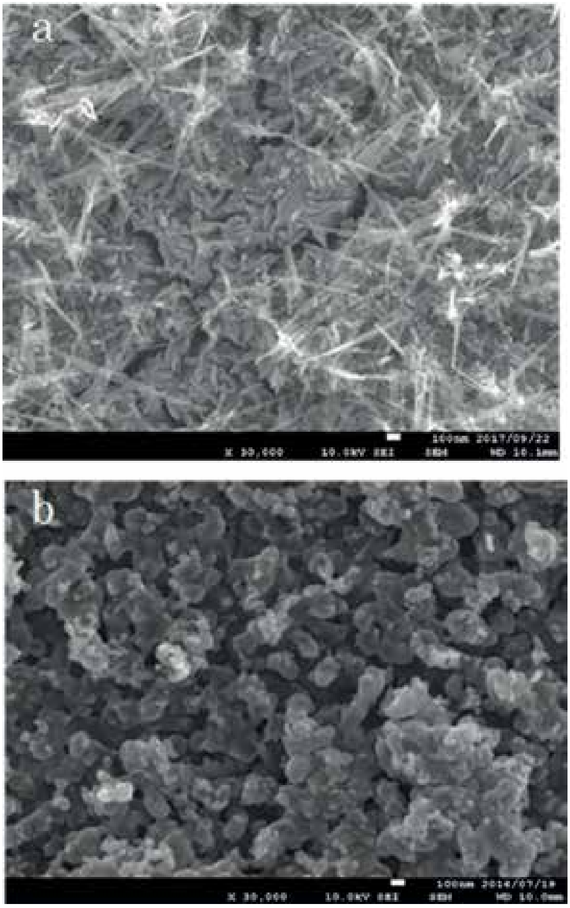

Figure 11. SEM image of the iron oxide film by potential pulse deposition ($E_c = -1.0$ V, $E_a = 0.2$ V vs. Ag/AgCl, $t_c = t_a = 1$ s) for 30 min in aqueous 10 mM $FeCl_2$–0.1 M KCl solution under O_2 bubbling (a) and N_2 bubbling (b), and heated at 500°C for 1 h in air.

3. Photoelectrochemical characterization of hematite

In order to characterize the hematite film in the aspect of a functional material for photocatalytic water purification and artificial photosynthesis, understanding of hematite electrode/electrolytic solution interface is important. Here, the Mott-Schottky relation and photocurrent response are mentioned as follows.

3.1. Mott-Schottky relation of hematite electrode/electrolytic solution interface

The measurement of capacitance for hematite electrode/electrolytic solution interface is useful in understanding of properties of hematite as an n-type semiconductor. The hematite film connected to a lead wire was used as a hematite working electrode. The capacitance of hematite electrode/electrolytic solution interface (C) was measured at a different electrode potential (E). At the semiconductor electrode/electrolyte interface, Motto-Schottky relation can be observed as represented by Eq. (28).

$$\frac{1}{C^2} = \frac{2}{eN\varepsilon\varepsilon^0}\left(E - E_{fb}\right) \tag{28}$$

where e is the quantity of charge on an electron, N the carrier density, ε is the dielectric constant of electrode material, ε^0 is the permittivity of free space and E_{fb} is the flat-band potential corresponding to the potential indicating no band bending of semiconductor electrode.

Figure 12a, **b** shows the plots of $1/C^2$ against E in 0.1 M aqueous Na_2SO_4 solution (pH = 5.7) for the hematite electrodes prepared from current pulse deposition (I_c = −7 mA, I_a = +1 mA, t_c = t_a = 1 s) under O_2 bubbling and N_2 bubbling for 100 s, respectively. The capacitance measurement was carried out with the frequency of 1 kHz. The values of flat-band potential (E_{fb}) and carrier density (N) of these hematite electrodes were −0.57 V vs. Ag/AgCl (−0.35 V vs. NHE) and 1.35×10^{18} cm^{-3} (a), −0.33 V vs. Ag/AgCl (−0.11 V vs. NHE) and 3.53×10^{18} cm^{-3} (b) from the intercept of the linear portion extrapolated to the potential axis and its slope by using ε^0 of 120. The Mott-Schottky relation was also confirmed on the hematite electrode

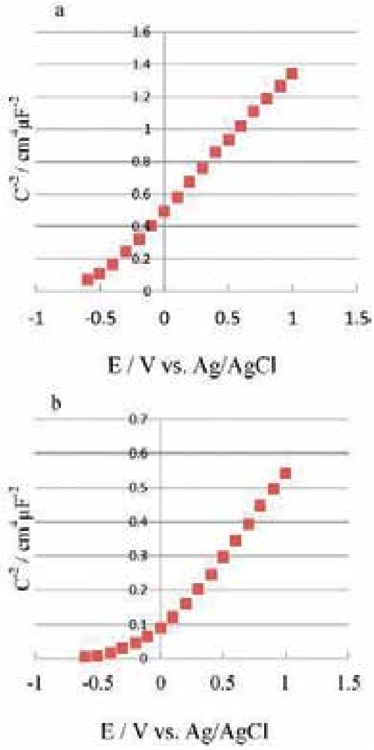

Figure 12. Plots of $1/C^2$ against E in 0.1 M aqueous Na_2SO_4 solution (pH = 5.7) for the hematite electrodes prepared from current pulse deposition (I_c = −7 mA, I_a = +1 mA, t_c = t_a = 1 s) under O_2 bubbling (a) and N_2 bubbling (b) for 100 s.

prepared from potential pulse deposition (E_c = −1.0 V vs. Ag/AgCl, E_a = +0.2 V vs. Ag/AgCl, $t_c = t_a = 1$ s) under N_2 bubbling for 30 min and heat treatment at 500°C for 1 h in air. In this case, the values of E_{fb} of 0.00 V vs. Ag/AgCl (+0.22 V vs. NHE) and N of 4.52×10^{18} cm^{-3} were obtained in 1.0 M aqueous Na_2SO_4 solution (pH = 5.9). According to the other researchers, the hematite prepared by thermal oxidation of iron showed E_{fb} of −0.95 V vs. SCE (−0.68 V vs. NHE) and N of about 3×10^{18} cm^{-3} in 1.0 M aqueous NaOH solution [1], and that prepared by a spray-pyrolytic method E_{fb} of −0.74 V vs. SCE (−0.47 V vs. NHE) and N of 2.2×10^{20} cm^{-3} in 1.0 M NaOH solution [9]. Supposing a pH dependence of E_{fb} was 59 mV/pH, the value of F_{fb} for above-mentioned hematite in the solution (pH = 5.7) would be −0.19 and 0.02 V vs. NHE. These mean that the values of E_{fb} and N for hematite depend on preparation methods. Because the value of E_{fb} for n-type semiconductor electrode is approximately equal to the potential for the bottom of conduction band, the hematite from current pulse deposition under O_2 bubbling to the solution may have more negative potential of the conduction band.

3.2. Photocurrent response of hematite to visible light irradiation

In the n-type semiconductor electrode/electrolytic solution interface, the Schottky barrier due to the band bending is formed at more positive potential of semiconductor electrode than flat-band potential as shown in **Figure 13**. In this case, no currents may flow on the electrode because of the existence of the Schottky barrier in the dark. Under irradiation of the light with higher energy than band gap, the transfer of photo-generated electrons to the bulk and that of holes to the surface of n-type semiconductor could proceed due to the band bending and thus photoanodic current may flow on the electrode.

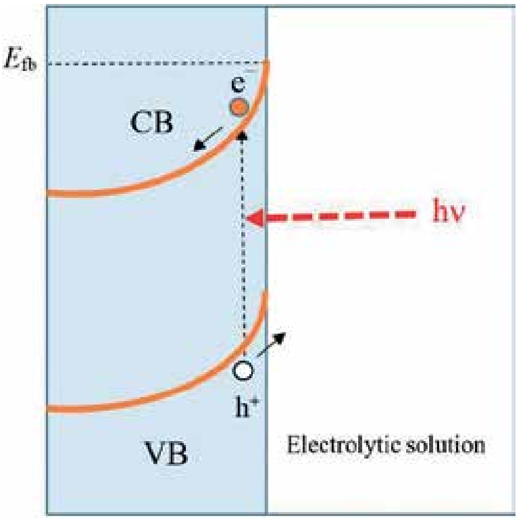

Figure 13. Interface of n-type semiconductor electrode/electrolytic solution VB: Valence band, CB: Conduction band, e^-: Photo-generated electron, h^+: Photo-generated hole.

Figure 14a, **b** shows the photocurrent response of the hematite prepared current pulse deposition under O_2 and N_2 bubbling to the solution, respectively. In this case, repetitive on–off irradiation of the visible light (wavelength: 490 nm, light intensity: 3.8 mW/cm^2) was supplied to the surface of the hematite electrode at 1.0 V vs. Ag/AgCl in 0.1 M aqueous Na_2SO_4 solution. A clear photoanodic current was observed in both the hematite electrodes, but the hematite from N_2 bubbling showed a higher photocurrent. The hematite prepared from potential pulse deposition under N_2 bubbling also had a higher photocurrent response compared with that prepared under O_2 bubbling.

The photocurrent response of the iron oxide depending on heat treatment temperature (100–600°C) in air is shown in **Figure 15**. In this case, the iron oxide film was prepared from potential pulse deposition (E_c = −1.0 V, E_a = +0.2 V, t_c = t_a = 1 s) under N_2 bubbling for 30 min. The iron oxide treated at different temperatures was irradiated with the visible light (wavelength: 490 nm, light intensity: 3.8 mW/cm^2) at the potential of 1.0 V vs. Ag/AgCl in 0.1 M aqueous Na_2SO_4 solution. The XRD of the film with the corresponding heat treatment temperatures is also shown in **Figure 16**. No photocurrent was detected on the

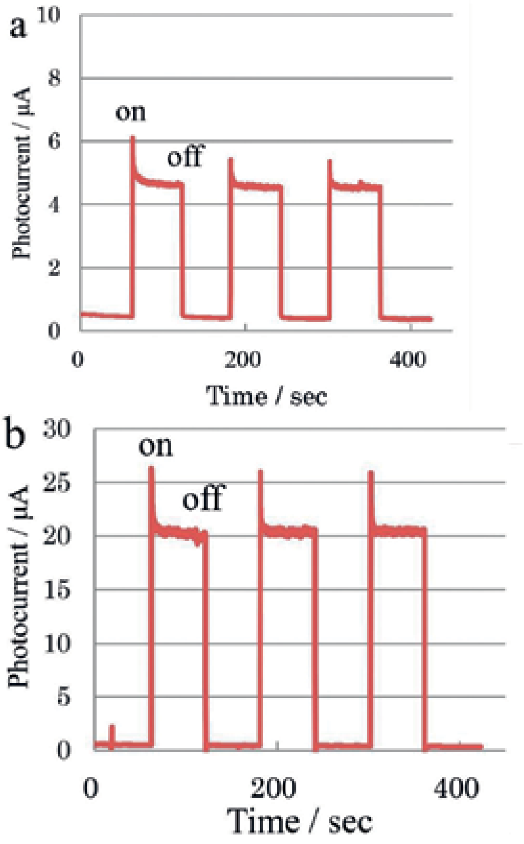

Figure 14. Photocurrent response of the hematite prepared from current pulse deposition (I_c = −7 mA, I_a = +1 mA, t_c = t_a = 1 s) for 100 s in aqueous 10 mM $FeCl_2$–0.15 M NaCl solution under O_2 bubbling (a) and N_2 bubbling (b), and heated at 600°C for 1 h in air.

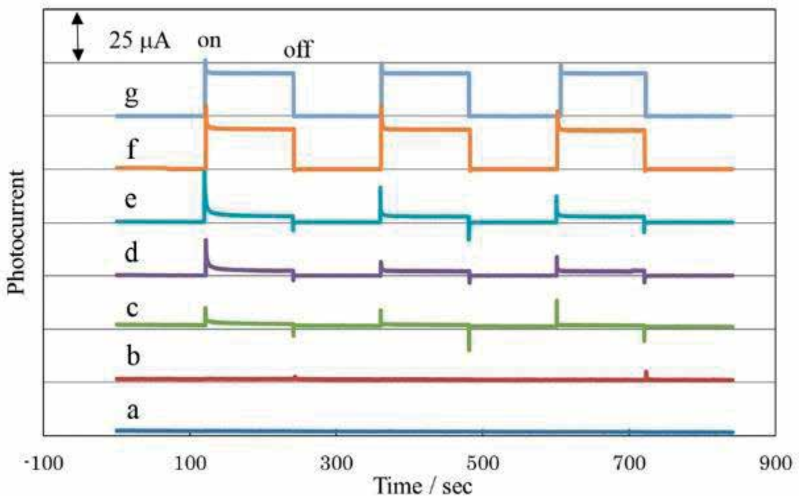

Figure 15. Dependence of photocurrent response of the iron oxide upon heat treatment temperature at 100–600°C in air iron oxide was prepared from potential pulse deposition ($E_c = -1.0$ V, $E_a = 0.2$ V vs. Ag/AgCl, $t_c = t_a = 1$ s) for 30 min in aqueous 10 mM $FeCl_2$–0.1 M KCl solution under N_2 bubbling. The as-deposited film (a) was heated at different temperatures of 100°C (b), 200°C (c), 300°C (d), 400°C (e), 500°C (f) and 600°C (g).

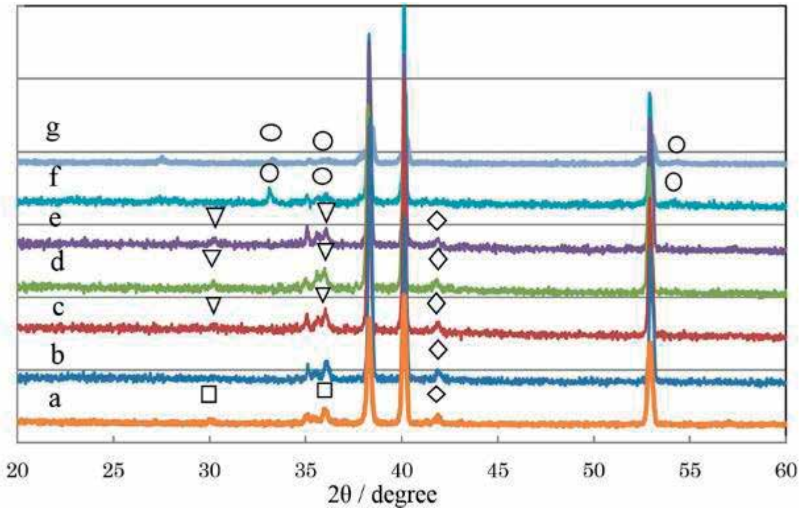

Figure 16. XRD of the iron oxide with same heat treatment as that in **Figure 15**. ○ hematite □ magnetite ◇ wustite ▽ maghemite.

as-deposited film. This suggests that both magnetite and wustite may have no ability as a photoelectrode. The iron oxide film heat treated at 200°C or higher temperature showed a photoanodic current response and a remarked photocurrent was observed on the film heat treated at 500°C. It has been reported that the DTA peak of transition from magnetite to maghemite (γ-Fe_2O_3) and that of transition from maghemite to hematite appeared at about 150 and 480°C, respectively, on the thermal analysis for magnetite particles [32].

From this, both maghemite and hematite have a photocurrent response to visible light, but the response of hematite is much higher. **Figure 17** shows the photocurrent response of the iron oxide film treated at the temperature of 400–500°C. The XRD of the corresponding iron oxide films is shown in **Figure 18**. All the films showed a photoanodic current response. A marked increase in photocurrent was observed on the film treated at 450°C.

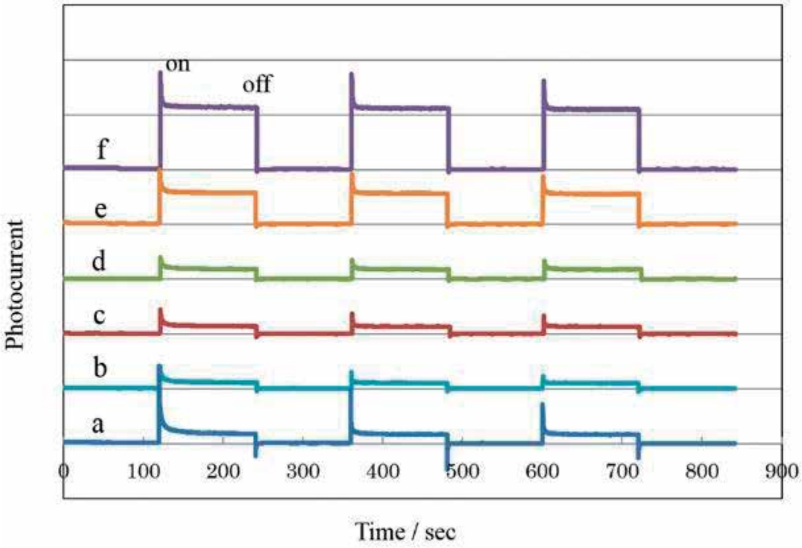

Figure 17. Dependence of photocurrent response of the iron oxide upon heat treatment temperature at 400–500°C in air. Iron oxide was prepared from potential pulse deposition ($E_c = -1.0$ V, $E_a = 0.2$ V vs. Ag/AgCl, $t_c = t_a = 1$ s) for 30 min in aqueous 10 mM $FeCl_2$–0.1 M KCl solution under N_2 bubbling. The heat treatment temperatures of as-deposited film were 400°C (a), 410°C (b), 420°C (c), 430°C (d), 450°C (e) and 500°C (f).

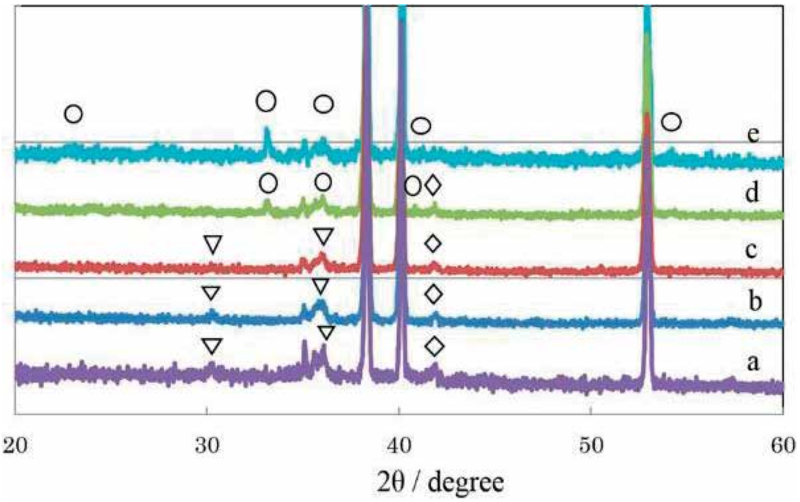

Figure 18. XRD of the iron oxide treated at different temperatures of 400–500°C in air. The heat treatment temperatures were 400°C (a), 410°C (b), 420°C (c), 430°C (d) and 500°C (e).

The intensity of maghemite XRD peaks on the films decreased with heat treatment temperature from 400 to 420°C and hematite peaks appeared on the film treated at 430°C as shown in **Figure 18**.

Figure 19 shows the relationship between electrode potential and photocurrent on the hematite in 0.1 M aqueous Na_2SO_4 solution during irradiation. This hematite was prepared from the potential pulse deposition under N_2 bubbling and heat treatment at 500°C. In the dark, anodic current did not flow up to the potential of 1.2 V vs. Ag/AgCl. In the irradiation of UV light (wavelength: 365 nm, intensity: 5.5 mW/cm^2) to the hematite, the onset potential of photo-anodic current was about 0.0 V vs. Ag/AgCl, almost equal to the value of F_{fb}. In the irradiation of visible light (wavelength: 490 nm, intensity: 4.8 mW/cm^2), the onset potential was more positive than F_{fb}. This means a necessity of fair band bending for the separation of photo-generated electron-hole pair in the absorption of visible light.

Figure 20 shows the relationship between photocurrent quantum efficiency and wavelength of irradiation light on the hematite at the potential of 1.0 V vs. Ag/AgCl in 0.1 M aqueous Na_2SO_4 solution containing 1 mM hydroxyl acid. The hematite was prepared from the potential pulse deposition under N_2 bubbling and heat treatment at 500°C. The photocurrent quantum efficiency (η_{elec}) represents the ratio of the number of electrons for photocurrent to photon number of incident light. The value of η_{elec} in the presence of hydroxyl acid was much higher than that in aqueous Na_2SO_4 solution containing no hydroxyl acids. The values of η_{elec} at wavelength in the range of 400–500 nm were 22–7, 17–5 and 14–4% in the presence of citric acid, tartaric acid and malic acid, respectively. The lower value of 5–2% in aqueous Na_2SO_4 solution may reflect a slow transfer of photo-generated holes in the valence band of hematite to water molecules. The highest photocurrent response obtained in the presence of citric acid was probably due to a rapid hole transfer to citric acid molecules. According to the reports [33, 34] on zinc oxide and

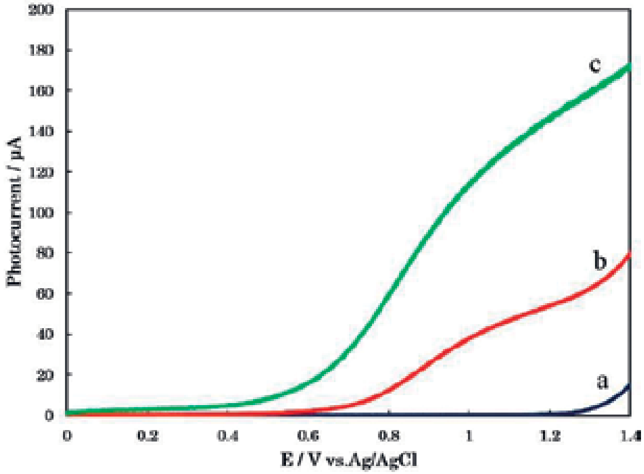

Figure 19. Relationship between electrode potential and photocurrent on the hematite in 0.1 M aqueous Na_2SO_4 solution under irradiation of visible light and UV light. Hematite was prepared from potential pulse deposition (E_c = −1.0 V, E_a = 0.2 V vs. Ag/AgCl, $t_c = t_a$ = 1 s) for 30 min in aqueous 10 mM $FeCl_2$–0.1 M KCl solution under N_2 bubbling, and heated at 500°C for 1 h in air. Three relation curves of a, b and c are corresponding to no irradiation, visible light and UV light irradiation, respectively.

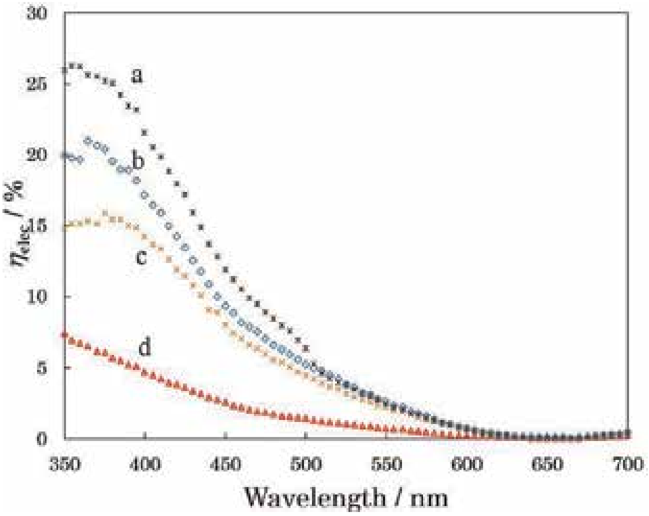

Figure 20. Relationship between photocurrent quantum efficiency and wavelength of irradiation light on the hematite at 1.0 V vs. Ag/AgCl in 0.1 M aqueous Na_2SO_4 solution containing 1 mM hydroxyl acid. Hematite was prepared from potential pulse deposition (E_c = −1.0 V, E_a = 0.2 V vs. Ag/AgCl, t_c = t_a = 1 s) for 30 min in aqueous 10 mM $FeCl_2$–0.15 M NaCl solution under N_2 bubbling, and heated at 500°C for 1 h in air. Each of citric acid (a), tartaric acid (b) and malic acid (c) was added to aqueous Na_2SO_4 solution (d).

rutile photoelectrodes in aqueous formic acid solution, a distinct increase in photocurrent could be observed because formic acid might act as the hole scavenger of these photoelectrodes. But, a clear increase in photocurrent was not observed on the hematite photoelectrode in formic acid solution.

4. Photoreaction of chemical species on hematite photoelectrode

A photoelectrochemical system consisting of a semiconductor working electrode and a counter electrode may be suitable for performance of water purification and artificial photosynthesis because an effective separation of photo-generated hole and electron pair under irradiation could proceed due to the existence of space charge layer at the semiconductor electrode/electrolytic solution interface. In the case of using n-type semiconductor, photoanodic oxidation and cathodic reduction occur at a working and a counter electrodes, respectively. Photodecomposition of water by using titanium dioxide electrode, Honda-Fujishima effect, is well known as a typical photoelectrochemical process. In order to understand photo-oxidation response of hematite to chemical species, we checked oxidation behavior of citric acid, Pb^{2+} ion and aniline on the hematite photoelectrode.

4.1. Photo-oxidation of citric acid on hematite in aqueous solution under visible light irradiation

The HPLC analysis of organic acids in the solution was carried out to reveal the reaction process of citric acid on hematite photoelectrode in aqueous solution [29]. This hematite was

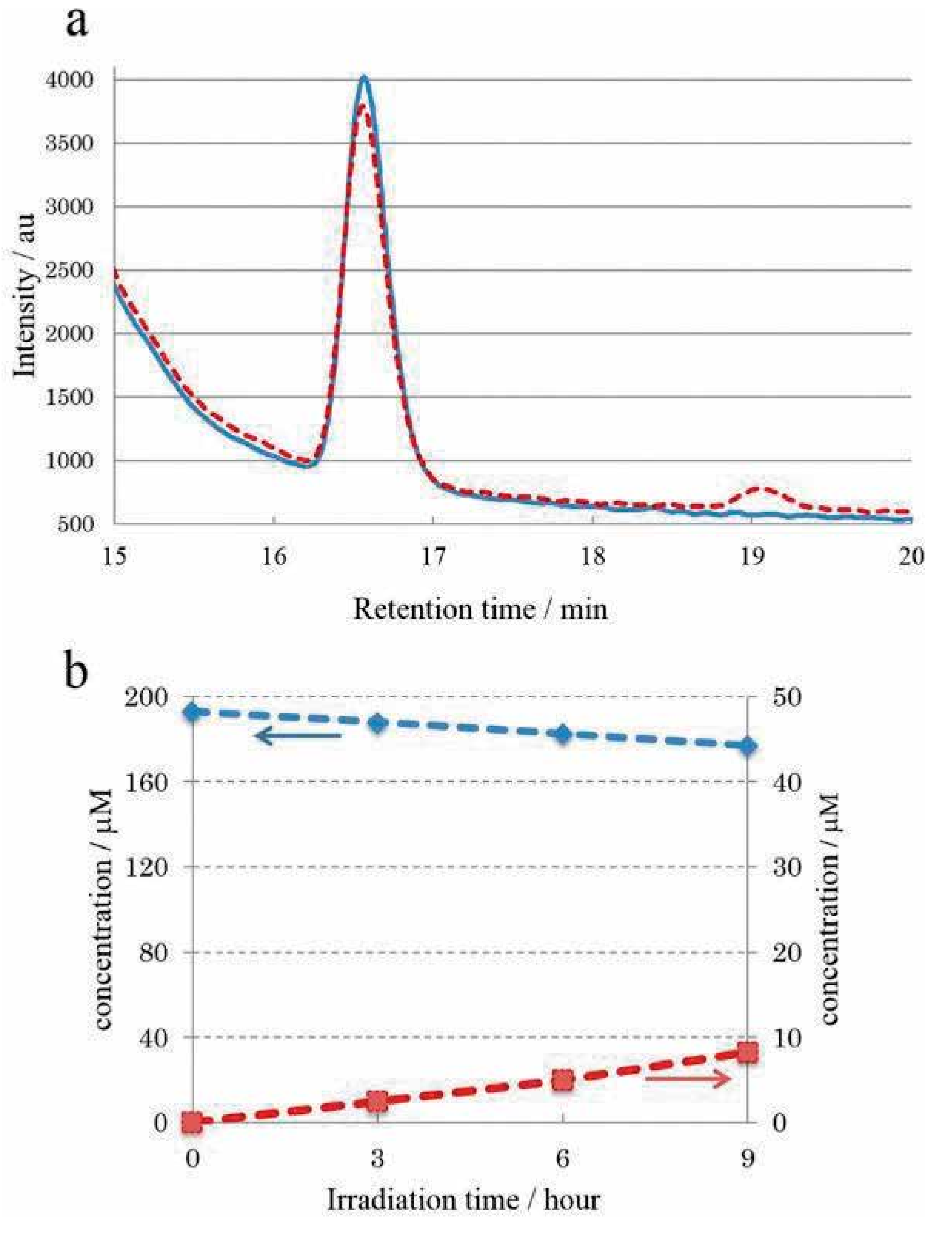

Figure 21. A chromatograms of the citric acid solution before and after irradiation of visible light (wavelength: 490 nm, intensity: 3.8 mW/cm^2) to the hematite electrode at 1.0 V vs. Ag/AgCl for 9 hours, b: Relationship among concentration of citric acid, concentration of acetonedicarboxylic acid and irradiation time. Hematite was prepared from current pulse deposition (I_c = −7 mA, I_a = +1 mA, t_c = t_a = 1 s) for 100 s in aqueous 10 mM $FeCl_2$–0.15 M NaCl solution under O_2 bubbling, and heated at 600°C for 1 h in air.

prepared from the current pulse deposition (I_c = −7 mA, I_a = +1 mA, t_c = t_a = 1 s) under O_2 bubbling for 100 s and heat treatment at 600°C for 1 h in air. **Figure 21a** shows the chromatogram of the aqueous solution of 0.1 M Na_2SO_4 and citric acid (initial concentration: 200 μM) at the hematite electrode potential of 1.0 V vs. Ag/AgCl. Before irradiation, the only peak due to citric acid was observed at the retention time of 16.5 min. This chromatogram was not changed after immersion of the hematite electrode for 9 h in the dark. After irradiation of the visible light (wavelength: 490 nm, intensity: 3.8 mW/cm^2) for 9 h to the surface of hematite electrode, the intensity of the citric acid peak was decreased and a new peak due to acetonedicarboxylic acid appeared at the time of 19.0 min. **Figure 21b** shows the relationship between concentration of citric acid and irradiation time as well as between concentration of acetonedicarboxylic acid and irradiation time. The concentration of citric acid decreased and that of acetonedicarboxylic acid increased with irradiation time. From this result, the photo-oxidation of citric acid to acetonedicarboxylic acid proceeded on the hematite photoelectrode according to Eq. (29).

$$\begin{aligned}&\mathrm{CH_2(COOH)C(OH)(COOH)CH_2(COOH)} \rightarrow \mathrm{CH_2(COOH)COCH_2(COOH)}\\&+\mathrm{CO_2} + 2\mathrm{H}^+ + 2\mathrm{e}^-\end{aligned} \tag{29}$$

Table 1 summarizes the significant values of photocurrent quantum efficiency, quantum efficiency and current efficiency derived from the data of photocurrent measurement and HPLC analysis concerning the photo-oxidation of citric acid on the hematite photoelectrode in aqueous solution under visible light irradiation for 9 h. $N_{\mathrm{h}\nu}$ is the photon number of incident light to the surface of hematite electrode, Q_{elec} is the amount of electric quantity for the photocurrent flowing during irradiation, N_{elec} is the number of electrons from Q_{elec}, η_{elec} is the photocurrent quantum efficiency represented as the term of $(N_{elec}/N_{h\nu})$ ×100, ΔC is the change in concentration of citric acid during photo-oxidation from HPLC data, N_{mole} is the number of citric acid molecules oxidized, η_{mole} is the quantum efficiency represented as the term of $(N_{mole}/N_{h\nu}) \times 100$ and I_{effi} is the current efficiency in the photo-oxidation process of citric acid to acetonedicarboxylic acid. The value of I_{effi} was evaluated from the term of $(2\eta_{mole}/\eta_{elec}) \times 100$ by consideration of Eq. (29). The value of 100.0% was obtained as I_{effi} in the process under visible light irradiation. All the photocurrent was derived from the photo-oxidation of citric acid to acetonedicarboxylic acid. This means that the holes photo-generated by visible light could oxidize only the citric acid molecules.

The HPLC analysis of citric acid under UV light irradiation was carried out to make clear a difference between visible light and UV light affecting the hematite electrode. **Figure 22a** shows the chromatogram of the aqueous solution of 0.1 M Na_2SO_4 and citric acid (initial concentration: 200 μM) at the hematite electrode potential of 1.0 V vs. Ag/AgCl before and after irradiation of UV light (wavelength: 360 nm, intensity: 4.2 mW/cm^2). A distinct decrease in the intensity of citric acid peak and also a distinct increase in that of acetonedicarboxylic acid peak were observed after UV irradiation to the surface of the hematite electrode for 9 h.

$N_{h\nu}$	Q_{elec} (C)	N_{elec}	η_{elec} (%)	ΔC (μmol)	N_{mole}	η_{mole} (%)	I_{eff} (%)
3.04×10^{20}	0.273	1.71×10^{18}	0.56	1.42	8.65×10^{17}	0.28	100

Table 1. Values in relation to the photoanodic oxidation on the hematite electrode in 0.1 M aqueous Na_2SO_4 solution containing initial concentration of 200 μM citric acid under irradiation of visible light (wavelength: 490 nm, intensity: 3.8 mW/cm^2) for 9 h.

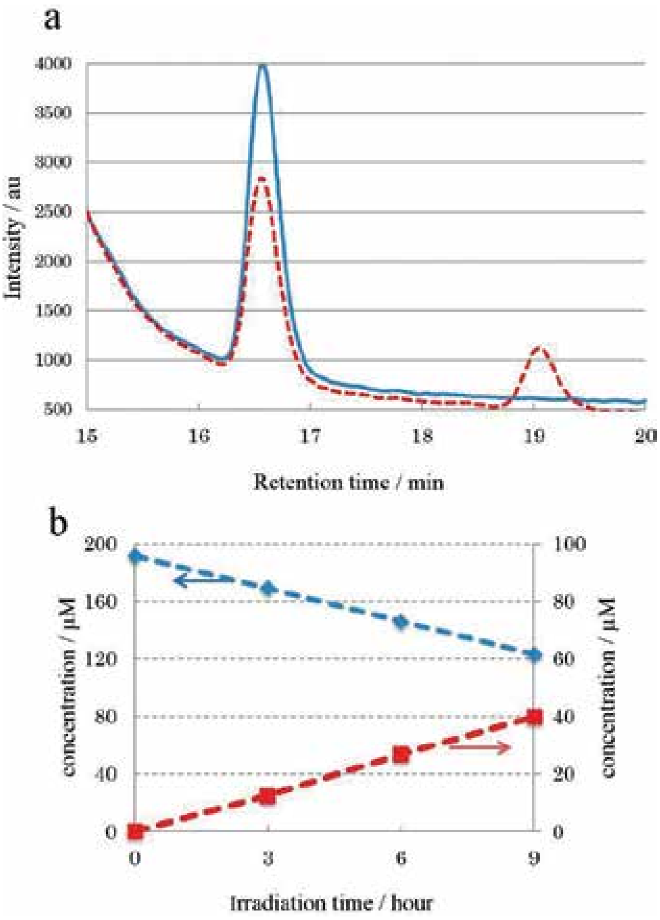

Figure 22. A chromatograms of the citric acid solution before and after irradiation of UV light (wavelength: 360 nm, intensity: 4.2 mW/cm^2) to the hematite electrode at 1.0 V vs. Ag/AgCl for 9 hours, b: Relationship among concentration of citric acid, concentration of acetonedicarboxylic acid and irradiation time. Hematite was prepared by the same method as that in **Figure 21**.

Figure 22b shows the relationship between concentration of citric acid and irradiation time as well as between concentration of acetonedicarboxylic acid and irradiation time. The UV light irradiation accelerated the photo-oxidation of citric acid to acetonedicarboxylic acid. **Table 2** summarizes the values concerning photocurrent quantum efficiency, quantum efficiency and current efficiency for the photo-oxidation of citric acid to acetonedicarboxylic acid on the

N_{hv}	Q_{elec} (C)	N_{elec}	η_{elec} (%)	ΔC (μmol)	N_{mole}	η_{mole} (%)	I_{eff} (%)
2.47×10^{20}	1.91	1.19×10^{19}	4.82	6.14	3.70×10^{18}	1.50	62

Table 2. Values in relation to the photoanodic oxidation on the hematite electrode in 0.1 M aqueous Na_2SO_4 solution containing initial concentration of 200 μM citric acid under irradiation of UV light (wavelength: 360 nm, intensity: 4.2 mW/cm^2) for 9 h.

hematite electrode under UV light irradiation for 9 h. The higher value of η_{elec} and η_{mole} means that the UV light could facilitate a transfer of hole of the hematite to the citric acid molecule. This may be ascribed to the photo-generation of a pair of hole and excited electron in the vicinity of the surface of the hematite irradiated with UV light. The I_{effi} value of 62% suggests the occurrence of the photo-oxidation of not only citric acid but also water. This reflects the competitive process of hole transfer to the molecules of chemical species and water in aqueous solution. The I_{effi} value of 100% in the visible light irradiation could be interpreted in terms of the photo-generation of a pair of hole and excited electron at the inside of space charge layer due to a deeper penetration of visible light. In this case, the hole moving from the inside to the surface might prefer citric acid molecule to water molecule probably from the aspect of oxidation rate. The hematite also showed a distinct photo-oxidation response to other hydroxyl acids such as tartaric acid, malic acid and glycolic acid. These results imply possibility of photo-oxidation synthesis of organic materials by using hematite under visible light irradiation.

4.2. Photo-oxidation of Pb^{2+} ion to PbO_2 on hematite in acid solution under visible light irradiation

The photo-oxidation treatment of Pb^{2+} ions in aqueous solution was examined by using hematite for the purpose of elimination of them from the solution [25, 24]. The hematite in this case was prepared from thermal oxidation of iron plate at 600°C for 3 h in air. The cell consisting of the hematite working electrode in 0.1 M HNO_3–10 μM $Pb(NO_3)_2$ and of the graphite counter electrode in 0.1 M H_2SO_4–10 mM $Ce(SO_4)_2$ aqueous solution was used as a photocell performing without applied voltage. The flow of photocurrent was observed by irradiation of visible light to the hematite electrode. **Figure 23** shows the dependence of photocurrent on irradiation time in this cell and also in the cell with the graphite electrode solution of 0.1 M H_2SO_4–10 mM $Fe_2(SO_4)_3$ aqueous solution. In this case, the hematite and graphite electrodes acted as a photoanode and a cathode, respectively. It is clear that the presence of Ce^{4+} in the cathode solution was effective for the performance of the cell based on the hematite photoanode. Since the standard equilibrium potential of Ce^{4+}/Ce^{3+} system of 1.44 V vs. NHE is more positive than that of Fe^{3+}/Fe^{2+} system of 0.771 V vs. NHE, Ce^{4+} may act as a stronger electron acceptor. **Figure 24** shows the SEM image of the surface of the hematite electrode before and after irradiation for 6 h in 0.1 M HNO_3–10 μM $Pb(NO_3)_2$ solution. The photo-deposition of many particles was observed on the surface of hematite. The XRD peak due to PbO_2 was confirmed on the hematite after irradiation. This suggests the occurrence of the following photoelectrochemical reactions in Eqs. (30)–(32). The photo-generated hole (h^+) and electron (e^-) pair was separated to oxidize Pb^{2+} to PbO_2 by hole at the hematite photoanode and reduce Ce^{4+} to Ce^{3+} by electron at the graphite cathode according to Eqs. (30) and (31). The total reaction is represented as Eq. (32). With regard to the standard Gibbs free energy change, ΔG^0, for reaction (32), the positive value 48.2 kJ/mol could be evaluated by using the standard equilibrium potential of Pb^{4+}/Pb^{2+}, 1.69 V and that of Ce^{4+}/Ce^{3+}, 1.44 V vs. NHE. This means that the reaction (32) is not spontaneous reaction and the light energy causes it to proceed. The hematite prepared from thermal oxidation of iron showed the value of E_{fb} of 0.31 V vs. NHE in the 0.1 M aqueous HNO_3 solution. Therefore, the position of valence band edge of hematite

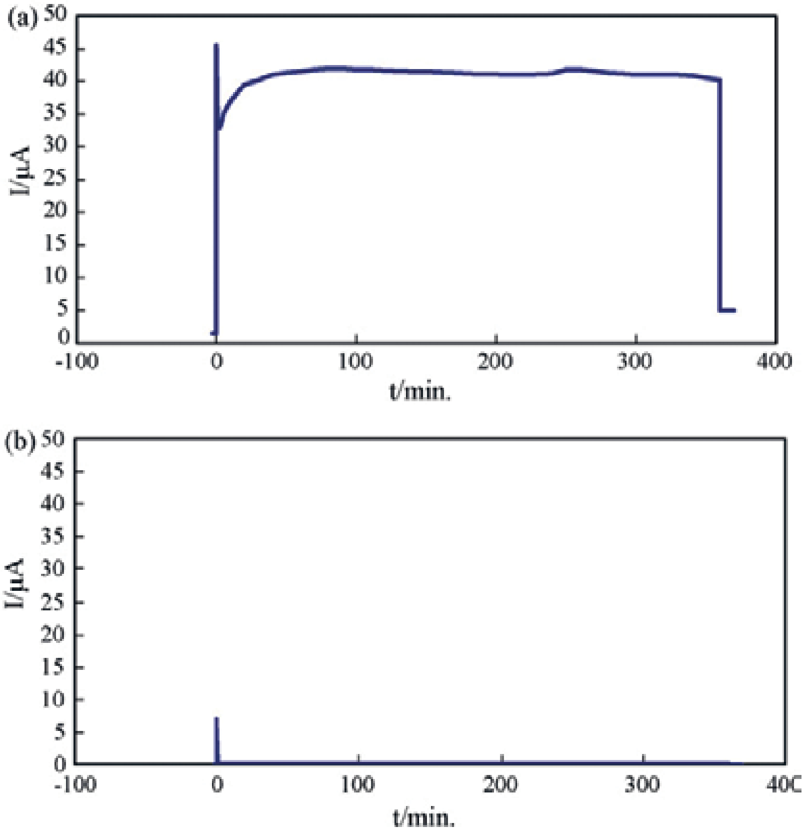

Figure 23. Dependence of photocurrent on irradiation time in the cell consisting of the hematite 0.1 M HNO_3–10 μM Pb $(NO_3)_2$ and of the graphite cathode in 0.1 M H_2SO_4–10 mM $Ce(SO_4)_2$ solution (a) and also in the cell of the photoanode in the same solution and of the cathode in 0.1 M H_2SO_4–10 mM $Fe_2(SO_4)_3$ solution (b). Hematite was prepared from thermal oxidation of iron at 600°C for 3 h in air.

could be regarded approximately as 2.3 V vs. NHE in the solution (pH = 1) by referring to the band gap energy of 2.0 eV. The occurrence of photo-oxidation of Pb^{2+} to PbO_2 deposition on hematite may be supported by this positive potential of valence band edge. For 0.1 M aqueous HNO_3 solution containing 10 μM $Pb(NO_3)_2$, the removal rate of Pb^{2+} ions due to visible light irradiation was checked by atomic absorption analysis. In the case of using Ce^{4+} electron acceptor without applied voltage, 8.9% of the initial concentration of Pb^{2+} was removed from the solution after 6 h irradiation. By holding the potential of hematite at 1.50 V vs. Ag/AgCl, a marked increase in the removal rate was confirmed. The values of 27.0, 38.7 and 53.2% were obtained after 2, 4 and 6 h irradiation, respectively.

$$Pb^{2+} + 2H_2O + 2\,h^+ \rightarrow PbO_2 + 4H^+ \tag{30}$$

$$2Ce^{4+} + 2e^- \rightarrow 2Ce^{3+} \tag{31}$$

$$Pb^{2+} + 2H_2O + 2Ce^{4+} \rightarrow PbO_2 + 4H^+ + 2Ce^{3+} \tag{32}$$

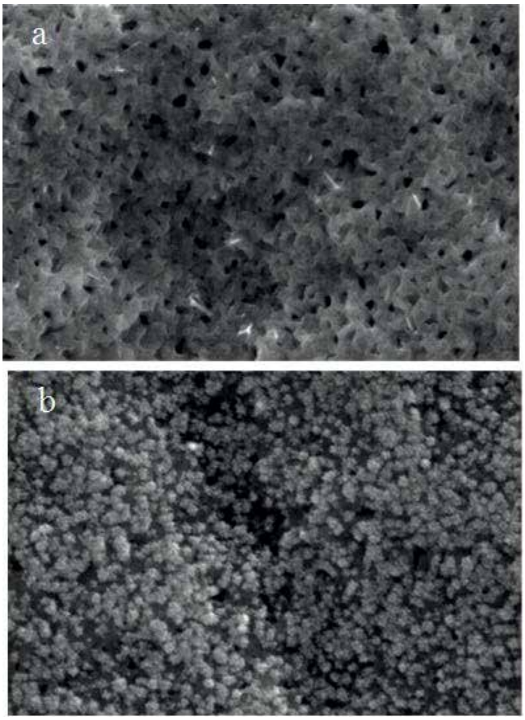

Figure 24. SEM images of the surface of the hematite electrode before and after visible light irradiation for 6 h in 0.1 M HNO_3–10 μM $Pb(NO_3)_2$ solution. Hematite was prepared from thermal oxidation of iron at 600°C for 3 h in air.

4.3. Photo-polymerization of aniline on hematite and characteristics of polyaniline/hematite electrode under visible light irradiation

The photo-polymerization of aniline was carried out by the photoelectrochemical cell consisting of the separated parts of hematite photoanode in 0.1 M $HClO_4$–0.1 M aniline and the graphite cathode in 0.1 M H_2SO_4–10 mM $Ce(SO_4)_2$ aqueous solutions under visible light irradiation [27]. This hematite was prepared from thermal oxidation of iron at 600°C for 3 h in air. These electrolytic solutions were connected by a KCl salt bridge. The deposition of many particles was observed on the surface of the hematite electrode after irradiation. The photo-anodic polymerization of aniline due to the photo-generated hole could proceed on the hematite electrode without applied voltage by using Ce^{4+} ions as an electron acceptor. Because the potential for the bottom of conduction band is positive as understood from the positive E_{fb} value of hematite, the presence of a strong oxidizing agent as an electron acceptor may be necessary for occurrence of photoelectrochemical reaction on the hematite without application of electric power.

The polyaniline/hematite electrode has a unique property. **Figure 25** (**a**–**c**) shows the Mott-Schottky plots of the hematite electrode, the polyaniline electrode prepared from anodic deposition of polyaniline film on the glassy carbon and the polyaniline/hematite electrode in 0.1 M aqueous $HClO_4$ solution, respectively, at the frequency of 1 kHz. On the hematite

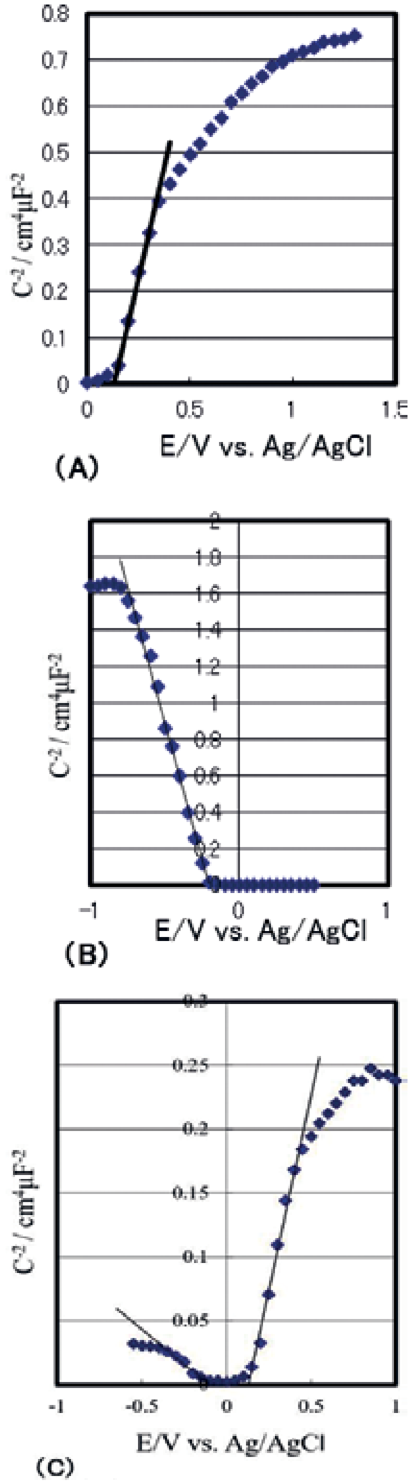

Figure 25. Mott-Schottky plots of the hematite electrode (a), the polyaniline-glassy carbon electrode (b) and the polyaniline-hematite electrode (c) in 0.1 M aqueous $HClO_4$ solution. Hematite was prepared from thermal oxidation of iron at 600°C for 3 h in air.

electrode in $HClO_4$ solution, a linear relation due to the n-type semiconductor electrode/electrolytic solution interface was observed. The value of E_{fb} of the hematite in this solution by extrapolation of the linear line was 0.13 V vs. Ag/AgCl. On the polyaniline electrode in $HClO_4$ solution, a linear relation due to the p-type semiconductor electrode/electrolytic solution interface was observed. The state of undoped polyaniline could be regarded as the p-type semiconductor. The value of E_{fb} of undoped polyaniline in this solution was −0.20 V vs. Ag/AgCl. On the polyaniline/hematite electrode in $HClO_4$ solution, the two linear relations were observed. The linear portion at less positive potential than −0.10 V vs. Ag/AgCl was ascribed to the undoped polyaniline/electrolytic solution interface. Because the doped polyaniline has high electric conductivity to be regarded as metal, the linear portion at more positive potential than 0.12 V vs. Ag/AgCl reflects the hematite/doped polyaniline interface.

The photocurrent on the hematite under visible light irradiation decayed immediately with time at less positive potential than 0.70 V vs. Ag/AgCl in aqueous $HClO_4$ solution. This means that the band bending of hematite is not enough in this potential range because of slow transfer of photo-generated hole to water molecule. The polyaniline/hematite electrode showed a stable photocurrent response to visible light at less positive potential than 0.70 V vs. Ag/AgCl in aqueous $HClO_4$ solution. On the polyaniline/hematite electrode, the rapid transfer of photo-generated hole to the polyaniline and simultaneous occurrence of ClO_4^- ion doping may proceed. The polyaniline/hematite electrode showed a distinct increase in photocurrent in the presence of glycolic acid. The linear relationship between photocurrent and concentration of glycolic acid (1–10 mM) was recognized under visible light irradiation. On the hematite electrode, the linear dependence of photocurrent on concentration was not observed. This implies a possibility of application of the polyaniline/hematite electrode to an amperometric sensor for glycolic acid. Hematite has the demerit that iron dissolution may proceed in acid solution. The amount of iron dissolution after immersion of hematite in 0.1 M aqueous $HClO_4$ solution for 1, 2, 3 and 4 h was 4.89, 11.77, 15.18 and 17.55 ppm, respectively, by atomic absorption analysis. The polyaniline/hematite showed the suppression of iron dissolution. The high stability of the polyaniline/hematite in acid solution was supported by the amount of iron dissolution of 0.01, 0.02, 0.03 and 0.04 ppm after immersion in 0.1 M aqueous $HClO_4$ solution for 1, 2, 3and 4 h, respectively.

5. Conclusion

As a preparation method of hematite film, the process for electrochemical deposition of iron oxide and its heat treatment in air was mentioned in relation to the equilibrium potential of iron oxide in aqueous solution. The current and potential pulse electrolysis may be useful in deposition of homogeneous iron oxide film. The hematite from the heat treatment of iron oxide at 500°C or higher temperature in air showed a clear photocurrent response and brought the photo-oxidation of chemical species such as citric acid, Pb^{2+} ion and aniline under visible light irradiation. On the hematite electrode in aqueous solution containing organic materials under visible light irradiation, photo-oxidation processing of organic materials with suppression of water photo-oxidation may be possible. This will lead to application of photo functionality of hematite to a new method for organic synthesis.

Acknowledgements

I am grateful to Dr. Y. Morinaga, Dr. D. Kodama, Mrs. Y. Itoh, Mr. H. Yoshida, Mr. H. Hamada, Mr. K. Ota and Mr. Y. Kanada for experimental contribution in photoelectrochemistry of hematite.

Author details

Yasuhisa Maeda

Address all correspondence to: maeda.yasuhisa@shizuoka.ac.jp

Department of Applied Chemistry, Graduate School of Integrated Science and Technology, Shizuoka University, Japan

References

[1] Curran JS, Gissler W. The different photoelectrochemical behavior of sintered and flame-oxidized Fe_2O_3. Journal of the Electrochemical Society. 1979;**126**:56-59

[2] Sahami S, Kennedy JH. Open-circuit photopotentials and photoelectrochemical behavior of the Si-doped α-Fe_2O_3 semiconductor electrode in acetonitrile solutions. Journal of the Electrochemical Society. 1985;**132**:1116-1120

[3] Glasscock JA, Barnes PRF, Plumb IC, Savvides N. Enhancement of photoelectrochemical hydrogen production from hematite thin films by the introduction of Ti and Si. Journal of Physical Chemistry C. 2007;**111**:16477-16488

[4] Schrebler R, Llewelyn C, Vera F, Cury P, Munoz E, del Rio R, Meier HG, Cordova R, Dalchiele EA. Dalchiele, An electrochemical deposition route for obtaining α-Fe_2O_3 tin films, II. EQCM study and semiconductor properties, Electrochemical and Solid State Letters. 2007;**10**:D95-D99

[5] Schrebler RS, Altamirano H, Gez P, Herrera FV, Munoz EC, Ballesteros LA, Cordova RA, Gomez H, Dalchiele EA. The influence of different electrodeposition E/t programs on the photoelectrochemical properties of α-Fe_2O_3 thin films. Thin Solid Films. 2010;**518**: 6844-6852

[6] Schrebler RS, Ballesterus L, Burgos A, Munoz EC, Grez P, Leinen D, Martine F, Ramos-Barrado JR, Dalchiele EA. Electrodeposited nanostructured α-Fe_2O_3 photoanodes for solar water splitting: Effect of surface co-modification on photoelectrochemical performance. Journal of the Electrochemical Society. 2011;**158**:D500-D505

[7] Tamboli SH, Rahman G, Joo O. Influence of potential, deposition time and annealing temperature on photoelectrochemical properties of electrodeposited iron oxide thin films. Journal of Alloys and Compounds. 2012;**520**:232-237

[8] Kennedy JH, Anderman M. Photoelectrolysis of water at α-Fe_2O_3 electrodes in acidic solution. Journal of the Electrochemical Society. 1983;**130**:848-852

[9] Khan SUM, Akikusa J. Photoelectrochemical splitting of water at nanocrystalline n-Fe_2O_3 thin-film electrodes. The Journal of Physical Chemistry. B. 1999;**103**:7184-7189

[10] Gondal MA, Hameed A, Yamani ZH, Suwaiyan A. Production of hydrogen and oxygen by water splitting using laser induced photo-catalysis over Fe_2O_3. Applied Catalysis A: General. 2004;**268**:159-167

[11] Duret A, Gratzel M. Visible light-induced water oxidation on mesoscopic α-Fe_2O_3 films made by ultrasonic spray pyrolysis. The Journal of Physical Chemistry. B. 2005;**109**:17184-17191

[12] Kay A, Cesar I, Gratzel M. New benchmark for water photooxidation by nanostructured α-Fe_2O_3 films. Journal of the American Chemical Society. 2006;**128**:157, 15714-16721

[13] Kleiman-Shwarsctein A, Hu Y, Forman AJ, Stucky GD, McFarland EW. Electrodeposition of α-Fe_2O_3 doped with Mo or Cr as photoanodes for photocatalytic water splitting. Journal of Physical Chemistry C. 2008;**112**:15900-15907

[14] Saremi-Yarahmadi S, Vaidhyanathan B, Wijayantha KGU. Microwave-assisted low temperature fabrication of nanostructured α-Fe_2O_3 electrodes for solar-driven hydrogen generation. International Journal of Hydrogen Energy. 2010;**35**:10155-10165

[15] Kment S, Hubicka Z, Krysa J, Zlamal M, Olejnicek J, Cada M, Ksirova P, Remes Z, Schmuki P, Schubert E, Zboril R. On the improvement of PEC activity of hematite thin films deposited by high-power pulsed magnetron sputtering method. Applied Catalysis B: Environmental. 2015;**165**:344-350

[16] Pulgarin C, Kiwi J. Iron oxide-mediated degradation, photodegradation, and biodegradation of aminophenols. Langmuir. 1995;**11**:519-526

[17] Pal B, Sharon M. Preparation of iron oxide thin film by metal organic deposition from Fe (III)-acetylacetonate: A study of photocatalytic properties. Thin Solid Films. 2000;**379**: 83-88

[18] Bandara J, Mielczarski JA, Lopez A, Kiwi J. 2. Sensitized degradation of chlorophenols on iron oxides induced by visible light comparison with titanium oxide. Applied Catalysis B: Environmental. 2001;**34**:321-333

[19] Valenzuela MA, Bosch P, Jimenez-Becerrill J, Quiroz O, Paez AI. Preparation, characterization and photocatalytic activity of ZnO, Fe_2O_3 and $ZnFe_2O_4$. Journal of Photochemistry and photobiology A: Chemistry. 2002;**148**:177-182

[20] Kawahara T, Yamada K, Tada H. Visible light photocatalytic decomposition of 2-naphthol by anodic-biased α-Fe_2O_3 film. Journal of Colloid and Interface Science. 2006;**294**:504-507

[21] Zhang Z, Hossain MF, Takahashi T. Self-assembled hematite (α-Fe_2O_3) nanotube arrays for photoelectrocatalytic degradation of azo dye under simulated solar light irradiation. Applied Catalysis B: Environmental. 2010;**95**:423-429

[22] Fujishima A, Hashimoto K, Watanabe T. TiO_2 Photocatalysis Fundamentals and Applications. Bkc. Inc.; 1998

[23] Hoffmann MR, Martin ST, Choi W, Bahnemann DW. Environmental applications of semiconductor photocatalysis. Chemical Reviews. 1995;**95**:69-96

[24] Maeda Y, Morinaga Y, Kobayashi K. Photoelectrochemical behavior of iron oxide electrode prepared from thermal oxidation of iron. Journal of the Surface Finishing Society of Japan. 2007;**58**:376-378

[25] Maeda Y, Morinaga Y, Tomita Y, Kobayashi K. Photoanodic response of iron oxide electrode in aqueous solution and its application to Pb^{2+} removal under visible light irradiation. Electrochimica Acta. 2009;**54**:1757-1761

[26] Itoh Y, Kohno Y, Maeda Y. Photoelectrochemical behavior of iron oxide under visible light irradiation, 62nd Annual Meeting of the International Society of Electrochemistry; 2011

[27] Morinaga Y, Kohno Y, Morinaga Y, Kohno Y, Tomita Y, Kobayashi K, Maeda Y. Photoelectrochemical characteristics of iron oxide/polyaniline in aqueous acidic solution. Electrochemistry. 2011;**79**:168-171

[28] Maeda Y, Yoshida, Hamada H, Kohno Y. Preparation of iron oxide film and its photoelectrochemical behavior in aqueous solution, 65th Annual Meeting of the International Society of Electrochemistry; 2014

[29] Maeda Y, Itoh Y, Kodama D, Kohno Y. Photoanodic response of hematite electrode to citric acid in aqueous solution. Journal of Electroanalytical Chemistry. 2017;**785**:166-171

[30] Bard AJ, Parsons R, Jordan J. Standard Potentials in Aqueous Solution. Marcel Dekker, Inc; 1985. pp. 391-393

[31] Pourbaix M. Atlas of Electrochemical Equilibria in Aqueous Solutions. Houston: NACE; 1966. pp. 308-310

[32] Kikuchi T, Okazaki Y, Ikeda K. Fine iron oxide powder as a raw material of soft ferrites. JFE Technical Report. 2005:26-31

[33] Morrison SR, Freund T. Chemical reactions of electrons and holes at the ZnO/electrolyte-solution interface. Electrochimica Acta. 1968;**13**:1343-1349

[34] Dutoit EC, Cardon F, Gomes WP. Electrochemical reactions involving holes at the illuminated TiO_2 (rutile) single crystal electrode. Berichte der Bunsengesellschaft für Physikalische Chemie. 1976;**80**:1285-1288

Chapter 9

Iron Oxide-Based Catalyst for Catalytic Cracking of Heavy Oil

Eri Fumoto, Shinya Sato and
Toshimasa Takanohashi

Additional information is available at the end of the chapter

http://dx.doi.org/10.5772/intechopen.72719

Abstract

This chapter describes an iron oxide catalyst containing Zr and Al for production of light hydrocarbons by catalytic cracking of petroleum residual oil in a steam atmosphere. The catalyst was hematite structure and useful for decomposition and desulfurization of residual oil. After lattice oxygen of iron oxide reacted with heavy oil fraction of residual oil, oxygen species generated from steam were supplied to iron oxide lattice and reacts with heavy oil fraction, producing light hydrocarbons and carbon dioxide. When the oxygen species were generated from steam, hydrogen species were simultaneously generated from steam. The hydrogen species were transferred to light hydrocarbons, hydrogen sulfide, and residue deposited on the catalyst. Supplies of the hydrogen species to light hydrocarbons suppressed alkene generation. Generation of hydrogen sulfide indicated decomposition of sulfur compounds of residual oil. The sulfur concentration of product oil decreased compared to the concentration of residual oil. Some oxygen species could be transferred to sulfur dioxide. Accordingly, hydrogenation and oxidation by the hydrogen and oxygen species derived from steam provided the decomposition and desulfurization of residual oil with the iron oxide-based catalyst in a steam atmosphere.

Keywords: iron oxide catalyst, atmospheric residue, steam catalytic cracking

1. Introduction

Petroleum refineries require production of transportation fuels by decomposition of petroleum residual oil. The residual oil has low H/C ratio, high viscosity, and impurities, such as sulfur, vanadium, and nickel. Hence, decomposition of the residual oil is not easy.

The conventional process to convert heavy oil, such as petroleum residual oil, to light hydrocarbons was coking, visbreaking, residue fluidized catalytic cracking (RFCC), and hydrocracking

[1, 2]. Heavy oil was decomposed with Ni-Mo or Co-Mo catalysts to produce light hydrocarbons with less coke under high hydrogen pressure in the hydrocracking process. The hydrocracking is a useful technique to produce light hydrocarbons, which has high H/C ratio, although hydrogen is expensive.

Steam can be an alternative hydrogen source for conversion of heavy oil to light hydrocarbons with catalysts. This technique requires the following catalyst properties: (i) a high ability to decompose heavy oil, (ii) stable activity under high steam temperature, and (iii) resistance to deposition of coke, sulfur, and metals. Iron oxide is not expensive and can be a candidate the catalyst to decompose heavy oil in a steam atmosphere.

This chapter describes an iron oxide-based catalyst for decomposition of heavy oil to produce light hydrocarbons. Properties of the catalyst and catalyst activity to decompose residual oil and desulfurization in a steam atmosphere are discussed.

2. Properties of iron oxide catalyst

Several studies reported the catalytic cracking of heavy oil with iron oxide catalysts. Fumoto et al. developed the ZrO_2-supporting α-Fe_2O_3 catalysts for oxidative cracking of petroleum residual oil under high steam temperature [3]. Hosseinpour et al. reported catalytic cracking of petroleum residual oil using silica-supported α-Fe_2O_3 nanoparticles under super critical water [4]. Nguye-Huy and Shin studied steam catalytic cracking of petroleum residual oil using ZrO_2-impregnated macro-mesoporous red mud, which consisted of α-Fe_2O_3 and TiO_2 [5]. Phase diagram of ferrite showed that Fe_2O_3 is alloyed with Al_2O_3 homogeneously [6]. Hence, Fumoto et al. modified the ZrO_2-supporting α-Fe_2O_3 catalysts by addition of Al to enhance the catalyst durability [7, 8]. We described the properties of the α-Fe_2O_3 catalysts containing Zr and Al in this section.

2.1. Preparation of α-Fe_2O_3 catalyst containing Zr and Al

The α-Fe_2O_3 catalyst containing Zr and Al was prepared by a coprecipitation method using aqueous solution of $FeCl_3·6H_2O$ (Special grade, Wako Pure Chemical Industries, Ltd., 146 mol/m^3), $AlCl_3·6H_2O$ (Special grade, Wako Pure Chemical Industries, Ltd., 19 mol/m^3), and $ZrOCl_2·8H_2O$ (Special grade, Wako Pure Chemical Industries, Ltd., 9 mol/m^3) with aqueous ammonia [9, 10]. The catalyst was pelletized without binder, crushed, and sieved to obtain particles of 300–850 μm after the treatment at 873 K for 1 h in a stem atmosphere. The atomic ratio of Fe, Zr, and Al in the catalyst was 1:0.06:0.13.

2.2. Structure of α-Fe_2O_3 catalyst containing Zr and Al

The morphology of the α-Fe_2O_3 catalyst containing Zr and Al was analyzed by scanning electron microscope (SEM, JSM-6010LA, JEOL Ltd.). **Figure 1** showed a SEM image of α-Fe_2O_3 catalyst containing Zr and Al prepared by a coprecipitation method. The catalyst was composed of randomly shaped particles.

The crystalline construction of the catalyst was analyzed by X-ray diffraction (XRD, M03XHF22, Mac Science Co. Ltd.). **Figure 2** showed the XRD patterns of the catalyst and regent iron (III) oxide (α-Fe_2O_3, first grade, Wako Pure Chemical Industries, Ltd.) [9]. The patterns of the catalyst corresponded to that of α-Fe_2O_3. Absence of peaks corresponding to ZrO_2 and Al_2O_3 indicates high dispersion of Al and Zr in the α-Fe_2O_3 matrix [7]. The peaks of the catalyst are broader compared to the reagent iron oxide, indicating that the domain size of the α-Fe_2O_3 lattice was small. The catalyst containing Zr and Al showed smaller domain size than the ZrO_2-supporting α-Fe_2O_3 catalyst without Al, and the small domain size positively affected the catalyst durability [7, 8].

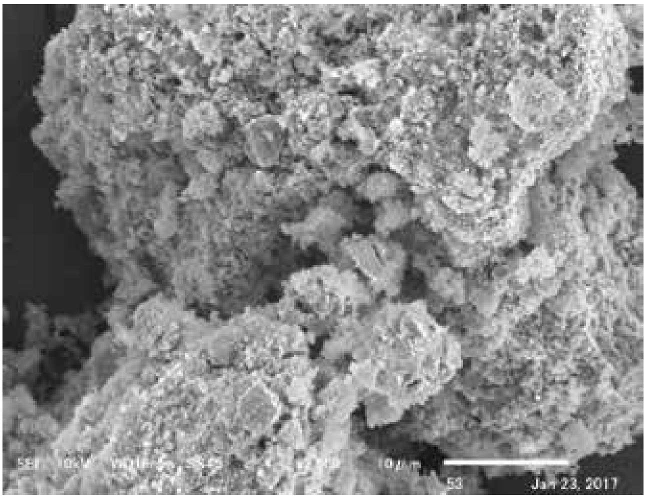

Figure 1. SEM image of α-Fe_2O_3 catalyst containing Zr and Al.

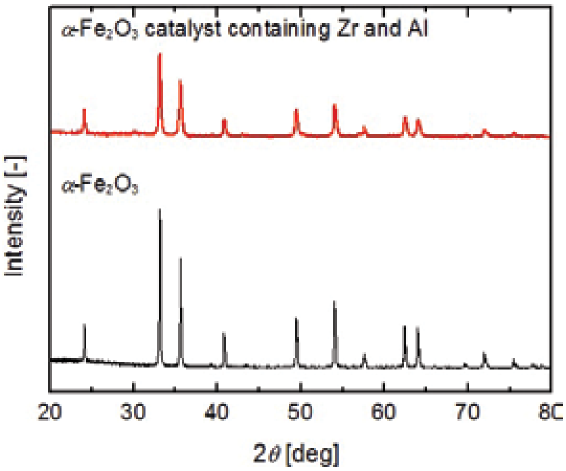

Figure 2. XRD patterns of α-Fe_2O_3 catalyst containing Zr and Al and regent α-Fe_2O_3 (reproduced from elsewhere [9]).

3. Activity of α-Fe_2O_3 catalyst containing Zr and Al for decomposition of heavy oil

The α-Fe_2O_3 catalyst containing Zr and Al was used for catalytic cracking of atmospheric residual oil (AR) derived from Middle East crude [9]. **Table 1** showed the properties of AR [11]. Composition of light oil (boiling point <623 K), vacuum gas oil (VGO, boiling point 623–773 K), and vacuum residue (VR, boiling point >773 K) was determined by the gas chromatographic distillation (HP6890, Agilent Technologies) with a wide-bore capillary column according to ASTM D 2887. AR has high viscosity, low H/C ratio, and high content of high-boiling-point components. This section describes the activity of the catalyst to decompose AR in a steam atmosphere.

3.1. Decomposition of AR

Catalytic cracking of AR was conducted using a downflow-type fixed-bed reactor loaded with 1.5 g of catalyst at 748 K under atmospheric pressure [9, 12]. A 10 wt% solution of AR with toluene was fed to the reactor at flow rate (*F*) of 1.1 g/h using a syringe pump. AR was diluted with toluene to reduce the viscosity of AR, and the catalyst was confirmed to be

	AR
Composition [wt%]	
Light oil	7
VGO	49
VR	44
Density [g/cm^3]	0.944
Elemental analysis [wt%]	
C	85.7
H	11.6
N	0.16
S	2.48
H/C [mol/mol]	1.63
Conradson carbon residue [wt%]	5.8
Metals [ppm]	
V	10
Ni	4
Fe	10

Reproduced from elsewhere [11].

Table 1. Properties of AR.

almost inactive to toluene. Total flow rate of mixture of steam and nitrogen was adjusted to 80 cm^3(STP)/min. After 2 h of operation, the pump of AR solution was stopped, and the reactor was cooled. The gas products were separated through an ice trap and analyzed by gas chromatography (GC-12A and GC-14A, Shimadzu Corp.) with thermal conductivity and flame ionization detectors equipped with Porapak-Q and Unibeads 3S columns, respectively. The boiling point distribution was determined by the gas chromatographic distillation. The residue deposited on the catalyst was analyzed by elemental analysis (EA1110, Finningan Mat).

Figure 3 showed the composition of AR and product yield of the AR cracking at flow rate ratio of steam to AR solution (F_S/F) of 0.42 g/g [9]. The high-boiling-point components, such as VGO and VR, decreased, producing light oil, CO_2, organic gas (C_1–C_4), and residue. Generation of CO_2 indicated that the heavy oil fraction was oxidatively cracked.

Figure 4 showed the XRD patterns of the used catalysts after the catalytic cracking of AR with and without steam [9]. The patterns of reagent iron (III) oxide (α-Fe_2O_3) and iron (II, III) oxide (Fe_3O_4, Strem Chemicals, Inc.) were shown for comparison. The patterns of both used catalysts consisted of α-Fe_2O_3 and Fe_3O_4. The peaks of Fe_3O_4 mainly appeared in the patterns of the used catalyst without steam. These results indicated that part of lattice oxygen of α-Fe_2O_3 reacted with heavy oil fractions to produce light hydrocarbons and CO_2 at first [12]. Then, oxygen species generated from steam were incorporated into the iron oxide lattice and reacted with heavy oil fractions. Hence, the α-Fe_2O_3 structure was partially maintained after the reaction with steam. Consequently, the heavy oil fractions were oxidatively cracked using oxygen species derived from steam.

When dodecylbenzene was used as a model compound of heavy oil, a small amount of oxygen containing compounds, such as phenol, acetophenone, undecanone, and hydroxybiphenyl, was produced in the catalytic cracking of dodecylbenzene [9]. Kondoh et al. reported that the catalytic cracking of heavy oil with heavy oxygenated water ($H_2{}^{18}O$) produced CO_2 containing

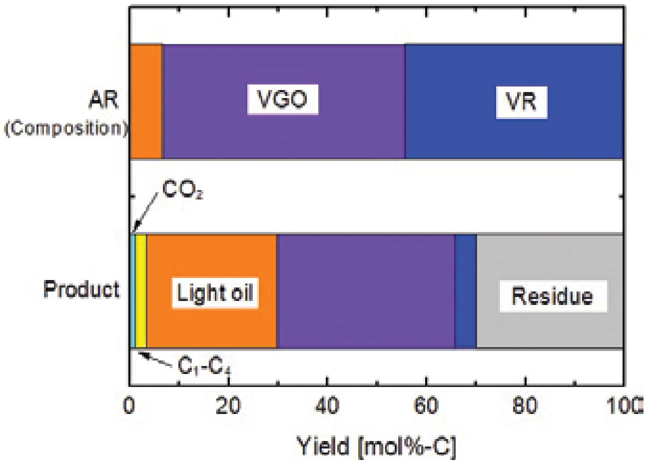

Figure 3. Product yield of catalytic cracking of AR with steam (F_S/F = 0.42) and composition of AR (reproduced from elsewhere [9]).

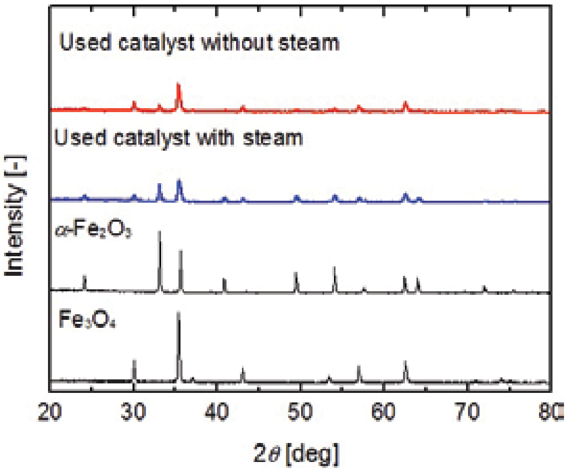

Figure 4. XRD patterns of used catalysts for catalytic cracking of AR with and without steam (F_S/F = 0, 0.42), regent α-Fe_2O_3, and reagent Fe_3O_4 (reproduced from elsewhere [9]).

heavy oxygen ($CO^{18}O$) [13]. Accordingly, most of oxygen species were supplied to form CO_2, and a small amount of oxygen species was supplied to oxygen –containing compounds.

The α-Fe_2O_3 catalyst containing Zr showed the higher activity than the α-Fe_2O_3 catalyst without Zr because ZrO_2 in the catalyst promotes the generation of oxygen species from steam [3]. Addition of Al to the catalyst enhanced the durability of the catalyst. The activity of the ZrO_2-supporting α-Fe_2O_3 catalyst without Al decreased after the sequence of reaction and regeneration because of phase change of iron oxide and subsequent peeling of ZrO_2 [7].

3.2. Effect of steam on product of AR cracking

To examine the effect of steam flow rate on product yield of AR cracking, catalytic cracking of AR was conducted at various steam flow rates (F_S/F = 0–3.0), and the product yield was shown in **Figure 5** [9]. The yields of light oil, VGO, VR, and residue little changed, suggesting that steam concentration hardly affected the decomposition of heavy oil. The heavy oil fractions reacted with oxygen species incorporated from steam to the iron oxide lattice after the lattice oxygen of α-Fe_2O_3 reacted with heavy oil fractions. The CO_2 yield increased with increase in the flow rate ratio of steam to AR solution due to increase in oxygen species derived from steam.

When oxygen species were generated from steam and reacted with heavy oil, hydrogen species were simultaneously generated from steam [9]. Consumed amount of steam was calculated from the CO_2 yield in the catalytic cracking of AR at flow rate ratio of steam to AR solution (F_S/F) of 3.0 g/g and shown in **Figure 6**. If half of the sulfur compounds in AR were converted to H_2S by the reaction of hydrogen species and sulfur compounds, approximately 14% of hydrogen species were supplied to form H_2S. Approximately 19% of hydrogen species

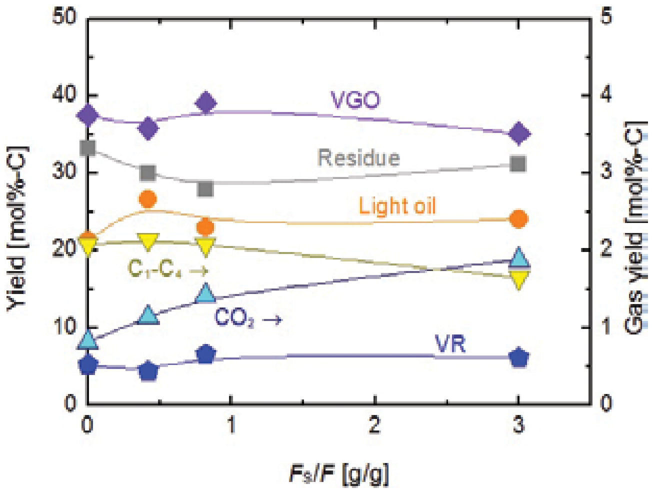

Figure 5. Product yield of catalytic cracking of AR with and without steam (F_S/F = 0–3.0) (reproduced from elsewhere [9]).

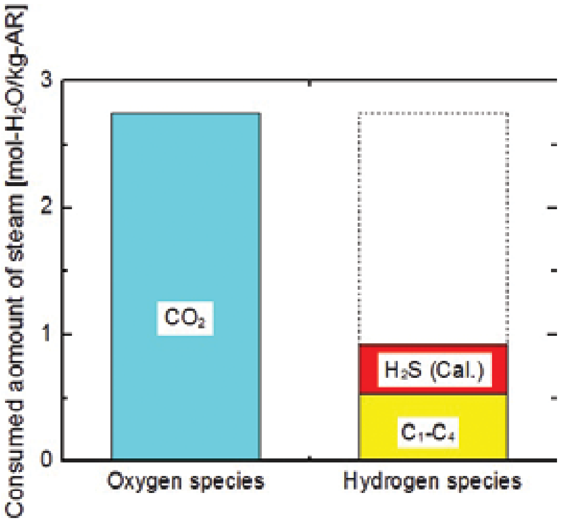

Figure 6. Consumed amount of steam for catalytic cracking of AR with steam (F_S/F = 3.0).

were supplied to form C_1–C_4 hydrocarbons if two moles of hydrogen species were supplied to 1 mole of C_1–C_4 hydrocarbons. Hence, the remaining hydrogen species (approximately 67%) might be supplied to liquid hydrocarbons and residue.

Supplies of hydrogen species from steam to liquid hydrocarbons and residue resulted in decrease in alkene generation and increase in H/C of residue [9]. **Figure 7** showed the alkene/alkane ratio of aliphatic hydrocarbons and H/C ratio of residue produced by the catalytic cracking of AR with and without steam. The aliphatic hydrocarbons in the liquid

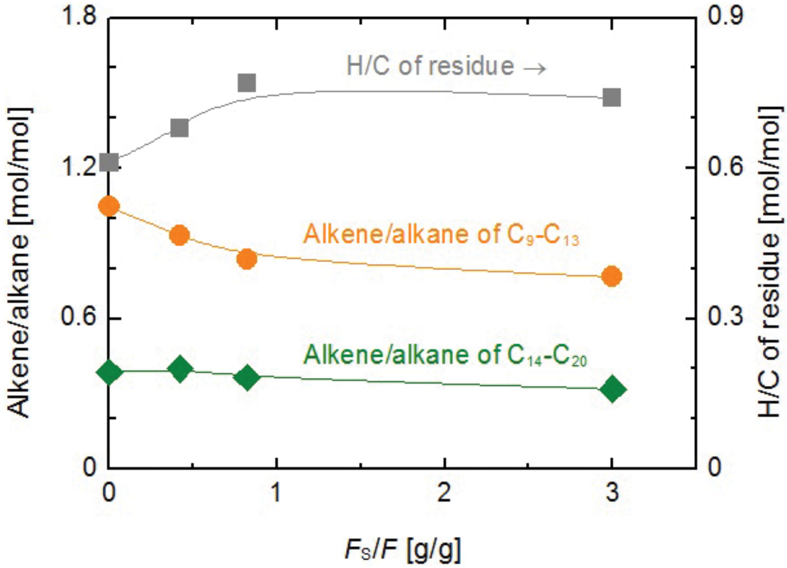

Figure 7. Alkene/alkane ratio of aliphatic hydrocarbons and H/C ratio of residue produced by the catalytic cracking of AR with and without steam (F_S/F = 0–3.0) (reproduced from elsewhere [9]).

product were analyzed by gas chromatography with a flame ionization detector (GC-FID, 6890N, Agilent Technologies) and mass spectrometry (GC-MS, HP6890-HP5973, Agilent Technologies) with capillary columns. The alkene/alkane ratio of light hydrocarbons (C_9–C_{13}) decreased with increase in flow rate ratio of steam to AR solution, suggesting that hydrogen transfer from steam to light hydrocarbons suppressed alkene generation. The H/C ratio of residue produced by the AR cracking with steam was higher than that produced by the AR cracking without steam. Some hydrogen species supplied from steam to the residue and others supplied to light hydrocarbons.

4. Activity of α-Fe_2O_3 catalyst containing Zr and Al for desulfurization of heavy oil

The petroleum residual oil including AR contains sulfur. Hydrodesulfurization is the useful method to remove sulfur from petroleum, producing high-quality oil. The residual oil contains acyclic sulfur compounds, such as thiols and disulfides, and cyclic compounds including thiophene ring. The decomposition of the cyclic sulfur compounds was harder than acyclic compounds [14].

The catalytic cracking of heavy oil with steam using the α-Fe_2O_3 catalyst containing Zr and Al produced the hydrogen species during the reaction of heavy oil with the oxygen species derived from steam [9]. Some hydrogen species were supplied to hydrocarbons and residue. The remaining hydrogen species might react with sulfur compounds in AR and be supplied to form H_2S [10]. Hence, desulfurization of AR with the catalyst in a steam atmosphere was examined in this section.

4.1. Desulfurization of AR

Catalytic cracking of AR with the α-Fe_2O_3 catalyst containing Zr and Al was conducted in a steam atmosphere ($F_S/F = 2.7$) [10]. The reaction conditions were the same as decomposition of AR at 3.1. Produced amounts of H_2S and SO_2 were measured by gas detecting tube (GASTEC Corp.). Sulfur content in liquid products was determined by oxidative microcoulometry according to JIS K 2541-2. Sulfur contents deposited on the catalyst were measured by elemental analysis (EA1110, Finningan Mat.)

Catalytic cracking of AR produced approximately 61 mol%-C of oil product, 4 mol%-C of gas product, and 35 mol%-C of residue. Sulfur concentration in the product oil decreased to 1.4 wt% compared to the 2.5 wt% of sulfur in AR, and H_2S was generated, indicating that sulfur compounds in AR were decomposed [10]. When desulfurization was conducted using dibenzothiophene as a model compound of a cyclic sulfur compound in AR, dibenzothiophene was decomposed producing CO_2, H_2S, hydrocarbons, and sulfur compounds [10]. Hence, acyclic and cyclic sulfur compounds might be decomposed with the catalyst in a steam atmosphere.

4.2. Effect of steam on desulfurization of AR

To examine the effect of steam on desulfurization of AR, catalytic cracking of AR was conducted at various steam flow rates (F_S/F = 0–2.7) [10]. **Figure 8** showed the sulfur yield of catalytic cracking of AR at flow rate ratio of steam to AR solution (F_S/F) of 0–2.7. The carbon yield of oil and residue was almost constant as shown in **Figure 5**. The catalytic cracking of AR without steam produced little H_2S, and the H_2S yield increased with increase in flow rate ratio of steam to AR solution. The CO_2 yield also increases with increase in the flow rate ratio of steam to AR solution. These results indicated that sulfur compounds reacted with some hydrogen species derived from steam to produce H_2S when oxygen species reacted with heavy oil.

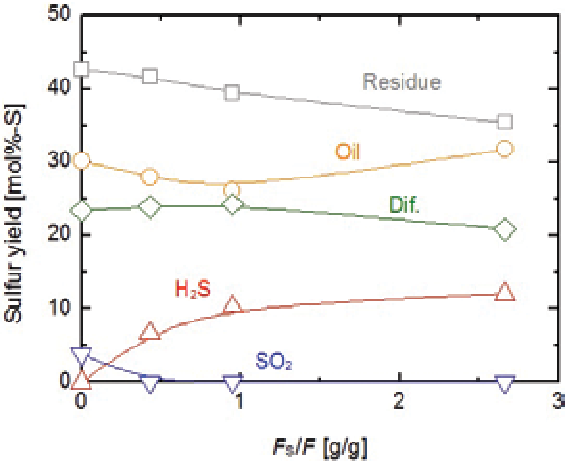

Figure 8. Sulfur yield of catalytic cracking of AR with and without steam (F_S/F = 0–2.7) (reproduced from elsewhere [10]).

The SO_2 was detected only in the reaction without steam. The lattice oxygen of iron oxide reacted with sulfur compounds, producing SO_2 in the catalytic cracking of AR without steam. The SO_2 has high solubility in water (1.4 mol/kg at 25°C [15]). Hence, no SO_2 might be detected in the catalytic cracking of AR with steam, even if oxygen species generated from steam reacted with sulfur compounds to form SO_2. Some H_2S produced in the reaction also could be dissolved in water. When nitrogen was injected into the water collected in this reaction, H_2S was detected [10]. The difference was approximately 23 mol%-S because of sulfur content, such as H_2S and SO_2, in water and measurement errors of sulfur concentration.

Sulfur content in residue decreased with increase in flow rate ratio of steam to AR solution. Larger amounts of hydrogen species were generated at higher ratio of steam to AR solution and reacted with heavy sulfur compounds deposited on the catalyst to produce light sulfur compounds and H_2S. Sulfur concentration in the oil decreased because sulfur compounds were decomposed to produce H_2S. Increase in sulfur concentration in the oil at $F_S/F = 2.7$ was resulted from production of light sulfur compounds by the reaction of heavy sulfur compounds with large amounts of oxygen and hydrogen species.

5. Conclusion

Decomposition and desulfurization of AR were examined using α-Fe_2O_3 catalyst containing Zr and Al in a steam atmosphere. The catalyst was prepared by coprecipitation method. Heavy oil fraction of AR was decomposed with the catalyst, producing CO_2, light hydrocarbons, and residue. The lattice oxygen of α-Fe_2O_3 reacted with heavy oil at first. Then, oxygen species generated from steam were supplied to the iron oxide lattice and react with heavy oil fraction, producing light hydrocarbons and CO_2. Hydrogen species generated from steam during the reaction of the oxygen species, and heavy oil fraction supplied to light hydrocarbons, H_2S, and residue. Supplies of the hydrogen species to light hydrocarbons suppressed alkene generation. Some hydrogen species reacted with sulfur compound of AR, producing H_2S. Some SO_2 could be generated by the reaction of sulfur compound and oxygen species derived from steam. Consequently, hydrogen species and oxygen species derived from steam reacted with heavy oil fraction and sulfur compound of AR with the α-Fe_2O_3 catalyst containing Zr and Al in a steam atmosphere to produce light hydrocarbons.

Acknowledgements

This work was partially supported by Grants-in-Aid for Young Scientist B (21760622, 23760733) and Scientific Research C (25420822) from the Japan Society for the Promotion of Science (JSPS).

Author details

Eri Fumoto*, Shinya Sato and Toshimasa Takanohashi

*Address all correspondence to: e-fumoto@aist.go.jp

Research Institute of Energy Frontier, National Institute of Advanced Industrial Science and Technology, Tsukuba, Japan

References

[1] Moulijn JA, Makkee M, Van Diepen A. Chemical Process Technology. Hoboken, NJ: John Wiley & Sons, Ltd; 2001. pp. 32-78

[2] Sahu R, Song BJ, Im JS, Jeon YP, Lee CW. A review of recent advances in catalytic hydrocracking of heavy residues. Journal of Industrial and Engineering Chemistry. 2015;**27**:12-24

[3] Fumot E, Tago T, Tsuji T, Masuda T. Recovery of useful hydrocarbons from petroleum residual oil by catalytic cracking with steam over zirconia-supporting iron oxide catalyst. Energy & Fuels. 2004;**18**:1770-1774

[4] Hosseinpour M, Ahmadi SJ, Fatemi S. Successive co-operation of supercritical water and silica-supported iron oxide nanoparticles in upgrading of heavy petroleum residue: Suppression of coke deposition over catalyst. The Journal of Supercritical Fluids. 2015;**100**:70-78

[5] Nguyen-Huy C, Shin E. Amelioration of catalytic activity in steam catalytic cracking of vacuum residue with ZrO_2-impregnated macro–mesoporous red mud. Fuel. 2016;**179**:17-24

[6] Kubaschewski O, Schmid-Fetzer R, Petzow G, Effenberg G, editors. Ternary Alloys. Vol. 5. Weinheim, Germany: VCH; 1992. p. 334

[7] Fumoto E, Tago T, Masuda T. Production of lighter fuels by cracking petroleum residual oils with steam over zirconia-supporting iron oxide catalysts. Energy & Fuels. 2005;**20**:1-6

[8] Fumoto E, Tago T, Masuda T. Recovery of lighter fuels from petroleum residual oil by oxidative cracking with steam over Zr–Al–FeO x catalyst. Chemistry Letters. 2006;**35**:998-999

[9] Fumoto E, Sugimoto Y, Sato S, Takanohashi T. Catalytic cracking of heavy oil with iron oxide-based catalysts using hydrogen and oxygen species from steam. Journal of the Japan Petroleum Institute. 2015;**58**:329-335

[10] Fumoto E, Sato S, Takanohasi T. Desulfurization of heavy oil with iron oxide-based catalysts using steam. Journal of the Japan Petroleum Institute. 2015;**58**:336-340

[11] Fumoto E, Sato S, Takanohashi T. Catalytic cracking of heavy oil over a complex metal oxide catalyst in a steam atmosphere. In: Dalai AK, editor. Nanocatalysis for Fuels and Chemicals. Washington, DC: American Chemical Society; 2012. pp. 75-85

[12] Fumoto E, Matsumura A, Sato S, Takanohashi T. Recovery of lighter fuels by cracking heavy oil with Zirconia−Alumina−Iron Oxide catalysts in a steam atmosphere. Energy & Fuels. 2009;**23**:1338-1341

[13] Kondoh H, Hasegawa N, Yoshikawa T, Nakasaka Y, Tago T, Masuda T. Effects of H_2O addition on oil sand bitumen cracking using a CeO_2−ZrO_2−Al_2O_3−FeOx catalyst. Energy & Fuels. 2016;**30**:10358-10364

[14] Mochida I, Choi K. An overview of hydrodesulfurization and hydrodenitrogenation. Journal of the Japan Petroleum Institute. 2004;**47**:145-163

[15] National Institute of Standards and Technology. NIST Chemistry WebBook [Internet]. Available from: http://webbook.nist.gov/chemistry/

Mn-Zn Ferrite as Recycled Material Resource Based on Iron Oxide Suitable to Functional Green Devices

Roberto Baca

Additional information is available at the end of the chapter

http://dx.doi.org/10.5772/intechopen.72418

Abstract

Today manufacturing stages in electronic device industry of wide-scale production can be restricted due to the high costs resulting from energy consumption, the use of organic solvents, production of hazardous intermediates, and formation of waste products leading to environmental pollution and several biological risks which damage society's ability to sustain the planet for future generations. As recycled material resource based on iron oxide, the Mn-Zn ferrite is an interesting candidate. In the last decades, this material has been manufactured by using ceramic process technologies to design magnetic devices as components useful in switching mode electronic systems. However, these processing technologies have generated negative environmental impact as emission of toxic gases and higher use of energy resources. The Mn-Zn ferrites employed in consumer electronics deteriorate the earth when its final placement as waste in landfills occurs. Then, attitudes in resource recovery should allow the recycling of the materials from electronic waste to converting those to new products; therefore, uncommon physical properties from shredding processes are available when bulk ferrites are converted to foil ferrites. This chapter provides a comprehensive study on recyclability of the Mn-Zn ferrites, exploring both structure and conduction properties in foil ferrites to use their nonlinear behavior in functional green devices.

Keywords: electronic waste, shredding phase, life-cycle analysis, foil ferrite, functional green device

1. Introduction

In the past, a large number of physical and chemical processes have been widely used to manufacturing the different types of electronic devices with the desired characteristics [1, 2]. Beyond the supply of raw materials during manufacturing cycles, however, the environmental and human health impacts have restricted the wide-scale production [3, 4]. In response to those concerns, coherent procedures that enable device manufacturers to reduce or eliminate toxic substances in their designs will be a major advance toward green development.

It is well known that for the materials selection for conventional electronic devices, the primary purpose is link material and function. The latter has been achieved by focusing on selected material attributes, including mechanical, thermal, electrical, optical, and chemical properties, and processing characteristics [5]. Also, traditionally selection has been focused solely on cost; nevertheless, availability, environmental consequences of use, and recycling must also become important factors. Recycling is the transformation of waste into usable products or materials; it is sometimes referred as resources recovery which might be often more environmentally gentle than using raw materials owing to reduced energy use and elimination of hazardous gases and other pollutants [6].

The assessment of recycling potential must be based on established principles, including knowledge of the relative ease of "liberation" of the materials of interest and specific characteristics during physical separation technology and shredding in accordance with the international materials life-cycle initiative established by the United Nations Environmental Program (UNEP) and the Society for Environmental Toxicology and Chemistry (SETAC) [7]. Conversely, design of products profoundly will affect the potential recyclability of the resources they contain [8].

The chapter is focused on recovery of one useful material based on iron oxide well known as Mn-Zn ferrite extracted from unusable electronic systems. Using a scientific tool known as life-cycle assessment (LCA), which takes into account all stages of the life cycle of products or materials, including processing technology, manufacturing processes, use phase, and end-of-life routes, will deliver powerful basis to quantifying the recycling performance. Thus, researching Mn-Zn ferrites in foil shape will provide theoretical basis for open-loop recycling, converting waste materials into suitable materials in its second life.

This chapter is organized as follows. After introducing the recycling concept and their environmental advantages, it presents the Mn-Zn foil ferrites as recycled material resource explaining the source of their uncommon physical properties. Then the following sections are focused on analysis of both structure and conduction properties to functional green devices into engineering applications.

2. Recycled material resource: Mn-Zn ferrite

Ferrites are ceramic, homogeneous materials composed of various oxides with iron oxide as their main constituent. Ferrites have several distinct crystal structures. However, for this chapter, only the Mn-Zn ferrites of cubic crystal structure are concerned. Mn-Zn ferrites are used for frequencies less than 2 MHz and at room temperature have a resistivity lower at 10^5 Ωm [9]. Their first practical application was as inductors used in LC filters for frequency division multiplex equipment. The combination of high resistivity and good magnetic properties made these ferrites an excellent material for these filters operating over the 50–450 kHz frequency range. For five decades ferrite components have been employed in a widening range of applications [10]. Currently these are useful as magnetic devices into applications such as switching mode power supplies (SMPS) and lighting electronic ballasts, matching and storage devices, interference suppression, etc.

It is well known that the magnetic structure of a Mn-Zn ferrite is noncollinear in a certain range of temperatures and magnetic fields, which results from competitions between antiferromagnetic interactions of their sublattices, aligning the sublattice magnetizations antiparallel to each other, and under an external field will try to align them parallel to each other [11]. Such magnetic interactions between d ions had allow to predict magnetic properties and thus to calculate composition with structure parameters; however, dominant interaction is exchange coupling between Mn and Fe ions caused by the magneto-crystalline anisotropy. Furthermore, it has been shown that the states of Mn and Fe ions support both ferromagnetic and antiferromagnetic long-range orders [12]. At lower field conditions, bulk ferrites always are accompanied by characteristic anomalies in their physical properties, like domain structure [13]. The last indicates that the resistivity in their grain boundaries will be short-circuited due to the domain wall excitation by the applied alternating magnetic field when the frequency changes from 10 kHz to 1 MHz [14].

Mn-Zn ferrites have been manufactured by a complex composition of iron oxide (Fe_2O_3) mixed with manganese oxide (MnO) and zinc oxide (ZnO) by using ceramic process technologies. Ceramic process can be divided into four functions: preparation of the powder, forming powder into cores, sintering cycle, and finishing stage [9, 10]. Thus, taking into account environmental impacts, the use of energy resources, etc., efficiency in the processing technology of bulk ferrites must be studied into LCA methodology, including product manufacturing, use phase, and end of life. **Figure 1** illustrates the schematic of the life-cycle assessment methodology for bulk ferrites.

LCA methodology with the stages coverage in **Figure 1** is understood in accordance with the following. During the preparation of the powder, raw material (Fe_2O_3) and MnO and ZnO oxides as constitutes are weighed and thoroughly mixed into a homogeneous mixture to form slurry and then mixed in a ball mill [9, 15]. After calcining process in air atmosphere at the powder temperature of approximately $1000^{\circ}C$, partial decomposition of the carbonates and oxide evaporation of impurities occurs.

Besides, forming powder into core geometries is done by dry pressing process, and to achieve final magnetic and mechanical characteristics in bulk ferrites, sintering cycle must be completed. This phase consists in gradual ramping up from room temperature to approximately $800^{\circ}C$ into air atmosphere. After, the temperature is further increased to the final temperature cycle from 1000 to $1500^{\circ}C$, after a cool-down cycle is needed at reduced oxygen pressure. Finally, most ferrites will require some shape of finishing in accordance with their magnetic performance. Subsequently, the Mn-Zn bulk ferrites are in general employed as SMPS into product manufacture (see **Figure 1**). However, severe problems as the combination of core losses (hysteresis, eddy currents, and residual), winding losses, and failures in power semiconductor

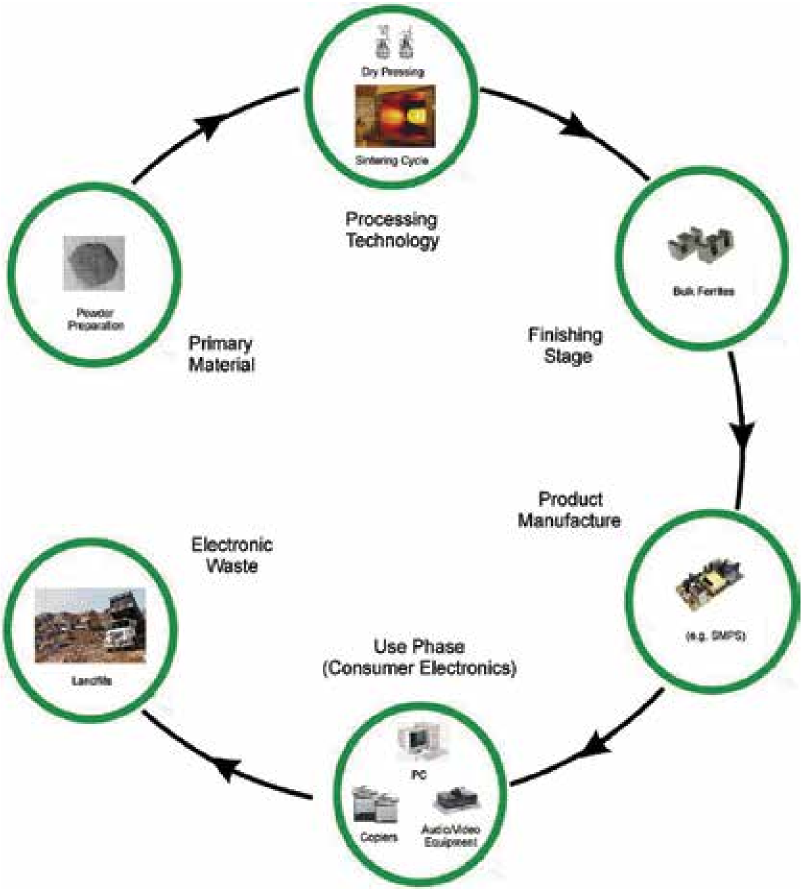

Figure 1. Schematic of the LCA methodology as applied to Mn-Zn bulk ferrite production including manufacturing stages and final disposal.

devices under extreme switching conditions increase losses by temperature rise resulting in thermal runaway which reduce end of life of the consumer electronics [16].

The LCA studies confirm that the processing technology of Mn-Zn bulk ferrites in their first life, including powder preparation, SMPS manufacturing, and final disposition of constituent materials, results in negative environmental impact such as emission of toxic gases during powder preparation, higher use of energy resources into sintering cycle, and electronic waste by the poorly processing technology and inadequate design of SMPS which has taken at the final placement of such these ferrites often in landfills as shown in **Figure 1**.

From earlier studies it has been identified that power losses in Mn-Zn ferrites under low-frequency excitation are close to zero, because chemical composition and oxidation degree depend on temperature like semiconductor materials; then a small grained ferrite (<5 μm) with a single magnetic domain structure would be capable to drive at low frequencies (< 10 kHz) when bulk ferrites are converting in foil ferrites [15, 17]. Hence, such grain-reduced crystalline structure must be evaluated using a recycling model to identify critical parameters in view of recycling performance and resource efficiency; therefore, a methodology such as Life-Cycle Green Strategy (LCGS) is proposed here. **Figure 2** illustrates the recycling model based on LCGS for recovery of Mn-Zn foil ferrites from bulk ferrites. The recycling model represents the liberation of bulk ferrites during different phases from dismantling, physical separation, and shredding phase as a function of the device-manufacture characteristics, specifically the parameters that will characterize the foil ferrites as physical dimensions to operability into an electronic signal processor (see **Figure 2**) [18].

Ferrites with E core geometry of different dimensions have been recovered from three systems: LC filter, lighting electronic ballast, and SMPS. The foil ferrites with area of 5 x 5 mm^2 and thickness of 1 mm are processed by using shredding phase. Shredding phase consists in cut into the small bulk ferrite pieces to get ease fracture pathways along each piece. The fracture strength will be depending on carefully applied mechanical stress, and when the critical fracture length occurs, uniform foil ferrites of different dimensions and thickness are attained.

The following sections in this chapter will demonstrate technological potential of foil ferrites to design suitable functional green devices. Therefore, due to the arduous task in composition

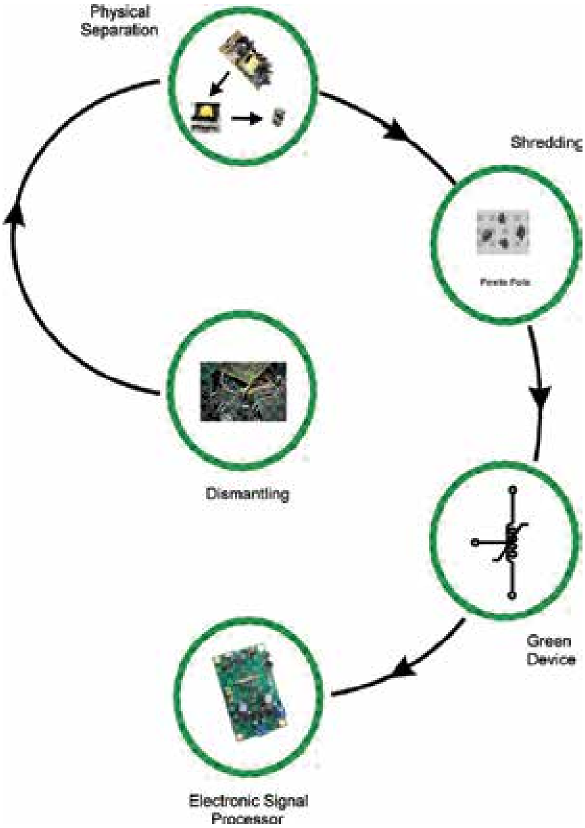

Figure 2. Schematic of recycling model based on LCGS as applied to recovery of foil ferrite samples.

finding of the Mn-Zn ferrites, predicting theoretically their uncommon properties is a possibility in foil ferrite analysis; then studying structure and conduction properties makes it possible to estimate their physical behavior.

3. Structure and conduction properties in foil ferrites

This section discusses structure and conduction properties in foil ferrites. It then reviews general capabilities of x-ray diffraction (XRD) and electrical characterization techniques for the study of foil ferrites and behavior with emphasis on knowledge of their properties. The interrelation of structure and conduction properties as a function on their magnetic ordering is the key issue in green electronic device design.

Usually, copper source with CuKα radiation (λ = 0.154 nm) is employed in x-ray diffraction studies; however, features of Mn-Zn ferrites at higher wavelengths are indistinguishable. Thereby, a PANalytical x-ray diffractometer with CoKα radiation (λ = 0.179 nm) is used here to obtain XRD patterns in foil ferrite samples. Cobalt source allows higher diffraction angles and peak spreads. Current-voltage measurements are performed by using a digital storage oscilloscope (Tektronix, TDS1012C) at room temperature. A function generator (Matrix, MFG-8250A) is used to produce a linear-ramp signal at low frequency (f = 100 Hz) with voltage scanned from −10 V to 10 V to ensure that the magnetic saturation in the samples does not occur.

3.1. X-ray diffraction analysis

Figure 3 shows the XRD patterns of the foil ferrite samples analyzed here and labeled as FF-1, FF-2, and FF-3. These samples are polycrystalline with spinel oxide structure. Several peaks appear, which correspond to the (111), (022), (113), (004), (224), (115), (044), (026), and (335) crystallographic planes of the magnetite phase ($\mathrm{Fe_3O_4}$).

Frequently, structural defects in Mn-Zn ferrites are classified as grain boundaries, where there is a face-centered cubic lattice of oxygen ions with a unit cell consisting of eight functional units [19, 20]. Such configurations indicate the presence of clusters which are interpreted in terms of complex defects consisting of Fe ions in an interstitial tetrahedral site with two adjacent octahedral Fe vacancies, which suggest that the foil ferrites are nonstoichiometric oxides in composition. Thus, in foil ferrite samples, their chemical formula can be written as $Mn_x Zn_y Fe_2 O_4$, where the Mn cations occupy the tetrahedral sites and the Zn cations occupy the octahedral sites, while x and y will be defined as composition parameters [21].

The relative number of planes oriented in a certain direction can be related to the area under the XRD peak, as well as the peak height which will represent that reflection; here XRD is used to determine the orientation corresponding to the significant plane in the foil ferrite structure, being it the c-axis orientation as the area under the (113) reflection peak. The effect of powder preparation and sintering cycle on the crystal size and thickness in ceramic process technologies for Mn-Zn ferrites is associated with the full width at half maximum (FWHM) and elastic strain ($\epsilon_{2\theta}$) [22].

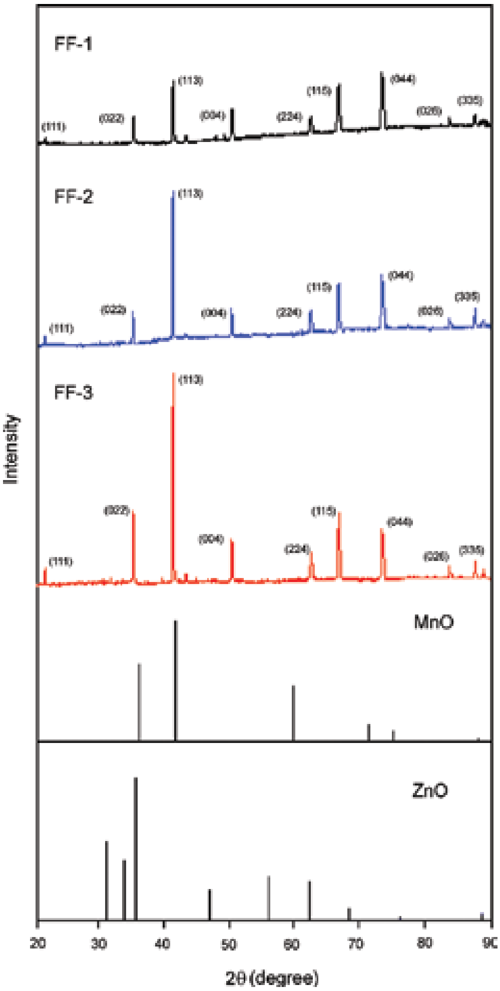

Figure 3. XRD patterns of three different foil ferrite samples, where XRD patterns of MnO and ZnO are included as reference for analysis of the strain and chemical composition.

In the case of the foil ferrite irradiated by CoKα radiation, the Debye-Scherrer relation becomes $D = N[(FWHM)\cos\theta]^{-1}$, where D is the mean crystallite size, $N \approx c/r$ is the interatomic spacing with c = 8.494 Å for magnetite, r = 0.64 Å as the radius of Fe^{+3} ion, and θ is the reflection angle to the (113) orientation, while the Scherrer relation $t = \lambda\,[\epsilon_{2\theta}\cos\theta]^{-1}$, where t is the minimum thickness for carrier conduction in the absence of scattering events and $\epsilon_{2\theta} = (d - d_0)/d$ with d as the actual atomic plane spacing and d_0 the unstrained atomic plane spacing [23]. **Table 1** gives the structure parameters attained from XRD patterns in foil ferrite samples.

To know the effect of the complex composition of Fe_2O_3 mixed with MnO and ZnO on lattice strain, it can be well studied by using $\frac{\Delta d}{d} = \frac{\Delta\theta}{\tan\varphi}$, where Δd/d is the average strain along the (113) reflection peak with respect to the substrate, $\Delta\theta$ as the difference between incident angle for measured (113) plane and the (113) plane corresponding at the magnetite, and φ is the angle with respect to the

Sample	2θ	FWHM	$\epsilon_{2\theta}$	D (nm)	t (nm)
FF-1	40.88°	0.19	1.22×10^{-4}	13.34	1565.86
FF-2	40.93°	0.19	1.07×10^{-3}	13.35	178.55
FF-3	40.93°	0.19	1.07×10^{-3}	13.35	178.55

Table 1. Structure parameters in foil ferrites.

substrate planes [24]. As the Mn-Zn ferrite is a powder composition with Fe_2O_3 as their main constituent, a foil ferrite can be approximately seem as a structure MnO/Fe_2O_3/ZnO where diffusion processes occur; then, for strain analysis the equivalent substrate planes will be both MnO and ZnO as reference XRD patterns (see **Figure 3**) [1]. **Table 2** provides the average strain estimated from XRD patterns in foil ferrite samples.

3.2. Electrical analysis

Figures 4 and **5** explain the measuring strategy to know electrical performance in foil ferrite samples labeled as FF-1, FF-2, and FF-3. Two conditions are performed, both longitudinal and transverse bias as shown in **Figures 4(a)** and **5(a)**, respectively. Current-voltage (I-V) curves are displayed in **Figure 4(b)** at longitudinal bias and at transverse bias in **Figure 5(b)**. Two aluminum electrodes of circular geometry with cross section area of 3.14 mm^2 are placed on each foil ferrite sample to inject and collect voltage signals. A resistor of 1 kΩ is used to measure the output voltage and thus calculate the current flow by Ohm's law. Ohmic behavior is observed in I-V curves for voltage bias from −2 to 2 V, while at higher voltages, I-V curves indicate that current and voltage follow a power-law relationship $I = \alpha V^n$ with n = 1.5. Such power-law dependence is characteristic of space-charge-limited conduction (SCLC) [25]. Analysis in I-V curves by using a SCLC model is the experimental method used here with current-voltage dependence proportional to $\alpha = \frac{9}{8}\varepsilon_0 \varepsilon_r \mu S L^{-3}$, where $\varepsilon_0 \varepsilon_r$ is the dielectric constant, μ is the carrier mobility, L is the spacing between electrodes, and S is the cross-sectional area.

Sample	2φ (ZnO)	2φ (MnO)	$\Delta\theta$	$\left(\frac{\Delta d}{d}\right)_{ZnO}$	$\left(\frac{\Delta d}{d}\right)_{MnO}$
FF-1	34.42°	40.89°	-5×10^{-3}	−0.016	−0.013
	62.86°			−0.008	
FF-2	34.42°	40.89°	44×10^{-3}	0.14	0.11
	62.86°			0.072	
FF-3	34.42°	40.89°	44×10^{-3}	0.14	0.11
	62.86°			0.072	

Table 2. Average strain in foil ferrites associated with ZnO and MnO.

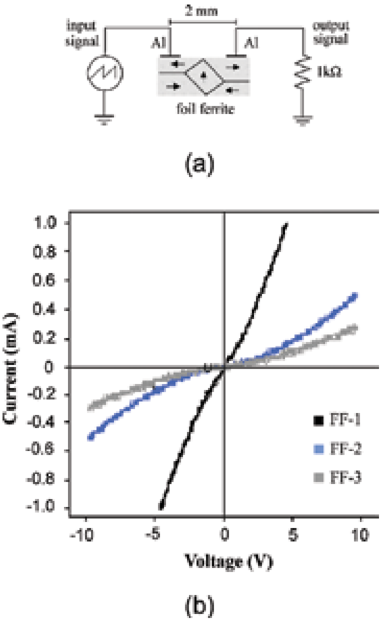

(a)

(b)

Figure 4. (a) Schematic diagram of the foil ferrites in cross-sectional view connected in the test circuit. (b) Current-voltage (I-V) curves of the three different foil ferrite samples, which are longitudinally biased.

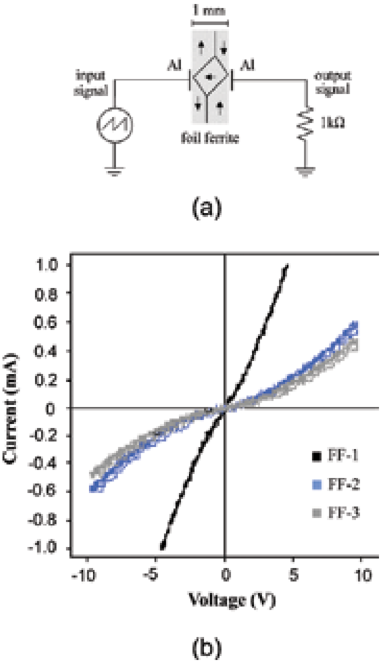

(a)

(b)

Figure 5. (a) Schematic diagram of the foil ferrites in cross-sectional view connected in the test circuit. (b) Current-voltage (I-V) curves of the three different foil ferrite samples, which are transversally biased.

To obtain conduction parameters in foil ferrite samples, the parameter α was initially calculated from I-V curves. Then, by tracing slopes on I-V curves, the critical voltage, $V_C = 10enL^2(\varepsilon_0\varepsilon_r)^{-1}$, and trap-filled limit voltage, $V_{TFL} = 6eN_tL^2(\varepsilon_0\varepsilon_r)^{-1}$, are found as in earlier methodologies, where both carrier concentration, n, and trap concentration, N_t, has been well estimated [26, 27]. Also, adiabatic activation energy, ΔG^*, should be responsible for the diffusion processes (displacement reactions) during sintering cycle in processing technology of Mn-Zn bulk ferrites in contrast to the overall activation energy under SCLC. Theoretical studies have reported ΔG^* with value of 0.5 eV for pure hematite (Fe_2O_3) smaller than the activation energy of about 1 eV at $T > 800^\circ C$ for conductivity [28]; then as reference ΔG^* can be estimated as a function of V_C for this analysis.

Thus, $\Delta G^* = 0.5V_C$ will be used to evaluate conduction properties in foil ferrite samples as a function of the mobility $\mu \sim exp\left(-\frac{\Delta G^*}{kT}\right)$, where k is the Boltzmann constant and T is equivalent at the processing temperature during sintering cycle. Finally, knowing α and μ parameters, $\varepsilon_0\varepsilon_r$ was estimated for both longitudinal and transverse bias. **Table 3** summarizes the conduction parameters at longitudinal bias where L = 2 mm, W = 1 mm (physical width of each foil ferrite under test), and $S = t \times W$ with t as the thickness previously estimated by XRD analysis in Section 3.1, while the conduction parameters at transverse bias are registered in **Table 4**, where L = 1 mm and $S = 3.14 \times 10^{-2}\,\mathrm{cm}^2$ is the cross section area of the aluminum electrodes.

Chemical formula $Mn_xZn_yFe_2O_4$ allows explaining structure and conduction properties in foil ferrites where magnetite Fe_3O_4 is equivalent to $Fe \cdot Fe_2O_4$ with Fe^{+3} ion substituted by Mn^{+2} in the tetrahedral sites and Zn^{+2} in the octahedral sites. As radius of Fe^{+3} is smaller than that of Zn^{+2} and greater than that of Mn^{+2}, structural disorder will occur; therefore, exchange interactions via the oxygen ions will define magnetic properties as a function of the distance and angle of the Mn—O—Zn bonds; also, SCLC will depend on different conduction mechanisms related to the exponential distribution of defects (grain boundaries) [13, 27]. From results attained here, it is confirmed that the sample FF-1 exhibits lower $\epsilon_{2\theta}$ than FF-2 and FF-3 samples. Chemical composition approximately proportional to the average strain ($x \sim \left(\frac{\Delta d}{d}\right)_{MnO}$ and $y \sim \left(\frac{\Delta d}{d}\right)_{Zno}$) in samples FF-2 and FF-3 resulted to be positive associated to tensile stress while negative in sample FF-1 related to compressive stress. In the samples, x and y are connected by the coupling type dominant in the Mn-O-Zn bonds, where tensile stress dominated by longer distance and angle of 180° is *antiferromagnetically coupled*, while compressive stress is *ferromagnetically coupled* at shorter distance with angle of 90°. The V_C and V_{TFL} voltages from **Tables 3** and **4** were extracted to evaluate the charge concentration (carrier distribution), resulting n in the range from 10^{20} to $10^{22}\,\mathrm{cm}^{-3}$ at the surface while N_t in the range from 10^{15} to $10^{17}\,\mathrm{cm}^{-3}$ at the bulk of each sample, which reveals that major differences of $\varepsilon_0\varepsilon_r$ and magnetic ordering are correlating to the charge concentration differences of foil ferrites.

Sample	α	V_C (V)	ΔG^* (eV)	V_{TFL} (V)	μ $(cm^2V^{-1}s^{-1})$	$\varepsilon_0\varepsilon_r$ $(F\,cm^{-1})$
FF-1	0.92×10^{-4}	1.12	0.56	2.32	$5.49\,x\,10^{-3}$	7.61
FF-2	1.32×10^{-5}	1.44	0.72	2.88	$1.43\,x\,10^{-3}$	36.87
FF-3	0.85×10^{-5}	1.68	0.84	2.64	$4.83\,x\,10^{-4}$	632.74

Table 3. Conduction parameters at longitudinal bias.

Sample	α	V_C (V)	ΔG^* (eV)	V_{TFL} (V)	μ $(cm^2\,V^{-1}\,s^{-1})$	$\varepsilon_0\,\varepsilon_r$ $(F\,cm^{-1})$
FF-1	0.92×10^{-4}	1.12	0.56	2.32	5.49×10^{-3}	4.74×10^{-4}
FF-2	1.82×10^{-5}	1.28	0.64	2.42	2.97×10^{-3}	1.73×10^{-4}
FF-3	0.48×10^{-5}	1.12	0.56	2.56	5.49×10^{-3}	2.47×10^{-5}

Table 4. Conduction parameters at transverse bias.

4. Foil ferrite as functional green device

This section discusses the possibility of the functional green devices built by foil ferrite samples. Electrical performance under both longitudinal and transverse bias conditions has confirmed nonlinear behavior which obeys at the conduction properties through orderly small grained structure being it equivalent to the magnetic-electrical conduct of a self-inductor with hysteresis when it is connected as shown in **Figure 6**. Current-voltage (I-V) curves are obtained by using a digital storage oscilloscope (Tektronix, TDS1012C) at room temperature. A function generator (Matrix, MFG-8250A) was used to produce the input voltage signals.

To connect the input signal and collect the output signal in the applications shown here, two aluminum electrodes of circular geometry with cross section area of 0.1 × 0.1 cm^2 have been placed on each foil ferrite; also, a resistor has been used to measuring of the output signals.

4.1. Mixer circuit

Modulation is the process of converting information one wants to obtain into one or more properties of a sinusoidal signal called the carrier. This information can be analogic signal, such as a varying voltage or current, or a digital signal, which consists of sequence of bits, i.e., 0 and 1 values. In general several modulation schemes can be represented by using mixer circuits. The main type of modulator recently employed is the quadrature mixer [29].

To disclose the performance of a foil ferrite as mixer circuit to modulation process, a basic schematic diagram of **Figure 7** has been built. A full-rectified signal with amplitude of 15 V was applied on first outer node at operating frequency of 120 Hz. In the middle node, a sinusoidal signal with amplitude of ±7.5 V at operating frequency of 500 Hz was applied. The full-rectified signal was obtained by a variable self-transformer of alternating voltage from 0 to 150 V. A resistor of 1 kΩ is connected in the second outer node to monitoring of mixing signal (see **Figure 7**). It is observed that the mixing signal follows the shape of the full-rectified signal when it is larger than the sinusoidal signal, producing an output signal with amplitude of ±3.5 V. Otherwise, when the amplitude of the sinusoidal signal is greater with respect to the full-rectified signal, mixing process is negligible, because there are strong anisotropy differences among longitudinal and transverse paths on foil ferrite samples related to its structural disorder. Therefore, a foil ferrite will operate in the electronic signal processors integrated by mixer circuits to drive control systems as a function of complex signals at low-power excitation [30].

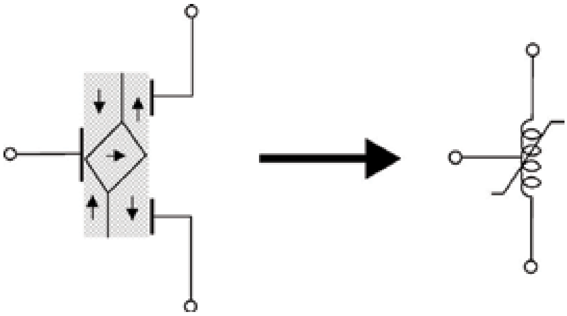

Figure 6. Foil ferrite equivalent at the self-inductor with hysteresis.

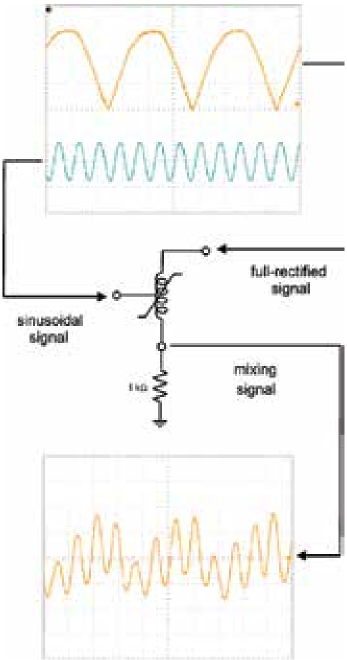

Figure 7. Schematic of the mixer circuit done with foil ferrite FF-1 when it is operating under full-rectified and sinusoidal signals to produce mixing signal.

4.2. Phase detector

A phase detector produces a voltage proportional to e(t) = u(t) – y(t) as the phase difference between the signals u(t) and y(t) in the block diagram of **Figure 8**. This block diagram corresponds to phase-locked loop (PLL) system. A PLL is comprised of three blocks: phase detector, filter, and voltage-controlled oscillator (VCO).

The voltage e(t) upon filtering is used as control signal for the VCO. The VCO produces a frequency proportional to input signal u(t), and any time variant signal appearing on the filter output will modulate the VCO frequency [31]. A feedback path among VCO and phase detector

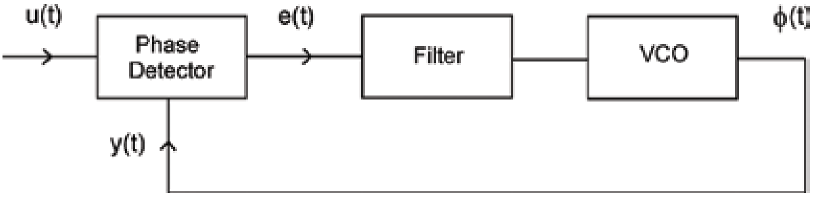

Figure 8. Block diagram of a conventional phase-locked loop (PLL) system.

produces unity gain, and as a result, the PLL provides an online estimate of the synchronized fundamental component, y(t), and its phase angle, ϕ(t), with output frequency equal to that of the input during phase lock. The PLL is an adaptive system which follows variations in amplitude, phase angle, and frequency of signal u(t). Hence, the structure of a PLL is simple, and this makes it suitable for real-time applications for hardware implementations [32].

The schematic circuit of **Figure 9** was used to evaluate the performance of the foil ferrite sample as phase detector. A resistor of 10 kΩ is connected in node V_0 to monitoring of output signal. To simulate phase difference between two sinusoidal signals, a low-pass filter built with a simple RC circuit was implemented [33]. Signal connected to the RC circuit input relates V_1, while signal collected from RC circuit matches with V_2. Such signals are applied on nodes V_1 and V_2 where ±10 V is fixed in V_1 at operating frequency in the range of 0.5 to 5 kHz. The resulting waveforms are shown from **Figure 10(a)–(c)**.

At 0.5 kHz, the phase angle between signals V_1 and V_2 is 22.5°, while to 1 kHz is 40.5° and when operating frequency increase until 5 kHz resulted to be 58.5°. Meanwhile, at the output node V_0, when frequency is 0.5 kHz, 1 kHz, and 5 kHz, the phase angle corresponds to 4.5°, 9.2°, and 1.2°, respectively. It is observed that the phase angle between V_0 and V_1 signals is close to zero when phase angle between V_1 and V_2 signals shift from 0 to 90°.

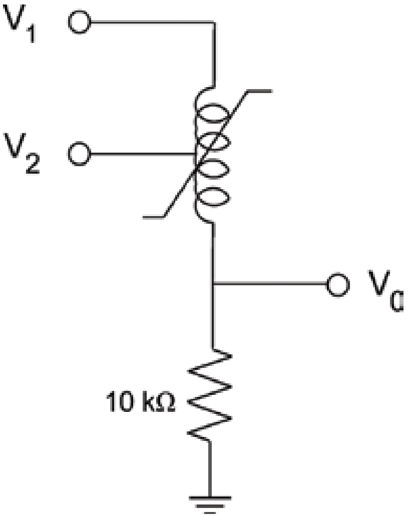

Figure 9. Schematic circuit to evaluate the performance of the foil ferrite FF-3 as phase detector.

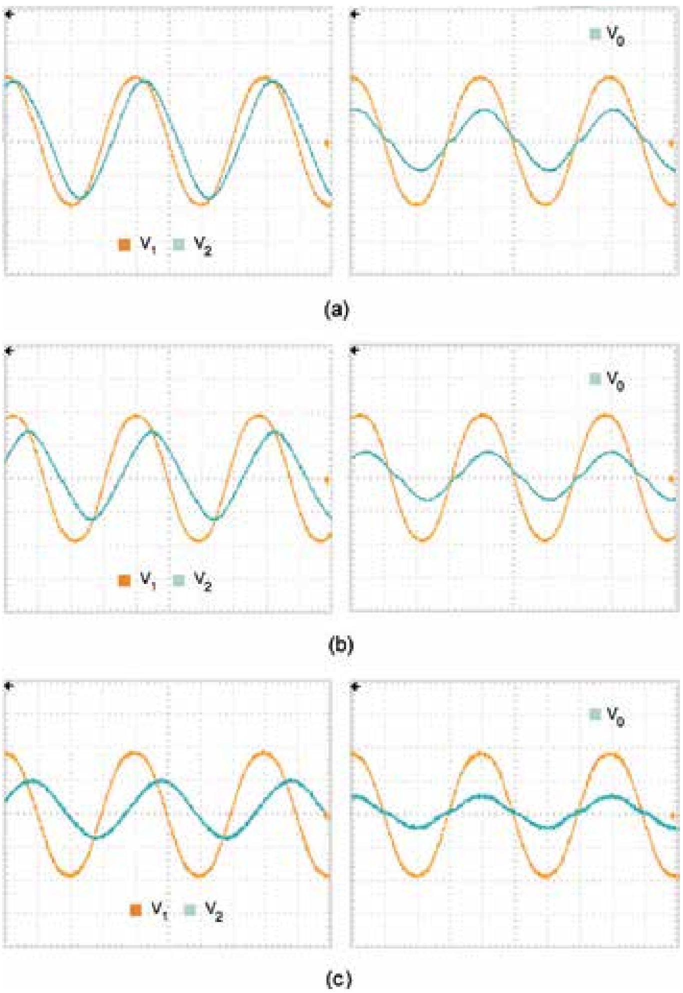

Figure 10. Waveforms monitored from the schematic circuit of **Figure 9** driven at three operating frequencies: (a) 0.5, (b) 1, and (c) 5 kHz. The input and output signals are shown.

Also, V_2 and V_0 signals decrease slowly as frequency rises. Results from **Figure 10** indicate that foil ferrite samples of grain-reduced crystalline structure with single magnetic domain offer controllable power losses under low-frequency excitation. Hence, a foil ferrite will operate like PLL system.

5. Summary

Since 1994, initiatives in response to the environmental and ecotoxicological concerns in manufacturing processes based on life-cycle assessment (LCA) have been established. To manufacturing electronic devices with desired characteristics, the conventional selection of raw materials had depended on link between material and function; however, environmental consequences of use, availability, and recycling have not been taken into account. Nevertheless, to ensure availability of the materials for future generations, the transformation of waste into usable materials has been discussed here, as more environmentally beneficial which implies that resource disposal and material flow will require well-designed systems into manufacturing stages. The latter is a challenge for engineers and scientists responsible with the current state of the nature resources.

The Mn-Zn ferrites have been chosen as recycled material resource because it provides suitable uncommon physical properties when it is converted from bulk ferrite to foil ferrite. Also, negative environmental impact such as emission of toxic gases during powder preparation, higher use of energy resources into sintering cycle, and electronic waste from consumer electronics has demonstrated that Mn-Zn ferrites in bulk shape take their final placement often in landfills. But, to take advantages of the properties in foil ferrites, a recycling model has been employed here as a methodology based on Life-Cycle Green Strategy (LCGS) to ensure recycling efficiency during all overall stages into the green manufacturing.

Due to the interrelation of the structure and conduction properties as a function on magnetic ordering which is the key issue in green electronic device design, the x-ray diffraction and electrical studies have been done on foil ferrites to know if the operating parameters are useful and when it would be used as functional green device. Those studies have confirmed that structural disorder and carrier concentration under longitudinally and transversally bias conditions are responsible of the nonlinear behavior which obeys at the carriers' conduction into their small grained crystalline structure.

Finally, it has been shown that fundamental tools such as recycling practices and basic characterization routes are needed to provide theoretical basis for the green materials exploration, converting waste materials into suitable materials in its second life. Discovering the fascinating properties of the materials, especially structure, conduction, and magnetic parameters is a key to continue the trends to green processing and then synthesize adaptive oxide materials intended for electronic signal processors.

Author details

Roberto Baca

Address all correspondence to: rbaca02006@yahoo.com.mx

Department of Electronics, National Polytechnic Institute, México City, Mexico

References

[1] Grove AS. Physics and Technology of Semiconductors Devices. 1st ed. United States of America: John Wiley & Sons; 1972. 357 p

[2] Keyser CA. Materials Science in Engineering. 6th ed. United States of America: Prentice-Hall, Inc; 1972. 460 p

[3] Ogunseitan OA, Schoenung JM. Human health and ecotoxicological considerations in materials selection for sustainable development. Materials Research Bulletin. 2012;**37**:356-363. DOI: 10.1557/mrs.2012.8

[4] Shamaila S, Leghari Saijad AK, Ryma N-ul-A, Anis Farooqi S, Jabeen N, Majeed S, et al. Advancements in nanoparticle fabrication by hazard free eco-friendly green routes. Applied Materials Today. 2016;**5**:150-199. DOI: 10.1016/j.apmt.2016.09.009

[5] Nakamura S. Current Status of GaN-Based solid state lighting. Materials Research Bulletin. 2009;**34**:101-107

[6] Baca R, Cheong KY. Green synthesis of iron oxide thin-films grown from recycled iron foils. Materials Science in Semiconductor Processing. 2015;**29**:294-299. DOI: 10.1016/j.mssp.2014.05.014

[7] Díaz Coutiño R. Desarrollo Sustentable. 2nd ed. Mexico: McGraw-Hill/INTERAMERICANA EDITORES; 2011. 305 p

[8] Reuter M, Van Schaik A. Opportunities and limits of recycling. A dynamic-model-based analysis. Materials Research Bulletin. 2012;**37**. DOI: 10.1557/mrs.2012.57

[9] Lee J-P, Kim JH, Pyo Chae K, Bae-Lee Y. Crystallographic and magnetic properties of Zn-Mn ferrite. Journal of the Korean Physical Society. 2006;**49**(2):604-607

[10] Magnetic Materials Producers Association. Soft Ferrites. A User's Guide [Internet]. 1998. Available from: http://www.google.com/mmpa SFG-98.pdf

[11] Zvezdin AK, Kostyuchenko VV. Magnetic-field-induced phase transitions in molecular ferrimagnets with two compensation points. Physics of the Solid State. 2001;**43**(9): 1715-1719

[12] Tian G-S, Lin H-Q. Phase transition and ferrimagnetic long-range order in the mixed-spin Heisenberg model with single-ion anisotropy. Physical Review. 2004;**70**:104412

[13] Blundell S. Magnetism in Condensed Matter. 2nd ed. Great Britain: Oxford University in Press; 2008. 234 p

[14] Fiorillo F. DC and AC magnetization processes in soft magnetic materials. Journal of Magnetism and Magnetic Materials. 2002;**242-245**

[15] Verma A, Alam MI, Chatterjee R, Goel TC, Mendiratta RG. Development of a new soft ferrite core for power applications. Journal of Magnetism and Magnetic Materials. 2006;**300**. DOI: 10.1016/j.jmmm.2005.05.040

[16] Chan Samuel SM, Chung Henry SH, Hui Ron SY. Self-oscillating dimmable electronic ballast for fluorescent lamps. IEEE Power Electronics Letters. 2004;**2**(3):87-91. DOI: 10.1109/LPEL.2004.838777

[17] Cao J, Wu J. Strain effects in low-dimensional transition metal oxides. Materials Science and Engineering R. 2011;**71**. DOI: 10.1016/j.mser.2010.08.001

[18] Khalil HK. Nonlinear Systems. 1st ed. United States of America: Macmillan Publishing Company; 1992. 564 p

[19] Hamdeh HH, Ho JC, Oliver SA, Willey RI, Oliveri G, Busca G. Magnetic properties of partially-inverted zinc ferrite aerogel powders. Journal of Applied Physics. 1997;**81**. DOI: 10.1063/1.364068

[20] Wang Z, Schiferl D, Zhao Y, O′Neill HStC. High pressure Raman spectroscopy of spinel-type ferrite $ZnFe_2O_4$. Journal of Physics and Chemistry of Solids. 2003;**64**:2517-2523. DOI: 10.1016/j.jpcs.2003.08.005

[21] Kundaliya DC, Ogale SB, Lofland SE, Dhar S, Metting CJ, Shinde SR, et al. On the origin of high-temperature ferromagnetism in the low-temperature processed Mn-Zn-O system. Nature Materials. 2004;**3**:709-714. DOI: 10.1038/nmat.1221

[22] Wang C, Chen Z, He Y, Li L, Zhang D. Structure, morphology properties of Fe-doped ZnO films prepared by facing-target magnetron sputtering system. Applied Surface Science. 2009;**255**:6881-6887. DOI: 10.1016/j.apsusc.2009.03.008

[23] Fewster PF. X ray Scattering from Semiconductors. 2nd ed. Great Britain: Imperial College Press; 2003. 299 p

[24] Baca-Arroyo R. Structural characterization of the chromium-iron alloy formed by thermal diffusion processes. Advances Materials Research. 2013;**651**:284-288. DOI: 10.4028/www.scientific.net/AMR.651.284

[25] Grinberg AA, Luryi S, Pinto MR, Schryer NL. Space-charge-limited current in a film. IEEE Transactions on Electron Devices. 1989;**36**(6):1162-1170

[26] Xu W, Chin A, Ye L, Ning CZ, Hu H. Charge transport and trap characterization in individual GaSb nanowires. Journal of Applied Physics. 2012;**111**:104515. DOI: 10.1063/1.4720080

[27] Baca-Arroyo R. Nonlinear-electronic transport in Fe_2O_3 thin films grown from grain-oriented iron foils. Advances in Materials Science and Engineering. 2013;**2013**:987572

[28] Liao P, Caspary Toroker M, Carter EA. Electron transport in pure and doped hematite. Nanoletters. 2011;**11**:1775-1781. DOI: 10.1021/nl200356n

[29] Aidin Bassan S, Chen W, Helaoui M, Ghannouchi FM. Transmitter architecture for CA. IEEE Microwave Magazine. 2013;**14**(15):78-86. DOI: 10.1109/MMM.2013.2259399

[30] Terrovitis MT, Meyer RG. Intermodulation distortion in current-commutating CMOS Mixers. IEEE Journal of Solid-State Circuits. 2000;**35**(10):1461-1473

[31] Zhao B, Mao X, Yang H, Wang H. A voltage-controlled oscillator with an ultra-low supply voltage and its application to a fractional-N phase-locked loop. International Journal of Electronics. 2009;**96**(10):1012-1022

[32] Karimi-Ghartermani M, Mokhtari H, Reza Iravani M, Sedighy M. A signal processing system for extraction of harmonics and reactive current of single-phase systems. IEEE Transactions on Power Delivery. 2004;**19**(3)

[33] Sedra AS, Smith KC. Microelectronic Circuits. 4th ed. United States of America: Oxford University in Press; 1998. 1400 p

The Investigation of Removing Direct Blue 15 Dye from Wastewater Using Magnetic *Luffa sponge* NPs

Hayrunnisa Nadaroglu, Semra Cicek,
Hicran Onem and Azize Alayli Gungor

Additional information is available at the end of the chapter

http://dx.doi.org/10.5772/intechopen.73216

Abstract

In this study, loaded *Luffa sponge* membrane forms were modified with ZnO, Fe_3O_4, ZnO/Fe_3O_4 nanoparticles (NPs) to remove of Direct Blue 15 (DB15), which is a carcinogenic azo dye in aqueous solution. ZnO and Fe_3O_4 NPs were synthesized using purified peroxidase enzymes from *Euphorbia amygdaloides* using green synthesis method. Adsorption of DB15 azo dyes was separately studied with membrane forms (LS-pure, LS-ZnO, LS-Fe_3O_4, and LS-ZnO/Fe_3O_4). Optimum contact time, optimum pH, optimum temperature, optimum dye concentration, and optimum LS amount were found as 45 min, pH 8.0, 20°C, 200 mg/L, and 0.025 g in line with the optimization studies, respectively. The obtained membrane forms were characterized using SEM, FT-IR, and XRD techniques. According to obtained results, NPs loaded LS membrane forms are promising in removal of DB15 from textile wastewater contaminated water.

Keywords: Fe_3O_4, ZnO, nanoremediation, *Luffa sponge*, Direct Blue 15

1. Introduction

There are more than 3000 different dyes available and half of them belong to the azo dyes compounds class [1]. Azo dyes are the most frequently used dyes in textile industry and are characterized by the presence of one or more azo linkages (—N=N—), usually in number of one or four, linked to phenyl and naphthyl radicals, which are usually replaced with some combinations of functional groups including: amino ($—NH_2$), chlorine (—Cl), hydroxyl (—OH), methyl ($—CH_3$), nitro ($—NO_2$), sulfonic acid ($—SO_3H$), and sodium salts ($—SO_3Na$) [2–4]. These compounds can lead to significant ecological problems because of the creation of carcinogenic or mutagenic compounds [5–7]. Several azo dyes have been described to lead human bladder cancer, splenic sarcomas, and hepatocarcinoma, because azo dye reduction in the intestinal tract release aromatic amines which are absorbed by the intestine and excreted in the urine [8]. The acute toxicity of azo dyes, with respect to the criteria of the European Union for the sorting of unsafe substances, is low and the values of LD_{50} are 250–2000 mg/kg body weight [9, 10].

The textile dyes can be removed by using physical, chemical, and biological methods [11]. Nevertheless, most of these methods, which simply accumulate or concentrate the dyes, and trigger secondary contamination, resulted in the extreme usage of chemical materials [11, 12].

Because of nanoparticles' features arising from size effect, nanotechnology has emerged in many scientific and industrial fields [13, 14]. It involves studies of measurement, modeling, and manipulation of substance in nanoscale. Nanoremediation is economic and has improved overall efficiency of fragmentation process. Potential catalytic activity of Au, Ag, Pd, Mg, Cu, Zn, and Fe nanoparticles have been reported for degradation of some aqueous cationic and anionic dyes [14–18]. Researchers studied degradation of Methyl Orange, Sunset Yellow, Acid Blue A azo dyes using zero valent iron nanoparticles (NZVI) with diameters between 20 and 110 nm. Methyl Orange, Sunset Yellow, Acid Red A were removed using solution prepared with 2 g NZVI rate of 79.9, 98.9, and 98.8, respectively [19].

However, nanoparticles are left in the ecosystem after their use in the removal of environmental contaminants. Thus, nanoparticles immobilized on a support material are to the fore for environmental remediation [20, 21]. LS is eco-friendly, cost effective, easy to use matrix material successfully used as a biotechnological tool for variety of systems, purposes and applications. LS immobilized cell systems have efficiently studied toward biofilm development for remediation of domestic and industrial wastewater containing toxic metal, paint, chlorinated compounds [22, 32].

In this study, ZnO and Fe_3O_4 nanoparticles were obtained by catalyzing using purified peroxidase enzymes from *Euphorbia amygdaloides* with green synthesis method. Membrane forms have been created by immobilizing the obtained nanoparticles on LS support material. Carcinogenic DB15 azo dye was used to evaluate effectiveness of ones to remove dye (molecular structure of DB15 shown in **Figure 1**). Optimum contact time, pH, temperature, and concentration of dye were analyzed using UV-visible spectrometry. The resulting adsorbents (LS-pure, LS-ZnO,

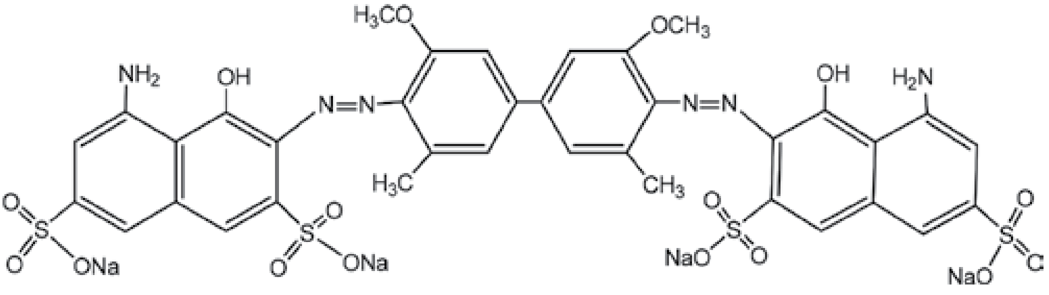

Figure 1. Molecular structure of DB15.

LS-Fe_3O_4, and LS-ZnO/Fe_3O_4) were characterized by SEM, FT-IR, and XRD. Also, adsorption isotherms and kinetics and thermodynamics of these membrane forms were investigated.

2. Materials and methods

2.1. Materials

Direct Blue 15 (CAS no: 2429-74-5), $FeCl_2$, $ZnCI_2$, and other chemicals were purchased from Sigma-Aldrich. Euphorbia (*Euphorbia amygdaloides*) was collected from near the town of Hasankale of Erzurum. Also, LS which is fruit of *Luffa cylindrica* was obtained from a local point of spices sale in Erzurum, Turkey, and they were identified with the helping of taxonomists. All solutions were made in deionized water.

2.2. Green synthesis of Fe_3O_4 and ZnO nanoparticles

2.2.1. Collection of plant sample and preparation of plants extract

Plants (*Euphorbia amygdaloides*) were collected from Hasankale town of Erzurum city. They were washed with distilled water several times for cleaning dust and soil on plants. Then, plants were cut into small pieces. Small pieces (50 g) were thoroughly shattered to form a homogeneous mixture in blender using 250 mL, 10 mM sodium phosphate buffer (pH 6.0). Then, it was centrifuged at 5000×*g* for 10 min and the supernatant was used for enzyme purification [23].

2.2.2. Partial purification of the peroxidase enzyme with ammonium sulfate precipitation

Prepared Euphorbia (*Euphorbia amygdaloides*) plant homogenate was saturated from 60 to 80% with ammonium sulfate, then the peroxidase enzyme was precipitated by centrifuged at 8000×*g*, 10 min. Obtained precipitate was dissolved at 10 mM sodium phosphate buffer (pH 6.0) and was incubated at 4°C for further analysis [23].

2.2.3. Peroxidase enzyme activity test

Determination of peroxidase activity was made by substrate of 1 mM 2,2′-azino-bis(3-ethylbenzthiazoline-sulfonic acid) diammonium salt (ABST) prepared in 0.1 M phosphate buffer at pH 6. For this purpose, 2.8 mL ABST was transferred to a test tube, and then the reaction mixture was formed by the addition 100 μL of 80% enzyme and 100 μL of 3.2 mM H_2O_2 solution into the test tube. The change in absorbance was monitored at 412 nm using UV–Visible spectrophotometer at 1 min intervals for 3 min. Blank test tube was prepared using distilled water instead of enzyme in the reaction mixture.

2.2.4. Synthesis of Fe_3O_4 and ZnO nanoparticles

100 μL of purified peroxidase enzyme from Euphorbia (*Euphorbia amygdaloides*) plant were added in sample $FeCl_2$ of solution (2.9 mL, 10 mM) and incubated in a closed space for 4 h.

The solution was becoming dark red, which indicates the presence of Fe_3O_4 nanoparticles. The same procedures were repeated using 2.9 mL of 10 mM $ZnCl_2$ solution to obtain ZnO nanoparticles. The solution became a white turbid state indicating the presence of ZnO nanoparticles. Then, water was removed by the help of an evaporator, and synthesized iron and zinc oxide nanoparticles were dried at 70°C for 24 h.

2.2.5. *Characterization of Fe_3O_4 and ZnO nanoparticles*

Synthesized Fe_3O_4 and ZnO NPs were characterized by scanning at range of 200–1000 nm by using UV-Vis spectrophotometer (Epoch nanodrop spectrophotometer). Determination of topography for Fe_3O_4 and ZnO nanoparticles was performed by SEM (Scanning Electron Microscope). In addition, XRD analysis (X-ray diffraction analysis) and FT-IR (Fourier transform infrared spectroscopy) were performed for Fe_3O_4 and ZnO NPs.

Contact time, pH, temperature, and metal ion concentration were determined for the purpose of optimization synthesized Fe_3O_4 and ZnO NPs. For determination of the optimum contact time, samples were spectrophotometrically measured between 0 and 240 min with 3 min intervals. Synthesis of Fe_3O_4 and ZnO NPs was performed in sodium phosphate buffer at pH 2.0–3.0, sodium acetate buffer at pH 4.0–6.0, sodium phosphate buffer at pH 7.0–8.0 and sodium carbonate buffer at pH 9.0–11.0 and the values of absorbance were measured. pH was adjusted by using 0.1 N HCl and 0.1 N NaOH. Synthesis of NPs was separately carried out from 10° to 90°C, respectively, and changes in absorbants of the samples were measured. Synthesis of NPs was performed by using related solution at 0.5, 1, 3, 5, and 7 mM and the absorbance of samples was measured. All measurements were performed by UV–VIS spectrophotometer and deionized water was used for blank sample.

2.3. Preparation of LS material, immobilization of nanoparticles procedure

Dried LS material was made into small pieces and was autoclaved for 20 min to soften the fibrous structure. Then, it was transformed into dough using blender. It was incubated for 4 h with 1 N NaOH at 80°C. Then, the fibers were collected and were thoroughly washed with distilled water until NaOH is resolved. About 0.1% hypochlorite was used for decoloration of washed fibers and then, they were washed with distilled water. Fibers with the length of 10–50 μm were collected and were dispersed with distilled water to form a suspension form. The suspension was filtered under aseptic conditions using filter paper and obtained LS fibers were dried on filter paper at 40°C for 4 h [24]. Immobilization was performed by treatment solutions containing Fe_3O_4 and ZnO NPs with LS which was pretreated in ultrasonic bath for 1 h. Then, the obtained membrane forms (LS-pure, LS-ZnO, LS-Fe_3O_4, LS-ZnO/Fe_3O_4) was dried in oven for 2 h.

2.4. Azo dye remediation

The prepared membranes were used for decolorization of DB15 solution which was prepared in the laboratory. Synthetic wastewater was prepared by dissolving DB15 dye. A calibration curve was prepared in the range 0–40 ng/cm^3 of DB15. The reaction mixture was prepared by adding membrane forms and in flasks containing 50 mL volume DB15 dye solution. The samples were taken out from the flasks periodically with a micropipette and were centrifuged at 5000 rpm for 10 min. The supernatant solutions were filtered with 0.45 mm filters. Then, the concentration of DB15 was measured with a UV–VIS spectrophotometer at $\lambda = 596$ nm. Scanning electron microscopy (SEM) was used to examine the surface of the adsorbents before and after dye adsorption (JEOL JSM-6400 SEM) and FTIR, XRD were performed for dye adsorption. Optimum contact time, pH, temperature, concentration of dye to determine optimal conditions for the decolorization of DB15 azo dye were analyzed using UV-Visible spectrophotometer.

The amounts of the dyes adsorbed onto LS-pure, LS-ZnO, LS-Fe_3O_4, and LS-ZnO/Fe_3O_4 (q_e in mg/g) were calculated from the equation:

$$q_e = \frac{(C_o - C_e) \times V}{m} \tag{1}$$

where C_o and C_e are the initial and equilibrium concentrations of dye in solution (mg/L); V is the volume of solution (L) and m is the mass of adsorbent (g).

2.5. Adsorption isotherms

Plots of $\ln(C/C_0)$ and time were drawn to estimate rate constants (k values) for decolorization as a function of dye concentration, where C_0 and C represent remaining color intensity at the start of the experiment (zero time) and at any time t, respectively, for various fixed concentrations of dye.

3. Results and discussion

3.1. Partial obtaining peroxidase enzyme from *Euphorbia amygdaloides* plant

The data obtained in the purification process of peroxidase enzyme are given in **Table 1**.

There are many studies on the purification of peroxidase enzyme in the literature. Plants such as wheat seeds, barley and wheat, soybeans, fava beans, sorghum, watermelon seeds, red beets, cotton, pearl millet seedlings, Asian rice, lettuce, wild radish, and pearl barley hybrids were used for the purification of peroxidase enzyme [25–29].

Peroxidase enzyme was purified by ammonium sulfate precipitation from *Euphorbia amygdaloides* plant with CM-cellulose ion exchange chromatography and Sephacryl S-100 gel filtration chromatography. According to the data obtained in 75% ammonium sulfate precipitation step, the enzyme was purified with purification coefficient of 6.4 and 51.6 for 10 mL volume [23]. In our study, the enzyme was purified with a purification coefficient of 149.5 and a yield of 29.5 for 20 mL volume, according to the order of 60–80% ammonium sulfate precipitation step.

Enzyme fraction	Volume (mL)	Activity (EU/mL)	Total activity (EU) 10^3/%	Protein (mg protein) (mL)	Specific activity (EU/mg)	Purification coefficient (EU/mg)
Crude extract	50	236.4 ± 1.0	11.82/100	3.82×10^2± 0.7	0.62	—
$(NH_4)_2SO_4$ (60–80%)	20	174.3 ± 1.02	3.49/29.5	1.88 ± 0.16	92.71	149.54

Table 1. Purification process of peroxidase enzyme from *Euphorbia amygdaloides* plant.

3.2. Characterization of Fe_3O_4 and ZnO NPs

The results of the optimization studies for the green synthesis of nanoparticles are given in **Table 2**.

No research has been found in the literature on the green synthesis of Fe_3O_4 and ZnO NPs from the *Euphorbia amygdaloides* plant. *Euphorbia milii* was used for the synthesis of ZnO nanoparticles [30]. A study on the green synthesis of the Fe_3O_4 nanoparticle using the *Euphorbia amygdaloides* plant is not available in the literature. However, studies on the green synthesis of Pd/Fe_3O_4 nanoparticles using *Euphorbia condylocarpa M. bieb* root extract and *Euphorbia stracheyi Boiss* root extract have been carried out [31]. Our study provides a contribution to the literature. The highest peak in the optical absorption spectrum of the ZnO nanoparticles synthesized by pulsed laser ablation was at 300 nm [32]. In our study, the highest peak value of ZnO nanoparticles was read at 304 nm (**Table 2**). The sharpness of ZnO absorption indicates the uniform nanoparticle distribution [33, 34]. Fe_3O_4 nanoparticles exhibit an absorption band in the range of 330–450 nm of the UV–Vis spectrum in the literature and Fe_3O_4 nanoparticles peak observed at 330 nm in a work [35]. The highest peak value of the Fe_3O_4 nanoparticles used in our study was read as 481 nm. This range is above the range available in the literature. Nagarajan and Kuppusamy [36] studied the optical properties of ZnO nanoparticles obtained from marine algae of Mannar Bay in India. They did not observe any peak between pH 5.0–7.0 and pH 9.0–10.0 in their pH optimization studies. The maximum yield was obtained at pH 8.0. In our study, pH 6.0 was determined as the optimum pH for ZnO nanoparticle synthesis. Optimum pH for Fe_3O_4 nanoparticles is found at 8.0. Manouchehr et al. [37] reported that they performed the synthesis of Fe_3O_4 nanoparticles in the pH 7.0–9.0 environment. These values are close to the values we have obtained in our study. While the highest absorbance values were obtained at a concentration of 5 mM $ZnCl_2$ in the synthesis of ZnO nanoparticles, the highest absorbance values were obtained at a concentration of 1 mM $FeCl_2$-Fe_2Cl_3 in the synthesis of Fe_3O_4 nanoparticles.

Nanoparticle	Wavelength (nm)	Contact time (h)	pH	Temperature (°C)	Metal ion concentration (mM)
ZnO	304	4	6.0	60	5
Fe_3O_4	481	4	8.0	30	1

Table 2. The results of the optimization studies for the green synthesis of nanoparticles.

SEM (scanning electron microscope) basically works on the basis of obtaining the images of the surface morphology which are scanned with the help of electrons. The electrons sourced from tungsten tip are sent to the surface to be scanned. After that, the emitted electrons are captured by the detector and the image is formed. SEM analysis images of ZnO and Fe_3O_4 nanoparticles in this study taken in this way are shown in **Figure 2**. The SEM image recorded for the Fe_3O_4 nanoparticle structure resembled a dust particle, suggesting that it may be a soft structure. It has been determined that these nanoparticle structures obtained by the surface characterization process have an average size of 30–80 nm. The SEM image for ZnO nanoparticle was taken at 5 μm. In this image, the nanoparticle structure exhibits a wavier surface. Generally, the liquid containing peroxidase enzyme prevents the formation of ZnO nanoparticle formations composed of dust and flake-like structures. However, it appears that the powder and flake structures combine in some regions and exhibit a wavy appearance after this enzyme liquid is evaporated. After the surface characterization analysis of ZnO nanoparticles, it was found that these structures vary between 60 and 80 nm on average.

The Fourier Transform Infrared Spectrophotometer (FTIR) is used to determine the bond formation between the elements present in the structure to be measured. In this direction, the structural formation that the sample possesses can be understood by measuring the vibrations of the bond occurrences in the structure at certain frequencies. This helps in the determination of the functional groups in the material being measured. The FT-IR spectrums of ZnO and Fe_3O_4 nanoparticles are given in **Figure 3**.

When looking at **Figure 3A**, it is possible to observe the absorbance at 510–564 cm^{-1}, which is indicative of Zn-O band formation in this analysis which was carried out to detect the biomolecule by revealing the stabilization ability and bandwidth of the metal nanoparticles synthesized by green synthesis [38]. Geetha et al. [30] synthesized ZnO nanoparticles by green synthesis using the *Euphorbia spindle* plant. They applied FT-IR analysis in their characterization studies

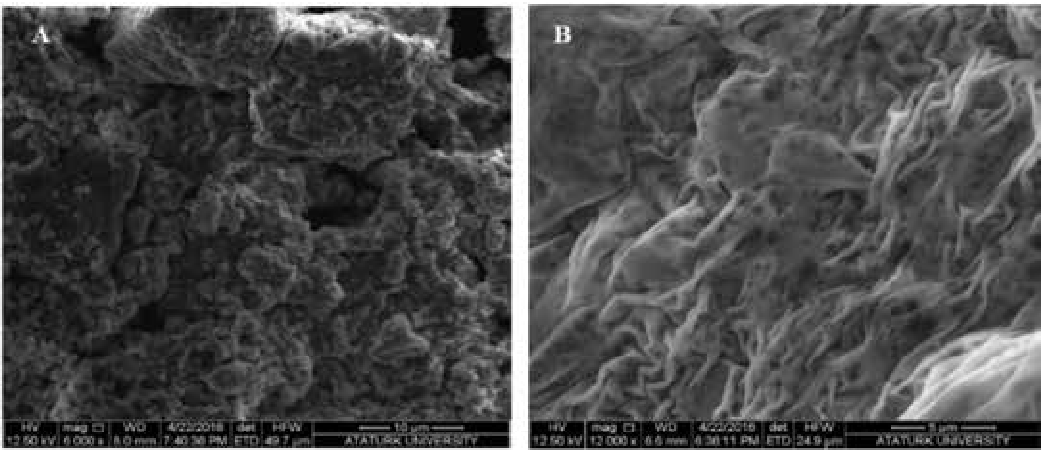

Figure 2. SEM analysis images of ZnO and Fe_3O_4 nanoparticles.

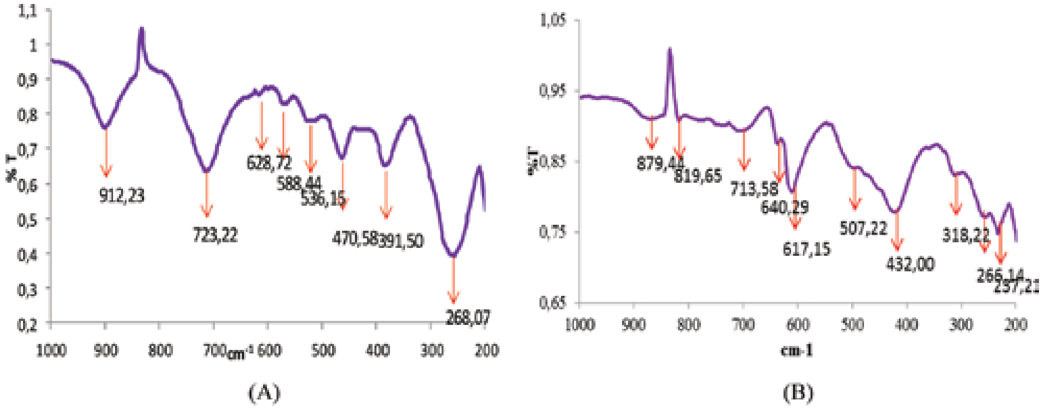

Figure 3. FTIR spectrum of (A) ZnO and (B) Fe_3O_4 nanoparticle.

in the range of 400–4500 cm^{-1}. The researchers noted that the observed transmittance band at 435 cm^{-1} corresponds to ZnO bonding, confirming the formation of ZnO particles.

In the FT-IR spectrum of the Fe_3O_4 nanoparticle structure shown in **Figure 3B**, there are oscillations of bond structures that oxygen forms with iron. It is known that this nanoparticle structure oscillates between 200 and 650 cm^{-1}. In this direction, as shown in the graph, the Fe_3O_4 nanoparticle structure obtained by green synthesis exhibited oscillations indicating specific bonds between iron and oxygen elements between 256 cm and 636 cm^{-1}.

XRD (X-ray diffraction) method was used for the analysis of crystallized structures of nanoparticles used in the study. In this method, since the diffraction pattern to be produced by each structure will be different, the planar structure of the elements arranged symmetrically or periodically can be determined. The graphs obtained by XRD analysis of ZnO and Fe_3O_4 nanoparticles are given in **Figure 4**.

Plots of 100, 002, 101, 102, 110, 103, 200, 112, 201, 004, and 202 were determined in the XRD analysis graph to show the crystallized structure of the ZnO nanoparticle. ZnO nanoparticle

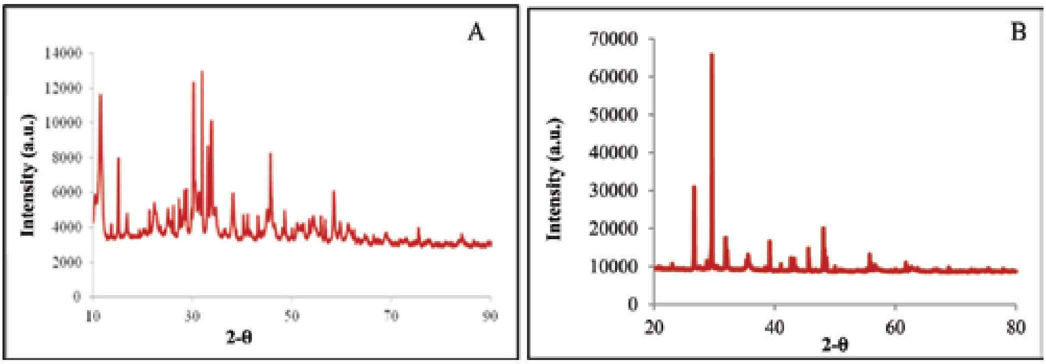

Figure 4. XRD spectrum for (A) ZnO and (B) Fe_3O_4 nanoparticle.

structures are located at 2θ angles of 31.77, 34.40, 36.22, 47.61, 56.58, 62.85, 66.41, 67.93, 69.08, 72.54, and 76.85° corresponding to the plane distances of the atoms present in the structure of the nanoparticle. In this case, the XRD chart confirms that the nanoparticle we are analyzing is a ZnO nanoparticle.

Nearly all of the characterization studies for ZnO nanoparticles synthesized by different methods in the literature are discussed according to XRD analysis results. In the analyses, the planes are generally observed at the highest peak 101 with the planes of 100, 002, 101, 102, 110, 103, 112 [30, 39]. In parallel with these studies in the XRD spectrum we obtained in our study, the 101 plane has the highest peak.

The peaks obtained in the XRD spectrum of the Fe_3O_4 nanoparticles reveal that the desired nanoparticle structure is obtained in the green synthesis process carried out. 2θ values specific to this nanoparticle were determined as 30, 33, 44, 53, 56, and 62°.The distances between the planes determined in this direction are 220, 311, 400, 422, 511, and 440 respectively. In the light of this information, it is determined that the Fe_3O_4 nanoparticle structure is in a spherical crystal structure.

3.3. Immobilization efficiency

The data obtained for the immobilization of nanoparticles on the LS are given in **Table 3**.

3.4. Adsorption studies

Analytical methods used for quantitative analysis require calibration. Calibration is a process for accurately determining the relationship between the signal measured at the output of any device and the concentration of the material causing the signal. The curve obtained is a straight line. Since the calibration curve R^2 value is 0.9941, the slope is assumed to be 0.0094.

As seen in **Figure 5**, the DB15 azo dye had value of about qe = 80 mg/L with all membrane forms in the first 15 min. Measurements at 30, 45, and 60 min resulted in 80–100 mg/L qe. However, since the highest values were noted at 45 min, optimum contact time for this azo dye was accepted as 45 min. ZnO and Fe_3O_4 NPs have been used to study the remodeling of many azo dyes [40, 41]. The LS-ZnO membrane form provided slightly lower adsorption compared to the LS-Fe_3O_4 NPs membrane form. The highest adsorption was obtained with LS-ZnO/Fe_3O_4 NPs membrane form.

Nanoparticle solution	Wavelength (nm)	Absorbance before immobilization	Absorbance after immobilization	% immobilization
ZnO	304	0.147	0.012	91.83
Fe_3O_4	481	0.188	0.015	92.02
ZnO/Fe_3O_4	209	0.202	0.014	93.07

Table 3. Data of immobilization efficiency.

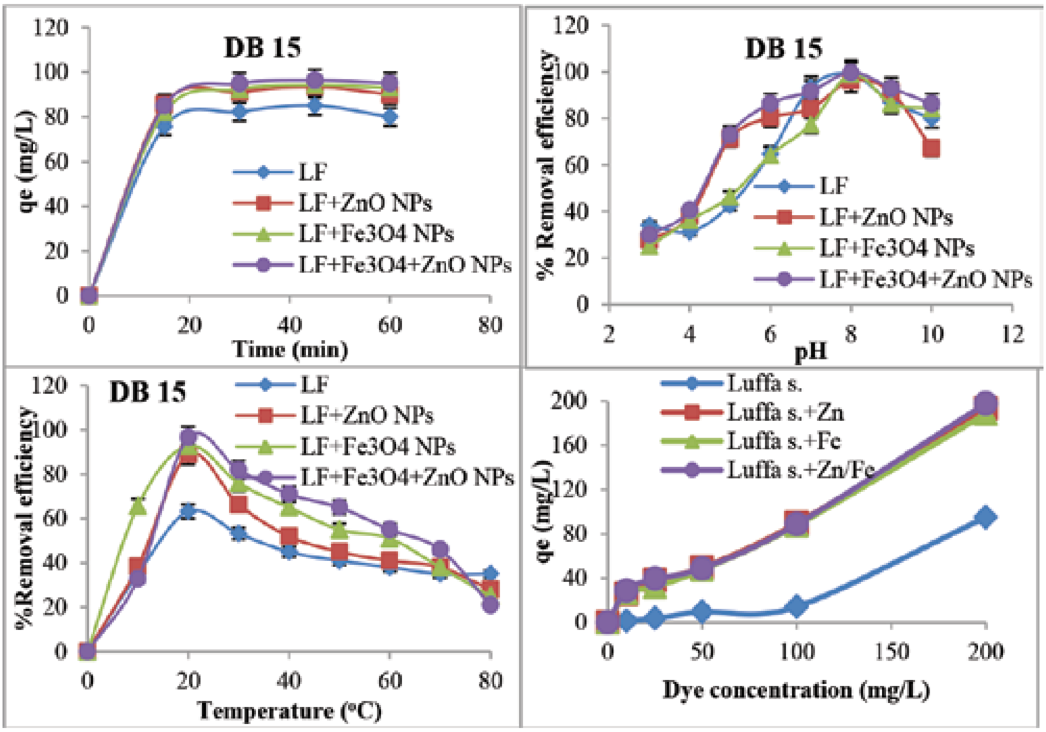

Figure 5. The effects of contact time, pH, temperature and dye concentration on the adsorption of the DB15 azo dye solution with the formed membrane forms.

Maximum adsorption peaks were observed at pH 8.0 in the spectrophotometric measurements performed on pH optimizations for the adsorption of DB15 azo dye solution at 50 mg/L concentration with the formed membrane forms. According to adsorption data obtained with LS-ZnO NPs and LS-Fe_3O_4 NPs membrane forms in pH 7.0 medium, pure LS membrane form provides a more effective adsorption in this pH environment. However, at pH 7.0, the same adsorption data were observed for LS-ZnO/Fe_3O_4 NPs and pure LS membrane forms (**Figure 5**).

In some studies performed onto Fenton process, a high decolorization rate was achieved for DB15 azo dye in highly acidic media such as pH 3.0 and 4.0 [42, 43]. Providing maximum yield in alkaline environment such as pH 8.0 near neutral with the formed membrane forms is advantageous in terms of operating.

The adsorption of the DB15 azo dye solution with membrane form exhibited the highest adsorption peaks at 20°C. However, when the temperature was gradually increased above 20°C, the adsorption with membrane forms showed an inverse proportion and gradually decreased. This result is quite advantageous in terms of the industrial application because the approximate temperature of 20°C is accepted as the optimum value.

In the work for the degradation of DB15 azo dye using copper hydroxide nitrate as a catalyst by wet peroxide oxidation, it has been reported that degradation activity of 85 and 90% of this dye is obtained after 10 and 60 min at 60°C [44]. In another study, remediation of DB15 azo dye was studied with Fenton reaction, and in this study, the degradation efficiency of the system was increased in parallel with the temperature increasing from 20 to 40°C [42]. The temperatures in these studies are very high and cause extra energy consumption and therefore financial loss. In this respect, the membrane forms proposed in our work offer advantages at 20°C with effective performance.

When **Figure 6** is examined, the adsorption of concentration of 200 mg/L DB15 azo dye solution prepared with the membrane forms had the highest value. The adsorption of the DB15 azo dye solution prepared at the concentration of 200 mg/L with LS-ZnO NPs, LS-Fe_3O_4 NPs, and LS-ZnO/Fe_3O_4 NPs membrane forms showed the highest values were measured according to the adsorption of azo dye solutions prepared at other concentrations (10, 25, 50, and 100 mg/L). The use of nanoparticles has affected adsorption quite positively. Pure LS membrane form showed very low efficiency in dye adsorption compared to nanoparticle loaded membrane forms.

Adsorption values were read close to each other in the adsorption study of the DB15 azo dye solution with membrane forms formed with LS quantities of 0.025, 0.05, 0.1, 0.3, and 0.5 g. In the adsorption study of azo dye solution with nanoparticle-loaded membrane forms formed with all LS quantities used in the experiment, higher adsorption values were obtained compared to the pure LS membrane form used in the same amount. The highest percentage of recovery was obtained with 0.025 g LS (**Figure 6**). Kesraoui et al. [45] conducted biosorption of the Alpasit Blue with LS. In this study, maximum efficiency was obtained with 1 g LS fibrils after 2 h in pH 2.0 medium with 20mg/L concentration dye. In our study, the highest yield was achieved with an adsorbent amount of 0.025 g. In addition, nanoparticle loading has made this more efficient.

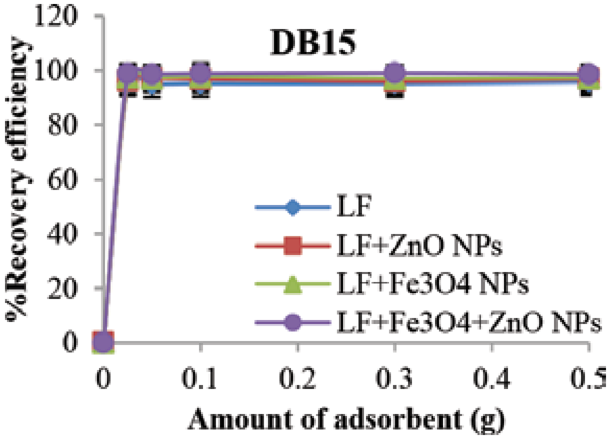

Figure 6. Effect of amount of adsorbent on adsorption with membrane forms formed by DB15 azo dye.

3.5. Characterization studies of dye absorption with prepared nanoparticle loaded membrane forms

SEM images for the adsorption of DB15 azo dye with the membrane forms obtained in the study are given in **Figure 7**. SEM images were taken at a size of 10 μm at 8000× magnification. It is seen that the DB15 azo dye has drained the membrane forms like a cover.

As shown in **Figure 8**, membrane forms formed with LS material exhibit significant peaks, especially at permeability of 1000 cm^{-1}. At the same time, certain peaks were observed at about 500 and around 3350 cm^{-1}. In fact, FT-IR bands specific to the cellulose structure of LS seen here. C—H bands and —OH groups are found at around 3350 and 2800–2900 cm^{-1} [46, 47]. In the adsorption of DB15 azo dye with LS membrane forms, FT-IR bands were observed especially for Fe_3O_4 nanoparticle-loaded membrane forms. ZnO NPs loaded membrane had higher permeability to dye adsorption than other membrane types.

The XRD spectrum of the LS membrane form showed peaks at 2θ = 15, 20, and 38 areas. The peak intensity is above 30,000 in the area 2θ = 20. However, in the XRD spectrum of DB15 azo dye adsorption with this membrane form, the 2θ = 20 area shifted to 2θ = 22 and the peak intensity approached 60.000 in this area. In addition, additional peak was observed at 2θ = 35, 38, 43, and 50 areas. Nanoparticle-loaded membrane forms exhibited significant changes in XRD spectra when DB15 azo dye adsorbed with these membrane forms. These membrane forms exhibited very low XRD peaks compared to the pure LS membrane form, but they exhibited very high XRD peaks especially in the 2θ = 15 and 20 areas after dye adsorption. A distinctive feature of ZnO and Fe_3O_4 NPs in the adsorption of this azo dye was not observed in the XRD spectrum. The values were very close to each other (**Figure 8**) [47–49].

3.6. Langmuir and Freundlich adsorption isotherm studies

The following Langmuir isotherm equation is used to plot Langmuir adsorption isotherm graphs for the adsorption of DB15 azo dye with the membrane forms in this study. The correlation between $\frac{Ce}{qe}$ and C_e calculated from experimental results is given in **Figure 9**.

$$\frac{Ce}{q_e} = \frac{1}{k\,V_m} + \frac{C_e}{V_m} \tag{2}$$

Using the following Freundlich adsorption isotherm equation, Freundlich adsorption isotherm graph for the adsorption of DB15 azo dyes of the working membrane forms was drawn. This graph showing the relation between log q_e and log C_e was given in **Figure 9**.

$$log q_e = \log K_F + \frac{1}{n} log C_e \tag{3}$$

The Langmuir adsorption isotherm is generally used to describe the maximum adsorption capacity of an adsorbent. qm and b values were calculated from the above equation. b is a constant related to adsorption net enthalpy (L/mg), and qm is the amount of adsorbed material (mg/g) in the unit weight of the adsorbent to form a single layer at the surface. In the Langmuir isotherm study, the highest q_m value was obtained LS-ZnO/Fe_3O_4 membrane form

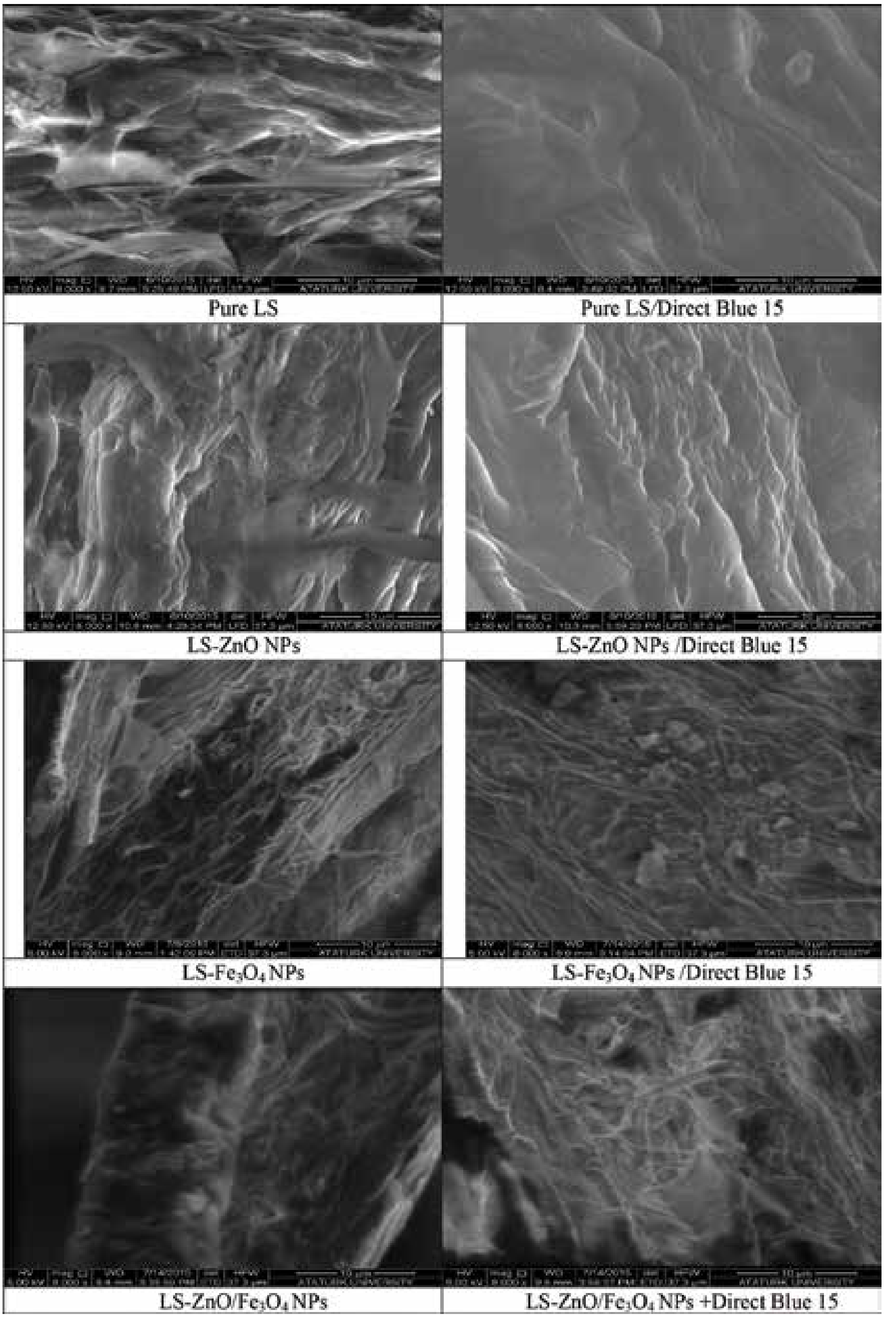

Figure 7. SEM images of adsorption of DB15 azo dye with membrane forms.

with 274.6 mg/g and the lowest q_m value was obtained with pure LS membrane form with 45.0 mg/g. The highest b value was achieved with the pure LS membrane form with 1.186 L/mg and the LS-ZnO/Fe_3O_4 NPs membrane form with a minimum b value of 0.06 L/mg. High

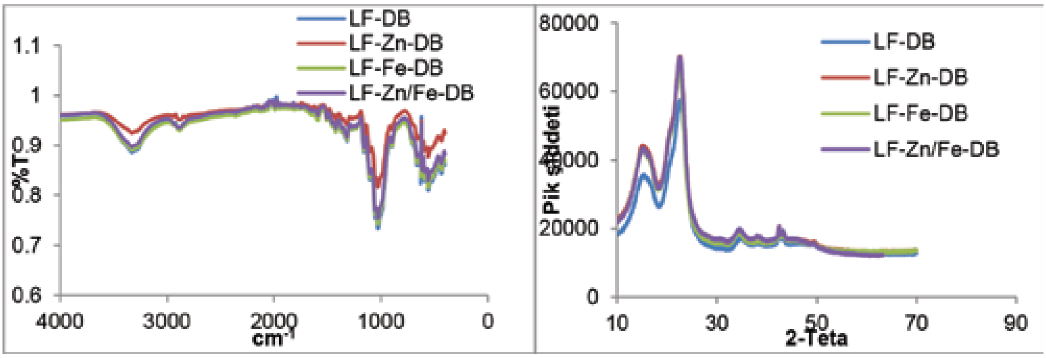

Figure 8. FT-IR and XRD spectrums of adsorption of DB15 azo dye with membrane forms.

correlation coefficient R^2 (0.9605) was provided with Langmuir model, the linear form application for LS-Fe_3O_4. This indicates that the sorption system of Langmuir isotherm provides a good model for this membrane form (**Table 4**).

Freundlich isotherm model is an empirical relationship that defines the adsorption of solubles from a liquid to a solid surface and assumes that there are different areas with several adsorption energies. Freundlich constants are related to the sorption capacity of the adsorbent (mg/g) and adsorption energy. In the Freundlich model, K_F and n are constants that show the adsorption capacity and intensity, respectively. High K_F and n values indicate high adsorption capacity and magnitude of n value is an indication of the suitability of adsorption. The LS-ZnO NPs membrane form with 2.65 values of n had a good adsorption capacity relative to the Freundlich isotherm. The pure LS membrane form is quite advantageous according to R^2 (0.9885) (**Table 4**).

3.7. Reaction kinetics of first and second order

The adsorption kinetics of DB15 azo dye with LS, LS-ZnO NPs, LS-Fe_3O_4 NPs, LS-ZnO/Fe_3O_4 NPs membrane forms and were investigated against 10, 25, 50, 100, and 200 mg/L concentrations of dye solutions. To determine the adsorption constants, first order conformity to reaction

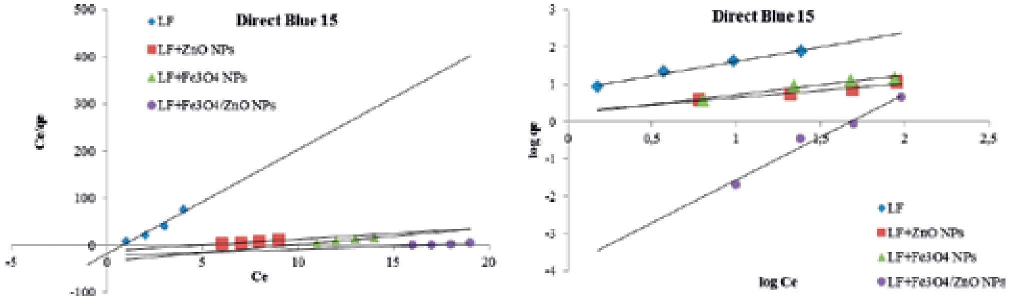

Figure 9. Langmuir and Freundlich adsorption isotherm for DB15 azo dye adsorption with membrane forms.

	DB15			
	LS	**LS-ZnO**	**LS-Fe_3O_4**	**LS-ZnO/Fe_3O_4**
Langmuir constants				
q_m (mg/g)	45.0	48.6	128.1	274.6
b(L/mg)	1.186	0.216	0.103	0.06
R^2	0.9503	0.9371	0.9605	0.7641
Freundlich constants				
K_F (mg/g) $(L/mg)^{1/n}$	6.85	1.84	1.53	1.36×10^{-4}
n	1.29	2.65	1.899	0.44
R^2	0.9885	0.9378	0.9637	0.9716

Table 4. Langmuir and Freundlich isotherm parameters.

kinetics was investigated. For this purpose, the time-dependence of $\ln(q_e - q_t)$ was plotted and R^2 values were calculated for 10, 25, and 50 mg/L concentrations of dye (**Table 5**).

The k_1 constant is calculated using the first order reaction equation given below:

$$\ln(q_e - q_t) = \ln q_e - k_1 t \tag{4}$$

Then, its suitability of second-order reaction kinetics was investigated to calculate the adsorption constants of DB15 azo dye. (t/qt) depicting the time dependence graphs were plotted and R^2 values for 10, 25, and 50 mg/L concentrations of DB15 azo dyes were calculated (**Table 5**).

The second-order reaction equation is used to calculate the k_2 constant and all calculated values ($qe_{experimental}$, $qe_{calculated}$, k_1, k_2, R^2) for adsorption of azo dye DB15 are shown in **Table 5**.

When **Table 5** is examined, there is high difference between values of $qe_{experimental}$ and $qe_{calculated}$ in the reaction kinetics of the first- and second-order in dye adsorption with pure LS membrane form. Furthermore, when the R^2 values are examined, it is clear that the second order is inadequate. There is lower difference than the other concentration between values of $qe_{experimental}$ and $qe_{calculated}$ in reaction kinetics of the second order in adsorption of azo dye at a concentration of 10 mg/L with the LS-ZnO NPs membrane form. However, when we take into account the R^2 values, there is a compatibility with the first-order reaction kinetics. We see that the adsorption of azo dye at 25 mg/L concentration with Fe_3O_4 NPs-loaded membrane forms is more appropriate for the second-order reaction kinetics in terms of R^2 values.

3.8. Calculation of thermodynamic parameters

Plots of LnK_L against 1/T obtained in adsorption experiments with membrane forms of DB15 azo dye are given in **Figure 10**.

Values for ΔG° Gibbs free energy, ΔH° enthalpy change and ΔS° entropy thermodynamic parameters for membrane forms used in the adsorption of DB15 azo dyes are given in **Table 6**.

DB15

Adsorbent	**Initial dye conc.**	**qe_{exp} (mg/g)**	**First order**			**Second order**		
			k_1 (L/min)	**qe_{cal} (mg/g)**	**R^2**	**k_2 (g/mg min)**	**qe_{cal} (mg/g)**	**R^2**
LS	10	8.8	0.034	0.845	0.9954	5.77×10^{-4}	16.53	0.9751
	25	12.6	0.030	0.978	0.9977	2.27×10^{-3}	20.70	0.9955
	50	33.6	0.0.28	1.296	0.9873	6.8×10^{-5}	96.15	0.6882
LS-ZnO NPs	10	9.1	0.053	0.809	0.9974	2.63×10^{-3}	12.03	0.9702
	25	17.1	0.038	1.071	0.9986	1.03×10^{-3}	26.46	0.9923
	50	49.65	0.049	1.395	0.9744	8.78×10^{-5}	95.24	0.9547
LS-Fe_3O_4 NPs	10	8.6	0.055	0.949	0.925	2.03×10^{-3}	13.14	0.9912
	25	22.7	0.049	1.113	0.9983	1.45×10^{-3}	27.25	0.991
	50	44.3	0.054	1.414	0.9603	1.48×10^{-4}	76.33	0.9654
LS-ZnO/Fe_3O_4 NPs	10	8.9	0.047	0.839	0.9821	2.83×10^{-3}	12.76	0.9971
	25	24.0	0.039	1.075	0.9494	1.23×10^{-3}	29.94	0.9537
	50	48.6	0.054	1.400	0.9715	2.54×10^{-4}	67.57	0.9876

Table 5. First- and second-order adsorption rate constants in DB15 azo dye removal.

ΔG° values decreased as the temperature increases in adsorption of DB15 azo dye with all membrane forms. This shows an increasing tendency in the feasibility and spontaneity of DB15 azo dye adsorption. The fact that ΔG° has negative values means that the adsorption of DB15 azo dye is spontaneously. The negative values of ΔH° confirm the exothermic structure of the adsorption process. Therefore, the adsorption of DB15 azo dye with membranes formed by the use of

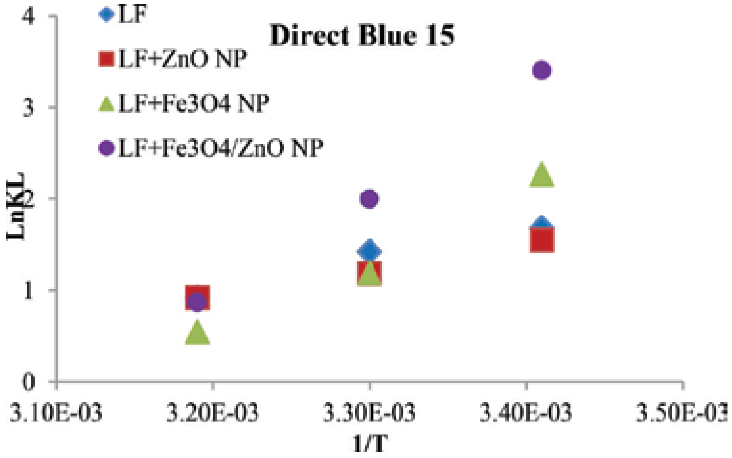

Figure 10. Thermodynamic kinetics graph for adsorption of DB15 azo dye with formed membrane forms.

DB15			
	ΔG° (kJ/mol K)	**ΔH° (kJ/mol)**	**ΔS° (kJ/mol)**
LS 20°C	−24235.32	−417.7	−84.14
LS 25°C	−24656.02		
LS 30°C	−25076.72		
LS-ZnO NPs 20°C	−19855.73	−346.62	−68.95
LS-ZnO NPs 25°C	−20200.48		
LS-ZnO NPs 30°C	−20545.23		
LS-Fe_3O_4 NPs 20°C	−58727.95	−941.5	203.65
LS-Fe_3O_4 NPs 25°C	−59746.20		
LS-Fe_3O_4 NPs 30°C	−60764.45		
LS-ZnO/Fe_3O_4 NPs 20°C	−86188.31	−1386.46	298.89
LS-ZnO/Fe_3O_4 NPs 25°C	−87682.76		
LS-ZnO/Fe_3O_4 NPs 30°C	−89177.21		

Table 6. Calculated thermodynamic constants.

LS and nanoparticle is a natural chemical. Positive values of ΔS° indicate increasing disorder and randomness at the solid solution interface of the adsorbent and DB15 azo dye [49]. This was observed in membrane forms immobilized with Fe_3O_4 NPs (**Table 6**).

4. Conclusion

In this study on remediation, the possibilities offered by the environment are evaluated. ZnO and Fe_3O_4 NPs were produced by green synthesis with catalyzed peroxidase enzyme partially purified from *Euphorbia amygdaloides* plant. In this phase of the study, a new plant source was presented to literature for the green synthesis of nanoparticles. It has also been shown that produced nanoparticles may play an active role in dye adsorption. The synthesis of this plant with other nanoparticles will be further studied.

LS is a natural plant that can grow in many countries, can be used for many purposes, and has recently undergone a lot of research. In this study, nanoparticles were immobilized successfully on this material. In this way, it is aimed to prevent the nanoparticles accumulation in the environment and the creation of a separate pollution. Adsorption of DB15, a carcinogenic azo dye, was studied with nanoparticle-loaded membrane forms. Optimization, characterization, kinetic, thermodynamic studies demonstrated effectiveness of the membrane forms used in dye adsorption. For this reason, we can easily say that this work will be a source for commercialized membrane systems in the future.

Acknowledgements

This research was performed under the project numbered 115Z810 and supported by the Scientific and Technical Research Council of Turkey (TUBITAK). The authors acknowledge the support of TUBITAK, Turkey for this work.

Author details

Hayrunnisa Nadaroglu[1,2]*, Semra Cicek[3], Hicran Onem[2] and Azize Alayli Gungor[4]

*Address all correspondence to: hnisa25@atauni.edu.tr

1 Department of Food Technology, Erzurum Vocational Training School, Ataturk University, Erzurum, Turkey

2 Department of Nano-Science and Nano-Engineering, Faculty of Engineering, Ataturk University, Erzurum, Turkey

3 Department of Agricultural Biotechnology, Faculty of Agriculture, Ataturk University, Erzurum, Turkey

4 Department of Chemical Technology, Erzurum Vocational Training School, Ataturk University, Erzurum, Turkey

References

[1] Majcen-Le Marechal A, Slokar YM, Taufer T. Decoloration of chlorotriazine reactive azo dyes with H_2O_2/UV. Dyes and Pigments. 1997;**33**:281-298

[2] Shaul GM, Lieberman RJ, Dempsey CR, Dostal KA. Treatability of water soluble azo dyes by the activated sludge process. Proceedings of the Industrial Wastes Symposia WPCF. 1986:1-18

[3] Gomes JR. Estrutura e Propriedades dos Corantes. Braga, Portugal: Barbosa e Xavier Lda; 2001

[4] Pereira L, Alves M. Dyes—Environmental impact and remediation. In: Malik A, Grohmann E, editors. Environmental Protection Strategies for Sustainable Development, Strategies for Sustainability. Netherlands: Springer; 2012. pp. 111-154

[5] Balan DSL. Biodegradação e toxicidade de efluentes têxteis. Revista Brasileira de Técnicos Têxteis - ABTT. 2009;**1**(1):16-18

[6] Gupta VK, Khamparia S, Tyagi I, Jaspal D, Malviya A. Decolorization of mixture of dyes: A critical review. Global Journal of Environmental Science and Management. 2015;**1**:71-94

[7] Campos-Takaki GM, Vilar Junior JC, Cavalcanti DL, Alves da Silva CA, Andrade RFS. Decolorization of black B azo dye by *Pseudomonas aeruginosa*. International Journal of Current Microbiology and Applied Sciences. 2015;**4**(7):720-728

[8] Gunasekaran P, Puvaneswari N, Muthukrishnan J. Toxicity assessment and microbial degradation of azo dyes. Indian Journal of Experimental Biology. 2006;**44**:618-626

[9] Clarke EA, Anliker R. Organic dyes and pigment. In: Hutzinger O, editor. The Handbook of Environmental Chemistry. 3. A. Anthropogenic Compounds. United States: Springer-Verlag; 1980. pp. 1-215

[10] Ventura-Camargo BC, Marin-Morales MA. Azo dyes: Characterization and toxicity—A review. Textiles and Light Industrial Science and Technology (TLIST). 2013;**2**(2):85-103

[11] Robinson T, Mcmullan G, Marchant R, Nigam P. Remediation of dyes in textile effluent: A critical review on current treatment technologies with a proposed alternative. Bioresource Technology. 2001;**77**:247-255

[12] Jadhav JP, Parshetti GK, Kalme SD, Govindwar SP. Decolourization of azo dye methyl red by *Saccharomyces cervisiae* MTCC 463. Chemosphere. 2007;**68**:394-400

[13] Karn B, Kuiken T, Otto M. Nanotechnology and in situ remediation: A review of the benefits and potential risks. Environmental Health Perspectives. 2009;**117**:1823-1831

[14] Nam S, Tratnyek PG. Reduction of azo dyes with zero-valent iron. Water Research. 2000;**34**:1837-1845

[15] Gupta N, Singh HP, Sharma RK. Metal nanoparticles with high catalytic activity in degradation of methyl orange: An electron relay effect. Journal of Molecular Catalysis A: Chemical. 2011;**335**:248-252

[16] Wang JQ, Liu YH, Chen MW, Louzguine-Luzgin DV, Inoue A, Perepezko JH. Excellent capability in degrading azo dyes by MgZn-based metallicglass powders. Scientific Reports. 2012;**2**:418-423

[17] Vidhu VK, Philip D. Catalytic degradation of organic dyes using biosynthesized silver nanoparticles. Micron. 2014;**56**:54-62

[18] Philip D, MeenaKumari M. Degradation of environment pollutant dyes using phytosynthesized metal nanocatalysts. Spectrochimica Acta Part A: Molecular and Biomolecular Spectroscopy. 2015;**135**:632-638

[19] Rahman N, Abedin Z, Hossain MA. Rapid degradation of azo dyes using nano-scale zero valent iron. American Journal of Environmental Sciences. 2014;**10**(2):157-163

[20] Adams LK, Lyon DY, Alvarez PJJ. Comparative ecotoxicity of nanoscale TiO_2, SiO_2 and ZnO water suspensions. Water Research. 2006;**40**:3527-3532

[21] Lovern SB, Strickler JR, Klaper R. Behavioral and physiological changes in *Daphnia magna* when exposed to nanoparticle suspensions (titanium dioxide, nano-C_{60} and $C_{60}H_xC_{70}H_x$). Environmental Science & Technology. 2007;**41**(12):4465-4470

[22] Saeed A, Iqbal M. Loofa (Luffa cylindrica) sponge: Review of development of the biomatrix as a tool for biotechnological applications. Biotechnology Progress. 2013;**29**:573-600

[23] Güngör AA, Demir N, Demir Y. Purification of peroxidase from latex of euphorbia (*Euphorbia amygdaloides*) and investigation of kinetic properties. Asian Journal of Chemistry. 2008;**20**(1):477-482

[24] Su CH, Liu DZ, Jiang PL, Chien MY, Sheu MT, Huang YY, Chen MH. Dried fruit of the *Luffa sponge* as a source of chitin for applications as skin substitutes. BioMed Research International. 2014;**2014**:1-9 [article ID 458287]

[25] Converso DA, Fernandez ME. Peroxidase isozymes from wheat germ: Purification and properties. Phytochemistry. 1995;**40**:1341-1345

[26] Billaud C, Louarme L, Nicolas J. Comparison of peroxidases from barley kernel (*Hordeum vulgare* L.) and wheat germ (*Triticum aestivum* L.): Isolation and preliminary characterization. Journal of Food Biochemistry. 1999;**23**:145-172

[27] Chen Z, Mabrouk PA. Isolation and purification of soybean peroxidase from "Montsew" Chinese soybeans. National Undergraduate Research Clearinghouse; 2000. pp. 2-7

[28] Dicko MH, Gruppen H, Hilhorst R, Voragen AG, Berkel WJV. Biochemical characterization of the major sorghum grain peroxidase. FEBS Journal. 2006;**273**:2293-2307

[29] Suzuki T, Honda Y, Mukasa Y, Kim SJ. Characterization of peroxidase in buckwheat seed. Phytochemistry. 2006;**67**:219-224

[30] Geetha MS, Nagabhushana H, Shivananjaiah HN. Green mediated synthesis and characterization of ZnO using *Euphorbia Milli* latex as fuel. IJSR. 2016;**5**(4):158-163

[31] Nasrollahzadeh M, Sajadi SM. Preparation of Pd/Fe_3O_4 nanoparticles by use of *Euphorbia stracheyi Boiss* root extract: A magnetically recoverable catalyst for one-pot reductive amination of aldehydes at room temperature. Journal of Colloid and Interface Science. 2016;**464**:147-152

[32] Slman AA. Antibacterial activity of ZnO nanoparticle on some gram-positive and gram-negative bacteria. Iraq. Journal de Physique. 2012;**10**(18):5-10

[33] Ng JCY, Cheung WH, McKay G. Equilibrium studies for the sorption of lead from effluents using chitosan. Chemosphere. 2003;**52**:1021-1030

[34] Sharma P, Sreenivas K, Rao KV. Analysis of ultraviolet photoconductivity in ZnO films prepared by unbalanced magnetron sputtering. JJAP. 2003;**93**:3963-3970

[35] Rahman OU, Mohapatra SC, Ahmad S. Fe_3O_4 inverse spinal super paramagnetic nanoparticles. Materials Chemistry and Physics. 2012;**132**:196-202

[36] Nagarajan S, Kuppusamy KA. Extracellular synthesis of zinc oxide nanoparticle using seaweeds of gulf of Mannar, India. Journal of Nanbiotechnology. 2013;**11**:39

[37] Manouchehr N, Mehriana A, Reza L, Rostami MH. The optimum conditions for synthesis of Fe_3O_4/ZnO core/shell magnetic nanoparticles for photodegradation of phenol. IJEHSE. 2014;**12**(21):1-6

[38] Gnanasangeetha D, Sarala TD. Benign ZnO nanoparticle as a practical adsorbent for removal of As^{3+} embedded on activated silica using *Ocimum Sanctum*. Discovery. 2014;**16**(46):33-41

[39] Davar F, Majedi A, Mirzaei A. Green synthesis of ZnO nanoparticles and its application in the degradation of some dyes. Journal of the American Ceramic Society. 2015;**98**(6):1739-1746

[40] Rasool K, Lee DS. Effect of ZnO nanoparticles on biodegradation and biotransformation of co-substrate and sulphonated azo dye in anaerobic biological sulfate reduction processes. International Biodeterioration & Biodegradation. 2016;**109**:150-156

[41] Sharma ACD, Sun Q, Li J, Wang Y, Suanon F, Yang J, Yu CP. Decolorization of azo dye methyl red by suspended and co-immobilized bacterial cells with mediators anthraquinone-2,6-disulfonate and Fe_3O_4 nanoparticles. International Biodeterioration & Biodegradation. 2016;**112**:88-97

[42] Sun JH, Shi SH, Lee YF, Sun SP. Fenton oxidative decolorization of the azo dye direct blue 15 in aqueous solution. Chemical Engineering Journal. 2009;**155**(3):680-683

[43] Weng CH, Lin YT, Chang CK, Liu N. Decolourization of direct blue 15 by Fenton/ultrasonic process using a zero-valent iron aggregate catalyst. Ultrasonics Sonochemistry. 2013;**20**(3):970-977

[44] Zhan Y, Zhou X, Fu B, Chen Y. Catalytic wet peroxide oxidation of azo dye (direct blue 15) using solvothermally synthesized copper hydroxide nitrate as catalyst. Journal of Hazardous Materials. 2011;**187**(1-3):348-354

[45] Kesraoui A, Moussa A, Ben Ali G, Seffen M. Biosorption of Alpacide blue from aqueous solution by lignocellulosic biomass: *Luffa cylindrica* fibers. Environmental Science and Pollution Research. 2016;**23**(16):15832-15840

[46] Siquera G, Bras J, Follain N, Belbekhouche S, Marais S, Dufresne A. Thermal and mechanical properties of bionanocomposites reinforced by *Luffa cylindrica* cellulose nanocrystals. Carbohydrate Polymers. 2013;**91**:711-717

[47] Tong Y, Zhao S, Ma J, Wang L, Zhang Y, Gao Y, Xie YM. Improving cracking and drying shrinkage properties of cement mortar by adding chemically treated luffa fibres. Construction and Building Materials. 2014;**71**:327-333

[48] Chen C, Luo Wen J, Tong Q. Elemental analysis, chemical composition, cellulose crystallinity, and FT-IR spectra of *Toona sinensis* wood. Abrégé en. Monatshefte fuer Chemie. 2014;**145**(1):175-185

[49] Kalkan E, Nadaroglu H, Celebi N, Tozsin G. Removal of textile dye reactive black 5 from aqueous solution by adsorption on laccase-modified silicafume. Desalination and Water Treatment. 2014;**52**(31-33):6122-6134

Chapter 12

Preclinical Aspects on Magnetic Iron Oxide Nanoparticles and Their Interventions as Anticancer Agents: Enucleation, Apoptosis and Other Mechanism

Elena-Alina Moacă, Elena Dorina Coricovac,
Codruta Marinela Soica, Iulia Andreea Pinzaru,
Cornelia Silvia Păcurariu and
Cristina Adriana Dehelean

Additional information is available at the end of the chapter

http://dx.doi.org/10.5772/intechopen.74176

Abstract

The broad area of magnetic iron oxide nanoparticle (M-IONP) applications and their exclusive physico-chemical characteristics (superparamagnetic properties *per se*, solubility and stability in aqueous solutions, and high bioavailability *in vivo*) make these nanoparticles suitable candidates for biomedical uses. The most employed magnetic iron oxides in the biomedical field are magnetite and maghemite. Cancer represents a complex pathology that implies multiple mechanisms and signaling pathways, this complexity being responsible for the increased resistance to therapy and the lack of an effective curative treatment. A potential useful alternative was considered to be the use of magnetic iron nanoparticles. The M-IONPs proved to be effective as contrast agents in magnetic resonance imaging, as drug delivery carriers for different therapeutic agents, in magnetic cell separation assays, and are suitable to be engineered in terms of size, targeted delivery and substance release. Moreover, their *in vivo* administration was considered safe, and recent studies indicated their efficiency as anticancer agents. This chapter aims to furnish an overview regarding the physico-chemical properties of M-IONPs (mainly magnetite, maghemite and hematite), the synthesis methods and their *in vitro* biological impact on healthy and cancer cell lines, by describing their potential mechanism of action—enucleation, apoptosis or other mechanisms.

Keywords: magnetic iron oxide nanoparticles (M-IONPs), cancer, enucleation, apoptosis, magnetite, maghemite, combustion method

IntechOpen

1. Introduction

Due to the wide potential of applications in various fields, such as biotechnology, biomedicine, magnetic fluids, catalysis, magnetic data recording and storage media, magnetic resonance imaging, magnetic fluid hyperthermia, magnetic drug delivery, cell separation, magnetic paper and more recently in environmental protection, magnetic iron oxide nanoparticles (M-IONPs) are the main components of the modern technology [1–15]. In nature, many forms of iron oxides are found, but the most technologically used are the magnetite (Fe_3O_4), maghemite (γ-Fe_2O_3) and hematite (α-Fe_2O_3) (**Figure 1**).

Magnetite (Fe_3O_4), a natural mineral known as the black iron oxide, is relatively stable at room temperature, very quickly transforms in maghemite and shows the strongest magnetism compared to other transition metal oxides [16]. Fe_3O_4 has an inverse spinel structure with all the Fe^{2+} ions and half of the Fe^{3+} ions distributed in the octahedral sites and the other half of the Fe^{3+} ions distributed in the tetrahedral sites being surrounded by four oxygen atoms [17].

Spin magnetic moments of Fe^{3+} ions distributed in octahedral positions are parallely aligned, as well as those of Fe^{3+} ions distributed in tetrahedral positions but in the opposite direction, leading to an antiparallel coupling. Therefore, the spin moments of all Fe^{3+} ions mutually cancel out and do not contribute to the net magnetization of magnetite (**Figure 2**). All Fe^{2+} ions have magnetic moments aligned in the same direction so that their total magnetic moment is responsible for the net magnetization of magnetite. Therefore, the saturation magnetization of magnetite corresponds to the product between the spin magnetic moment of each Fe^{2+} ion and the number of Fe^{2+} ions, which corresponds to the mutual alignment of all Fe^{2+} ions in magnetite.

Magnetite is oxidized in the presence of air to maghemite, which is also ferrimagnetic, but has a slightly lower magnetic response. This process is called maghemitization and occurs at the surface of the crystals. Crystal centers are also oxidized, and the process is being carried out by diffusion of Fe^{2+} ions from inside to the surface of the crystals, where they are converted to Fe^{3+}. The rate of the oxidation process is determined by the diffusion rate of Fe^{2+} ions and the distance to the surface. Therefore, the particles remain unaffected by the phenomenon of maghemitization, while the small ones are susceptible to oxidation even at room temperature.

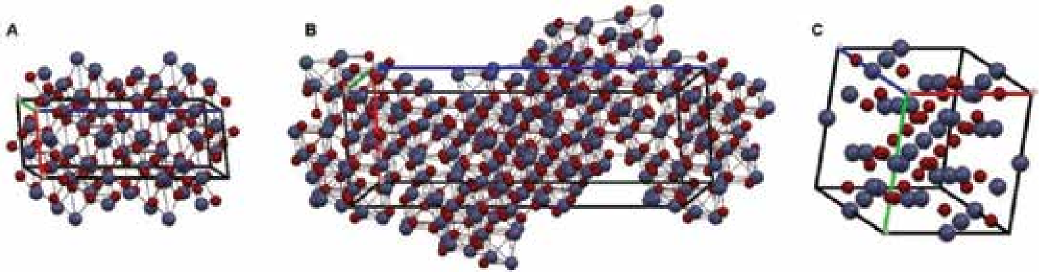

Figure 1. Crystal structure of: A—hematite, B—maghemite and C—magnetite (the blue sphere is Fe^{2+}/Fe^{3+} and the red sphere is O^{2-}). The structures were adapted after the structures found in the Crystallography Open Database (http://www.crystallography.net).

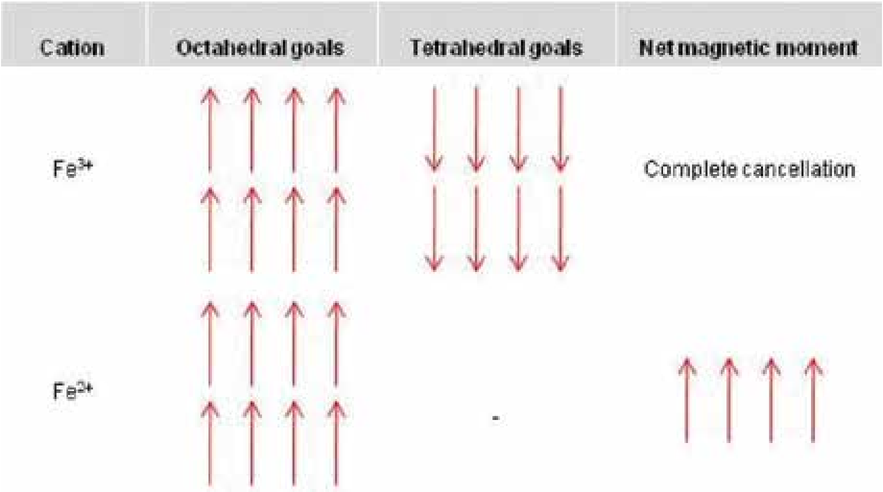

Figure 2. Spin magnetic moment distribution of Fe^{2+} and Fe^{3+} ions in the elemental cell of magnetite.

As magnetite, maghemite (γ-Fe_2O_3) has a spinel structure with the oxygen ions disposed in a closely packed cubic lattice and the iron ions located at interstices. In γ-Fe_2O_3 not all the sites

Property	**Oxide**		
	Magnetite	**Maghemite**	**Hematite**
Molecular formula	Fe_3O_4	γ-Fe_2O_3	α-Fe_2O_3
Color	Black	Reddish-brown	Red
Density (g/cm^3)	5.18	4.87	5.26
Melting temperature (°C)	1583–1597	—	1350
Hardness	5.5	5	6.5
Type of magnetism	Ferrimagnetic	Ferrimagnetic	Weakly ferromagnetic/ anti-ferromagnetic
Curie temperature (K)	858	820–986	956
Saturation magnetization (M_s) at 300 K [A·m^2/kg]	92–100	60–80	0.3
Standard Gibbs free energy of formation (ΔG_f^0) [kJ/mol]	−1012.6	−711.1	−742.7
Crystallographic system	Cubic	Cubic or tetrahedral	Rhombohedral, hexagonal
Structure type	Inverse spinel	Defect spinel	Corundum
Lattice parameter (nm)	$\alpha = 0.8396$	$\alpha = 0.83474$ (cubic); $\alpha = 0.8347$; $c = 2.501$ (tetragonal)	$\alpha = 0.5034$; $c = 1.375$ (hexagonal); $\alpha_{Rh} = 0.5427$; $\alpha = 55.3°$ (rhombohedral)

Table 1. Physical and magnetic properties of iron oxides [22].

are occupied, Fe^{3+} ions are regularly distributed in only two-thirds of the sites and the rest of the sites remain vacant. After two sites filled with Fe^{3+} ions follows one vacant site [18, 19]. Maghemite is a metastable oxide, product of magnetite oxidation or a product resulting from the heating of other iron oxides.

At temperatures over 300°C, magnetite is oxidized to hematite (α-Fe_2O_3)—an anti-ferromagnetic iron oxide. Hematite (α-Fe_2O_3) has a corundum crystal structure with Fe^{3+} ions distributed in octahedral sites and oxygen ions in hexagonal close-packed arrangement. α-Fe_2O_3, the final product of the transformation of other iron oxides, is a red powder when it is finely divided, very stable at room temperature and very widespread in rocks and soils (**Table 1**) [20, 21].

2. Properties of magnetic nanoparticles

2.1. Magnetic behavior

Magnetic iron oxide nanoparticles (M-IONPs), magnetite (Fe_3O_4) and maghemite (γ-Fe_2O_3) are materials with iron-magnetic properties under their Curie temperatures (858 K and 986 K) (**Table 1**). The ferro- and ferrimagnetic compounds in their raw state present a multidimensional magnetic structure, without a permanent magnetic moment. The magnetic properties of a material depend on following parameters: (i) temperature, (ii) pressure and (iii) applied magnetic field. The properties of iron oxide nanoparticles by their usual sizes are not similar to the properties of larger scale compounds, which explain their use and interest in nanomedicine [23]. In order to define the behavior of the magnetic field, the key lays in the size and distribution of nanoparticles morphology [24]. A spherical, small nanoparticle made of soft materials with a diameter below the domain size shows an expendable magnetic anisotropy, so that their magnetic moment is free to rotate relatively to the particle and is thus superparamagnetic, i.e., paramagnetic under the Curie temperature [25]. The direction of the magnetic moment of the nanoparticles is determined by thermal fluctuation and the magnetic anisotropy, which tend to fixate on the crystalline structure or particle morphology [26].

The interaction between an external magnetic field and the magnetic field of a nanoparticle determines: (i) the orientation of the magnetic moment of the particle as to become parallel with the magnetic field applied to minimize energy and bipolar interaction and (ii) the transition of the particle in the direction of the gradient, as in magnetophoresis [26]. Many applications of the magnetic nanoparticles are based on their ability to be manipulated using magnetic fields. This capability depends on the effectiveness of the magnetophoretic force, determined by the time of the particle and the magnetic field gradient, to fasten or to move the particle [25]. The magnetophoretic force exercised over superparamagnetic nanoparticles with a single core is less effective due to their small diameter and magnetic moment, but in the case of multicore particles, the magnetic momentum induced in the field is strong enough to allow magnetic targeting to moderate values of the magnetic field intensity and field gradient. Therefore, in order to assess the applicability of magnetic particles or magnetic fixing, the magnetic momentum of the particles is more relevant than mass magnetization [25, 27].

2.2. Size

The size and the size distribution of superparamagnetic iron oxide nanoparticles are important parameters for their biological application. Also, their magnetic properties are in close touch with their size. It has been demonstrated that the magnetic dipole-dipole interactions are significantly reduced in superparamagnetic iron oxide nanoparticles due to their scale of r6, r being the radius of the particle [28]. The advantages of using magnetic nanoparticles with sizes smaller than 100 nm are due to their surface efficiency to easily attach ligands and small settling velocities which give a high stability in suspension and improve tissue diffusion. Particles should be small enough to bypass the endothelial reticule system. They are supposed to remain in circulation after injection and be able to pass through the capital systems, organs and tissues, avoiding the embolus. Particle size is also important for getting an effect of improved permeability and retention. For example, particles larger than 10 nm may not penetrate the endothelium in physiological conditions, but can enter in pathological conditions, such as inflammations or tumors [28].

When magnetic nanoparticles loaded with medicinal substances are injected into the systemic circulation, size, morphology and surface charge are the three important parameters for their behavior in the bloodstream. Kupffer cells in the liver are very sensitive to both microorganisms and nanoparticles. Plasma proteins can easily adsorb onto their surface nanoparticles, depending on their size, surface charging and their morphology. Particles with sizes larger than 200 nm or below 10 nm are not suitable due to their absorption by the endoplasmic reticulum system [28].

2.3. Charge

Loading surface and biodistribution of superparamagnetic iron oxide nanoparticles play an important role in the colloidal stability. Surface charging can be described qualitatively by the nature and behavior of surface groups in the solution at a given pH and in the presence of an electrolyte. In terms of quantity, it can be measured as an electric potential in the double layer of the interfacial surface of the nanoparticles found in a suspension state. A high value of zeta potential is an indication of stability in dispersion of superparamagnetic iron oxide nanoparticles due to electrostatic interaction. Composition and structure of nanoparticles are very important for their interaction with biological fluids. In a known environment, superparamagnetic nanoparticle characteristics, such as the chemical composition, both core and neural crest cells, its size and size distribution, shape and angles of curvature, its crystalline structure, smoothness or surface roughness and hydrophobic or hydrophilic levels, are important for their *in vivo* applications. These features can determine their stationary time in the circulatory system [28].

Osaka and his colleagues [29] have reported a correlation between surface charge of magnetite nanoparticles and their cellular absorption efficiency on different cell lines. For example, a superparamagnetic particle with positive charge showed a greater internalization in human breast cancer cells in comparison with those charged negatively, while there was no difference in the degree of internalization in endothelial cells of human umbilical bladder. Thus, the superparamagnetic nanoparticles absorption depends not only on their surface properties but also on cell type.

2.4. Surface functionality and colloidal stability

Both the surface chemistry of magnetite particles and its properties are particularly important in various applications. Iron atoms at the surface of the magnetite particle that are not bound to oxygen atoms act as Lewis acids and coordinate the molecules that can give a pair of electrons. In aqueous systems, these atoms coordinate water molecules that rapidly dissociate resulting magnetite with functionalized surface with Fe-OH hydroxyl groups. So, the chemistry of the surface of magnetite particles is strongly dependent on the pH value; at low pH values, the surface of the magnetite particles is protonated (positively charged), and at high pH values, it is negatively charged (**Figure 3**). The preformed hydroxyl groups on the surface of magnetite have amphoteric character; therefore, they can react either as acids or bases [30].

Another problem that arises after obtaining the magnetic iron oxide nanoparticles (M-IONPs) is their agglomeration that is installed due to the van der Waals forces and the magnetic forces. Nanoparticles without coatings (naked nanoparticles) are not stable in aqueous environments, easily aggregating and precipitating. After application *in vivo*, nanoparticles often form aggregates in the bloodstream and are retained by the macrophages. Therefore, they must be covered with a variety of fragments which have the property to eliminate or minimize their aggregation in physiological conditions [31]. The magnetic nanoparticles are coated with an impervious wrapper so that oxygen does not reach at the surface of the magnetic nanoparticles in order to ensure an effective stabilization of iron oxide nanoparticles. Some stabilizers, such as a surfactant or a polymer, usually are added during preparation to prevent the aggregation of nanosized particles. Most of these polymers stick to the nanoparticles surface in a specific substrate manner. Nanoparticle surfaces can be composed of several organic and inorganic materials, including polymer. Also, polymer coating materials can be classified in turn into synthetic and natural. Polymers such as poly-ethylene-co-vinyl acetate, poly-vinylpyrrolidone,

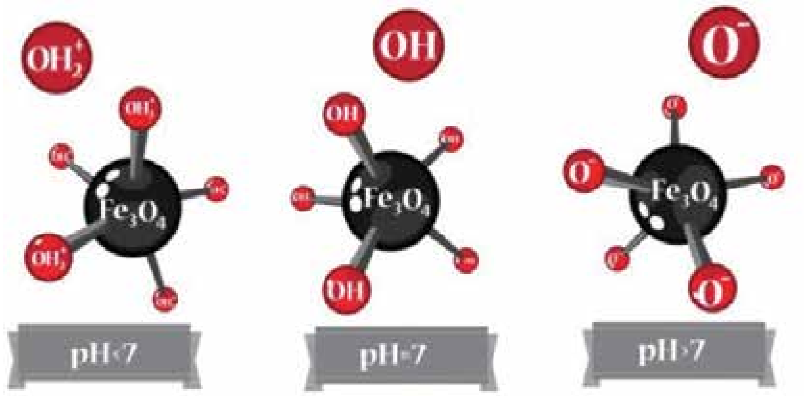

Figure 3. The behavior of Fe_3O_4 nanoparticles depending on pH.

poly-acid-lactic-co-glycolic, polyethylene glycol, etc. are typical examples of synthetic polymeric systems. Natural polymer coatings include gelatin, dextran, chitosan, etc. The molecules used for stabilization of magnetic nanoparticles must be biocompatible and biodegradable. The most common surfactant molecules are oleic acid, lauric acid, acids, sulfonic acids, alkanes and alkane phosphonates. The surfactants are amphiphilic compounds and they manifest their role at the interface between nanoparticles and solvent. However, magnetic nanoparticles covered with organic compounds, in suspension cannot be used for biological purposes, especially in the delivery of medicines. Changing the surface of nanoparticles post-synthesis is known as core-shell nanoparticles, also used widely. The most commonly used materials are polymers, silica or metals (e.g. gold, cadmium, selenium, silver). Coating materials protect the core against oxidation and therefore keep the magnetic property of nanoparticles. It is known that the iron oxide nanoparticles are non-toxic, but some coating materials may be toxic. For example, silicon dioxide is biocompatible, but is not biodegradable [28].

Many researchers have prepared magnetic nanoparticles covered with various surfactants or biomolecules that have been introduced directly in the synthesis process. For example, Salavati-Niasari et al. [32] have synthesized Fe_3O_4 nanoparticles covered with octanoic acid using a facile chemical precipitation method. The surfactant was present in the reaction system to improve dispersity. The authors have obtained magnetic nanoparticles with a size range of 25 nm. Liu et al. prepared magnetic nanoparticles coated with chitosan, for the immobilized lipase, using the co-precipitation method. They replaced water with 2% chitosan in acetic acid solution during the reaction process [33].

Atomic transfer radical polymerization (ATRP) is another common way to cover magnetic nanoparticles, developed by Wang et al. [34]. Due to the magnetic interaction of the iron oxide nanoparticles with biological fluids, the process of formation of free radicals of oxygen reactive species may be increased. To protect the environment *in vivo* from these toxic by-products, some materials have been used for biocompatible and rigid coatings, such as gold [28].

3. M-IONPs synthesis methods

In the past decade, numerous synthesis methods have been developed to obtain M-IONPs. On the basis that the method of preparation plays an essential role in obtaining nanoparticles with tailored properties, the research work regarding the development of new synthesis methods to control the size, shape, morphology and magnetic properties of these nanoparticles is a permanent challenge. In the same time, the synthesis method has to be environmentally friendly, simple, inexpensive and reproducible. Many scientific publications have described efficient synthesis methods, which allow the obtaining of monodisperse magnetic nanoparticles, stable for a long time with controlled shape.

The synthesis method has to ensure the obtaining of magnetic nanoparticles with specific properties to their application domain by changing the experimental reaction conditions. For biomedical applications, superparamagnetic iron oxide nanoparticles with a specific surface chemistry (for *in vivo* applications), high magnetization values and a narrow size distribution of the particles with size below 100 nm are needed. Magnetite (Fe_3O_4) and maghemite (γ-Fe_2O_3) have attracted particular attention because, under certain synthesis conditions, they are superparamagnetic, being also biocompatible, thus becoming the magnetic nanomaterials most commonly used in medical applications.

Hereinafter, the most popular synthesis methods used for obtaining M-IONPs will be described. After the chemical surface modification of magnetic nanoparticles by binding drugs, proteins, enzymes, antibodies, etc., they can be directed to an organ, tissue or tumor with the help of an external magnetic field. The methods described below allow to obtain magnetic nanoparticles with narrow size dimensions, desired shape and morphology, by changing the conditions and/or parameters of the synthesis. The most used and popular method for the synthesis of magnetite, being in the same time simple and efficient, is the chemical precipitation of iron salts [35–39].

3.1. Precipitation method

The first synthesis of superparamagnetic iron oxide nanoparticles was reported by Massart, and the method consists in mixing two salts of Fe^{3+} and Fe^{2+} in a molar ratio of 2:1 in aqueous medium followed by precipitation of these salts using a precipitating agent (a base – NH_3) under inert atmosphere or at elevated temperature, resulting a black magnetic precipitate [40]. The equation of the chemical reaction which underlies the formation of magnetite may be written as Eq. (1):

$$Fe^{2+} + 2Fe^{3+} + 8OH^{-} \rightarrow Fe(OH)_2 + 2Fe(OH)_3 \rightarrow Fe_3O_4\downarrow + 4H_2O \qquad (1)$$

Magnetite is not stable at room temperature, being sensitive to oxidation in contact with air, easily transforming into maghemite, according to Eq. (2):

$$2Fe_3O_4 + \tfrac{1}{2}O_2 \rightarrow 3\gamma - Fe_2O_3 \qquad (2)$$

The precipitation process is based on two steps regarding the formation of the solids [41, 42]: (i) nucleation—a very short period, occurs only when the concentration of the constituent species reaches suprasaturation and (ii) slow controlled growth of the preformed nuclei, by diffusion from the solutions to the surfaces of the crystal. To avoid the formation of polydispersed nanoparticles, it is necessary that the two stages to be separated, i.e., nucleation does not take place simultaneously with crystal growth. By controlling the two processes, monodispersed magnetic particles can be obtained. If the nuclei start to form in the same time, the growth of these nuclei leads to particles with very narrow size distribution. Therefore, the size of the obtained particles can be controlled but only in the nucleation step because the size of the particles does not change during the growth process.

It has been shown that by controlling both the pH of the reaction medium and the ionic strength, it is possible to control the mean size of the particles. Jiang et al. have demonstrated that the size of the particles has an inverse proportionality with the pH and the ionic strength of the precipitation medium [43]. These two parameters (pH and the ionic strength) also affect the chemical surface of the crystals and the electrostatic surface charge [44].

Other parameters that can influence the size, shape and composition of the magnetic iron oxide nanoparticles are the nature of iron salts (chlorides, perchlorates, nitrates, sulfates, etc.) and the molar ratio Fe^{3+}/Fe^{2+}. Roth and co-workers published a good analysis regarding the influence of the reaction conditions on the formation of superparamagnetic iron oxide nanoparticles. The authors demonstrated that for obtaining particles with a size between 3 and 17 nm with high saturation magnetization a higher reaction temperature, higher iron salt concentration, Fe^{3+}/Fe^{2+} molar ratio below 2 and a molar ratio of hydroxide ions/iron ions of 1.4:1 are needed [45].

Wu et al. investigated the effect of the vacuum drying method on the change of the morphology and magnetic properties of magnetic iron oxide nanoparticles (M-IONPs). They revealed that the obtained nanoparticles tend to agglomerate more easily when their average diameter decreased, but the structure and morphology are maintained better by ambient air drying. They also obtained magnetic nanoparticles with high saturation magnetization after drying the obtained nanoparticles in a vacuum at 70°C [36].

The same group of researchers in another study has synthesized Fe_3O_4 nanoparticles by utilizing ultrasonic-assisted chemical co-precipitation. They used high purity iron separated from iron ore tailings by an acidic leaching method and obtained superparamagnetic iron oxide nanoparticles without a protecting gas [46]. Pereira and co-workers have synthesized superparamagnetic Fe_3O_4 nanoparticles with small particle size (4.9–6.3 nm) and improved magnetic properties by one-step aqueous precipitation route based on the use of a new type of alkaline agents [47]. The alkaline agents that they have used include alkanolamines, isopropanol amine and diisopropanolamine. The base that they have used, instead of the most used—NaOH, leads to smaller particle sizes (up to 6 times) and enhanced saturation magnetization (up to 1.3 times). Generally, the size of the particles is proportionally with the magnetization saturation, but the above results showed improved magnetic properties while keeping their small size.

Besides the many advantages of the precipitation method (high saturation magnetization, rapid synthesis with high yield, versatility, nanoparticles with the desired morphology and characteristics), it shows several disadvantages, like oxidation, magnetic nanoparticles with particle size distribution that cannot be controlled, polydispersion and weak crystallization which leads to nanoparticles with low saturation magnetization.

3.2. Thermal decomposition

Thermal decomposition of organometallic compounds in high boiling organic solutions in the presence of stabilizers is also a popular method for the synthesis of the spinel structured Fe_3O_4 and a very promising technique for obtaining high-quality superparamagnetic iron oxide nanoparticles. The magnetic nanoparticles obtained by this method proved to be superior to those obtained by precipitation, because the nucleation process can be separated by the growth process and the hydrolysis reaction is avoided [48].

The method is based on the decomposition of an iron precursor at high temperature in the presence of solvents which contain stabilizing surfactants (such as oleic acid or oleylamine) [49–51]. By varying the reaction mixtures and modifying the synthesis condition, it can be obtained M-IONPs with controlled size, size distribution and composition. The most commonly used precursors employed to prepare monodispersed M-IONPs with diameter ranging from 3 to 50 nm are of the form: (I) metal acetylacetonate—[$M(acac)_n$] (where M = Fe, Co, Ni, Mn, Cr; n = 2 or 3) [52]; (II) metal cupferronates—[$M^x(cup)_x$] (where cup = N-nitrosophen ylhydroxylamine); (III) metal oxalate—[$M(C_2O_4)_n$•$2H_2O$]; (IV) metal carbonyl—$Fe_3(CO)_{12}$ [53] or $Fe(CO)_5$ [50]; (V) metal acetate—[$M(CH_3COO)_n$]; (VI) metal carboxylate, (VII) metal-urea complex—[$Fe(CON_2H_4)_6$](NO_3)$_3$ [54]; (VIII) Prussian Blue—Fe_4[$Fe(CN)_6$•$14H_2O$] [55, 56]; (IX) metal chloride and (X) ferrocene—$Fe(C_2H_5)_2$ [57].

Using the thermal decomposition method, it can be easy to control the size and morphology of magnetic nanoparticles by controlling the ratio of the starting reagents, i.e. the ratio between the organometallic compounds, surfactant and solvent. Reaction time, temperature and aging period are equally important for the control of size and morphology. Hyeon obtained monodispersed iron oxide nanoparticles with size range from 4 to 20 nm by thermal decomposition of $Fe(CO)_5$ in the presence of oleic acid at 100°C. Initially, he obtained an iron-oleic acid complex, which was leaved to aging at high temperature (300°C) [50].

Pérez-Mirabet et al. used oleylamine both as stabilization agent (for the stabilization of the particles in solution) and as capping ligand (for the control of particles size), respectively, by one-pot thermal decomposition of $Fe(acac)_3$ and $M(acac)_2$ (M = Co, Mn, Cu and Zn) in oleylamine. They obtained magnetic spinel ferrite nanoparticles with average size of 12 nm and a saturation magnetization Ms = 76 emu/g, very close to the bulk magnetite (92 emu/g) [58].

This method is also suitable for synthesis of nanocubes and nanospheres, which are magnetic nanoparticles as well. Amara et al. synthesized Fe_3O_4 nanocubes and nanospheres by a new simple and single-step process [59]. They used various mixtures of ferrocene and polyvinylpyrrolidone (PVP) by solventless thermal decomposition. Lynch et al. obtained magnetic colloidal iron oxide nanoparticles by thermal decomposition. They generated gas bubbles (Ar) by boiling solvents. Their results illustrated that the argon bubbles had a stronger effect on the nucleation process of magnetic iron oxide nanoparticles than on their growth process [60]. Due to the nucleation process that involves boiling solvents, most often the accurate shape of the magnetic iron oxide nanoparticles is not fully reproducible using the thermal decomposition method.

3.3. Microemulsion method

A microemulsion is formed when a colloidal substance is dispersed in a solvent, that is not compatible with the substance (e.g. water and oil), through a surfactant. Finally, a microemulsion must be clear and stable, as long as it is an isotropic mixture of oil, water and surfactant. The surfactant forms a monolayer film at the oil/water interface, in which the hydrophilic head groups of the surfactant are dissolved in oil phase (consisting of a mixture of hydrocarbons and olefins) and the hydrophobic tail of the surfactant in the aqueous phase (consisting of metal salts) and vice versa, depending on the used surfactant. There are known two types of microemulsion: direct microemulsion, when the oil is dispersed in water and reversed microemulsion, when the water is dispersed in oil. Both have been used to synthesize the magnetic iron oxide nanoparticles with tailored size and shape. The most common surfactants that are widely used in the fabrication of M-IONPs by microemulsion method are bis(2-ethylhexyl) sulfosuccinate (AOT), sodium dodecyl sulfate (SDS), cetyltrimethylammonium bromide (CTAB) and poly-vinylpyrrolidone (PVP). Throughout time, the microemulsion method proved to be a simple and versatile method for fabrication of nanosized magnetic nanoparticles [61–65].

According to the literature, the size of the resulted nanoparticles can be controlled if the surfactant is proper chose and also by varying the ratio of water/oil/surfactant, the initial concentration of the reactants and the droplet size and by controlling the reaction temperature and time [66, 67]. The size of the synthesized nanoparticles can also be controlled in suitable narrow range by carrying out the reaction in nanoreactor [62, 64, 67].

Lu et al. demonstrated that the surfactant nature has an important role on the final properties of the nanoparticles [64]. The authors have investigated the effect of SDS (anionic surfactant), DTAB and CTAB (cationic surfactants) and non-ionic surfactant on the preformed crystal, on stoichiometric situations and on the magnetic properties of the resulted Fe_3O_4 nanoparticles. In all the cases, the authors have obtained Fe_3O_4 nanoparticles with size less than 16 nm, but in the case of using the cationic surfactants also obtained a good saturation magnetization, which is an essential parameter for biological applications.

Okoli et al. have prepared M-IONPs by the two types of microemulsion (water/oil and oil/water), to be used in binding and separation of proteins. The authors demonstrated that by using a water/oil microemulsion, it can obtain magnetic iron oxide nanoparticles with a surface area of 147 m^2/g compared to 304 m^2/g for the magnetic nanoparticles obtained by oil/water microemulsion [68, 69]. The M-IONPs specific surface area is inversely proportional with the size of nanoparticles, the higher is the specific surface area the smaller nanoparticles size is obtained.

The advantage of this method is the fact that it can be obtain magnetic nanoparticles with uniform morphology and controllable size; but the major drawbacks are the requirements of a large amount of solvent and the excess of surfactant that has to be eliminated.

3.4. Hydrothermal and solvothermal methods

In case of these methods, the reaction takes place in aqueous medium (the hydrothermal method) or in organic medium (solvothermal method), in reactors or autoclaves, at temperatures between 130 and 250°C under high vapor pressure, in the range 0.3–4 MPa [70–72]. Using this method, it can be obtained magnetic iron oxide nanoparticles with tailored properties (size and shape) by tuning the reaction conditions. The hydrothermal method is known as an environment-friendly process for the obtaining of M-IONPs, due to the raw materials used such as sulfates and chlorides—as cation source, dissolved in water [73].

Lin et al. [74] has used hydrothermal and solvothermal methods to obtain hollow M-IONPs. Briefly, they used $FeCl_3$ (as source of iron), ethylene glycol (as reducing agent), ammonium acetate and urea were used to guide the formation of hollow magnetite spheres. After homogeneous dispersion, the mixture is transferred to a Teflon-lined stainless steel autoclave and sealed to heat at about 200°C for 8–24 h. The authors demonstrated that the Fe^{3+} ions on the surface of the hollow spheres exist in the form of Fe_3O_4, and the results are confirmed by the Mössbauer measurements. Tian et al. synthesized ultra-small monodisperse Fe_3O_4 nanoparticles, with precise size control of 1 nm, by solvothermal method [75]. They used $Fe(acac)_3$ as iron source, n-octanol as a solvent and n-octylamine as a reductant. The authors obtained Fe_3O_4 nanoparticles with a size range from 4 to 6 nm, by varying the volume ratios of n-octylamine and n-octanol, without the need of a gas (N_2) bubbling or reflux conditions. By comparing this method with the thermal decomposition methods for obtaining Fe_3O_4 nanoparticles, this solvothermal process was more convenient.

Stoia et al. [14] synthesized Fe_xO_y and Fe_xO_y/C nanocomposite by solvothermal method, with the purpose of using these nanocomposites as adsorbents for methylene blue removal from aqueous solutions. The authors used $FeCl_3$ as iron source, 1,2-propanediol as solvent and diethylamine as precipitating agent. The activated carbon was introduced into system in order to obtain homogenous Fe_xO_y/C composites with high specific surface area and magnetic properties. Some researchers have attempted to modify the hydrothermal process. Ahmadi et al. obtained Fe_3O_4 nanoparticles at low temperature (140°C) without having to autoclave. They have studied kinetics of the reaction, but the magnetic properties of the resulted nanoparticles are inadequate in short reaction time (below 2 hours) [76].

As advantages, the hydrothermal and solvothermal methods are suitable for obtaining shape-controlled M-IONPs. As a disadvantage, in the case of hydrothermal technique, the reaction takes place for a long time and the amounts of resulting products are low [76].

3.5. Combustion method

The combustion method is an alternative to the currently used methods, being barely mentioned in the literature for the synthesis of M-IONPs. The combustion method have a lot of advantages due to the simplicity of the working technique, short reaction time and low energy consumption, being in the same time environmentally friendly.

The combustion method involves the strong exothermic redox reaction between an oxidizing agent (iron nitrate) and various reducing agents (fuels) of organic nature. The initiation of the combustion process takes place by rapidly heating the mixture of raw materials at relatively low temperatures below 500°C (**Figure 4**). The reaction stoichiometry has a decisive role in the characteristics of the reaction product, especially in the granule size, since a combustion reaction does not occur for any molar fuel/oxidizing agent ratio.

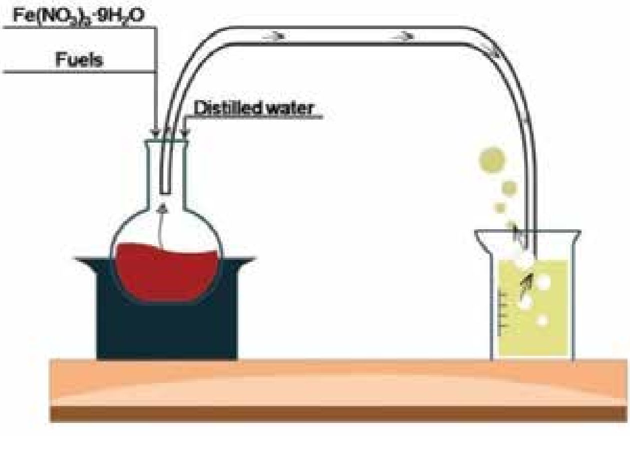

Figure 4. The general scheme for obtaining iron oxide magnetic powders using the combustion method.

The use of metallic nitrates in a mixture with a suitable fuel has the great advantage that, following the combustion reaction, the gases are released without a high risk of toxicity: CO_2, N_2 and H_2O [77]. By using a proper fuel, proper auxiliary additives, as well as an appropriate oxidizing agent/fuel ratio, it can be tailored the size of the particles, the specific surface area and the crystallinity degree of the obtained material [78, 79].

Ianoş et al. reported a new combustion synthesis technique for the preparation of nanosized Fe_3O_4 nanoparticles [80]. The authors developed a new, facile and cheap scheme of installation for combustion synthesis of Fe_3O_4 nanoparticles in the absence of air. They also investigated the effect of both the reaction atmosphere (in the presence or in the absence of air) and the fuels nature on the properties of the resulted nanoparticles. Using sucrose, citric acid and glucose as fuels, the authors demonstrated that the reaction atmosphere is very important for obtaining Fe_3O_4 nanoparticles as a single crystalline phase. There were obtained Fe_3O_4 nanoparticles in the size range of 10 (when glucose was used as fuel) to 18 nm (when citric acid was used as fuel).

Mihoc et al. also investigated the effect of both the fuels nature and the reaction atmosphere for obtaining magnetic nanoparticles used as adsorbent for the removal of phenol and p-chlorophenol from wastewater [81]. The authors revealed that the working atmosphere influences the phase composition of the combustion reaction product. Using urea with ammonium chloride as fuels, the final product of reaction was α-Fe_2O_3 (when the reaction took place in air). Working in the absence of air, using oxalic, tartaric and citric acid as fuel, the single phase resulted in combustion reaction was Fe_3O_4, irrespective of the nature of the fuel.

Using the combustion method, the magnetic oxide nanoparticles are covered with some organic residues resulting from fuel combustion. Mihoc et al. demonstrated that these materials exhibit better adsorption capacity as compared with the naked magnetic oxides [82].

However, if it is desired to remove the residual carbon resulting from the combustion process, Ianos et al. found a method in which the residual carbon was eliminated by washing the magnetic nanoparticles several times with H_2O_2. They revealed that by combustion reaction between $Fe(NO_3)_3 \bullet 9H_2O$ and $C_6H_{12}O_6$ a black magnetic nanoparticle containing γ-Fe_2O_3 and residual carbon was obtained. The authors demonstrated that by H_2O_2 treatment of the resulted magnetic nanoparticles the carbon was removed by chemical oxidation, from 32.7 to 0.4%, and the color of the sample changed from black to reddish brown [83].

M-IONPs proved to be versatile due to the large range board of applications in medicine. Nanomedicine is an emerging field that offers new approaches but especially new solutions for many medical problems. For example, the discovery of antibiotics has been of historic importance, but over time, antibiotic resistance has become an issue and new approaches are therefore needed. Many groups of researchers have already demonstrated that the synergic effects of the antimicrobials agents (not only the antibiotics) with nanoparticles can be promoted as a new method for the severe infection treatments, even with low antimicrobial doses.

For the biomedical uses, only the M-IONPs which fulfill the following requirements are proper: superparamagnetic properties at room temperature, large saturation of magnetizations, biocompatibility and sizes around 20 nm for *in vivo* administration. To convert the pure magnetic nanoparticles in biocompatible colloidal suspensions, many researchers have proposed the use of different polymers like covering agents or surfactants like starch, heparin, chitosan, dextran, oleic acid, polyethylene glycol (PEG), etc.

Polymer coating can be accomplished during or after the synthesis of magnetic nanoparticles. Polyethylene glycol (PEG) is a water-soluble, biocompatible hydrophilic polymer that can be used successfully in the synthesis of biocompatible nanoparticles with increased resistance to blood circulation [84]. Another alternative to covered magnetic nanoparticles is the use of copolymers that produce core-shell nanoparticles with possible applications in drug transport (drug vector) [85].

The use of inorganic compounds such as gold, silver, silica gel and carbon as surfactants not only provides good stability to the nanoparticles but also allows functionalizing their surface by grafting certain biological ligands. Covering of magnetic nanoparticles with gold seems to be ideal because of its low reactivity; however, coating the magnetic nanoparticles directly with gold is very difficult due to the different nature of the two surfaces [86–89]. The silica gel is the most widely used compound in the preparation of functionalized iron oxide nanoparticles surface, because it has several advantages: excellent biocompatibility, hydrophilicity, the feasibility of integrating other functional groups on the surface due to terminal silanol groups that can react with different coupling agents, provides good stabilization of the magnetic iron oxide nanoparticles in the solution, prevents the interaction between the nanoparticles thus preventing the agglomeration of the particles over time and ensures better encapsulation [90]. A very good coating of carbon layers provides an effective barrier against oxidation and acidic erosion of magnetic nanoparticles. It is therefore possible to synthesize carbon-coated magnetic nanoparticles that are thermally stable, biocompatible and also have high oxidation stability, which is crucial for certain applications [89].

4. *In vitro* biological impact

4.1. Magnetic iron oxide nanoparticle effect on normal cells

Iron ions play major biological roles in different physiological processes, including DNA synthesis, oxygen transport, mitochondrial respiration, heme synthesis, and in metabolic functions at central nervous system level (nitric oxide metabolism, oxidative phosphorylation and myelin and neurotransmitter synthesis). Moreover, iron proved to be an essential factor for an appropriate function of neurons by acting as cofactor for tyrosine hydroxylase, an enzyme with a critical role in dopamine synthesis and the viability of neural cells. A dysregulation of the iron homeostasis or transport leads to unbalanced physiological functions and cytotoxic reactions. The free intracellular Fe^{2+} ions react with hydrogen peroxide (H_2O_2) and determine the generation of reactive oxygen species (ROS), process known as Fenton reaction. An increased ROS concentration activates a cascade of events (release of iron ions into the cytosol by inducing an augmented permeability of the outer mitochondrial membrane and detrimental effects on lysosomal membrane; lipid peroxidation, damaged proteins, break of DNA chains and degradation of bases, mutations, deletions or translocations at nuclear level) that has as endpoint cell death. The pathologies that are associated with this type of cellular damage are aging, cancer and neurodegenerative diseases [91]. Another mechanism of inducing cell death by the iron ions is the apoptotic pathway via mitochondria, as follows: a high amount of iron ions into the mitochondria determine the opening of the mitochondrial transition pore, release of Ca^{2+} and cytochrome c and activation of apoptotic cascade [91, 92].

Based on these data, concerning the toxicity induced by iron ions, it is imperative to study the possible toxic effects induced by M-IONPs, mainly since these particles present a higher reactivity as compared with the normal sized ones. The magnetic character of iron oxide nanoparticles offers some advantages, including the capacity of this nanosized compounds to be driven to targeted sites by an external magnetic field, even to tissues and organs that are difficult to reach in normal conditions (blood brain barrier and central nervous system). M-IONPs penetrate into the cells via receptor-mediated endocytosis and settle into the lysosomes, organelles characterized by the presence of an acidic medium, where it takes place the metabolization of the nanoparticles and free iron ions are released into the cell [91].

In a previous study, it was demonstrated that M-IONPs penetrate differentially into the neural cells (glial cells, primary neurons of the cerebellum, microglia, astrocytes, oligodendrocytes and Schwann cells), based on their dimensions: large size nanoparticles were absorbed by endocytosis, whereas small sized ones via pinocytosis [91, 93]. It was also proved that exposure to M-IONPs has an impact on iron homeostasis by upregulating the proteins responsible for iron storage or export from the cell and by downregulating the proteins expression involved in iron uptake [94].

Besides these positive features, application of an external magnetic field leads to accumulation of M-IONPs in target cells and potential toxicity. The accumulation of iron into the cells after exposure to M-IONPs seems to be dependent on several factors, such as (i) concentration and dose of M-IONPs (high concentrations require a longer period for elimination—several months, whereas M-IONPs in low concentrations can be eliminated within 3 weeks), size (small size nanoparticles cumulate in increased concentrations as compared to large size nanoparticles), shape (spherical nanoparticles present a longer degradation process due to a small contact surface), coating (some coating agents may prolong the degradation process or may increase it), the functional groups (the positively charged functional groups present in M-IONPs structure increase their uptake by the cells) and cell type (microglia have a higher affinity for M-IONPs, whereas into the brain endothelial cells penetrate less nanoparticles) [91].

A significant number of studies sustained that M-IONPs exerted *in vitro* and *in vivo* toxicity. The main players responsible for toxic effects are considered to be the iron ions released from M-IONPs at lysosomal level, which react with hydrogen peroxide and lead to ROS generation [91]. Exposure of neural cells to M-IONPs was associated with a low concentration of ROS, but a reduced level of glutathione and mitochondrial membrane hyperpolarization [95]. Other studies conducted on healthy cell lines (both human and animal origin) pointed out that bare M-IONPs may induce cytotoxic effects via ROS generation, leading to cell death [96–98].

The oxidation state of iron (Fe^{2+} or Fe^{3+}) plays a major role in determining the nanoparticles toxicity according to the studies that affirm that Fe^{3+} in Fe_2O_3 is more toxic than Fe^{2+} in Fe_3O_4 and causes more DNA oxidation [91, 99].

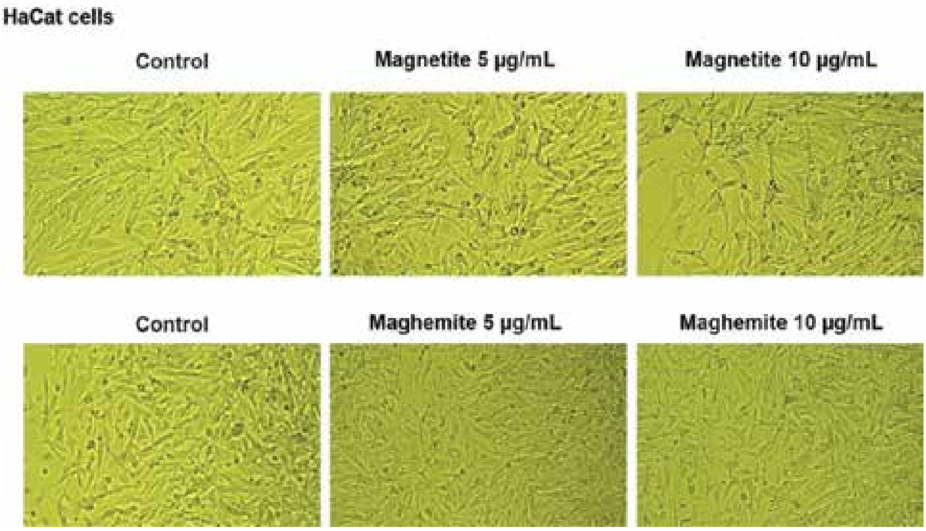

Figure 5. The impact of magnetite and maghemite obtained by combustion method on HaCat cell morphology after 24 h stimulation.

The concentration of M-IONPs is also important in the assessment of M-IONPs toxicity. In one of our previous studies developed on HaCat cells (human keratinocytes), it was shown that concentrations lower than 25 μg/mL did not induce toxicity in terms of viability and cytoskeleton changes (**Figure 5**) [100].

Shelat and coworkers indicated a dose-dependent cytotoxic effect of M-IONPs on mouse embryonic fibroblast (NIH 3 T3) [101]. It was also assessed the effect of negatively charged superparamagnetic iron oxide nanoparticles on heart cells and no changes in actin cytoskeleton were observed, whereas in the case of brain and kidney cells, a disruption of the actin cytoskeleton was detected, but some increased vascular permeability was seen after exposure [102].

Another sign of toxicity that was described after neural cells exposure to M-IONPs was represented by protein aggregation. In addition, it was shown that M-IONPs induce apoptosis of hepatocytes in a mitochondrial-dependent way consisting of upregulation of pro-apoptotic markers (Bax and Bad) and downregulation of bcl-2 (anti-apoptotic); decrease of mitochondrial membrane potential followed by the release of cytochrome c into the cytosol what leads to activation of caspases cascade and apoptosis induction (**Figure 6**) [91].

Based on the data that were presented in this section, it could be said that the mechanisms involved in M-IONPs toxicity are accumulation of iron ions, oxidative damage by generating reactive oxygen species, protein aggregation and apoptosis.

Mutagenic effects of M-IONPs on different murine and mammalian normal cell lines were clearly synthesized in an extensive review [103].

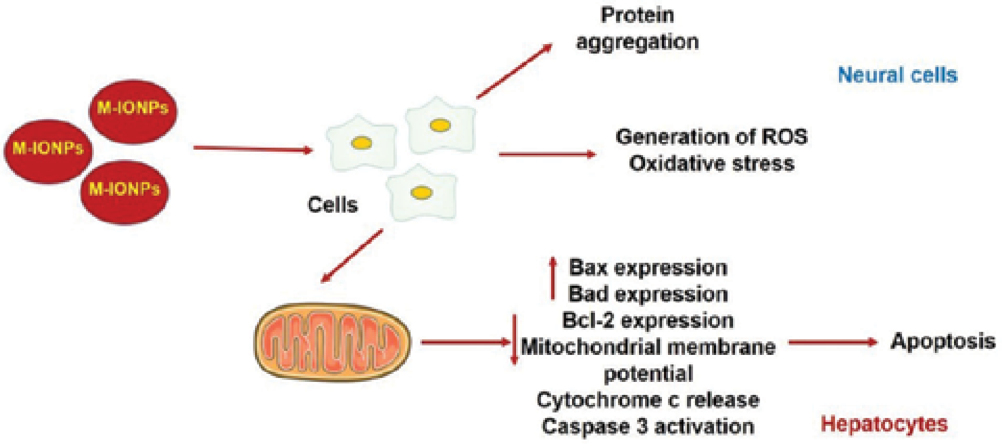

Figure 6. Mechanisms of toxicity induced by M-IONPs to normal cells (neural cells and hepatocytes): oxidative stress and apoptosis.

4.2. Magnetic iron oxide nanoparticles effect on cancer cells

SPIONs (superparamagnetic iron oxide nanoparticles) are the most frequently used iron oxide nanoparticles in the biomedical applications due to their proper size (range between 50 and 200 nm) and the magnetic properties responsible for the lack of particle aggregates *in vivo.* Another type of iron oxide nanoparticles is represented by USPIONs (ultra-small superparamagnetic iron oxide nanoparticles), which have a diameter lower than 50 nm. The mandatory features of M-IONPs that must be analyzed in order to establish the bioavailability and the possible interactions with endogenous compounds (proteins, immune system cells, etc.) are: (i) size (the recommendable size for biomedical applications is between 10 and 200 nm; the ones that are too big will be assimilated by liver and spleen cells, the ones that are too small will be filtrated by the kidneys and their life in the bloodstream is reduced); (ii) superparamagnetism and (iii) presence of a coating agent [104].

The affinity of liver, spleen, bone marrow and lymph nodes for SPIONs after their removal from the blood by the mononuclear phagocytic system (MPS) after intravenous administration represents the reason for the study of this type of nanoparticles as contrast agents but also for their use as delivery tools for chemotherapeutic agents. USPIONs due to their small size possess the capacity to escape macrophages of MPS surveillance and their circulation time is higher, but they also encounter macrophages in deeper compartments.

The changes concerning the surface of the nanoparticles by using a coating agent proved to exert multiple roles: to improve colloids stability, to enhance the bioavailability and the bloodstream half-life and to reduce precipitation and formation of conglomerates [104, 105]. M-IONPs were used as drug delivery agents and as contrast agents based on their potential to activate at cellular and molecular levels [105].

Due to the multiple applications of M-IONPs in biomedical fields (drug delivery, as contrast agents, hyperthermia treatment), it was also verified the effects of the hollow nanoparticles (without payload) on different tumor cell lines.

As mentioned in the previous section, M-IONPs mediate DNA lesions in normal cells, and this property is also exerted in the case of tumor cells. The effect observed was dose-dependent and time-dependent and consisted of damage of tail length and DNA strand breaks. The results were similar in all the tumor cell lines tested: human breast cancer cell line (MCF-7), human fibrosarcoma cells, lung cancer and cervix carcinoma cells [103].

Another mechanism of M-IONPs by which are able to harm cancer cells is represented by the ability to induce magnetic hyperthermia in the form of heat generated by the release of energy after applying a high-frequency alternating magnetic field. The principle of action of this technique consists in raising the cell temperature abnormally to 41–45°C, which leads to significant detrimental effects that can be reversible in the case of normal cells whereas irreversible for cancer cells [105].

A novel proposed mechanism for M-IONPs-induced cell death is enucleation described by Paunescu and coworkers, process observed after exposure of breast cancer cells (MCF-7) and human melanoma (SK-BR-3) to magnetic iron oxide nanoparticles obtained by combustion synthesis [106]. The enucleation phenomena is well described for erythroid terminal differentiation process and there is also used a term in the literature "enucleation sign" that is specific for enhanced computed tomographic images of the ruptured hepatocellular carcinoma. The definition for this term is "the separation of tumor content with intraperitoneal rupture into the perihepatic space, which is seen as low attenuating lesion from peripheral enhancing rim on arterial phase imaging" [107]. The process observed by Paunescu et al. was described as a non-physiological process and it was unrelated with the process described for erythroblast enucleation [106].

The M-IONPs proved a cytotoxic effect against murine melanoma cells B16, cytotoxicity evaluated by the means of MTT viability assay [108].

Other mechanisms of action as anticancer agents may be attributed to M-IONPs, mechanisms that are related with the effects induced by the chemotherapeutical agents loaded in the engineered nanoparticles. The large surface-to-volume ratio characteristic for M-IONPs make them suitable to adsorb proteins or load drugs and attractive for *in vivo* applications, such as MRI, drug and gene delivery, cancer treatment, hard tissue repair and tissue engineering and biosensors [105].

Recent studies mention the use of M-IONPs as improved contrast agents in the diagnosis of cardiovascular pathologies, mainly in atherosclerosis for detection of unstable plaques by the means of MRI (magnetic resonance imaging) [104]. The commercial products based on M-IONPs applied as contrast agents in MRI are: Ferumoxytol (Feraheme—detection of primary tumors and cancer lymph node metastasis), Ferumoxides (Feridex—detection of liver lesions), Ferucarbotran (Resovist—detection of small focal liver lesions), Ferumoxtran—10 (Combidex or Sinerem—detection of metastatic disease in lymph nodes), etc. [104]. Some of these products are included in clinical trials for additional effects, such as Endorem—for tracking monocytes and inflammation cells, Feridex—to keep track of adult bone marrow-derived stromal cells for severe cases of Multiple Sclerosis therapy and Supravist (ferucarbotran—small size nanoparticles)—as enhancing blood pool agent [104, 109].

5. Concluding remarks

The intrinsic magnetic properties, the biocompatibility and biodegradability and the capacity to respond to an external magnetic field are unique features that recommend magnetic iron oxide nanoparticles as promising nanomaterials in biomedical applications. The recent advances in this field led to the synthesis of engineered and targeted M-IONPs that might be successfully applied for smart therapies, including controlled drug release, hyperthermia treatment, magnetofection and gene delivery, mapping of lymph nodes and tissue engineering. M-IONPs could be considered theranostics tools based on their capacity to combine their use in diagnostic, treatment and follow-up of a pathology. Despite all these beneficial effects, an important matter should be taken into consideration when M-IONPs are administered *in vivo*, this matter consisting in the thorough analysis of the factors that might induce toxic reactions like size, charge, coating agent, functional groups and shape. There are still some challenges to achieve M-IONPs optimum efficacy and safety, but the existent drawbacks can be corrected by the improvement of their properties by the means of appropriate methods, further studies and inclusion in clinical trials.

Acknowledgements

This work was supported by a grant of Minister of Research and Innovation, CNCS-UEFISCDI, project number PN-III-P4-ID-PCE-2016-0765, within PNCDI III.

Author details

Elena-Alina Moacă[1], Elena Dorina Coricovac[1]*, Codruta Marinela Soica[1],
Iulia Andreea Pinzaru[1], Cornelia Silvia Păcurariu[2] and Cristina Adriana Dehelean[1]

*Address all correspondence to: dorinacoricovac@umft.ro

1 Faculty of Pharmacy, "Victor Babes" University of Medicine and Pharmacy, Timisoara, Romania

2 Faculty of Industrial Chemistry and Environmental Engineering, Politehnica University of Timisoara, Romania

References

[1] Reddy LH et al. Magnetic nanoparticles: Design and characterization, toxicity and biocompatibility, pharmaceutical and biomedical applications. Chemical Reviews. 2012;**112**:5818-5878

[2] Colombo M et al. Biological applications of magnetic nanoparticles. Chemical Society Reviews. 2012;**41**:4306-4334

[3] Shete PB et al. Water dispersible oleic acid-coated Fe_3O_4 nanoparticles for biomedical applications. Journal of Magnetism and Magnetic Materials. 2015;**377**:406-410

[4] Bica D. Preparation of magnetic fluids for various applications. Romanian Reports in Physics. 1995;**47**(3-5):265-272

[5] Mahmoudi H, Jafari AA. Facial preparation of sulfonic acid-functionalized magnetite-coated maghemite as a magnetically separable catalyst for pyrrole synthesis. ChemCatChem. 2013;**5**:3743-3749

[6] Wang YM et al. Synthesis of Fe_3O_4 magnetic fluid used for magnetic resonance imaging and hyperthermia. Journal of Magnetism and Magnetic Materials. 2011;**323**:2953-2959

[7] Cho M et al. Assembly of iron oxide nanocubes for enhanced cancer hyperthermia and magnetic resonance imaging. Nanomaterials. 2017;**7**(72):1-12

[8] Estelrich J et al. Iron oxide nanoparticles for magnetically-guided and magnetically-responsive drug delivery. International Journal of Molecular Sciences. 2015;**16**:8070-8101

[9] Lee JY et al. Low-density lipoprotein-mimicking nanoparticles for tumor-targeted theranostic applications. Small. 2015;**11**:222-231

[10] Hola K et al. Tailored functionalization of iron oxide nanoparticles for MRI, drug delivery, magnetic separation and immobilization of biosubstances. Biotechnology Advances. 2015;**33**(6-2):1162-1176

[11] Păcurariu C et al. Synthesis and characterization of gamma-Fe_2O_3/SiO_2 composites as possible candidates for magnetic paper manufacture. Ceramics International. 2015;**41**(1):1079-1085

[12] Gao D et al. Preparation and characterization of a new white magnetic paper. Materials Letters. 2014;**137**:487-490

[13] Tang L et al. Synergistic adsorption and reduction of hexavalent chromium using highly uniform polyaniline-magnetic mesoporous silica composite. Chemical Engineering Journal. 2014;**254**:302-312

[14] Stoia M et al. Solvothermal synthesis of magnetic Fe_xO_y/C nanocomposites used as adsorbents for the removal of methylene blue from wastewater. Journal of Thermal Analysis and Calorimetry. 2015;**121**:989-1001

[15] Shen X et al. One-step synthesis of water-dispersible cysteine functionalized magnetic Fe_3O_4 nanoparticles for mercury (II) removal from aqueous solutions. Applied Surface Science. 2014;**317**:1028-1034

[16] Majewski P, Thierry B. Functionalized magnetite nanoparticles—Synthesis, properties, and bio-applications. Critical Reviews in Solid State and Materials Sciences. 2007;**32**(3-4):203-215

[17] Collingwood JF, Telling ND. Chapter 7 – Iron oxides in the human brain. In: Faivre D, editor. Iron Oxides from Nature to Applications. Germany: Wiley-VCH; 2016. p. 143

[18] Crespo RG et al. Vacancy ordering and electronic structure of γ-Fe_2O_3 (maghemite): A theoretical investigation. Journal of Physics Condensed Matter. 2010;**22**(25):255401

[19] Cuenca JA et al. Study of the magnetite to maghemite transition using microwave permittivity and permeability measurements. Journal of Physics Condensed Matter. 2016; **28**(10):106002

[20] Woo K, Lee HJ. Synthesis and magnetism of hematite and maghemite nanoparticles. Journal of Magnetism and Magnetic Materials. 2004;**272**:1155

[21] Genuzio F et al. Phase transformations in thin iron oxide films: Spectromicroscopic study of velocity and shape of the reaction fronts. Surface Science. 2016;**648**:177-187

[22] Cornell RM, Schwertmann U. Chapter 2 – Crystal structure, In: The Iron Oxides: Structure, Properties, Reactions, Occurrences and Uses, 2nd ed., Weinheim: Wiley-VCH Verlag GmbH & Co. KGaA; 2003. p. 9

[23] Issa B et al. Magnetic nanoparticles: Surface effects and properties related to biomedicine applications. International Journal of Molecular Sciences. 2013;**14**(11):21266-21305

[24] Kuncser V et al. Chapter 7 – Engineering magnetic properties of nanostructures via size effects and interphase interactions. In: Kuncser V, Miu L, editors. Size Effects in Nanostructures: Basic and Applications. Berlin Heidelberg: Springer-Verlag; 2014. p. 169

[25] Krishnan KM. Biomedical nanomagnetics: A spin through possibilities in imaging, diagnostics, and therapy. IEEE Transactions on Magnetics. 2010;**46**(7):2523-2558

[26] Tombácz E et al. Magnetic iron oxide nanoparticles: Recent trends in design and synthesis of magnetoresponsive nanosystems. Biochemical and Biophysical Research Communications. 2015;**468**(3):442-453

[27] O'Mahony JJ et al. Synthesis of superparamagnetic particles with tunable morphologies: The role of nanoparticle-nanoparticle interactions. Langmuir. 2013;**29**(8):2546-2553

[28] Mahmoudi M et al. Superparamagnetic iron oxide nanoparticles (SPIONs): Development, surface modification and applications in chemotherapy. Advanced Drug Delivery Reviews. 2011;**63**(1-2):24-46

[29] Osaka T et al. Effect of surface charge of magnetite nanoparticles on their internalization into breast cancer and umbilical vein endothelial cells. Colloids and Surfaces. B, Biointerfaces. 2009;**71**(2):325-330

[30] Cornell RM, Schwertmann U. Chapter 14 – Transformation. In: The Iron Oxides: Structure, Properties, Reactions, Occurrences and Uses. 2nd ed. Weinheim: Wiley-VCH Verlag GmbH & Co. KGaA; 2003. p. 365

[31] Peng XH et al. Targeted magnetic iron oxide nanoparticles for tumor imaging and therapy. International Journal of Nanomedicine. 2008;**3**(3):311-321

[32] Salavati-Niasari M et al. Easy synthesis of magnetite nanocrystals via coprecipitation method. Journal of Cluster Science. 2012;**23**:597

[33] Liu Y et al. Studies of Fe_3O_4-chitosan nanoparticles prepared by co-precipitation under the magnetic field for lipase immobilization. Catalysis Communications. 2011;**12**:717

[34] Wang Y et al. Solvent-free atom transfer radical polymerization in the synthesis of Fe_2O_3@polystyrene core–shell nanoparticles. Nano Letters. 2003;**3**(6):789-793

[35] Sun YK et al. Synthesis of nanometer-size maghemite particles from magnetite. Colloids and Surfaces A: Physicochemical and Engineering Aspects. 2004;**245**:15-19

[36] Wu W et al. Preparation and characterization of magnetite Fe_3O_4 nanopowders. Rare Metal Materials and Engineering. 2007;**36**(3):238-243

[37] Martinez-Mera I et al. Synthesis of magnetite (Fe_3O_4) nanoparticles without surfactants at room temperature. Materials Letters. 2007;**61**:4447-4451

[38] Hui C et al. Large-scale Fe_3O_4 nanoparticles soluble in water synthesized by a facile method. The Journal of Physical Chemistry. B. 2008;**112**(30):11336-11339

[39] Khalil MI. Co-precipitation in aqueous solution synthesis of magnetite nanoparticles using iron (III) salts as precursors. Arabian Journal of Chemistry. 2015;**8**(2):279-284

[40] Massart R. Preparation of aqueous magnetic liquids in alkaline and acidic media. IEEE Transactions on Magnetics. 1981;**17**(2):1247-1248

[41] Baumgartner J et al. Nucleation and growth of magnetite from solution. Nature Materials. 2013;**12**(4):310-314. DOI: 10.1038/nmat3558

[42] Thanh NTK et al. Mechanisms of nucleation and growth of nanoparticles in solution. Chemical Reviews. 2014;**114**:7610-7630

[43] Jiang WQ et al. Preparation and properties of superparamagnetic nanoparticles with narrow size distribution and biocompatible. Journal of Magnetism and Magnetic Materials. 2004;**283**(2-3):210-214

[44] Tartaj P, et al. Synthesis, properties and biomedical applications of magnetic nanoparticles. In: Handbook of Magnetic Materials. Amsterdam: Elsevier; 2006. p. 403

[45] Roth HC et al. Influencing factors in the co-precipitation process of superparamagnetic iron oxide nanoparticles: A model based study. Journal of Magnetism and Magnetic Materials. 2015;**377**:81-89

[46] Wu S et al. Fe_3O_4 magnetic nanoparticles synthesis from tailings by ultrasonic chemical co-precipitation. Materials Letters. 2011;**65**:1882

[47] Pereira C et al. Superparamagnetic MFe_2O_4 (M = Fe, Co, Mn) nanoparticles: Tuning the particle size and magnetic properties through a novel one-step coprecipitation route. Chemistry of Materials. 2012;**24**:1496

[48] Li Z et al. Direct coprecipitation route to monodisperse dual functionalized magnetic iron oxide nanocrystals without size selection. Small. 2008;**4**:231-239

[49] Sun S, Zeng H. Size-controlled synthesis of magnetite nanoparticles. Journal of the American Chemical Society. 2002;**124**(28):8204-8205

[50] Hyeon T. Chemical synthesis of magnetic nanoparticles. Chemical Communications. 2003;**8**:927-934

[51] Xu Z et al. Organic phase synthesis of monodisperse iron oxide nanocrystals using iron chloride as precursor. Nanoscale. 2010;**2**(6):1027-1032

[52] Wang Y et al. One-pot reaction to synthesize superparamagnetic iron oxide nanoparticles by adding phenol as reducing agent and stabilizer. Journal of Nanoparticle Research. 2012;**14**:755

[53] Maity D et al. Synthesis of magnetite nanoparticles via a solvent-free thermal decomposition route. Journal of Magnetism and Magnetic Materials. 2009;**321**:1256-1259

[54] Asuha S et al. One step synthesis of maghemite nanoparticles by direct thermal decomposition of Fe-urea complex and their properties. Journal of Alloys and Compounds. 2009;**472**:L23-L25

[55] Hu M et al. Prussian blue microcrystals prepared by selective etching and their conversion to mesoporous magnetic iron(III) oxides. Chemical Communications. 2010;**46**(7):1133

[56] Hu M et al. Hierarchical magnetic iron (III) oxides prepared by solid-state thermal decomposition of coordination polymers. RSC Advances. 2012;**2**(11):4782

[57] Amara D, Margel S. Solvent less thermal decomposition of ferrocene as a new approach for the synthesis of porous superparamagnetic and ferromagnetic composite microspheres of narrow size distribution. Journal of Materials Chemistry. 2011;**21**(39):15764

[58] Pérez-Mirabet L et al. One-pot synthesis of stable colloidal solutions of MFe_2O_4 nanoparticles using oleylamine as solvent and stabilizer. Materials Research Bulletin. 2013;**48**(3):966-972

[59] Amara D et al. Solventless thermal decomposition of ferrocene as a new approach for one-step synthesis of magnetite nanocubes and nanospheres. Journal of Materials Chemistry. 2012;**22**(5):2188

[60] Lynch J et al. Gas-bubble effects on the formation of colloidal iron oxide nanocrystals. Journal of the American Chemical Society. 2011;**133**:12664-12674

[61] Han LH et al. In situ synthesis of hematite nanoparticles using a low-temperature microemulsion method. Powder Technology. 2011;**207**:42-46

[62] Wongwailikhit K, Horwongsakul S. The preparation of iron (III) oxide nanoparticles using w/o microemulsion. Materials Letters. 2011;**65**:2820-2822

[63] Malik MA et al. Microemulsion method: A novel route to synthesize organic and inorganic nanomaterials. 1st nano update. Arabian Journal of Chemistry. 2012;**5**(4):397-417

[64] Lu T et al. Surfactant effects on the microstructures of Fe_3O_4 nanoparticles synthesized by microemulsion method. Colloids and Surfaces A: Physicochemical and Engineering Aspects. 2013;**436**:675-683

[65] Ladj R et al. Individual inorganic nanoparticles: Preparation, functionalization and *in vitro* biomedical diagnostic applications. Journal of Materials Chemistry B. 2013;**1**(10):1381

[66] Tan TTY et al. Microemulsion preparative methods (overview). Comprehensive Nanoscience and Technology. 2011;**5**:399-441

[67] Li Y et al. Single-microemulsion-based solvothermal synthesis of magnetite microflowers. Ceramics International. 2014;**40**(3):4791-4795

[68] Okoli C et al. Application of magnetic iron oxide nanoparticles prepared from microemulsions for protein purification. Journal of Chemical Technology and Biotechnology. 2011;**86**(11):1386-1393

[69] Okoli C et al. Comparison and functionalization study of microemulsion-prepared magnetic iron oxide nanoparticles. Langmuir. 2012;**28**(22):8479-8485

[70] Wu W et al. Magnetic iron oxide nanoparticles: Synthesis and surface functionalization strategies. Nanoscale Research Letters. 2008;**3**(11):397-415

[71] Ge S et al. Facile hydrothermal synthesis of iron oxide nanoparticles with tunable magnetic properties. Journal of Physical Chemistry C. 2009;**113**:13593-13599

[72] Wang J et al. Synthesis of monodisperse nanocrystals of high crystallinity magnetite through solvothermal process. Materials Chemistry and Physics. 2009;**113**:6-9

[73] Kawai-Nakamura A et al. Rapid and continuous hydrothermal synthesis of metal and metal oxide nanoparticles with a microtube-reactor at 523 K and 30 MPa. Materials Letters. 2008;**62**(19):3471-3473

[74] Lin X et al. Formation mechanism and magnetic properties of hollow Fe_3O_4 nano-spheres synthesized without any surfactant. CrystEngComm. 2012;**14**(24):8658-8663

[75] Tian Y et al. Facile solvothermal synthesis of monodisperse Fe_3O_4 nanocrystals with precise size control of one nanometre as potential MRI contrast agents. Journal of Materials Chemistry. 2011;**21**(8):2476

[76] Ahmadi S et al. Synthesis of Fe_3O_4 nanocrystals using hydrothermal approach. Journal of Magnetism and Magnetic Materials. 2012;**324**(24):4147-4150

[77] Jung CH. Sintering characterization of Li_2TiO_3 ceramic breeder powders prepared by the solution combustion synthesis process. Journal of Nuclear Materials. 2005;**341**(2-3): 148-152

[78] Manukyan KV et al. Solution combustion synthesis of nano-crystalline metallic materials: Mechanistic studies. Journal of Physical Chemistry C. 2013;**117**(46):24417-24427

[79] Jadhav LD et al. Solution combustion synthesis: Role of oxidant to fuel ratio on powder properties. Materials Sciences Forum. 2013;**757**:85-98

[80] Ianos R et al. Solution combustion synthesis and characterization of magnetite, Fe_3O_4, nanopowders. Journal of the American Ceramic Society. 2012;**95**(7):2236-2240

[81] Mihoc G et al. Adsorption of phenol and p-chlorophenol from aqueous solutions by magnetic nanopowder. Water Science and Technology. 2014;**69**(2):385-391

[82] Mihoc G et al. Combustion synthesis of some iron oxides used as adsorbents for phenol and p-chlorophenol removal from wastewater. Journal of Thermal Analysis and Calorimetry. 2013;**112**:391-397

[83] Ianos R et al. γ-Fe_2O_3 nanoparticles prepared by combustion synthesis, followed by chemical oxidation of residual carbon with H_2O_2. Materials Chemistry and Physics. 2014;**148**:705-711

[84] Rudakovskaya PG et al. Synthesis and characterization of PEG-Silane functionalized iron oxide (II, III) nanoparticles for biomedical application. Nanotechnology in Russia. 2015;**10**(11-12):896-903

[85] Ulbrich K et al. Targeted drug delivery with polymers and magnetic nanoparticles: Covalent and noncovalent approaches. Chemical Reviews. 2016;**116**:5338-5431

[86] Montazerabadi AR, et al. Development of gold-coated magnetic nanoparticles as a potential MRI contrast agent. NANO: Brief Reports and Reviews. 2015;**10**(4):1550048-1550059

[87] Mahmoudi M, Serpooshan V. Silver-coated engineered magnetic nanoparticles are promising for the success in the fight against antibacterial resistance threat. ACS Nano. 2012;**6**(3):2656-2664

[88] Yang L et al. One-pot synthesis of aldehyde-functionalized mesoporous silica-Fe_3O_4 nanocomposites for immobilization of penicillin G acylase. Microporous and Mesoporous Materials. 2014;**197**:1-7

[89] Lee HJ et al. Photothermal cancer therapy using graphitic carbon–coated magnetic particles prepared by one-pot synthesis. International Journal of Nanomedicine. 2015;**10**:271-282

[90] Zhang CW et al. Preparation and characterization of surface-functionalization of silica-coated magnetite nanoparticles for drug delivery. NANO: Brief Reports and Reviews. 2014;**9**(4):1450042-1450050

[91] Yarjanli Z et al. Iron oxide nanoparticles may damage to the neural tissue through iron accumulation, oxidative stress, and protein aggregation. BMC Neuroscience. 2017;**18**(1):51. DOI: 10.1186/s12868-017-0369-9

[92] Farshbaf MJ, Ghaedi K. Does any drug to treat cancer target mTOR and iron hemostasis in neurodegenerative disorders? Biometals. 2017;**30**(1):1-16. DOI: 10.1007/s10534-016-9981-x

[93] Pinkernelle J et al. Magnetic nanoparticles in primary neural cell cultures are mainly taken up by microglia. BMC Neuroscience. 2012;**13**:32. DOI: 10.1186/1471-2202-13-32

[94] Mazuel F et al. Massive intracellular biodegradation of iron oxide nanoparticles evidenced magnetically at single-endosome and tissue levels. ACS Nano. 2016;**10**:7627-7638

[95] Pongrac IM et al. Oxidative stress response in neural stem cells exposed to different superparamagnetic iron oxide nanoparticles. International Journal of Nanomedicine. 2016;**11**:1701-1715

[96] Calero M et al. Efficient and safe internalization of magnetic iron oxide nanoparticles: Two fundamental requirements for biomedical applications. Nanomedicine: Nanotechnology, Biology, and Medicine. 2014;**10**:733-743. DOI: 10.1016/j.nano.2013.11.010

[97] Wu W et al. Recent progress on magnetic iron oxide nanoparticles: synthesis, surface functional strategies and biomedical applications. Science and Technology of Advanced Materials. 2015;**16**:023501 (43 p). DOI: 10.1088/1468-6996/16/2/023501

[98] Li L et al. Comparative *In Vitro* cytotoxicity study on uncoated magnetic nanoparticles: Effects on cell viability, cell morphology, and cellular uptake. Journal for Nanoscience and Nanotechnology. 2012;**12**:1-8. DOI: 10.1166/jnn.2012.6755

[99] Cortajarena AL et al. Engineering iron oxide nanoparticles for clinical settings. Nano. 2014;**1**(2):1-20

[100] Coricovac DE et al. Biocompatible colloidal suspensions based on magnetic iron oxide nanoparticles: Synthesis, characterization and toxicological profile. Frontiers in Pharmacology. 2017;**8**:154. DOI: 10.3389/fphar.2017.00154

[101] Shelat R et al. Detailed toxicity evaluation of β-cyclodextrin coated iron oxide nanoparticles for biomedical applications. International Journal of Biological Macromolecules. 2018;**110**:357-365. DOI: 10.1016/j.ijbiomac.2017.09.067

[102] Bostan HB et al. Cardiotoxicity of nano-particles. Life Sciences. 2016;**165**:91-99. DOI: 10.1016/j.lfs.2016.09.017

[103] Dissanayake NM et al. Mutagenic effects of iron oxide nanoparticles on biological cells. International Journal of Molecular Sciences. 2015;**16**(10):23482-23516. DOI: 10.3390/ijms161023482

[104] Montiel Schneider MG, Lassalle VL. Magnetic iron oxide nanoparticles as novel and efficient tools for atherosclerosis diagnosis. Biomedicine & Pharmacotherapy. 2017;**93**:1098-1115. DOI: 10.1016/j.biopha.2017.07.012

[105] Mohammed L, et al. Magnetic nanoparticles for environmental and biomedical applications: A review. Particuology. 2017;**30**:1-14. DOI: 10.1016/j.partic.2016.06.001

[106] Paunescu V et al. Enucleation: A possible mechanism of cancer cell death. Journal of Cellular and Molecular Medicine. 2014;**18**(6):962-965. DOI: 10.1111/jcmm.12271

[107] Singhal M et al. Enucleation sign: A computed tomographic appearance of ruptured hepatocellular carcinoma. Journal of Clinical and Experimental Hepatology. 2016;**6**(4):335-336. DOI: 10.1016/j.jceh.2016.05.004

[108] Zavisova V et al. The cytotoxicity of iron oxide nanoparticles with different modifications evaluated *in vitro*. Journal of Magnetism and Magnetic Materials. 2015;**380**:85-89

[109] Available from: https://clinicaltrials.gov/ct2/show/NCT01169935?term=Endorem&rank=9

Chapter 13

Bandgap-Engineered Iron Oxides for Solar Energy Harvesting

Munetoshi Seki

Additional information is available at the end of the chapter

http://dx.doi.org/10.5772/intechopen.73227

Abstract

Epitaxial films of Rh-substituted α-Fe_2O_3 were fabricated by a pulsed laser deposition technique, and their photoelectrochemical characteristics were investigated for the development of visible light-responsive photoanodes for water splitting. The photocurrent in the films upon irradiation in the visible region was significantly enhanced after Rh substitution. Moreover, a near-infrared photocurrent was clearly observed for Rh:Fe_2O_3 photoanodes, whereas no photoresponse could be detected for the α-Fe_2O_3 films. These improved photoelectrochemical properties are attributed to the increased light absorption due to the hybridization of Rh-4*d* states and O-2*p* states at the valence band maximum. Moreover, Rh substitution also strongly influences the photocarrier transport properties of the films. The electrical conductivity of Rh:Fe_2O_3 is higher than that for α-Fe_2O_3 by two orders of magnitude, which is possibly due to the extended 4*d* orbitals of the Rh^{3+} ions. Thus, the improved electrical properties may lead to an increased photocurrent by lowering the recombination rate of photogenerated carriers.

Keywords: solar water splitting, pulsed laser deposition, photoelectrochemical cell, iron oxides, bandgap engineering

1. Introduction

Iron oxides are well known to have various physical properties depending on their composition and crystal structures (see **Table 1**). They have been the subject of extensive investigation over the past decades from both fundamental and practical perspectives. For example, magnetite (Fe_3O_4) has been one of the most widely investigated oxides in various research fields owing to its high magnetic transition temperature (~585°C) and high spin polarization of carriers [1–3]. Numerous Fe_3O_4-based ferromagnetic semiconductors and related spintronics

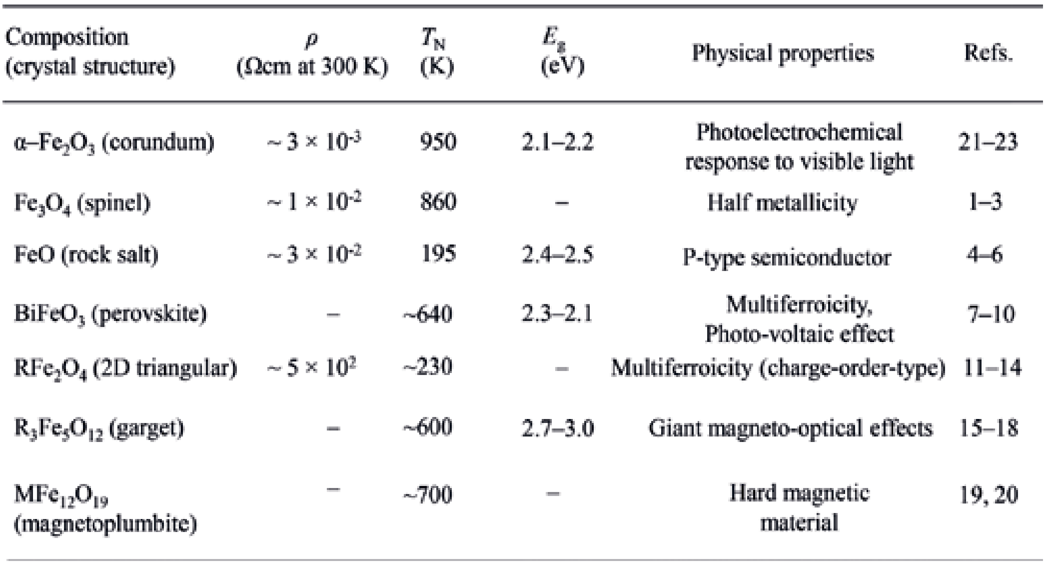

Composition (crystal structure)	ρ (Ωcm at 300 K)	T_N (K)	E_g (eV)	Physical properties	Refs.
α–Fe_2O_3 (corundum)	~ 3×10^{-3}	950	2.1–2.2	Photoelectrochemical response to visible light	21–23
Fe_3O_4 (spinel)	~ 1×10^{-2}	860	–	Half metallicity	1–3
FeO (rock salt)	~ 3×10^{-2}	195	2.4–2.5	P-type semiconductor	4–6
$BiFeO_3$ (perovskite)	–	~640	2.3–2.1	Multiferroicity, Photo-voltaic effect	7–10
RFe_2O_4 (2D triangular)	~ 5×10^{2}	~230	–	Multiferroicity (charge-order-type)	11–14
$R_3Fe_5O_{12}$ (garget)	–	~600	2.7–3.0	Giant magneto-optical effects	15–18
$MFe_{12}O_{19}$ (magnetoplumbite)	–	~700	–	Hard magnetic material	19, 20

Table 1. Various types of iron oxide and their physical properties (ρ: electrical resistivity, T_N: Néel temperature, and E_g: bandgap energy).

devices have been reported. Another simple iron oxide, wüstite (FeO) has attracted much attention in various fields such as Earth sciences, oxide electronics, spintronics, and chemical engineering [4–6]. Moreover, multifunctional bismuth ferrite ($BiFeO_3$, BFO) has been of great interest owing to its potential applications in numerous room temperature multiferroic devices [7–9]. BFO is also considered to be a good candidate for use in solar energy conversion systems because of its electrical polarization-induced photovoltaic effects [10]. The triangular antiferromagnet RFe_2O_4 (R = Ho, Y, Yb, Lu, and In) is a multilayered oxide and was discovered in the 1970s by Kimizuka et al. [11]. RFe_2O_4 is composed of alternating hexagonal Fe—O and R—O layers stacked along the *c*-axis, and Fe^{2+}/Fe^{3+} charge order occurs in the Fe—O layers below 320 K, which is followed by magnetic ordering below ~240 K [12]. Recently, a number of studies on RFe_2O_4 have been stimulated by the discovery of the giant magnetoelectric response in $LuFe_2O_4$ and its application to multiferroic devices is currently the subject of extensive investigations [13, 14]. A great number of investigations on the magneto-optical (MO) properties of garnet-type ferrites ($R_3Fe_5O_{12}$) have been carried out for applications in the field of optical communications. They are currently recognized as the most promising materials in magnonics and related areas. Especially, they are widely used in ferromagnetic resonance experiments and magnon-based Bose-Einstein-condensates owing to their extremely low damping [15–18]. Furthermore, there has been much interest in hexaferrites, $MFe_{12}O_{19}$ (M = Ba and Sr) [19, 20], which are commonly applied in a wide variety of data storage and recording devices. One of the most favorable characteristics of the above iron oxides is their chemical stability, and they are also nontoxic. Moreover, iron and oxygen are abundant in the Earth. These features imply that iron oxides are favorable materials for applications in environmentally friendly electronics, spintronics, and magnonics. The author focuses on α-Fe_2O_3 commonly referred as a hematite, which is known as a promising candidate for semiconductor photoanodes for pho toelectrochemical (PEC) water splitting [21–23]. A schematic of a PEC cell is shown in **Figure 1**. They consist of a photoactive electrode and a metal counter electrode immersed in a suitable electrolyte solution. The photogenerated electron-hole pairs are split by the electric field in the space-charge region at the surface of photoelectrodes. Since Honda and Fujishima's pioneered work on PEC water splitting with a TiO_2 photoelectrode [24], there has been worldwide research focused on the solar generation of hydrogen as a renewable and clean energy source. Many kinds of materials including TiO_2 have been investigated for their application as photoelectrodes. However, most of them are wide-gap semiconductors, and only a small fraction of the solar spectrum can be utilized by the PEC cells based on these materials. A high PEC responsivity to visible (VIS) and near-infrared (near-IR) light is required to harvest the lower energy region of the solar spectrum. From this viewpoint, α-Fe_2O_3 has attracted much attention because of its promising properties for application as a photoanode in a solar water splitting cell. It possesses a narrow bandgap energy (E_g) of 2.1 eV that allows for the absorption of up to 40% of solar spectrum. However, the reported efficiencies for PEC water splitting using α-Fe_2O_3-based photoelectrodes are significantly low. This poor PEC property of α–Fe_2O_3

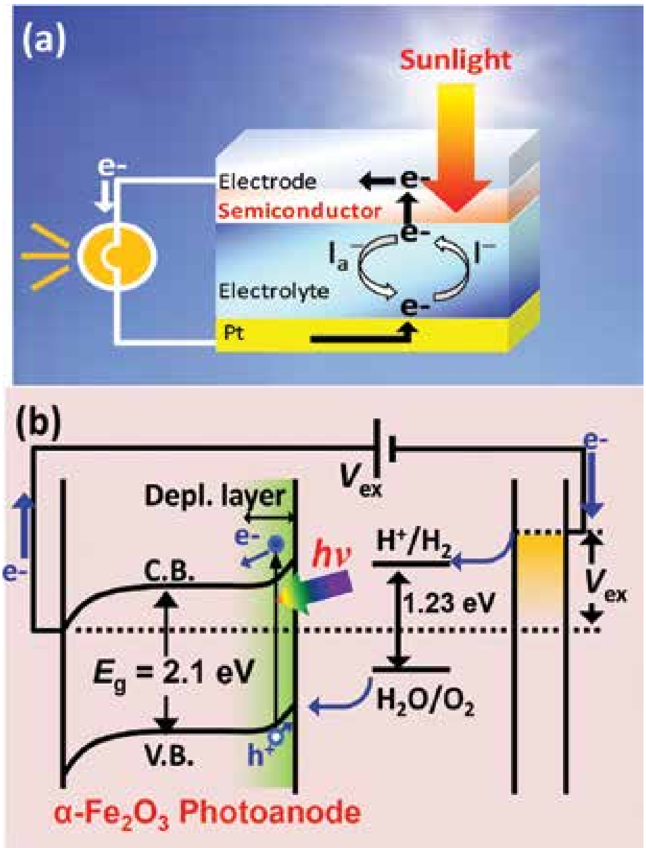

Figure 1. (a) Schematic of the photoelectrochemical (PEC) cell for solar water splitting and (b) electronic band structure of the PEC cell. Adapted by permission from Springer: Correlated Functional Oxides edited by H. Nishikawa, N. Iwata, T. Endo, Y. Takamura, G. Lee, and P. Mele (2017).

can be attributed to the short diffusion length of the photogenerated holes. For α–Fe_2O_3-based PEC cells, only the holes generated near the electrolyte/photoanode interface can oxidize water [25, 26]. That is, most of the photogenerated electron-hole pairs recombine before reaching the photoelectrode surface. The hematite lattice is composed of an alternating stack of Fe bilayers and O layers along c-axis as illustrated in **Figure 2**. Spins of Fe^{3+} ions within each bilayer are parallel, whereas adjacent Fe bilayers have opposite spins. 3d electrons of Fe can move by hopping via the change in the Fe^{2+}/Fe^{3+} valence within the Fe bilayers, whereas the exchange of electrons between neighboring Fe bilayers is spin forbidden [27–29]. Therefore, the orientation of a highly conducting (001) plane vertical to the substrate will facilitate the collection of photogenerated carriers and suppress their recombination. The author employed a Ta-doped SnO_2 (TTO) layer grown on α–Al_2O_3 (110) single-crystal substrates for the epitaxial growth of α–Fe_2O_3 films along the [110] direction. As shown in **Figure 3(a)**, the SnO_2 (101) plane matches the α–Fe_2O_3 (110) plane with a lattice mismatch of approximately 1.3%, which is favorable for the epitaxial growth of hematite along the [110] direction on the $SnO_2(101)/\alpha$–$Al_2O_3(101)$ substrate [30]. Another issue regarding α-Fe_2O_3 concerns its low responsivity to near-IR light. It is well known that the photocurrent in α-Fe_2O_3 is maximized at a wavelength (λ) of ~350 nm, exhibits a significant decrease with increasing λ, and approaches zero at approximately 600 nm, corresponding to its bandgap [31]. An improvement of the PEC responsivity in VIS and near-IR regions by controlling the bandgap would be useful for solar energy harvesting. Unfortunately, there exist few reports on such bandgap engineering in α-Fe_2O_3. From this viewpoint, the author focused on Rh-substituted α-Fe_2O_3 (FRO). α-Rh_2O_3 has a bandgap E_g of

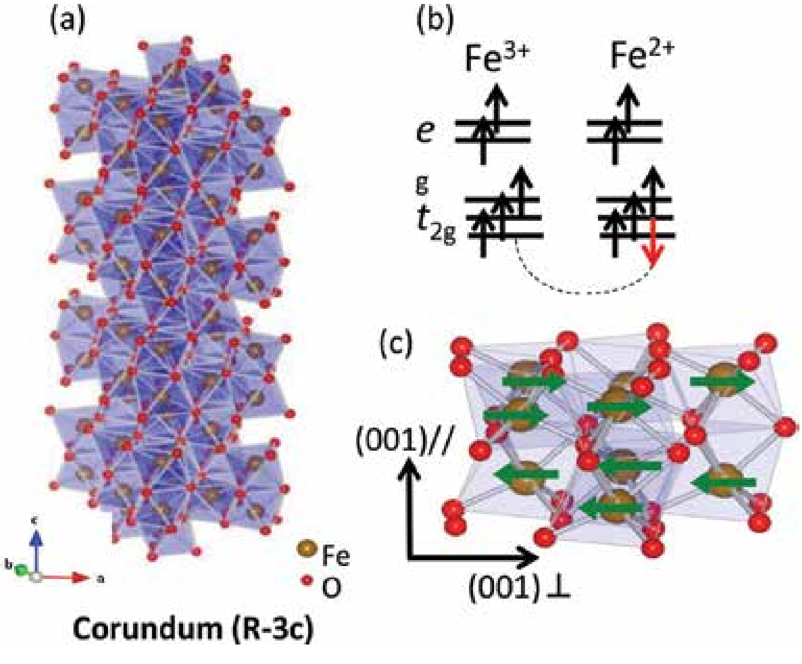

Figure 2. (a) Corundum-type crystal structure of α-Fe_2O_3. (b) The transport of electron in the Fe 3d band is schematically illustrated. (c) Antiferromagnetic spin coupling in α-Fe_2O_3. [Copyright (2014), The Japan Society of Applied Physics].

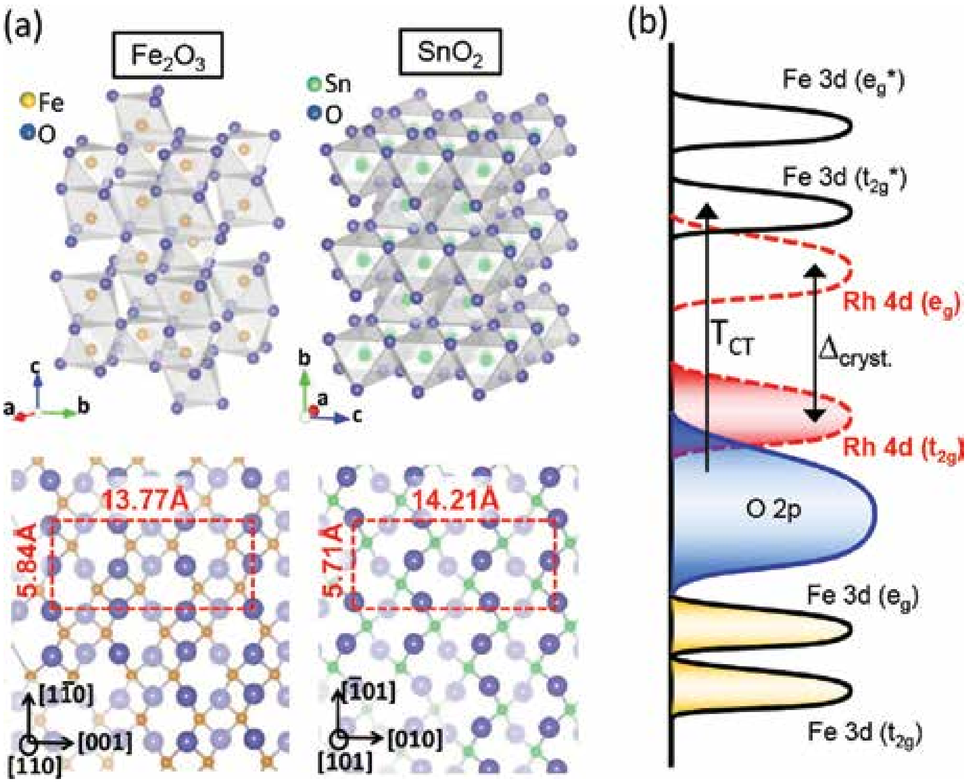

Figure 3. (a) Top: Crystal structures of α-Fe_2O_3 (corundum type) and SnO_2 (rutile type). Bottom: Schematic showing the in-plane atomic configuration of α-Fe_2O_3 and SnO_2. [Copyright (2012), The Japan Society of Applied Physics].

1.2–1.4 eV [32] and the same corundum-type crystal structure as α-Fe_2O_3. Therefore, the bandgap of α-Fe_2O_3 could be narrowed by Rh substitution in the films [33, 34]. **Figure 3(b)** shows a schematic of the band alignment of FRO [35, 36]. α-Fe_2O_3 is a charge transfer-type insulator with a bandgap between the Fe 3d state (upper Hubbard band) and the fully occupied O 2*p* state. In contrast, the bandgap of α-Rh_2O_3 originates from the ligand field splitting of the Rh 4*d* orbitals. The Rh 4*d* (t_{2g}) band in α-Rh_2O_3 lies near the O 2*p* band, and they effectively hybridize at the valence band maximum (VBM) [32, 37, 38]. In this chapter, the PEC characteristics of FRO photoanodes fabricated using pulsed laser deposition (PLD) are discussed in association with their electronic structures.

2. Experimental procedures

The FRO films were grown using a PLD technique with an argon fluoride (ArF) excimer laser (λ = 193 nm). The laser pulse frequency was 5 Hz. The fluence remained constant at 1.1 J/cm^2. The typical growth rate of the films was 0.5 nm/min. After deposition, the FRO films were annealed in air at 700°C to improve their crystallinity. The author employed two types of bottom electrodes, viz., TTO deposited onto an α-Al_2O_3 (110) substrate and polycrystalline fluorine-doped SnO_2 (FTO) formed on a soda-lime glass substrate. An $Fe_{2-x}Rh_xO_3$ (x = 0.0–2.0) pellet prepared by a solid-state reaction was used as a target for PLD. The growth temperature was kept at 700 and 800°C for the FRO and TTO films, respectively. The crystal structures of the samples were confirmed using X-ray diffraction (XRD). In the PEC measurement, the *I-V* properties were measured using an electrochemical analyzer under the illumination of Xe lamp (500 W). Optical measurements were conducted using a Vis-UV spectrometer. X-ray photoemission spectroscopy (XPS) was performed to evaluate the structure of the valence band (VB) in the FRO films.

3. Crystal structures

The XRD 2 theta-omega scan of the $FeRhO_3$ films is shown in **Figure 4(a)**. For the as-deposited sample, broad peaks are observed at 35 and 75°, which are ascribed to the (110) and (220)

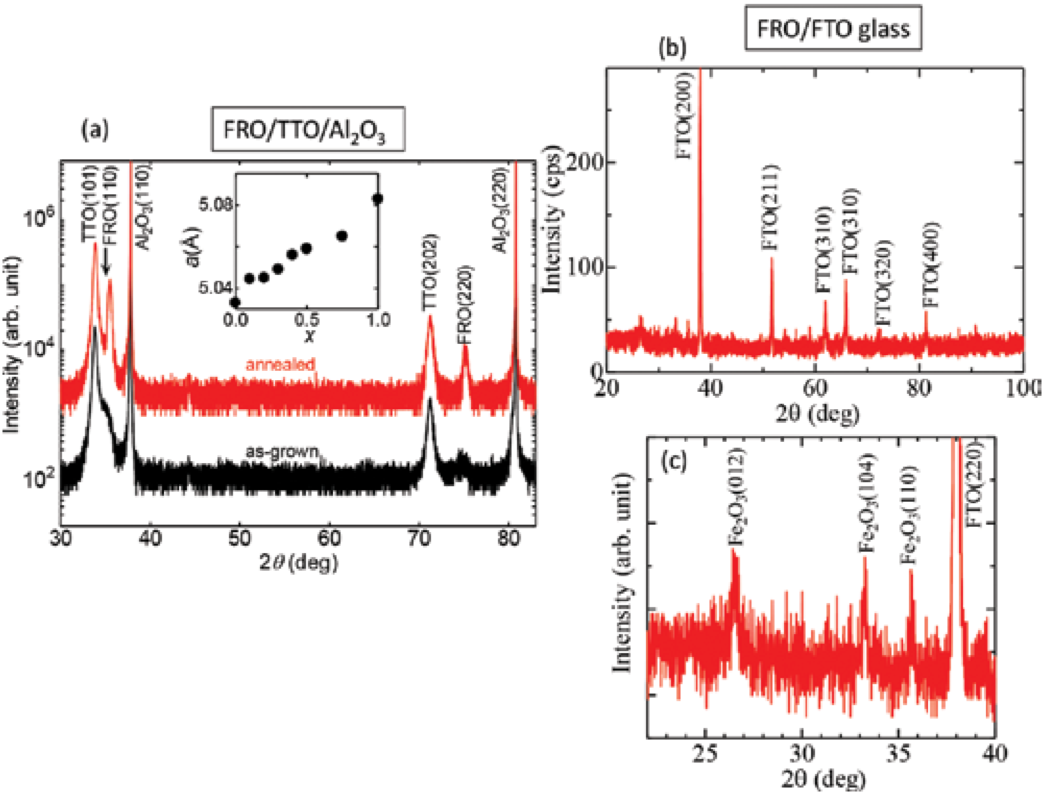

Figure 4. (a) XRD 2θ/ω scan of the FRO film (x = 1.0) grown on TTO/α-Al_2O_3(110). (b) XRD pattern of the FRO film (x = 0.2) grown on the FTO substrate. (c) Magnified image of the XRD pattern of (b). [Copyright (2012 and 2014), The Japan Society of Applied Physics].

reflections of corundum-type FRO, respectively. This indicates that the films grown along [110] despite their low crystalline quality. Sharp peaks appear after thermal annealing, suggesting an improvement in the crystallinity. The in-plane epitaxial relationship was evaluated to be TTO [010]//FRO [001] by in-plane XRD measurements. This result agrees with the atomic configurations in **Figure 3(a)** [30]. The lattice constants obey Vegard's law, implying that Fe had been appropriately substituted with Rh. In contrast to the films deposited onto the sapphire substrates, the films deposited on the glass substrates are polycrystalline in nature, as shown in **Figure 4(b)** and **(c)**.

4. Optical properties

Figure 5(a) shows the light absorption spectra of the films. The fundamental absorption edge of α-Fe_2O_3 is related to charge transfer from O 2*p* states to the upper Hubbard band promoted by photons [denoted by T_{CT} in **Figure 3(b)**]. For films with a higher Rh content, a broadband appears at 1.5–4.5 eV that is possibly related to α-Rh_2O_3. The optical transition in α-Rh_2O_3 is unclear; its absorption edge is considered to be associated with the *d*-*d* transition of Rh^{3+}, judging from the bandgap structure [31, 39]. **Figure 5(b)** shows the values of an indirect bandgap (E_g), which were derived from the Tauc relation, $\alpha h\nu \propto (h\nu - E_g)^2$ (α: optical absorption coefficient and $h\nu$: photon energy). E_g decreases as the content of Rh in the films increases according to the above discussion. Value of E_g of 2.1 and 1.2 eV were obtained for α-Fe_2O_3 and α-Rh_2O_3, respectively. These values are almost identical to those reported for polycrystalline films [40].

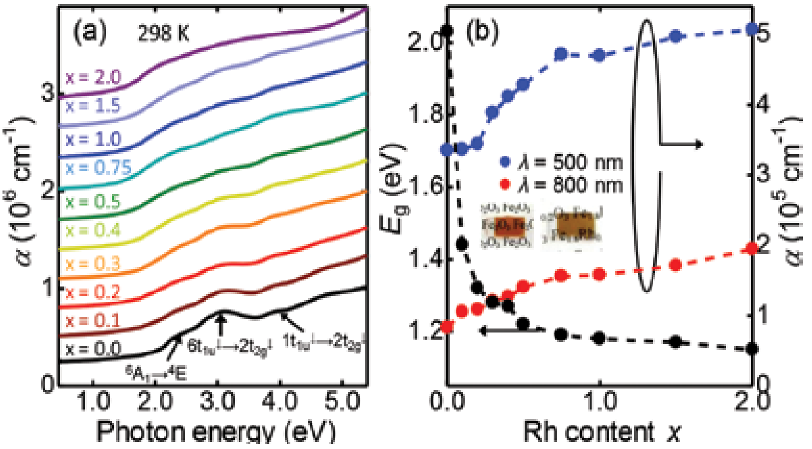

Figure 5. (a) Optical absorption coefficients as a function of the wavelength for FRO films on α-Al_2O_3(110) substrate at 298 K. For clarity, each spectrum is offset, with a spacing scaled to the composition. The peaks of α-Fe_2O_3 (x = 0.0) are assigned according to Ref. 19. (b) Compositional dependence of the indirect bandgap energy E_g and the absorption coefficients α at λ = 500 and 800 nm. The photographs of α-Fe_2O_3 (x = 0.0) and FRO (x = 0.2) films are inset. [Copyright (2012), The Japan Society of Applied Physics].

5. XPS spectroscopy

The results of XPS are presented in **Figure 6**. In the spectra of Fe 2*p* core level (**Figure 6(a)**), main peaks are at around 710 and 723 eV and are assigned to Fe $2p_{2/3}$ and $2p_{1/3}$ orbitals of α-Fe_2O_3, respectively [41–43]. These core level peaks become weaker as the Rh content increases. In turn, new distinct peaks appears at approximately 310 and 315 eV, which are assigned to Rh $3d_{3/2}$ and $3d_{5/2}$ orbitals, respectively [44, 45]. As seen in **Figure 6(c)**, the VBM of α-Fe_2O_3 is estimated to be 0.65 eV. In contrast, the VBM of α-Rh_2O_3 is located near the Fermi level (~0.0 eV). Three distinct peaks are observed in the VB spectrum of the films. The bands centered at 1, 2, and 3 eV in the VB spectrum of α-Fe_2O_3 are assigned to the Fe $3e_g$, $2t_g$, and $2e_g$ orbitals, respectively [46]. The crystal field splitting energy between the Fe $3e_g$ and $2t_g$ orbitals was estimated to be 2.5 eV in a previous study [47], which agrees with the experimental value (2.4 eV) well. In the VB spectrum of α-Rh_2O_3, three distinct peaks similarly appear. Unfortunately, there are

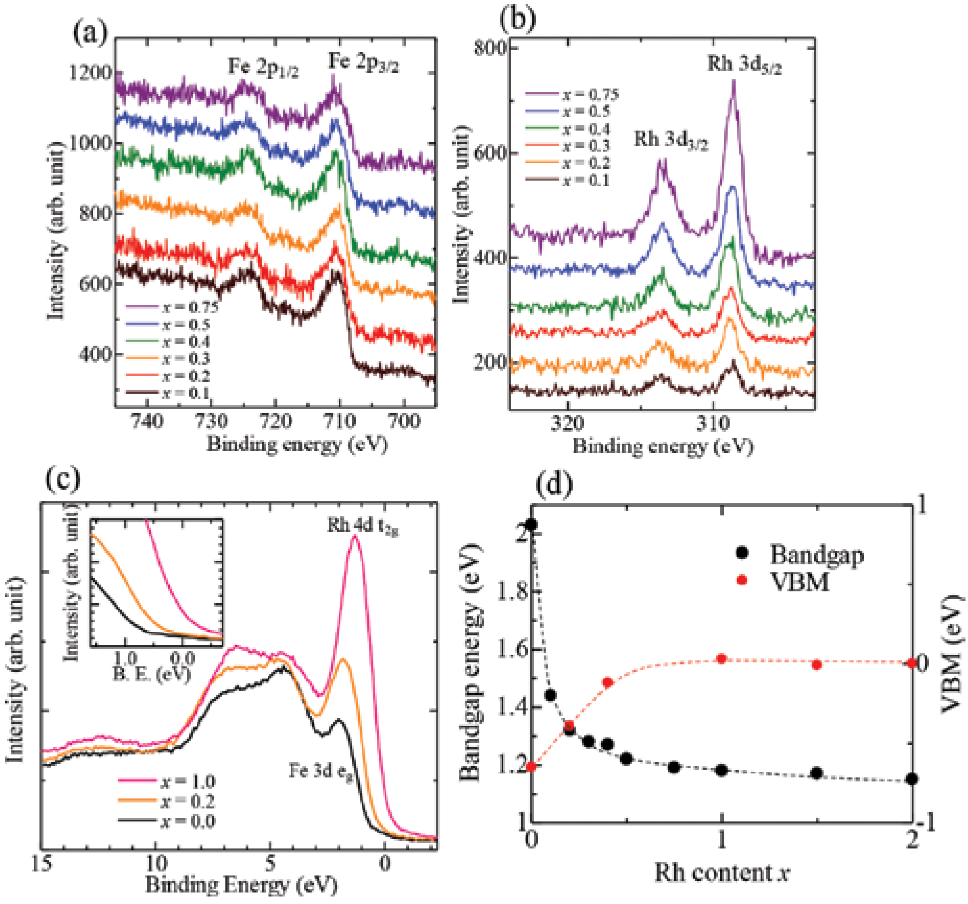

Figure 6. XPS spectra of (a) Fe 2p and (b) Rh 3d core levels for FRO films. (c) Valence band XPS spectra of FRO films. The inset shows the enlarged VB spectra near the Fermi level. (d) Compositional dependence of VBM and bandgap energy. [Copyright (2012), The Japan Society of Applied Physics].

hardly any reports of VB spectra for α-Rh_2O_3. However, by comparing with results obtained by ultraviolet photoemission spectroscopy (UPS) for $ZnRh_2O_4$ [48, 49], the peak observed at 1 eV is attributed to the t_{2g} orbitals of the RhO_6 octahedra in α-Rh_2O_3. The peaks at 2 and 3 eV are assigned to the Rh 4*d*, 5 *s*, and 5*p* mixed states [48]. The VBM and E_g exhibit a similar dependences on the Rh content, as shown in **Figure 6(d)**. In addition, the change in the VBM (0.7 eV) for $x = 1.0$ is close to the bandgap decrease (0.8 eV) for $x = 1.0$. From these results, we can conclude that the bandgap decrease by Rh substitution is due to the hybridization of the O 2*p* valence band with the Rh t_{2g} band at the VBM.

6. Photoelectrochemical properties

The current-potential curves of the films are shown in **Figure 7(a)** and **(b)**. For α-Fe_2O_3, the photocurrent is 2.87 μA/cm^2 at 0.5 V under irradiation with VIS light (λ = 400–700 nm). As shown in **Figure 7(a)**, the VIS photocurrent is remarkably increased after Rh substitution (17.3 μA/cm^2 at 0.5 V for $x = 0.2$). The effect of Rh substitution becomes more obvious with near-IR irradiation

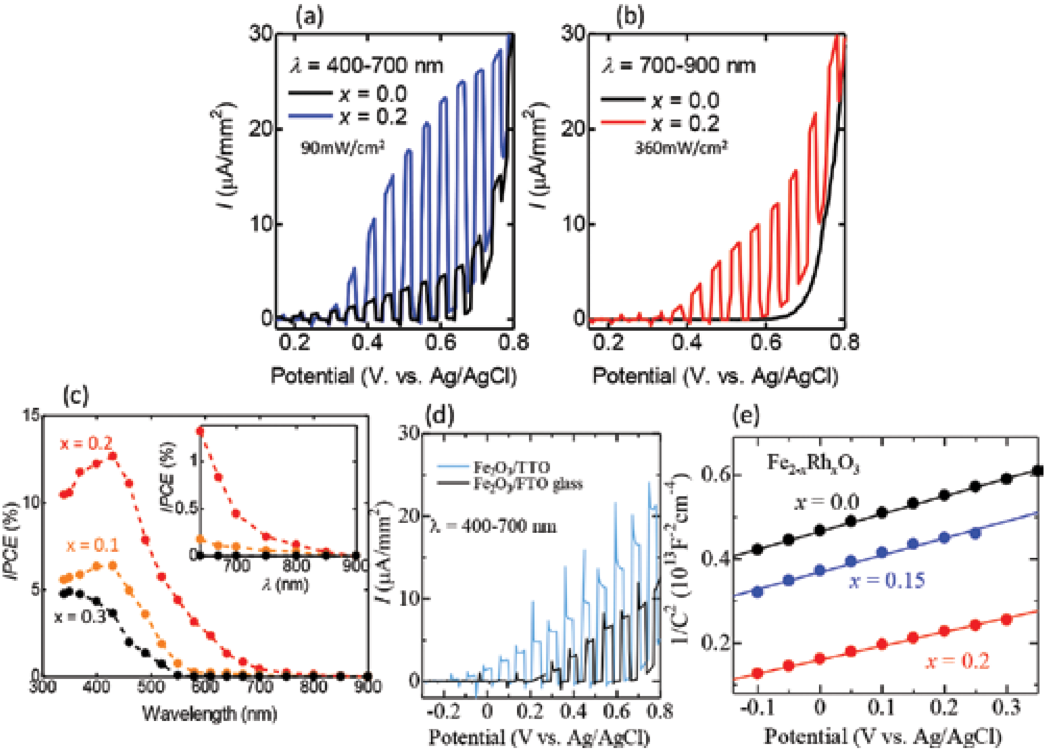

Figure 7. Chopped *I-V* curves under illumination with (a) VIS light (λ = 400–700 nm, 100 mW/cm^2) and (b) NIR light (λ = 700–900 nm, 640 mW/cm^2) for $x = 0.0$ and 0.2. (c) IPCE as a function of wavelength for the FRO films at 0.55 V vs. Ag/AgCl in an aqueous electrolytic solution containing 1.0 M NaOH. The inset shows the magnified IPCE spectra at λ = 600–900 nm (d) *I-V* curves of α-Fe_2O_3 films deposited on TTO/α-Al_2O_3(110) (blue) and FTO glass (black) substrates. (e) Mott-Schottky plots for FRO films. [Copyright (2012 and 2014), The Japan Society of Applied Physics].

(λ = 700–900 nm). As shown in **Figure 7(b)**, for $x = 0.2$, a near-IR photocurrent is evidently observed, whereas a photocurrent is hardly detected for the α-Fe_2O_3 film. These improved PEC properties of the FRO films may be caused by the increased light absorption in these wavelength regions. Furthermore, the electrical properties of the films also affect their PEC performance. The electrical conductivity for $x = 0.2$ ($\sigma = 3.8 \times 10^{-4}\ \Omega^{-1}\ cm^{-1}$ at 300 K) is significantly larger than that for $x = 0.0$ ($\sigma = 2.6 \times 10^{-6}\ \Omega^{-1}\ cm^{-1}$ at 300 K). This is possibly due to the extended profile of the Rh 4*d* state [50]. Thus, the improved electrical conductivity possibly causes an increased photocurrent by lowering the recombination rate of the photocarriers as in the case for Ti- or Si-doped α-Fe_2O_3 [22, 38, 40]. In **Figure 7(c)**, the spectra of the incident photon-to-current efficiency (IPCE) are shown. The IPCE was estimated using the following relationship: $IPCE\ (\%) = 100 \times [hc/e] \times I/[P \times \lambda]$, where h, c, e, I(mA/cm^2), and P(mW/cm^2) denote the Planck constant, the light velocity, the elementary charge, the photocurrent, and the power of the illumination per unit area, respectively [22]. The IPCE for $x = 0.1$ and 0.2 is much higher than that of α-Fe_2O_3 in the 340–850 nm wavelength region. For α-Fe_2O_3, the IPCE decreases to zero when the wavelength exceeds 610 nm, corresponding to its bandgap. On the other hand, for $x = 0.2$, the IPCE is 2.35% at 610 nm and gradually decreased to 0.11% at 850 nm as shown in the inset of **Figure 7(c)**. The IPCE decreases drastically when x exceeds 0.2 as shown in **Figure 7(c)**, and a photocurrent is hardly detected for $x \geq 0.75$ in the 340–900 nm wavelength region. These results possibly reflect the drastic change in the optical transition process caused by Rh substitution. On the one hand, the photogenerated carriers in α-Fe_2O_3 diffuse through the bands related to the Fe 3*d* and O 2*p* states [22]. On the other hand, the recombination probability of the carriers generated in α-Rh_2O_3 following the *d-d* transition in Rh^{3+} is significantly high [32, 51]. This nature impairs the PEC performance for a higher Rh content. We note that that the rate of decrease in E_g is drastically decreased when x exceeds 0.2. This result suggests that the band-edge electronic structure is not strongly influenced by Rh substitution; therefore, the *d-d* transition predominantly occurs for $x > 0.2$. The IPCE peak wavelength shifts from 350 to 430 nm as Rh content increases from $x = 0.0$ to 0.2. This is a desirable feature for energy harvesting, because the peak of the solar spectrum is at ~475 nm. The PEC properties of the polycrystalline film ($x = 0.2$) are shown in **Figure 7(d)**. The photocurrent of the single-crystal FRO grown on a TTO/Al_2O_3 (110) substrate is higher than that of the polycrystalline FRO grown on FTO glass. This result can be explained by the electronic transport properties of the films. The conductivity of the (110)-oriented single-crystalline film along the out-of-plane direction ($\sigma = 3.4 \times 10^{-4}\ \Omega^{-1}\ cm^{-1}$) is much larger than that of the polycrystalline film ($\sigma = 8.8 \times 10^{-6}\ \Omega^{-1}\ cm^{-1}$). The improvement in the electrical conductivity in the single-crystal films may accelerate the collection of photocarriers, resulting in their enhanced PEC properties. In **Figure 7(e)**, the Mott-Schottky plots are shown. The density of donors N is expressed as follows:

$$N = \left[2/(e_0\,\varepsilon_0\,\varepsilon)\right]\left[d(1/C^2)/dV\right]^{-1} \tag{1}$$

where e_0 represents an electron charge, and ε_0 and ε are the vacuum and relative electric permittivities, respectively. By employing the reported value of $\varepsilon = 80$ for hematite, the donor densities are calculated to be 4.2×10^{17} ($x = 0.2$) and 5.3×10^{17} cm^{-3} for $x = 0.0$ (hematite) and 0.2, respectively. Thus, the donor density does not significantly change after Rh substitution, in contrast to the case for Ti- or Si-doped α-Fe_2O_3. It is considered that the number of Fe^{2+} ions, which acts as electron donors, increases when Fe^{3+} is substituted with Ti^{4+} or Si^{4+} owing to the charge neutrality. In contrast, in the FRO films, the valence of the Rh ions is +3, and hence, the content of Fe^{2+} does not increase after Rh substitution. Nevertheless, the conductivity for $x = 0.2$ is two orders of magnitude larger than that for $x = 0.0$. Therefore, it is considered that the carrier mobility is remarkably increased after Rh substitution probably owing to the extended nature of the Rh 4*d* states.

7. Summary

The Rh-substituted α-Fe_2O_3 photoelectrodes were successfully fabricated using a pulsed laser deposition method. Their bandgap narrowed as the Rh content increased. XPS analyses revealed that the bandgap narrowing is brought by the hybridization of the Rh 4*d* state with the O2*p*–Fe 3*d* states at the VBM of α-Fe_2O_3. The photocurrent was significantly enhanced for lower Rh contents. Moreover, the PEC properties were improved by the control of crystal growth condition. These results will be utilized in the development of high-efficiency solar energy conversion devices based on iron oxides.

Acknowledgements

This work was supported by JSPS Core-to-Core Program, A. Advanced Research Networks, and JSPS KAKENHI grant numbers JP16K14226 and JP15H03563. The author would like to thank Prof. H. Tabata, Prof, H. Matsui, and Dr. H. Yamahara for their support and helpful discussion.

Author details

Munetoshi Seki

Address all correspondence to: m-seki@ee.t.u-tokyo.ac.jp

Center for Spintronics Research Network (CSRN), Graduate School of Engineering,
The University of Tokyo, Tokyo, Japan

References

[1] Bibes M, Berthelemy A. Oxide Spintronics. IEEE Transactions on Electron Devices. 2007;**54**:1003-1023. DOI: 10.1109/TED.2007.894366

[2] Zhang Z, Satpathy S. Electron states, magnetism, and the Verwey transition in magnetite. Physical Review B. 1991;**44**:13319-13331. DOI: 10.1103/PhysRevB.44.13319

[3] Seki M, Hossain AKM, Kawai T, Tabata H. High-temperature cluster glass state and photomagnetism in Zn and Ti-substituted $NiFe_2O_4$ films. Journal of Applied Physics. 2005; **97**:083541(1)-(6). DOI: 10.1063/1.1863422

[4] Seki M, Takahashi M, Adachi M, Yamahara H, Tabata H. Fabrication and characterization of wüstite-based epitaxial thin films: p-Type wide-gap oxide semiconductors composed of abundant elements. Applied Physics Letters. 2014;**105**:113105(1)-(4). DOI: 10.1063/1.4896316

[5] Bowen HK, Adler D, Auker BH. Electrical and optical properties of FeO. Journal of Solid State Chemistry. 1975;**12**:355-359. DOI: 10.1016/0022-4596(75)90340-0

[6] Srinivasan G, Seehra MS. Variation of magnetic properties of Fe_xO with nonstoichiometry. Journal of Applied Physics. 1984;**55**:2327-2329. DOI: 10.1063/1.333651

[7] Wang J, Neaton JB, Zheng H, Nagarajan V, Ogale SB, Liu B, Viehland D, Vaithyanathan V, Scholm DG, Waghmare UV, Spaldin NA, Rabe KM, Wutting M, Ramesh R. Epitaxial $BiFeO_3$ multiferroic thin film heterostructures. Science. 2003;**299**:1719-1722. DOI: 10.1126/science.1080615

[8] Polomska M, Kaczmarek W, Pajak Z. Electric and magnetic properties of $(Bi_{1-x}La_x)FeO_3$ solid solutions. Physica Status Solidi A. 1974;**23**:567-574. DOI: 10.1002/pssa.2210230228

[9] Sonowska I, Neumaier TP, Steichele E. Spiral magnetic ordering in bismuth ferrite. Journal of Physics C: Solid State Physics. 1982;**15**:4835-4846. DOI: 10.1088/0022-3719/15/23/020

[10] Yang SY, Martin LW, Byrnes SJ, Conry TE, Basu SR, Paran D, Reichertz L, Ihlefeld J, Adamo C, Melville A, Chu Y-H, Yang C-H, Musfeldt JL, Sholm DG, Ager III JW, Ramesh R. Photovoltaic effects in $BiFeO_3$. Applied Physics Letters. 2009;062909(1)-(3). DOI: 10.1063.1.3204695

[11] Kimizuka N, Katsura T. Standard free energy of formation of $YFeO_3$, $Y_3Fe_5O_{12}$, and a new compound YFe_2O_4 in the Fe-Fe_2O_3-Y2O_3 system at 1200°C. Journal of Solid State Chemistry. 1975;**13**:176-181. DOI: 10.1016/0022-4596(75)90116-4

[12] Ikeda N, Ohsumi H, Ohwada K, Ishii K, Imai T, Kakurai K, Murakami Y, Yoshii K, Mori S, Horibe Y, Kito H. Ferroelectricity from ion valence ordering in the charge frustrated system $LuFe_2O_4$. Nature. 2005;**436**:1136-1138. DOI: 10.1038/nature04039

[13] Xiang HJ, Whangbo M-H. Charge order and the origin of giant magnetocapacitance in $LuFe_2O_4$. Physical Review Letters. 2007;**98**:246403(1)–(4). DOI: 10.1103/PhysRevLett.98.246403

[14] Seki M, Konya T, Inaba K, Tabata H. Epitaxial thin films of $InFe_2O_4$ and $InFeO_3$ with two-dimensional triangular lattice structures grown by pulsed laser deposition. Applied Physics Express. 2010;**3**:105801(1)-(3). DOI: 10.1143/APEX.3.105801

[15] Kumar N, Kim NG, Park YA, Hur N, Jung JH, Ham KJ, Yee KJ. Epitaxial growth of terbium iron garnet thin films with out-of-plane axis of magnetization. Thin Solid Films. 2008;**516**:7753-7757. DOI: 10.1016/j.tsf.2008.05.032

[16] Krockenberger Y, Matsui H, Hasegawa T, Kawasaki M, Tokura Y. Solid phase epitaxy of ferromagnetic $Y_3Fe_5O_{12}$ garnet thin films. Applied Physics Letters. 2008;**93**:092505(1)-(3). DOI: 10.1063/1.2976747

[17] Yamahara H, Mikami M, Seki M, Tabata H. Epitaxial strain-induced magnetic anisotropy in $Sm_3Fe_5O_{12}$ thin films grown by pulsed laser deposition. Journal of Magnetism and Magnetic Materials. 2011;**323**:3143-3146. DOI: 10.1016/j.jmmm.2011.06.074

[18] Adachi M, Seki M, Yamahara H, Tabata H. Long-term potentiation of magnonic synapses by photocontrolled spin current mimicked in reentrant spin-glass garnet ferrite $Lu_3Fe_{5-2x}Co_xSi_xO_{12}$ thin films. Applied Physics Express. 2015;**91**:085118(1)-(7). DOI: 10.7567/APEX.8.043002

[19] Xu P, Han X, Wang M. Synthesis and magnetic properties of $BaFe_{12}O_{19}$ Hexaferrite nanoparticles by a reverse microemulsion technique. Journal of Physical Chemistry C. 2007;**111**:5866-5870. DOI: 10.1021/jp068955c

[20] Zi ZF, Sun YP, Zhu XB, Yang ZR, dai JM, Song WH. Structural and magnetic properties of $SrFe_{12}O_{19}$ hexaferrite synthesized by a modified chemical co-precipitation method. Journal of Magnetism and Magnetic Materials. 2008;**320**:2746-2751. DOI: 10.1016/j.jmmm.2008.06.009

[21] Chernomordik BD, Russell HB, Cvelbar U, Jasinski JB, Kumar V, Dautsch T, Sunkara MK. Photoelectrochemical activity of as-grown, α-Fe_2O_3 nanowire array electrodes for water splitting. Nanotechnology. 2012;**23**:194009(1)-(9). DOI: 10.1088/0957-4484/23/19/194009

[22] Kay A, Cesar I, Grätzel M. New benchmark for photooxidation by nanostructured α-Fe_2O_3 films. Journal of American Chemical Socety. 2006;**128**:15714-15721. DOI: 10.1021/ja0643801

[23] Thimsen E, Formal FL, Grätzel M, Warren SC. Influence of plasmonic Au nanoparticles on the photoactivity α-Fe_2O_3 electrodes for water splitting. Nano Letters. 2011;**11**:35-43. DOI: 10.1021/nl1022354

[24] Fujishima A, Honda K. Electrochemical photolysis of water at a semiconductor electrode. Nature. 1972;**238**:37-38. DOI: 10.1038/238038a0

[25] Sanchez C, Sieber KD, Somorjai GA. The photoelectrochemistry of niobium doped α-Fe_2O_3. Journal of Electroanalytical Chemistry and Interfacial Electrochemistry. 1988; **252**:269-290. DOI: 10.1016/0022-0728(88)80216-X

[26] Campbell AS, Schwertmann U, Stanjek H, Friedl J, Kyek A, Campbell PA. Si incorporation into hematite by heating Si-Fe ferrihydrite. Langmuir. 2002;**18**:7804-7809. DOI: 10.1021/la011741w

[27] Benjelloun D, Bonnet J-P, Doumerc J-P, Launay J-C, Onillon M, Hagenmuller P. Anisotropie des proprieties electriques de I'oxyde de fer $Fe_2O_3\alpha$. Materials Chemistry and Physics. 1984;**10**:503-518. DOI: 10.1016/0254-0584(84)90001-4

[28] Nakau T. Electrical conductivity of α-Fe_2O_3. Journal of the Physical Society of Japan. 1960;**15**:727-727. DOI: 10.1143/JPSJ.15.727

[29] Iordanova N, Dupuis M, Rosso KM. Charge transport in metal oxides: A theoretical study of hematite alpha-Fe_2O_3. Journal of Chemical Physics. 2005;**122**:144305(1)-(10). DOI: 10.1063/1.1869492

[30] Kwon J-H, Choi Y-H, Kim DH, Yang M, Jang J, Kim TW, Hong S-H, Kim M. Orientation relationship of polycrystalline Pd-doped SnO_2 thin film deposits on sapphire substrates. Thin Solid Films. 2008;**517**:550-553. DOI: 10.1016/j.tsf.2008.06.074

[31] Ling Y, Wang G, Wheeler DA, Zhang JZ, Li Y. Sn-doped hematite nanostructures for photoelectrochemical water splitting. Nano Letters. 2011;**11**:211-2125. DOI: 10.1021/nl200708y

[32] Koffyberg JP. Optical bandgaps and electron affinities of semiconducting Rh_2O_3(I) and Rh_2O_3(III). Journal of Physics and Chemistry of Solids. 1992;**53**:1285-1288. DOI: 10.1016/0022-3697(92)90247-B

[33] Seki M, Yamahara H, Tabata H. Enhanced photocurrent in Rh-substituted α-Fe_2O_3 thin films grown by pulsed laser deposition. Applied Physics Express. 2012;**5**:115801(1)-(3). DOI: 10.1143/APEX.5.115801

[34] Seki M, Takahashi M, Ohshima T, Yamahara H, Tabata H. Solid-liquid-type solar cell based on α-Fe_2O_3 heterostructures for solar energy harvesting. Japanese Journal of Applied Physics. 2014;**53**:05FA07(1)–(6). DOI: 10.7567/JJAP.53.05FA07

[35] Mashiko H, Oshima T, Otomo A. Band-gap narrowing in α-$(Cr_xFe_{1-x})_2O_3$ solid-solution films. Applied Physics Letters. 2011;**99**:241904(1)–(3). DOI: 10.1063/1.3669704

[36] Moore EA. First-principles study of the mixed oxide α-$FeCrO_3$. Physical Review B. 2007; **76**:195107(1)–(7). DOI: 10.1103/PhysRevB.76.195107

[37] Uemoto K, Wentzcovitch RM. Effect of the d electrons on phase transitions in transition metal sesquioxides. Physics and Chemistry of Minerals. 2011;**38**:387-395. DOI: 10.1007/s00269-010-0412-1

[38] Sartoretti CJ, Alexander BD, Solarska R, Rutkowska IA, Augustynski J, Cerny R. Photochemical oxidation of water at transparent ferric oxide film electrodes. Journal of Physical Chemistry B. 2005;**109**:13685-13692. DOI: 10.1021/jp051546g

[39] Beatham N, Orchard AF, Thornton G. X-ray and UV photoelectron spectra of the metal sesquioxides. Journal of Physics and Chemistry of Solids. 1981;**42**:1051-1055. DOI: 10.1016/0022-3697(81)90129-3

[40] Tang H, Matin MA, Wang H, Deutsh T, Al-Jassim M, Turner J, Yan Y. Synthesis and characterization of titanium-alloyed hematite thin film for photoelectrochemical water splitting. Journal of Applied Physics. 2011;**110**:123511(1)–(7). DOI: 10.1063/1/3671414

[41] Temesghen W, Sherwood P. Analytical utility of valence band X-ray photoelectron spectroscopy of iron and its oxides, with spectral interpretation by cluster and band structure calculations. Analytical and Bioanalytical Chemistry. 2002;**373**:601-608. DOI: 10.1007/s00216-002-1362-3

[42] Fujii T, Groot FMF, Sawatzky GA, Voogt FC, Hibma T, Okada K. In situ XPS analysis of various iron oxide films grown by NO_2-assisted molecular beam epitaxy. Physical Review B. 1999;**59**:3195-3202. DOI: 10.1103/PhysRevB.59.3195

[43] McIntyre NS, Zetaruk DG. X-ray photoelectron spectroscopic studies of iron oxides. Analytical Chemistry. 1977;**49**:1521-1529. DOI: 10.1021/ac50019a016

[44] Abe Y, Kato K, Kawamura M, Sakai K. Rhodium and rhodium oxide thin films characterized by XPS. Surface Science Spectra. 2001;**8**:117-125. DOI: 10.1116/11.20010801

[45] Blomberg S, Lundgren E, Westerström R, Erdogan E, Martin NM, Mikkelsen A, Andersen JN. Structure of the Rh_2O_3 (0001) surface. Surface Science. 2012;**606**:1416-1421

[46] Uekawa N, Kaneko K. Nonstoichiometric properties of nanoporous iron oxide films. Journal of Physical Chemistry B. 1998;**102**:8719-8724. DOI: 10.1021/jp982249x

[47] Tossell JA, Vaughan DJ, Johnson KH. Electronic structure of ferric iron octahedrally coordinated to oxygen. Nature Physical Science. 1973;**244**:42-45. DOI: 10.1038/physci244042a0

[48] Mizoguchi H, Hirano M, Fujitsu S, Takeuchi T, Ueda K, Hosono H. $ZnRh_2O_4$: A p-type semiconducting oxide with a valence band composed of a low spin state of Rh^{3+} in a $4d^6$ configuration. Applied Physics Letters. 2002;**80**:1207-1209. DOI: 10.1063/1.1450252

[49] Dekkers M, Rijnders G, Blank DHA. $ZnIr_2O_4$, a p-type transparent oxide semiconductor in the class of spinel zinc-d^6-transition metal oxide. Applied Physics Letters. 2007; **90**:021903(1)-(3). DOI: 10.1063/1.2431548

[50] Lee YS, Lee JS, Noh TW, Byun DY, Yoo KS, Yamaura K, Takayama-Muromachi E. Systematic trends in the electronic structure parameters of the 4d transition-metal oxides $SrMO_3$ (M = Zr, Mo, Ru, and Rh). Physical Review B. 2003;**67**:113101(1)–(4). DOI: 10.1103/PhysRevB67.113101

[51] Walter MG, Warren L, McKone JR, Boettcher SW, Mi Q, Santori EA, Lewis NS. Solar water splitting cells. Chemical Reviews. 2010;**110**:6446-6473. DOI: 10.1021/cr1002326

Edited by Volodymyr Shatokha

This book provides the multidisciplinary reading audience with a comprehensive state-of-the-art overview of research and innovations in the relationship between iron ores and iron ore materials. The book covers industrial sectors dealing with exploration and processing of iron ores as well as with advanced applications for iron ore materials and therefore entails a wide range of research fields including geology, exploration, beneficiation, agglomeration, reduction, smelting, and so on, thus encouraging life cycle thinking across the entire production chain.

Iron remains the basis of modern civilization, and our sustainable future deeply depends upon our ability to satisfy the growing demand for iron and steel while decoupling hazardous emissions from economic growth. Therefore, environmental sustainability aspects are also broadly addressed.

In response to socioeconomic and climatic challenges, the iron ore sector faces, this book delivers a vision for the new opportunities linked to deployment of the best available, innovative and breakthrough technologies as well as to advanced material applications.

Published in London, UK

IntechOpen

ISBN 978-1-83881-411-3
9 781838 814113